UNIVERSITÀ DEGLI STUDI DI NAPOLI FEDERICO II

PHD PROGRAM IN NOVEL TECHNOLOGIES FOR MATERIALS, SENSORS AND IMAGING (TIMSI) – XXVI CYCLE

PhD Dissertation

2D HIGHLY SENSITIVE PLASMONIC "LABEL FREE" NANOBIOSENSORS BASED ON PHOTONIC CRYSTALS AND PHOTONIC QUASI-CRYSTALS

TUTOR: PHD STUDENT:

DR. LUCIA PETTI   ROSSELLA CAPASSO

March 2014

To my parents

Their constant support made me what I am today.

For that, and for an infinity of other reasons,

I am forever indebted to them.

Preface

This work is submitted for a Doctor of Philosophy degree (PhD) in Novel Technologies for Materials, Sensors an Imaging. The work was supervised by Dr. L. Petti of the Cybernetic Institute of CNR (Pozzuoli-Naples).

The research activity of this PhD thesis has been carried out in between two different Institutes of CNR: the Cybernetic Institute for the nanofabrication of innovative materials and their optical characterization, and ICTP-CNR (now IPCB) for the Raman Characterization of SERS substrates. The experimental results obtained are due to a very close collaboration with Dr. Pellegrino Musto (Head of the Molecular Spectroscopy Lab at ICTP-CNR) and part of his team (Dr. Marianna Pannico and Dr. Pietro La Manna). A large contribution was also provided by Dr. Maria Grazia Maglione and Dr. Eugenia Bobeico from the UTTP group of ENEA Research Center (Portici) who both supported and offered us the possibility to use their thermal and e-beam evaporators for metal depositions. Silver Nanowires in ethanol used for some substrates were provided by Prof. W. Song group from Ningbo Institute of Material Technology and Engineering (NIMTE), China.

Abstract

The control of light with artificial structures is one of the key issues in modern photonics. Since the initial discovery of Surface-Enhanced Raman Scattering (SERS), an increased amount of work has been done on the research of substrates for highly efficient Raman scattering enhancement due to their extraordinary potential for trace analysis and biological tags. Recently, the plasmonic optical responses of metal nanoparticles, based on Localized Surface Plasmon Resonances (LSPR) in the visible and near IR region, have been intensively researched. It has been demonstrated that the plasmon resonance is closely related to the size and shape of metal nanoparticles and to the dielectric properties of the surrounding medium. In SERS spectroscopy it is of crucial importance to develop systems of interacting metal nanostructures capable of producing high field enhancement with highly reproducible characteristics on controllable metal-dielectric substrates. The possibility of engineering complex metal nanoparticle arrays with distinctive plasmonic resonances extending across the entire visible spectrum can have a significant impact on the design and fabrication of novel nanodevices based on broadband plasmonic enhancement. In the last decade, artificial Electro Magnetic (EM) materials, including photonic crystals (PCs) and photonic quasi-crystals (PQCs), have remarkably attracted the scientific community, due to the new possibilities enabled - still largely unexplored - to control the EM field in an unprecedented way. The potentials exhibited by such materials in several application scenarios are also of interest in the field of biological sensing. The degrees of freedom allowed by artificial materials, in fact, lead to an advanced control of the interaction between the EM field which arise in the proximity of a metallic nanostructures and the biological matter, with the possibility to design innovative EM sensors, characterized by superior performances with respect to their traditional counterparts. The principal object of this PhD research activity is the design, fabrication and characterization of plasmonic nanostructures to be used as biosensors. Exploiting PCs and PQCs, in fact, it is possible to synthesize innovative artificial structures, characterized by very selective EM responses to be used as plasmonically-active Surface Enhanced Raman Scattering (SERS) substrates. In order to fabricate SERS-active substrates suitable for sensing applications, a well-tested nanofabrication process by electron-beam lithography (EBL) technique, for the realization of easily manufacturable and reproducible devices, has been developed passing through the necessary design steps, and arriving at the fabrication, optical characterizations and experimental SERS characterizations first with a commercial molecular probe (p-mercaptoaniline - pMA) and then using a culture of Human prostate deseased cells as real analyte.

Herein, we report our successful attempt to utilize both bottom-up approach and a top-down technique to realize efficient SERS substrates. An effective and facile method for the fabrication of a SERS-active film with Silver nanowires (NWs) is proposed by drop casting of Silver NWs on glass with ethanol as the inducer. Alternatively, Au PCs and PQCs are proposed for the engineering of reproducible SERS substrates. Using a molecular monolayer of pMA as a Raman reporter, we show that high values of SERS enhancement factors can be achieved in PQCs structures and in Silver NWs substrates. To demonstrate the feasibility of the fabricated nanostructures as efficient SERS substrates for biological applications, we devised a method to deposit single cells (human prostatic) on the photonic surfaces. Preliminary results on SERS sampling of single prostatic human cells indicated that the proposed engineered metamaterials may be used as an ultrasensitive Raman probe to monitor subtle molecular changes in the cell and open up interesting new opportunities in biosensing.

Finally, novel types of sensing nanodevices, coupling biosensing to MetaMaterials properties have been realized, to explore the peculiar properties of such kind of structures in combination with plasmonic nano-optics.

These type of sensors would likelihood represent a promising step toward future reproducible single-molecule detection using engineered plasmonic substrates.

Acknowledgements

First and foremost I would like to deeply thank my supervisor Dr. Lucia Petti for the opportunity to be a part of her research group. She is truly a generous advisor and educator. I have acquired a tremendous amount of knowledge and real field experience from her deep understanding of nanofabrication and metamaterials. Her advices and encouragements, and expecially her patience and trust all along this thesis, have been very important for me. Also want to thank Dr. Pasquale Mormile for his presence and assistance all along my work. A special thank goes to Dr. Pellegrino Musto for his strong assistance in theoretical chemistry and spectroscopy. My experience with him represent for me a lasting education in academic research and beyond. A special thank also to hi fantastic team: Dr. Marianna Pannico for her help in this three years and expecially in this last month...“thank you Marianna for "having found time for me, even when you did not have enough for youself”, and Dr. Pietro La Manna for his precious contribution.

At ICIB-CNR, I had the opportunity to interact directly with, and learn from, a group of great scientists. I want to kindly thank Dr. Debora Paris, Dr. Maria Adamo and Dr. Roberto Russo for their moral support, advices and encouragements, and especially for having listened with patience to my crazy speeches; Dr. Massimo Rippa for having always paused his activities to answer my many questions on Optics, Physics (but not only on that) and for his fondamental scientific contributes to this thesis; Dr. Mikhail Lisitskiy for the support and competences he offered me in many occasions.

During the PhD activities I have established a wide network of collaborations and scientific friendships, and I want to thank all the people that, in a way or in another, helped me to achieve the results presented in this thesis, and in the other research activities I'm involved in: Dr. Giuseppe Nenna, Dr. Anna De Girolamo Del Mauro, Dr. Maria Grazia Maglione, Dr. Eugenia Bobeico (UTTP-ENEA); Dr. Vincenzo Caligiuri, Dr. Giovanna Palermo, Prof. Cesare Umeton (UNICAL); Dr. Luciano De Sio (Beam&Co.); Dr. Luca Maresca (DIETI-UNINA). I would like to thank them all expecially for the interesting and opening-mind conversations we had.

Furthermore, I want to share this great moment in my life with all my friends. Without their help, patience and support this work would surely not have been possible.

I will never thank enough my parents, my sister, Ilaria and my cat, Maya for their unconditioned endless love.

Finally, a special and sweet thank is for Luca firstly for his indispensable technical support, and foremost for his care and determination, and his encouragements throughout my endeavor...he was able to give me the best gift of my life: Love!

“It is our choices that show what we truly are, far more than our abilities”

J.K. Rowling

TABLE OF CONTENTS

Chapter 1: Introduction

There's Plenty of Room at the Bottom
Richard P. Feynman 1959

1.1 A tendency toward smaller and smaller

A new world is coming into being. A scientific revolution is in full swing – a revolution that could profoundly change our future on a daily basis and in many areas. A revolution that is already allowing us to conceive of smaller, lighter, less expensive products; that promises more powerful computers and faster communication, not to mention more effective medical treatments, a cleaner environment, a more pleasant lifestyle. A world that shall develop ever-smaller new materials and components, build new molecules atom-by-atom and assemble them to exploit new phenomena that will only appear on the nanometer's scale. In the last decade we have seen a true explosion of research in nanoscience and developments in nanotechnologies. One measure of the emergence of these fields is the growth of the literature dedicated to the new disciplines. Nanoscience and nanotechnology have, in the last years, witnessed not only an explosive growth in the number of relevant and important ''classical'' scientific journals, which have devoted, more and more, an increasing proportion of their published papers to ''nano''-related research, but also in the number of new journals which contain the stem ''nano''in their title. Only a few of them appeared before 2000 and most of them started their activity in the last four years.

Nanotechnology and nanoscience are concerned with material science and its application at, or around, the nanometer scale (1 nm = 10^{-9} m, 1 billionth of a meter). The nano scale, which is about 1 to 100 nanometers, can be reached either from the top down, by machining to smaller and smaller dimension, or from the bottom up, by exploiting the ability of molecules and biological systems to self-assemble tiny structures. Individual inorganic and organic nanostructures involve clusters, nanoparticles, nanocrystals, quantum dots, nanowires, and nanotubes, while collections of nanostructures involve arrays, assemblies, and superlattices of individual nanostructures. Rather than a new specific area of science, nanoscience is a new way of thinking. Its revolutionary potential lies in its intrinsic multidisciplinarity. Its development and successes strongly depend on efforts from, and fruitful interactions among, physics, chemistry, mathematics, life sciences, and engineering [1].

A great definition has come from Nanowerk defining nanoscience as:

'*The study of phenomena and manipulation of materials at atomic, molecular and macromolecular scales, where properties differ significantly from those at a larger scale; and nanotechnologies as the design, characterisation, production and application of structures, devices and systems by controlling shape and size at the nanometer scale.*'[2]

The ideas and concepts behind nanoscience and nanotechnology started with a talk entitled "*There's Plenty of Room at the Bottom*" by physicist Richard Feynman (*Fig. 1.1*) at an *American Physical Society meeting at the California Institute of Technology* (CalTech) on December 29, 1959. He described a process in which scientists would be able to manipulate and control individual atoms and molecole [3]. Over a decade later, in his explorations of ultraprecision machining, Professor Norio Taniguchi coined the term *nanotechnology*. It wasn't until 1981, with the development of the scanning tunneling microscope that could "see" individual atoms, that modern nanotechnology began.[4]
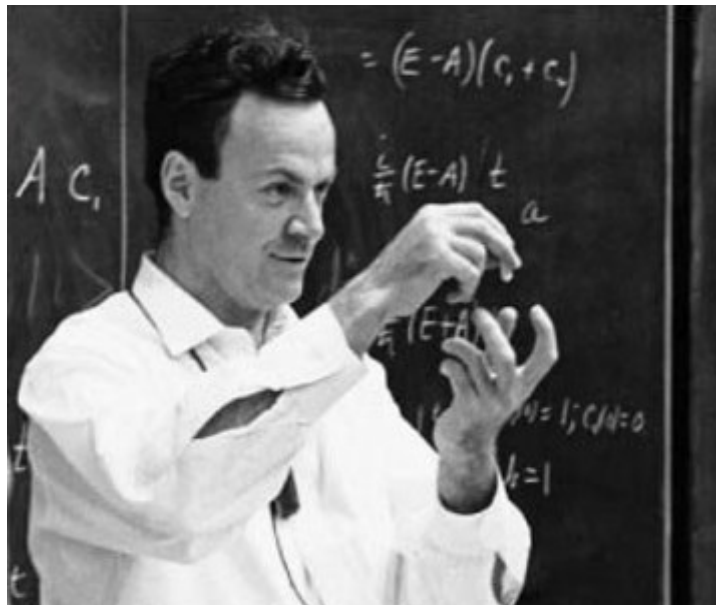
Fig. 1.1: Physicist Richard Feynman, the father of nanotechnology (CalTech archives)

When talking about the basics of nanotechnology, it is important to first know how small 'nano' actually is taking into account that 1 nanometre – 1,000,000,000th of a metre.

This clearly shows how small a nano is. It is even smaller than the wavelength of visible light and a hundred-thousandth the width of a human hair. But it is still small when compared to the atomic scale: Atomic diameter – 0.1 nanometre – 10000,000,000th of a metre.

The usual scale of some common man made materials are compared with nano devices in the following Fig. (*Fig. 1.2*)
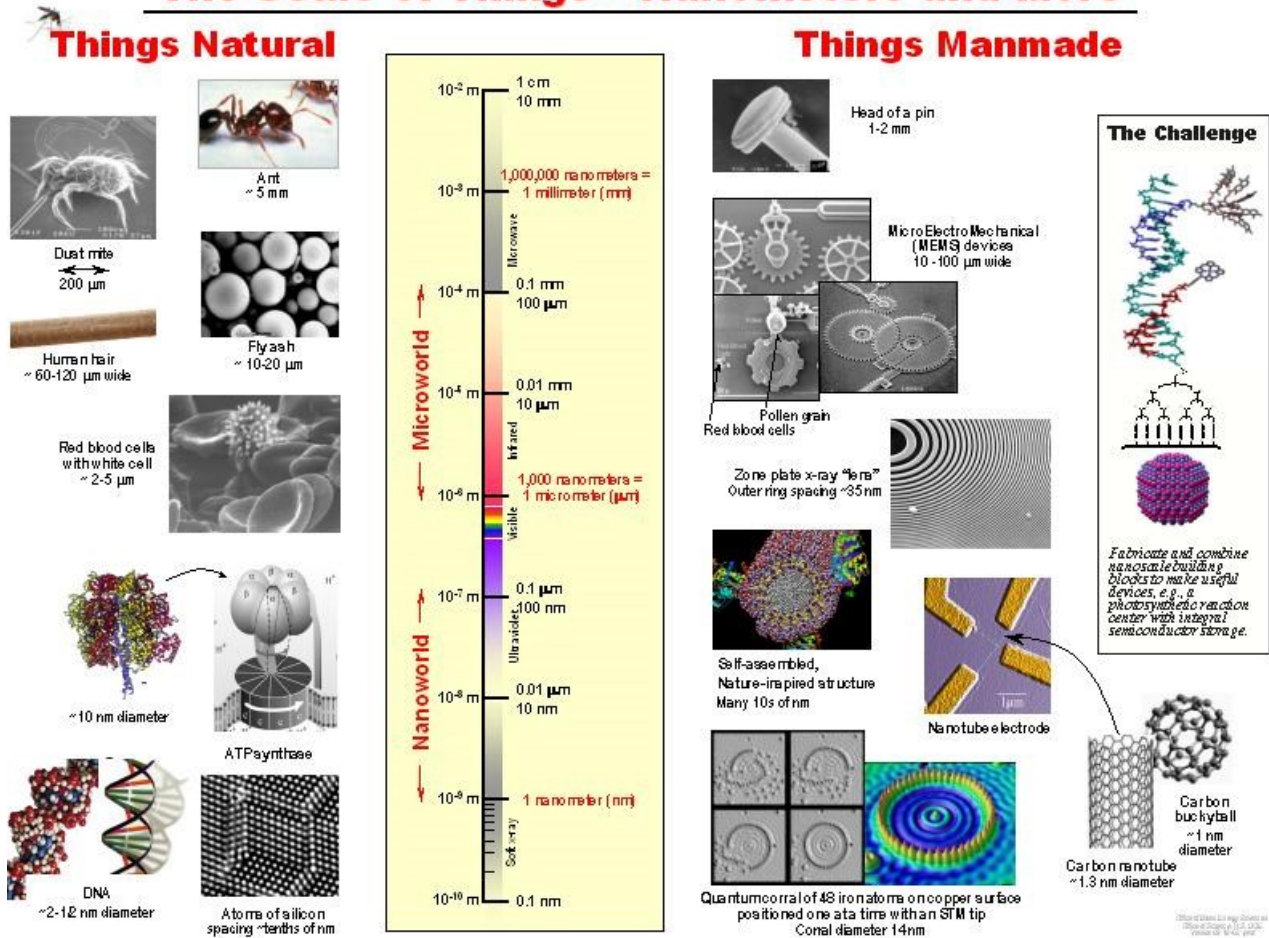
Fig. 1.2: Scale of Natural and man-made things

The microscopes needed to see things at the nanoscale were invented relatively recently—about 30 years ago. Once scientists had the right tools, such as the scanning tunneling microscope (STM) and the atomic force microscope (AFM), the age of nanotechnology was born.

Although modern nanoscience and nanotechnology are quite new, nanoscale materials were used for centuries. Alternate-sized gold and silver particles created colors in the stained glass windows of medieval churches hundreds of years ago. The artists back then just didn't know that the process they used to create these beautiful works of art actually led to changes in the composition of the materials they were working with.

*The **Lycurgus Cup** (Rome) is an example of **dichroic glass**; colloidal gold and silver in the glass allow it to look opaque green when lit from outside but translucent red when light shines through the inside.*
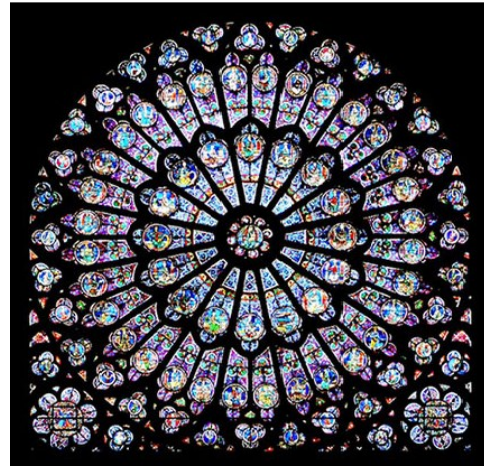
*The **South rose window** of Notre Dame Cathedral, Paris, about 1250*

Today's scientists and engineers are finding a wide variety of ways to deliberately make materials at the nanoscale to take advantage of their enhanced properties such as higher strength, lighter weight, increased control of light spectrum, and greater chemical reactivity than their larger-scale counterparts. Thus, nanotechnology is the engineering method in which fully functioning devices are manufactured at the molecular scale. Through this method, the devices that are manufactured will be having higher performance than the conventional ones.

Undoubtedly, nanotechnology is going to be the future (*Fig. 1.3*) as studies are going on in diversifying the technology from materials with dimensions in nano scale to materials in dimensions of atomic scale. Many unique properties and uses can be derived from structures built at the nanoscale, giving nanotechnology enormous potential for future development. Further into the future, nanotechnology will play a major role in medicine and longevity. Blood cell-sized devices will go directly into the human body, eradicating pathogens and keeping people healthy.

Meanwhile, so-called "nanofabricators" would allow the creation of macro-scale objects on an atom-by-atom basis. Home appliances using this technology could serve as 3-D printers - downloading products from the web and literally building them from scratch. Physical items would each have their own code or algorithm that would program the machine to create them. Quantum computers, invisibility cloaks and space elevators may one day become a reality, thanks to nanotech.
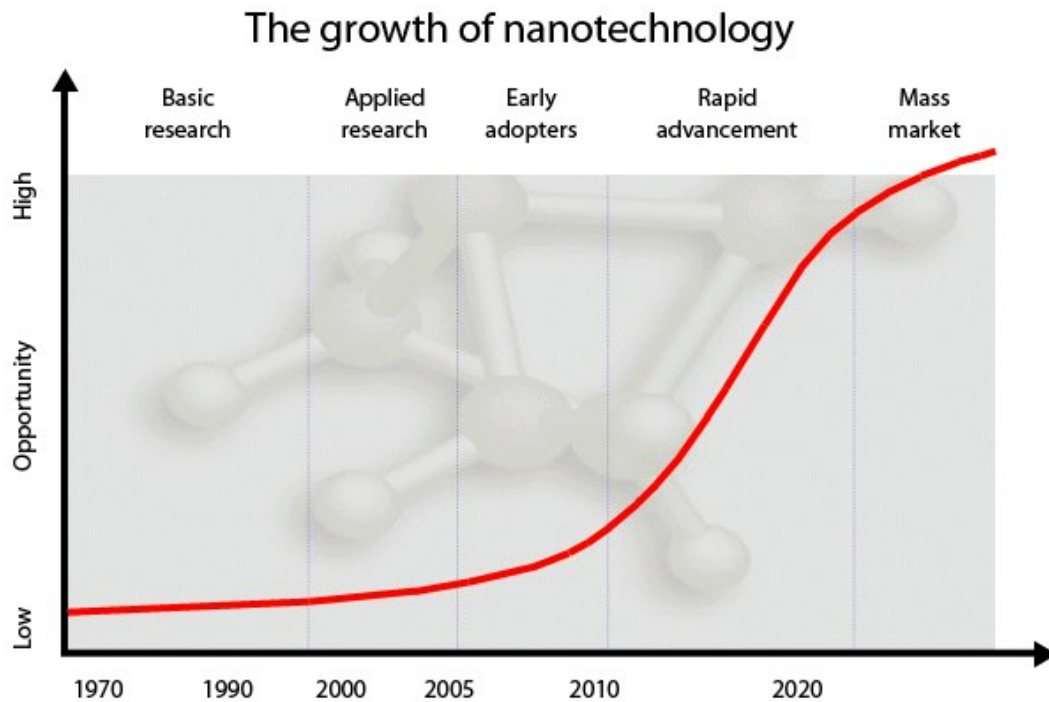
Fig. 1.3: A prevision of growth of nanotechnologies

1.2 Motivation and objectives

As the matter of fact that Nanotechnology is driven by the desire to fabricate materials with novel and improved properties that are likely to impact virtually all areas of physical and chemical sciences, biological sciences, health sciences, and other interdisciplinary fields of science and engineering, particularly, one of the major breakthroughs in nanotechnology science lies on the development of biomedicine applications, such as biological sensors.

They play an important role in different scientific fields, including disease diagnostics, environment monitoring, food integrity check, etc., and represent essential tools for the study of biological phenomena. From a general point of view, a biosensor may be defined as a measurement system, operating under the fundamental principles of biological recognition and sensing, consisting in two basic components (*Fig. 1.4*):

(1) a biochemical recognition element (the bioreceptor), which should provide the sensor with a high degree of selectivity and sensitivity towards the analyte to be detected and;

(2) a transducer, which converts the interaction of the analyte with the bioreceptor into some kind of detectable and/or measurable signal [5]

Fig. 1.4: A general scheme of a biosensor

Biosensors are usually classified in terms of the different physical mechanisms behind their operation. Sensors based on fluorescence [6] have been demonstrated to be useful, for instance, in the analysis of proteomic and genomic chains [7-8] and in probing single molecules in living cells [9]. However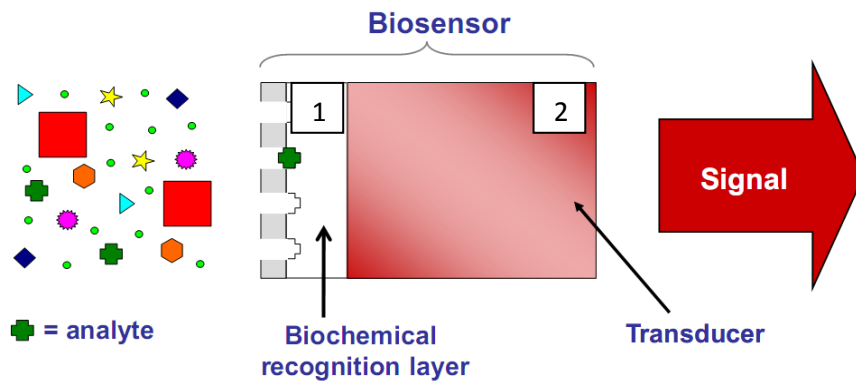, marking the molecules through fluorescent substances may result an expensive and lengthy procedure, and in some cases even not viable. The EM response of biological specimens and molecules, in fact, is typically related to their three-dimensional structures, which can be affected by the presence of the marker. For the aforementioned reasons, the recent trend in biological sensing is to avoid marking procedures and perform a direct measure of the sample. In this case, the transduction mechanisms used are different: mechanical (variation of the resonance frequency of piezoelectric resonators due to the adsorbed molecule) [10], electrical (variation of the electric conductivity of the sensor due to the molecule) [11], optical (variation of the resonance frequency of optical resonances due to the variation of the refractive index, caused by the presence of the molecule) [12]. For what concerns the latter transduction mechanism, which is the one assuring the best performance in terms of sensor selectivity and dimensions, the recently proposed devices are mainly based on the excitation of high-quality-factor surface plasmons on flat metallic surfaces. In this case, the frequency shift of the plasmonic resonance allows to determine the index of refraction of the biological sample, and, thus, the presence of the molecule. Though this method allows a direct sensing of the molecule without employing markers, the experimental setup required is rather complex, due to the need of prisms to couple the impinging light to the surface plasmons. The employment of either a patterned metallic surface or a surface consisting of a planar array of metallic nano-particles, led to solve

these experimental issues, to excite the needed plasmonic resonance through direct illumination of the surface, without using complex setups, and to perform the measurements by using conventional transmission spectroscopy techniques. The dramatic reduction of the complexity of the experimental setup has been certainly one of the key aspect for the success and for attracting the interest of the bio-sensing community in planar arrays of metallic nano-structures. In addition, this extremely easy experimental setup allows also a real-time analysis of a biological sample immobilized on the sensor (thanks to the shift of the peaks in transmission-reflection spectra) [13].

Recently, there has been growing interest in the applications of vibrational spectroscopic methods such as Raman spectroscopy for microbial and biomaterial analyses because it is extremely selective, non destructive with the advantage to analyze the sample on-line, in real time with minimum preparation. In particular, Surface enhanced Raman scattering (SERS), ought to its capability of increasing the Raman sensitivity, when molecules are attached or in close proximity of metal-nanostructures is one of the leading techniques for molecular analysis with sensitivity down to single molecule. SERS spectroscopy is a well-established and highly sensitive technique for investigating the specific vibrational response of a variety of different analytes with fingerprinting accuracy. Recent advances have led to many novel applications of SERS for biological analyses and medical diagnostics for cancer, diabetes, and other diseases. In particular, the SERS technique has been successfully applied to label-free chemical and biological sensing [14-15].

It is now generally believed that the dramatic enhancement of the Raman scattering efficiency observed in SERS experiments is mainly driven by the enhanced local electromagnetic fields in nanostructured metal surfaces. In fact, despite SERS enhancement can also be affected by the specific electronic resonances (electronic enhancement) of Raman-active molecules and by their direct contact with metal surfaces (chemical enhancement), the dominant factor originates from a resonance effect between the incident and the scattered radiation fields associated to the excitation of surface plasmon resonances. Therefore, in SERS spectroscopy it is of crucial importance to develop systems of interacting metal nanostructures capable of producing high field enhancement with highly reproducible characteristics on controllable metal-dielectric substrates. SERS substrates are very suitable in the study of biological systems where the ability to dynamically and quantitatively measure the molecular processes with high sensitivity, speed, flexibility, multiplexity, throughput, and reproducibility is strictly

required. SERS substrates can also be considered as **Plasmonic nanobiosensors** and are built on the synergetic combination of engineered plasmonic nanostructures, plasmonics, and surface biofunctionalization. They have **tunable optical properties** to fit a wide variety of applications, the frequency and intensity of the nanoparticle LSPR extinction or scattering bands are highly sensitive to size, shape, orientation, composition, and structure (e.g., shell-core structure) of NPs, and moreover have a **label-free nature**, so no fluorescent dyes are needed. Previous studies revealed that local electromagnetic fields can be dramatically enhanced in the junctions between closely separated particles, forming so-called electromagnetic "hot spots" [16]. Alternatively, individual nanoparticles deposited on planar substrates generate high Raman enhancements, which follow the plasmon resonance of individual particles. However, up to now (see Chapter 3-SERS substrates), the best approaches to generate efficient SERS surfaces rely on random "roughening" of metal surfaces by etching or by colloidal synthesis of nanoparticles resulting in aggregates statistically described by fractal morphologies [17]. Fractal aggregates and rough metal surfaces led to successful applications in single molecule spectroscopy, but they lack reproducibility and simple engineering design rules for deterministic optimization. Raman enhancement factors of $\sim 10^8$ have been reported in Ag nanoparticle arrays fabricated by the nanosphere lithography [18-20].

On the other hand, Electron beam lithography (EBL) can be considered as an ideal method for the fabrication of these engineered SERS substrates by controlling both the shape and the position of each particle at the nanoscale, with very high repeatability and reproducibility. The possibility of engineering complex metal nanoparticle arrays with distinctive plasmonic resonances extending across the entire visible spectrum can have a significant impact on the design and fabrication of novel nanodevices based on broadband plasmonic enhancement.

During the last decade, the tremendous advances in material science and technology have led to the synthesis and implementation of new classes of artificial materials, exhibiting anomalous effects, such as negative refraction, EM band-gaps, optical magnetism - all phenomena not readily available in natural materials at the frequencies of interest. Artificial materials are typically made of ordered or disordered arrangements of elementary electrically-small metallic or dielectric inclusions, spaced by distances which can be of the same order or very small compared to the operating wavelength. Among the possible classes, we consider here the so-called "photonic crystals" and "photonic quasi-crystals" (PQCs) - also known as photonic band-gap materials - characterized by inclusion spacing of the same order

of the wavelength, and the so-called "metamaterials" (MTMs), characterized by inclusion spacing smaller than the wavelength and, thus, describable through effective macroscopic constitutive parameters.

The tremendous potentials that such materials have already demonstrated in different application scenarios [21-28] are now eliciting great interest also in biological sensing. The degrees of freedom offered by artificial materials, in fact, allow an advanced and unprecedented control of the interaction between the EM field and biological matter, enabling the design of innovative EM sensors with superior performance with respect to their traditional counterparts.

A very important part of this PhD activity has been focused on studying artificial electromagnetic (EM) nanomaterials for developing innovative plasmonic nanobiosensors based on SERS (working in the visible frequency band). By means of Photonic crystals (PCs) and Photonic Quasi crystals (PQCs), it is possible to synthesize novel artificial structures characterized by selective EM responses exhibiting noticeable enhancement of Raman signals in presence of biological materials.

1.3 Organization of this PhD thesis

The research activity, both theoretical and experimental, object of this PhD thesis work, is described in nine chapters.

Chapter 1- Introduction: Introduce the PhD research activity with a brief overview on historical background and developments in nanotechnology and nano science, then motivations and objectives are explained with a particular focussing on the importance of nanobiosensors.

Chapter 2- Introduction to Raman Spectroscopy and SERS effect: A general historical and theoretical overview on Raman spectroscopy and Surface Enhanced Raman spectroscopy (SERS) effect mechanisms are provided.

Chapter 3- SERS substrates: State of the art: A brief overview on SERS substrates design is explained, followed by a brief discussion of various techniques, both bottom-up and top-down, currently used in the fabrication of SERS substrates.

Chapter 4- Photonic Crystals & Photonic Quasi-Crystals: A general introduction such as definition, history, theory and future aspects of photonic crystals and quasi-crystals are discussed.

Chapter 5- Experimental apparatus EBL litography*:* In this chapter, the fundamentals of the Electron Beam Lithography technique are presented. After an introduction about EBL technology and applications, the physics of the electron-beam exposure process is outlined through a thorough description of the electron-solid interactions, the proximity effect and a description of resist materials available.

Chapter 6- Fabrication of SERS substrates*:* Represents the core of the PhD research activity. A bottom-up approach in order to obtain Silver NanoWires (AgNWs) based substrate is described, and a top-down fabrication process exploiting EBL of engineered SERS substrates are outlined step-by-step. An in depth morphological and metrological Scanning Electron Microscopy (SEM) analysis of the obtained substrates is provided.

Chapter 7- Optical & Raman Spectroscopy characterization of SERS substrates*:* In this chapter firstly we show a morphological characterization of PQCs structures through a Far Field Diffraction (FFD) pattern analysis; then the Raman Characterization of the fabricated devices using a molecular probe (pMA) as test probe and the determination of the SERS enhancement factors are addressed; the experimental setup is described and the collected data analysed and compared.

Chapter 8- Nanobiosensors device realization and testing: the use of the fabricated device with biological analytes and the determination of the SERS spectra of human prostate cells, as first real analyte used, are discussed.

Chapter 9- Conclusions*:* The research activity is summarized and conclusive considerations about the obtained results are provided with a particular reference to future developments and further investigations about.

References

[1] Boriesko, Ossicini, *"What is the nanoworld – Handbook of Nanoscience and Nanotechnology"*, WILEY-VCH Verlag GmbH & Co.KGaA, Weinheim 2008

[2] http://www.nanowerk.com/nanotechnology/introduction/introduction_to_nanotechnology_1a.php

[3] http://www.feynmanlectures.caltech.edu/

[4] Norio Taniguchi, *Nanotechnology-Integrated Processing Systems for Ultra-precision and Ultra-fine Products,* Oxford University Press 1996

[5] T. Vo-Dinh *"Nanobiosensors"*, in Encyclopedia of Nanoscience and Nanotechnology, H.S. Nalwa, Ed., ***Am. Sci. Publishers***, Vol. 6, pp. 53-60 (2004)

[6] X. Michalet, et al. *"The power and prospects of fluorescence microscopies and spectroscopies,"* ***Annu. Rev. Biophys. Biomol. Struct***. 32, 161 (2003)

[7] G.H.W. Sanders, A. Manz, *"Chip-based microsystems for genomic and proteomic analysis,"* ***Trends Anal. Chem***. 19, 364 (2000)

[8] S. Solinas Toldo, et al. *"Matrix-based comparative genomic hybridization: biochips to screen for genomic imbalances,"* ***Genes Chromosomes Cancer*** 20, 399 (1997)

[9] S.E.D. Webb, et al. *"Single-molecule imaging and fluorescence lifetime imaging microscopy show different structures for high- and low-affinity epidermal growth factor receptors in A431 cells,"* ***Biophys. J.*** 94, 803 (2008)

[10] A. Janshoff, et al. *"Piezoelectric mass-sensing devices as biosensors: an alternative to optical biosensors,"* ***Angew. Chem. Int. Ed.*** 39, 4004 (2000)

[11] G.F. Zheng, et al. *"Multiplexed electrical detection of cancer markers with nanowire sensor arrays,"* ***Nat. Biotechnol***. 23, 1294 (2005)

[12] B. Liedberg, et al. *"Biosensing with surface plasmon resonance: how It all started,"* ***Sens. Actuators*** 4, 299 (1983)

[13] J. McPhillips, et al. *"High-performance biosensing using arrays of plasmonic nanotubes,"* ***ACS Nano*** 4, 2210 (2010)

[14] L. Dal Negro et Al., *"Plasmonic Nanogalaxies: Multiscale Aperiodic Arrays for Surface-Enhanced Raman Sensing"*, ***NanoLett.*** , 9, (2009)

[15] N.P.Johnson et Al., *"Asymmetric split ring resonators for optical sensing of organic materials"*, ***Opt.Exp.***, 17, (2009)

[16] H. Wei ry al., ""*Hot spots in different metal nanostructures for plasmon-enhanced Raman spectroscopy*", **Nanoscale**, 2013, 5, 10794-10805 (2013)

[17] S. Yang et al., "*Recent progress on surface pattern fabrications based on monolayer colloidal crystal templates and related applications*", **Nanoscale**, 2011, **3**, 2768-2782 **DOI:** 10.1039/C1NR10296F (2011)

[18] S.L. Kleinman, R.R. Frontiera, A.-I. Henry, J.A. Dlerlnger, R.P. Van Duyne, „*Creating, characterizing, and controlling chemistry with SERS hot spots*", **Phys. Chem. Chem. Phys**. 15, 21 (2013)

[19] S.L. Kleinman, B. Sharma, M.G. Blaber, A.-I. Henry, N. Valley, R.G. Freeman, M.J. Natan, G.C. Schatz, R.P Van Duyne, "*Structure Enhancement Factor Relationships in Single Gold Nanoantennas by Surface-Enhanced Raman Excitation Spectroscopy,*" *J. Am. Chem. Soc.* 135, 301 (2013)

[20] N.G. Greeneltch, M.G. Blaber, A.-I. Henry, G.C. Schatz, R.P Van Duyne, "*Immobilized Nanorod Assemblies: Fabrication and Understanding of Large Area SERS Substrates,*" **Anal. Chem**., 85, 2297-2303 (2013)

[21]D. R. Smith, et al. "*Composite medium with simultaneously negative permeability and permittivity,*" **Phys. Rev. Lett.** 84, 4184 (2000)

[22] V.M. Shalaev, et al. "*Negative index of refraction in optical metamaterials,*" **Opt. Lett**. 30, 3356 (2005)

[23] J.B. Pendry, "*Negative refraction makes a perfect lens,*" **Phys. Rev. Lett.** 85, 3966 (2000)

[24] D. Schurig, et. al., "*Metamaterial electromagnetic cloak at microwave frequencies*" **Science** 314, 977 (2006)

[25] W. Cai, et al. "*Optical cloaking with metamaterials,*" **Nat. Photon.** 1, 224 (2007)

[26] M.A. Noginov, et al. "*Demonstration of a spaser-based nanolaser,*" **Nature** 460, 1110 (2009)

[27] A. Della Villa, et al. "*Photonic quasicrystals: basics and examples,*" in **Metamaterials Handbook**, Vol. I, F. Capolino, ed. (CRC Press, Boca Raton, FL, USA, 2009), ch. 27

[28] D. N. Chigrin and A. V. Lavrinenko, "*Photonic applications of two-dimensional quasicrystals,*" in **Metamaterials Handbook**, vol. II, F. Capolino, ed. (CRC Press, Boca Raton, FL, USA, 2009), ch. 28

Chapter 2: Introduction to Raman Spectroscopy and SERS effect

2.1 A brief introduction to Raman spectroscopy

2.1.1 The discovery

When electromagnetic radiation of energy content $h\upsilon$ irradiates a molecule, the energy may be transmitted, absorbed or scattered. In the Tyndall effect the radiation is scattered by particles (smoke or fog, for example). In Reyleigh scattering the molecules scatter the light. No change in wavelength of individual photons occurs in either Tyndall or Reyleigh scattering. Another type of scattering known as the Raman effect was first theoretically predicted by an Austrian physicist A. Smekal in 1923, and later, in 1928, experimentally observed by Indian physicist C.V. Raman [1]. The effect was discovered using a trivial optical set up, i.e. sunlight as a light source telescope, color filters, and observer's eye as a detector [2]. Professor Raman was awarded the Nobel prize in physics in 1930 for his discovery.

2.1.2 Theoretical remarks

When a beam of monochromatic exciting radiation interacts with matter, there occurs both elastic (Rayleigh scattering) and inelastic scattering (Raman scattering). Reyleigh scattering can be looked on as an elastic collision between the incident photon and the molecule. Since the rotational and vibrational energy of the molecule is unchanged in an elastic collision, the energy and therefore the frequency of the scattered photon is the same as that of the incident photon. This is by far the strongest component of the scattered radiation. The Raman effect regards an inelastic collision between the incident photon and the molecule where as a result of the collision the vibrational or rotational energy of the molecule is changed by an amount ΔE_m. In order that energy may be conserved, the energy of the scattered photon, $h\upsilon_s$, must be different from the energy of the incident photon $h\upsilon_I$, by an amount equal to ΔE_m:

$$h\upsilon_i - h\upsilon_s = \Delta E_m \tag{2.1}$$

where υ_i and υ_s are incident and scattered frequencies respectively. On the basis of above equations, the scattered radiation can be classified as:

(a) $\Delta E_m = 0$, when $\upsilon_i = \upsilon_s$ **Rayleigh scattering;**

(b) $\Delta E_m > 0$, when $\upsilon_i > \upsilon_s$ **Stokes scattering;**

(c) $\Delta E_m < 0$, when $\upsilon_i < \upsilon_s$ **Antistokes scattering**

The schematic energy level diagram for Rayleigh, Stokes, and anti-Stokes scattering is shown in *Fig. 2.1*
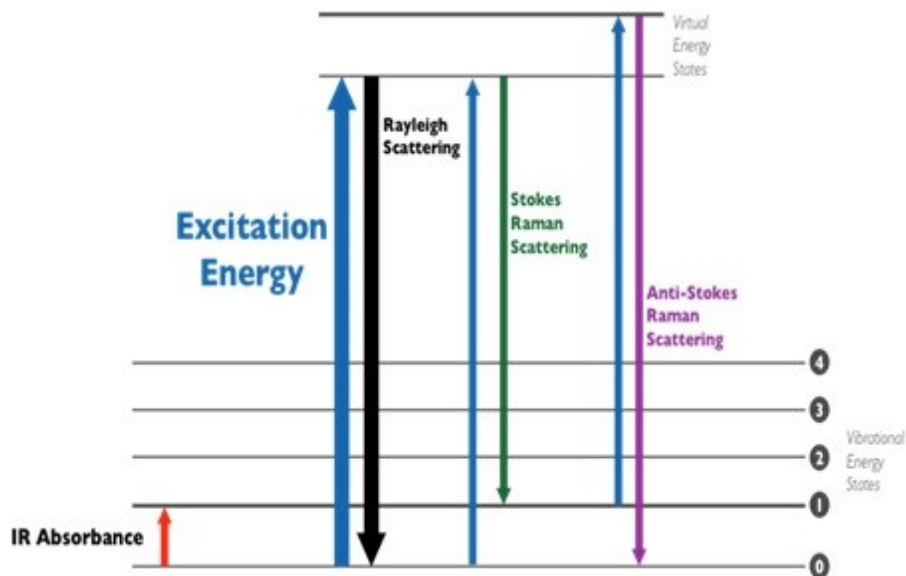

Fig. 2.1: Energy-level diagram of Rayleigh and spontaneous Raman scattering

In *Fig. 2.1* the lines designated represent the vibrational energy levels of a molecule (v = 0, 1, 2, 3, 4…).

The energy difference between these levels is given by $\Delta E_m = h\nu_m$. A transition directly between v = 0 and v = 1 causes the absorption of an infrared photon whose frequency is the same as the molecular frequency ν_m. In Rayleigh and Raman scattering the frequency of the incident photon is usually much greater than ν_m. When the incident photon interacts with a molecule in the ground vibrational state (v = 0), the molecule absorbs the photon energy and is raised momentarily to some high level of energy (virtual state) which is not a stable energy level. Therefore, the molecule immediately loses energy and, most probably, returns to the ground vibrational level, emitting a scattered photon whose energy and frequency is the same as that of the incident photon. This is Rayleigh scattering. However, a smaller portion of the molecules in the virtual state may fall, not to the ground vibrational level but to the v = 1 energy level. The scattered photon in this case has less energy than the exciting photon, the difference being

$$h v_i - h v_s = \Delta E_m = h v_m \tag{2.2}$$

so

$$v_s = v_i - v_m \quad when\ \Delta v = +1 \tag{2.3}$$

This scattered photon gives rise to a Stokes line in the Raman spectrum. According to quantum mechanism the allowed change in the vibrational quantum number for a Raman transition is $\Delta v = \pm 1$ for a harmonic vibration. The final possibility is that the molecule initially is in the excited state $v = 1$, absorbs the incident photon energy, and is raised to an unstable high level of energy. When the molecule falls to the ground vibrational level $v = 0$ the energy loss is made up for by emission of a photon whose energy is greater than that of the incident photon by $h\nu_m$. This scattered photon gives rise to an anti-Stokes line in the Raman spectrum. According to the Boltzmann distribution function the ratio of the number of molecules in the $v = 1$ state to the number in the $v = 0$ state for a given vibration is

$$\frac{n_1}{n_0} = e^{-\left(\frac{h\nu_m}{kT}\right)} \tag{2.4}$$

At ordinary temperatures most of the molecules exist in the ground state and therefore Stokes lines have greater intensities than anti-Stokes lines which originate from an excited level with lower population. This difference increases as the vibrational frequency increases.

Classically, the Raman effect is described by the inelastic scattering of photons as they interact with a molecular system. The energy shifts are collected as wavenumbers (cm^{-1}) and correspond to vibrational frequencies in the molecule. *The combination of the wavenumber bands gives a fingerprint or signature of the molecule*. Unfortunately, Raman scattering is a very weak process as it only occurs in approximately 1 in 10^6 photons and it is limited to measuring signals from molecules that change polarizability during vibrations.

2.1.3 Polarizability

If a molecule is placed in an electric field, electrons and nuclei get displaced. As a result an induced dipole moment is produced in a molecule; and a molecule is said to be polarised. If E is the strength of electric field and μ is the magnitude of induced dipole moment, then

$$\mu = \alpha E \tag{2.5}$$

where α is the polarizability of the molecule. The electric field strength of an electromagnetic radiation of frequency ν varies with time t according to

$$E = E_0 \cos 2\pi \nu t \tag{2.6}$$

Where E_0 is the amplitude of the electromagnetic radiation. Combining Eqs. (2.5) and (2.6)

$$\mu = \alpha E_0 \cos 2\pi \nu t \tag{2.7}$$

Equation (2.7) implies that interaction of electromagnetic radiation of frequency v induces a molecular dipole moment which oscillates with the same frequency.

However, the polarizability changes with small displacement from equilibrium position (i.e. molecular vibration), and is given by

$$\alpha = \alpha_0 + (r - r_{eq})\frac{\partial\alpha}{\partial r} \qquad (2.8)$$

where α_0 is equilibrium polarizability, r_{eq} and r are bond lenghts at equilibrium position and at any instant, respectively. If a molecule executes simple harmonic motion, the displacement can be represented as

$$r - r_{eq} = r_{max}\cos 2\pi\, v_j t \qquad (2.9)$$

where v_j is the vibrational frequency of a molecule and r_{max} is the maximum separation distance between atoms relative to their equilibrium position. Substituting equation (2.9) into equation (2.8) gives

$$\alpha = \alpha_0 + \left(\frac{\partial\alpha}{\partial r}\right)r_{max}\cos 2\pi\, v_j t \qquad (2.10)$$

Substituting equation (2.10) into equation (2.7) gives

$$\mu = \alpha_0 E_0 \cos 2\pi\, vt + E_0 r_{max}\left(\frac{\partial\alpha}{\partial r}\right)\cos 2\pi\, v_j t \cos 2\pi\, vt \qquad (2.11)$$

$$\mu = \alpha_0 E_0 \cos 2\pi\, vt + \frac{E_0}{2}r_{max}\left(\frac{\partial\alpha}{\partial r}\right)\cos[2\pi(v - v_j)]\,t$$
$$+ \frac{E_0}{2}r_{max}\left(\frac{\partial\alpha}{\partial r}\right)\cos[2\pi(v + v_j)]\,t \qquad (2.12)$$

The first term in equation (2.12) represents Rayleigh scattering and occurs at the excitation frequency v. The second and third terms correspond to stokes ($v - v_j$) and anti-Stokes ($v + v_j$) scattering. In both inelastic scattering, the excitation frequency has been modulated by the vibrational frequency of the bond.

2.1.4 Instrumentations

Modern instruments for Raman experiments mainly consist of four components: a laser source that irradiates the sample with a monochromatic light, a sample-illumination system, holographic optics, and a suitable spectrometer with a detector collecting the

scattered light (*Fig. 2.3*). Since the intensities of scattered radiation are very weak, an extremely intense source of radiation is needed. The most commonly used laser sources in Raman applications are Argon ion (488/514 nm), Krypton ion (530.9/647.1 nm), Helium/Neon (632.8 nm), Diode lasers (782/830 nm), and Nd/YAG (1064 nm) [3]. But intense incident radiation may result in higher fluorescence emission and photodecomposition of the sample. In order to minimize these effects while keeping a reasonable Raman sensitivity, He/Ne source has been extensively practised. Most recently, near infrared (NIR) laser sources such as diode lasers and Nd/YAG laser are in extensive use and are very advantageous in dramatically reducing fluorescence and photodecomposition of the sample. These lasers have gained additional attention due to the suitability for the excitation of localized surface plasmons on gold nanoparticles for surface-enhanced Raman applications [4].

There are two basic geometries used in collecting Raman scattering: 90° scattering and 180° scattering (*Fig. 2.2*). Both are effective. In 90° scattering, the laser beam is passed through the sample, say in a 1cm cuvette, and the scattered light is collected at 90° by placing a lens in a suitable position. This light is then imaged onto the entrance slit of the Raman spectrometer. Since the light is scattered as a sphere, the larger the cone of light which can be collected the better. Consequently quite large lenses, or lenses with short focal lengths, are used to cover the largest practicable angle. It has to be remembered that this is not the only consideration. It is also necessary to use the monochromator efficiently and to image the collected light efficiently onto the detector. As a result, the collection lenses have to be matched to the collection optics for efficient performance.

Fig. 2.2. 180° (left) and 90° (right) scattering arrangements. The low beam is shown as arriving vertically through a lens and a set of mirrors onto the sample (the black dot) a cone of scattered light is then collectcd into the spectrometer.

In the 180° system, the laser is delivered through the collection lens and the scattered light collected back through it. In the arrangement shown below, a small mirror is placed in front of the collections lens to achieve this. This is the common arrangement in systems which use a microscope to collect the light.

Charge coupled devices (CCDs) are the most commonly used detectors in Raman systems. The CCD consists of a series of silicon photosites (elements or pixels) in a two dimensional array known as a chip [5]. Each photosite has two conductive electrodes separated by thin silica dielectric layer and each pixel is also surrounded by a non-conductive barrier. When photon strikes on a chip, it induces a charge build-up on the surface of irradiated pixel, which in turn is stored in a capacitor or potential well located below the electrodes. Once the analytical signals are collected, the number of electrons generated in each pixel or data can be recorded by the control electronics and computer to give the acquired Raman spectrum [6]. CCDs have an ability to simultaneously collect the entire spectrum and are also over two orders of magnitude more sensitive (high quantum effciency and low noise) than photodiode array detectors. Such traits make CCDs an almost ideal detector for sensing weak Raman signal.
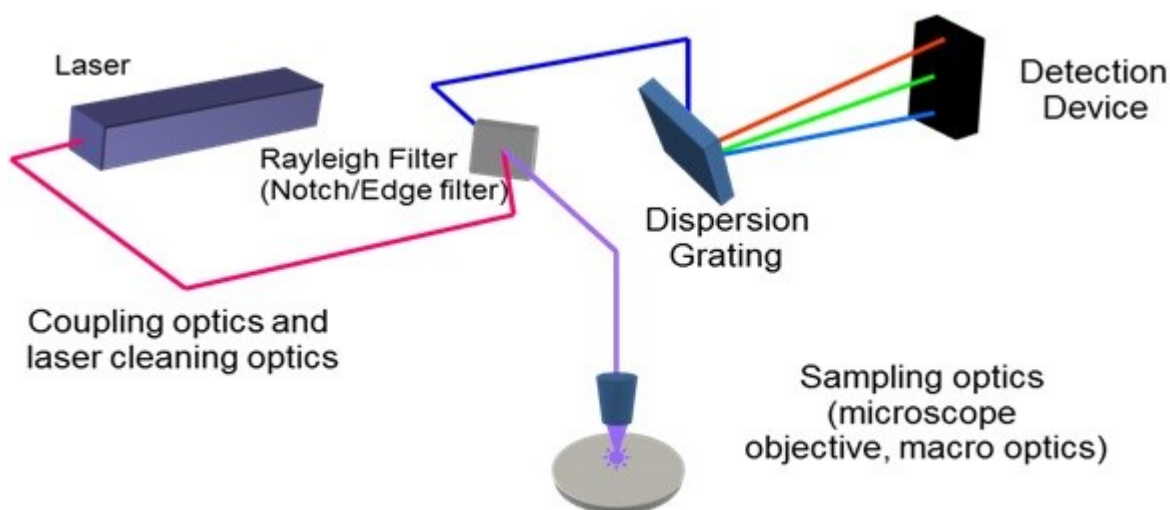

Fig. 2.3 *Basic scheme of a Raman spectroscopy system*

On many modern Raman spectrometers, the sample is simply presented to a microscope which is an integral part of the spectrometer. From the optical engineer's point of view, the use of a microscope to detect the scattering has some advantages; a relatively low-powered laser can be used since it will be focussed to give a very small spot giving a high power density at the sample and also a large collection angle. Further, the small excitation volume can be efficiently imaged into a small spectrometer and onto the detector. It can discriminate against fluorescence from a sample matrix since only the chosen microscopic feature in the sample is irradiated at high power, particularly when the microscope is set up confocally. There is a plasma filter to remove any specious radiation such as weak emission from lines other than the main exciting line in the laser and any background radiation from the laser. The radiation

is then arranged to hit a notch filter. These are interference filters, which work well when the beam is perpendicular to the plane of the filter. The advantages of using a microscope is the possibility to focussed not only on the *X-Y* plane but also in the *Z* direction. In the confocal arrangement (*Fig. 2.4*), the microscope contains a pinhole in its focal plane which enables only light focussed on the plane containing the sample to be collected efficiently. The pinhole filter stops most other light since it is not focussed sharply in the plane of the pinhole. An alternative system is adopted on some instruments. In this, a slit is placed in the focal plane of the microscope at right angles to the slit of the spectrometer. In this way, the two slits although well separated in the instrument are crossed to create essentially a pinhole. In either case the intention is to discriminate against light, which may arise from anywhere other than from the spot sharply focussed on the sample.
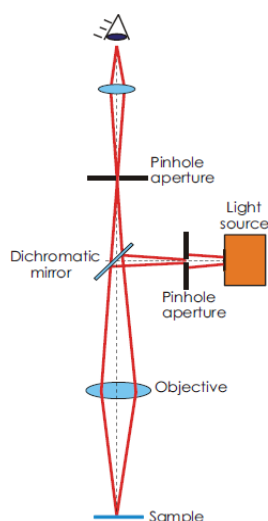

Fig. 2.4 Simplified scheme of the reflective confocal microscope with two pihole apertures.

Confocal Raman systems are useful for the efficient rejection of stray light and fluorescence. They offers several other advantages such as, low sample requirements, high throughput, good collection effciency, ability to collect signals from micron size samples with good lateral resolution [7].

2.1.5 Raman Imaging and mapping

The techniques of Raman mapping and imaging arise from the use of microscopy with Raman spectrometers. In the normal arrangement, the scattered light is separated into individual frequencies in the monochromator and focussed as a line on the CCD so that each separate frequency can be detected at a different point along the line. An alternative way of collecting

Raman scattering is that instead of using a monochromator to split up the different frequencies, a set of filters can be used, in a manner analogous to that used by Raman in the initial experiment. In this arrangement only light of a particular frequency range corresponding to the frequency of one of the major vibrations of the molecule to be detected can pass through to the detector. In this arrangement, there is no monochromator to split up the light and the detector operates exactly like a camera recording an image of the sample focussed under the microscope. The only difference is that only light of the frequency of the Raman active vibration can reach the detector so a Raman image is recorded. This is called *imaging*. An alternative method is to *map the surface*. Accurate positional devices are now readily obtainable and using a suitable XYZ device, it is possible to use the standard configuration to take a Raman spectrum from a small area, move the sample so that the next small area is under the microscope and take another spectrum. By doing this repeatedly, spectra from a selected area can be obtained. From this data, any one vibration can be selected and a colour map of the intensity variation for that vibration plotted. Mapping has the advantage that the whole spectrum is recorded and stored on the computer. A map of all vibrations observed could be obtained if required. However, it is very slow in practice. Obtaining Raman spectra by either of these techniques but in particular by mapping has large advantages in that the material can be immediately identified from the spectrum information obtained and its distribution in a heterogeneous sample determined.

2.2 Surface Enhanced Raman Scattering (SERS)

Currently there is a great deal of interest in the Surface-Enhanced Raman scattering (SERS) technique. SERS is employed to great enhance the number of photons that will be inelastically scattered by placing the molecule under investigation on a roughened noble metal surface. SERS is typically observed from molecular species in close proximity to nanostructured plasmonic surfaces. The technique is of particular interest in the analytical chemistry community, as the signals observed from SERS have been reported to have 12 or more orders of magnitude enhancement of normal Raman signals [9]. However one of the major characteristics of SERS is its interdisciplinary nature, so it involves physical (electromagnetic theory of plasmon resonances), chemical (molecular adsorption on nanostructured surfaces), engineering (reproducible SERS substrate fabrication), and biological (biomedical applications) studies [4].

Thus, SERS effect consists in the amplification of Raman signals (almost exclusively coming from molecules) by several orders of magnitude, and one of its relevant issues is the intricate link between SERS and plasmonics, i.e. the study and applications of the optical properties of metals. Infact, the enhancement is due to the electromagnetic interaction of light with metallic nanoparticles, which produces strong electromagnetic fields localized around nanoparticles through plasmon resonances. Molecules attached or in close vicinity to the nanostructured metallic surfaces can experience this intense plasmonic field and, as a consequence, the Raman signals of molecules result amplified.

2.2.1 The discovery of SERS

The enhanced Raman signal of pyridine adsorbed on roughened electrochemical silver electrode, observed by Fleischmann et. Al in 1974 [10], is considered to be the first observation of the SERS effect. The effect was observed as the researchers were trying to implement Raman spectroscopy as a possible means to observe molecules on surfaces at a monolayer coverage. Fleischmann et Al. interpreted the amplified Raman signal of pyridine as an outcome of increased surface area caused by the roughening of silver electrodes. However, there were many unanswered questions regarding this simple hypothesis. Later on in 1977, two independent research groups, Jeanmarie and Van Duyne [11] and Albrecht and Creighton [12] documented that the observed Raman enhancement could not be accounted for by increased surface area, instead other mechanisms exist. Since then several enhancement mechanisms were proposed in the early days of SERS, however only two mechanisms are now broadly accepted, i.e, Electromagnetic (EM) theory and Chemical Enhancement (CE) theory. CE theory depends on the chemical interaction between probe molecules and the noble metal and is said to contribute only a maximum of about 2-3 orders of magnitude [13]. The dominant EM theory, on the other hand, is based on the collective oscillation of free electron density generating localised surface plasmons (LSPs) and can contribute ten or more orders of magnitude enhancement [14].

2.3 SERS enhancement mechanisms

Since this technique was discovered experimentally, many theories were proposed, particularly in the early stages. To some extent almost all of them contain an element of truth. The problem is that our ability to describe theoretically the bonding or adsorption of an organic molecule to a roughened, probably corroded and oxidized metal surface in water is

very limited. As stated earlier, SERS enhancements are mainly attributed to the electromagnetic and chemical effects. In theory, EM enhancement is analyte independent while CE is probe-dependent and requires some sort of chemical interaction to the metal surface. Before briefly describing the theory, it is necessary to understand the nature of the roughened metal surface. Silver surfaces, like the surfaces of other metals, are covered with electrons. They arise from the conduction electrons held in the lattice by the presence of positive charge from the silver metal centres. At the surface, the positive charge is only on the metal side of the electrons. Consequently the electron density extends a considerable distance from the surface and there is also freedom of movement in a lateral direction along it. When a light beam interacts with these electrons, they begin to oscillate as a collective group across the surface. These oscillations are termed surface plasmons. Surface plasmons from small uniform particles, or from surfaces which have a single periodic roughness feature, have a resonance frequency at which they absorb and scatter light most efficiently. The frequency varies with the metal and the nature of the surface. It so happens that both silver and gold plasmons oscillate at frequencies in the visible region and therefore, they are suitable for use with the visible and NIR laser systems commonly used in Raman scattering. On a smooth surface the oscillation occurs along the plane of the surface. Absorption can occur but no light will be scattered. To get scattering, there needs to be an oscillation perpendicular to the surface plane and this is achieved by roughening the surface. This locates the plasmon in the valleys of the roughened metal surface and scattering is caused as the plasmons move up to the peaks.

2.3.1 Electromagnetic Enhancements

The majority of the overall SERS enhancements is due to EM enhancement mechanism and is a direct consequence of roughness present on the noble metal surfaces. In order to understand the EM enhancement mechanism, it is important to recall the phenomenological approach to Raman scattering. When monochromatic radiation of frequency v and electric field E interacts with a molecule, it induces a Raman dipole oscillating at a frequency v_R

$$\mu_R = \alpha_R E \tag{2.13}$$

The oscillating Raman dipole radiates a power proportional to $|\mu_R|^2$ at frequency v_R and is the frequency detected as Raman signal in far-field. The same phenomenological description can be applied to SERS. However, the presence of roughened metal surface alters the effects, such as:

(a) The electromagnetic field at the metallic surface can be dramatically increased and may results in a possible *local field enhancement*.

(b) The radiation properties of the Raman dipole, μ_R, is affected by the metallic environment and may results in a possible *radiation enhancement*.

Therefore, EM enhancement mainly concerns about understanding the two effects listed above.

Local field Enhancement

When electromagnetic radiation impinges on a suitable metal surface (that possess a negative real and small positive imaginary dielectric constant), the electromagnetic field in the vicinity of metallic surfaces gets strongly modified. This is due to the coherent oscillation of free electrons generating *surface plasmons*. Surface plasmons can be of two types, surface plasmon polariton (or propagating plasmon) - propagates in x and y directions along the metal-dielectric interface [15, 16] (*Fig. 2.5*),
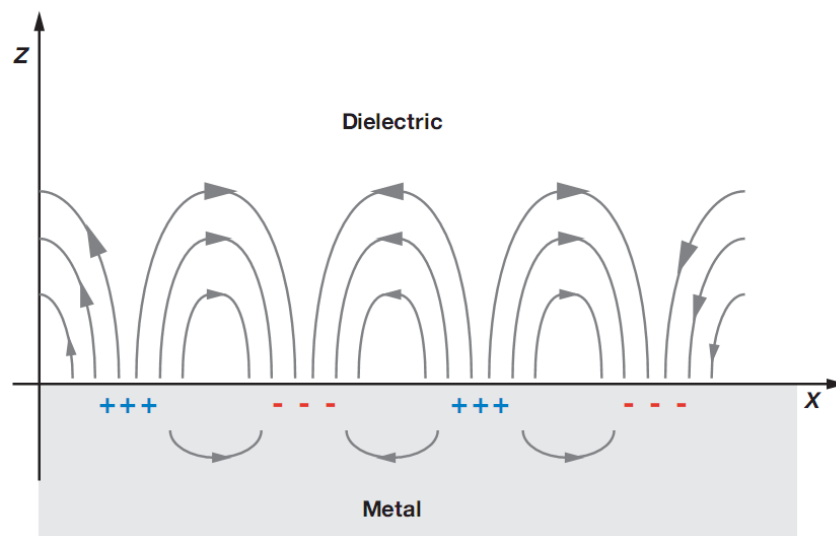
Fig. 2.5: Schematic diagram of Surface plasmon polaritons

or localized surface plasmons (LSPs) - localized on the surface of a nanoparticle (*Fig. 2.6*) with a frequency known as the localized surface plasmon resonance (*LSPR*) [17, 18].
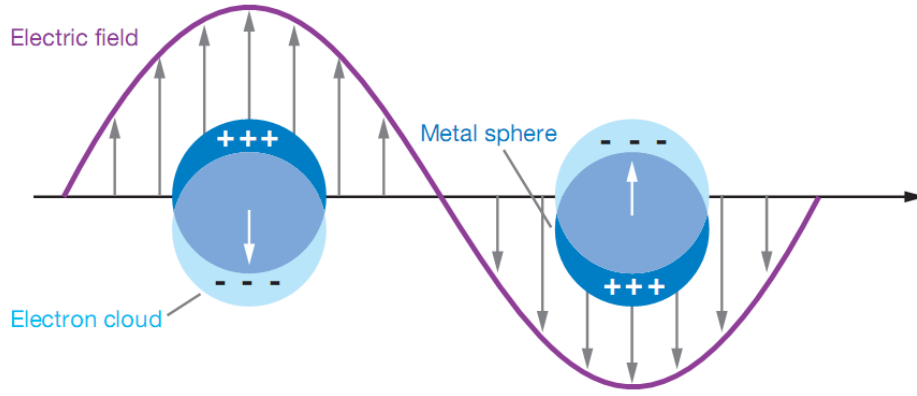
Fig. 2.6: Schematic diagram of Localized Surface plasmons

SERS is benefited from LSPR and the LSPs or local field on the metallic object at the molecular position, E_L, could be different from incident field, E, in terms of both magnitude and orientation. Usually, the magnitude of $|E_L|$ can be much larger than $|E|$. The local field induces a Raman dipole

$$\mu_R = \alpha_R E_L(v_L) \tag{2.14}$$

Therefore, the Raman dipole is enhanced by a factor of $|E_L(v_L)|/|E|$. If such Raman dipole radiates in free-space (i.e., in absence of metallic environment), the radiated energy which is proportional to $|\mu_R|^2$, would enhance by a factor

$$M_L(v_L) = \frac{|E_L(v_L)|^2}{|E|^2} \tag{2.15}$$

$M_L(v_L)$ is the local electric-field enhancement factor and characterizes the enhancement of the electric field intensity, but ignores any changes in the electric field polarization.

Radiation Enhancement

In SERS, Raman dipole radiates in presence of metallic objects, unlike in free-space. Therefore, the presence of metallic environment significantly alters dipole radiation as in the case of incident electric-field. It is known that the total power radiated by the dipole, P_{rad} can be either quenched or enhanced (relative to that in free space, P_0) depending on the relative dielectric function $\varepsilon(r)$ of the object, its geometry, and the dipole position, orientation and its emission frequency, v_R. For example, a small quenching is observed for a dipole parallel to the surface of non-absorbing dielectric sphere, like glass, with $\varepsilon(r) > 1$. For objects having negative real dielectric function, $\text{Re}(\varepsilon(r)) < 0$, the radiated power is strongly enhanced. The

large enhancement in the radiated power is due to coupling to the LSPR of metallic objects [4]. Therefore, the radiation enhancement factor is given by

$$M_{Rad} = \frac{P_{rad}}{P_0} \qquad (2.16)$$

$|E|^4$ *Approximation*

Considering local electric-field enhancement and radiation enhancement, EM enhancements of single-molecule SERS (SMSERS) can be simply expressed as [4]

$$Enhancement\ factor\ (EF) \approx M_L(v_L)M_{Rad}(v_R) \qquad (2.17)$$

$M_L(v_L)$ can be calculated by solving the electromagnetic problem under specific external excitation conditions with an incident field, E, which yields local-field everywhere. However, estimation of $M_{Rad}(v_R)$ is a rather difficult task. For this, it is necessary to solve the electromagnetic problem of dipolar emission, instead of external excitation, which itself is very complicated. To avoid these complications, it is often assumed that local electric-field enhancements and radiation enhancements are approximately equal. Hence, SERS enhancements can be expressed as

$$EF \approx M_L(v_L)M_{Rad}(v_R) \approx \frac{|E_L(v_L)|^2}{|E|^2}\frac{|E_L(v_R)|^2}{|E|^2} \qquad (2.18)$$

This equation provides a very simple way of estimation SERS enhancement factor from the calculation of local field at the excitation and Raman frequencies. In addition to this, in many cases, the Raman shift is small (or the plasmon width is often large compared to the Stokes shift), and an additional approximation can be made, i.e., $v_R \approx v_L$. This results into even more famous expression of the SERS enhancement

$$EF \approx \frac{|E_L(v_L)|^2}{|E|^2} \qquad (2.19)$$

In conventional SERS, EF is averaged over the surface area of the particles where molecules can adsorb to generate the observed enhancement factor $|EF|$ and is said to be *average* EF, while in *single-molecule* EF it is the maximum enhancement EF_{max} and represents the enhancement only at specific positions on the substrate. Since EF_{max} applies only to one or a

few specific regions of a SERS substrate, it is important to note that average EFs are typically several orders of magnitude less than single-molecule EFs.

2.3.2 The Chemical Enhancement

Although the existence and a definition of CE are a subject to controversy [19], it is believed that, in SERS, a second enhancement mechanism (multiplicative when co-existing) operates independent of EM enhancement. It is almost impossible to separate these effects from a system that supports EM enhancement. Nevertheless, several efforts have been made in understanding the existence of CE [13, 20-24]. CE mechanism is viewed as a resonance Raman mechanism and is attributed to the modification of electronic polarizability of the adsorbate due to the formation of metal-adsorbate complex. The mostly accepted explanation of CE is a charge-transfer (CT) mechanism [4, 25].

2.3.3 Analytical/Substrate Enhancement Factors

Although it is very diffcult to identify the exact origin of enhancement factors in most of the SERS experiments (as EM and CE enhancements exist together), it is not important to define them in any analytical measurements. For simplicity, researchers sometime use analytical enhancement factor (AEF) given below

$$AEF = \frac{I_{SERS}}{I_{RS}} \frac{C_{RS}}{C_{SERS}} \qquad (2.20)$$

Where I_{RS} is the Raman signal of an analyte at concentration C_{RS}. Similarly, I_{SERS} is the SERS signal measured for same analyte at concentration C_{SERS}. The definition of AEF has made the assumptions that I_{RS} or I_{SERS} scales linearly with incident power density and the concentration of analyte C_{RS} or C_{SERS}. However, the important drawback of the above equation is that it ignores the fact that SERS is a surface spectroscopy and only the adsorbed species contributes on SERS signal. To solve this problem, a following definition of SERS substrate enhancement factor (*SSEF* or G_{SERS}) has been widely used

$$SSEF = G_{SERS} = \frac{I_{SERS}}{I_{RS}} \frac{N_{Vol}}{N_{SERS}} \qquad (2.21)$$

Where $N_{Vol} = C_{RS}V$ is the average number of molecular in the scattering volume V, and N_{SERS} is the number of adsorbed molecules on the optically probed SERS substrates. This expression is considered as the best estimate of average SERS EF for a given substrate and has been extensively used in SERS experiments [4, 28-30].

2.4   Selection Rules

SERS spectra are not straightforward to interpret. New peaks which do not appear in normal Raman scattering can appear in SERS and some peaks which are strong in normal Raman scattering can become very weak or disappear altogether. In addition, the intensity changes which occur at different concentrations can be nonlinear. A classic example of this is with pyridine. Well below monolayer coverage, the pyridine spectrum is very weak but it becomes quite strong as monolayer coverage is approached. At low concentrations the molecules are present on the metal surface with the plane of the pyridine ring parallel to the plane of the surface. As the concentration increases the plane of the pyridine ring is forced into an orientation perpendicular to the surface to allow more molecules to pack. This causes a rapid rise in SERS intensity. The reason this alters the intensity of SERS has already been discussed in general when it was stated that one requirement for scattering is that there is a polarizability component perpendicular to the surface. When light interacts with the surface, the effect can be described by two electric dipole components parallel and perpendicular to the surface. It is molecular polarizability caused by the perpendicular component which leads to scattering from the rough surface. For pyridine, the plane of the ring will produce the greatest polarizability changes. Thus, if the molecule is lying with the plane parallel to the surface, most of the polarizability change will be parallel to the surface and consequently will not contribute to scattering. When the plane is perpendicular to the surface the scattering process will be efficient.

The appearance of new bands further complicates the assignment. The most common reason this occurs is when a molecule has a centre of symmetry. Adsorption of the molecule onto a metal surface will effectively break the centre of symmetry. This results in the mutual exclusion rule no longer being applicable, allowing some of the infrared active bands to break through and appear in the SERS spectrum. However, the situation is more complex than that. Some types of bands are naturally more intense in SERS than they are in normal Raman scattering. A consideration of the main effects led Creighton [53] to propose selection rules which work well in most circumstances. In theory they refer to electromagnetic enhancement

but seem to be applicable in many cases. The problem with chemical enhancement is that the nature of the species formed between the adsórbate and the surface is not clearly defined. In principle, the selection rules should refer to the surface species including the molecule and the metal atoms complexed to it. However, in practice, considering the molecule as a distinct entity and ignoring the effect of the metal atoms other than the change they cause in molecular symmetry appears to be effective in most cases. These simple selection rules have proved to be useful in determining the orientation of a molecule on the surface and explaining some of the differences between SERS spectra and normal Raman spectra. However, there is still much to be learned about the reasons for the intensities of SERS active bands.

The fact that there are selection rules is a problem in SERS. The appearance of new bands and the disappearance of existing ones makes much more difficult to relate the spectra obtained on the surface to that obtained from normal Raman scattering. In addition, since the sensitivity of SERS compared to normal Raman scattering is huge (a factor of 10^6), the dominant features of the spectrum could arise from a contaminant which sticks strongly to the surface. These problems make positive assignments difficult.

2.5   Applications of SERS

Since the Raman technique provides a unique "fingerprint spectrum" of a molecule, the technique is more specific and valuable for its structural information. However, due to the weak signal intensity, conventional Raman has lagged behind other analytical techniques like fluorescence. Surface enhanced Raman scattering (SERS) [10] is one of the promising methods for detection of trace amounts of molecules. It is most sensitive due to large ($\sim 10^{11}$) enhancements of the light fields at hot spots. With the gain in Raman intensity provided by SERS, the latter can be used in a variety of applications (already exploited by Raman) with improved sensitivity or limit of detection. In addition to the improvement on the conventional Raman technique, SERS can also be applied to the system that could not be envisaged with conventional Raman. The potential applications of SERS are in the field of analytical chemistry, biochemistry, forensic sciences, environmental and nuclear sciencs, etc. The technique has been successfully implemented for both trace detection of chemicals (drugs, explosives, environmental contaminations etc.) and sensing and monitoring of biofluids at higher concentrations [31-39]. Moreover, the technique has been implemented in several other applications, such as identification of dyestuffs for ancient paintings and medieval manuscripts [40-42], tissue imaging [43], protein detection [44-46], etc.

SERS is now extensively used in a wide range of scientific areas. As far as applications are concerned, SERS is taken as a big competitor to fluorescence spectroscopy [4]. Nevertheless, both techniques have pros and cons. Regardless, SERS has additional applications such as, tools to study surface plasmon resonances, adsorption properties of analyte, surface chemistries, etc, which could not have been envisaged by conventional Raman or fluorescence spectroscopy. Currently, a *qualitative* finger-printing detection capability of SERS is entering the bio-medical field supported by advances in hand-held SERS microscopes [47]. In real medical applications the complexity of Raman scattering from cells and large molecules in different spatial 3D conformations makes a quantitative analysis still challenging, e.g. sub-pM of sensitivity is strongly required for the early detection and initial treatment of various bio-markers such as cancer and Alzheimer, with high selectivity and quantitativeness, [48-49] especially without functionalized surfaces as demonstrated recently for red blood cells infected with malaria. [50-52]

References

[1] Krishnan, R. & Shankar, R. RAMAN Effect- History of the Discovery. Journal of Raman Spectroscopy 10, 1-8 (1981).

[2] Raman, C. & Krishnan, K. A new type of secondary radiation. Nature 121, 501-502 (1928).

[3] Skoog, D., Holler, F. & Nieman, T. (Thomson Learning, Inc., 1997), 5th edn.

[4] Le Ru, E. & Etchegoin, P. In Principles of Surface-Enhanced Raman Spectroscopy and Related Plasmonic Effects (Elsevier, 2009).

[5] Bowie, B., Chase, D. & Grifiths, P. Factors Affecting the Performance of Bench-Top Raman Spectrometers. Part I: Instrumental Effects. Applied Spectroscopy 54, 164A-173A (2000).

[6] Pitt, G. et al. Engineering Aspects and Applications of the New Raman Instrumentation. IEE Proceedings-Science Measurement and Technology 152, 241-318 (2005).

[7] Laplant, F. & Benamotz, D. Design and Construction of a Microscope-Based Raman System. Review of Scientific Instruments 66, 3537-3544 (1995).

[8] Borman, S. Non-Linear Raman-Spectroscopy. Analytical Chemistry 54, A021 (1982).

[9] Kneipp, K. et al. Single Molecule Detection using Surface-Enhanced Raman Scattering (SERS). Physical Review Letters 78, 1667-1670 (1997).

[10] Fleischmann, M., Hendra, P. & Mcquilla, A. Raman Spectra of Pyridine Adsorbed at a Silver Electrode. Chemical Physics Letters 26, 163-166 (1974).

[11] Jeanmaire, D. & Vanduyne, R. Surface Raman Spectroelectrochemistry.1. Heterocyclic, Aromatic, and Aliphatic-Amines Adsorbed on Anodized Silver Electrode. Journal of Electroanalytical Chemistry 84, 1-20 (1977).

[12] Albrecht, M. & Creighton, J. Anomalously Intense Raman-Spectra of Pyridine at a Silver Electrode . Journal of the Americal Chemical Society 99, 5215-5217 (1977).

[13] Campion, A. & Kambhampati, P. Surface-Enhanced Raman Scattering. Chemical Society Reviews 27, 241-250 (1998).

[14] Schatz, G. C., Young, M. A. & Van Duyne, R. P. Electromagnetic mechanism of SERS. In Surface-Enhanced Raman Scattering: Physics and Applications, vol. 103 of Topics in Applied Physics, 19-45 (2006).

[15] Brockman, J., Nelson, B. & Corn, R. Surface Plasmon Resonance Imaging Measurements of Ultrathin Organic Films. Annual Review of Physical Chemistry 51, 41-63 (2000).

[16] Knoll, W. Interfaces and Thin Films as Seen by Bound Electromagnetic Waves. Annual Review of Physical Chemistry 49, 569-638 (1998).

[17] Kelly, K., Coronado, E., Zhao, L. & Schatz, G. The Optical Properties of Metal Nanoparticles: The Influence of Size, Shape, and Dielectric Environment. Journal of Physical Chemistry B 107, 668-677 (2003).

[18] Haes, A. et al. Plasmonic Materials for Surface-Enhanced Sensing and Spectroscopy. MRS Bulletin 30, 368-375 (2005).

[19] Aroca, R. In Surface-Enhanced Vibrational Spectroscopy (John Wiley & Sons, Chichester, 2006).

[20] Campion, A., Ivanecky, J., Child, C. & Foster, M. On the Mechanism of Chemical Enhancement in Surface-Enhanced Raman Scattering. Journal of the American Chemical Society 117, 11807-11808 (1995).

[21] Kambhampati, P., Child, C., Foster, M. & Campion, A. On the Chemical Mechanism of Surface Enhanced Raman Scattering: Experiment and Theory. Journal of Chemical Physics 108, 5013--5026 (1998).

[22] Kambhampati, P., Child, C. & Campion, A. On the Role of Charge- Transfer Resonances in the Chemical Mechanism of Surface-Enhanced Raman Scattering. Journal of the Chemical Society-Faraday Transactions 92, 4775-4780 (1996).

[23] Child, C., Fieberg, J. & Campion, A. Surface Chemistry of Polyimide Formation on Cu(111). Surface Science 372, L254-L260 (1997).

[24] Aroca, R., Clavijo, R., Halls, M. & Schlegel, H. Surface-Enhanced Raman Spectra of Phthalimide. Interpretation of the SERS Spectra of the Surface Complex Formed on Silver Islands and Colloids. Journal of Physical Chemistry A 104, 9500-9505 (2000).

[25] Lombardi, J., Birke, R., Lu, T. & Xu, J. Charge-Transfer Theory of Surface Enhanced Raman Spectroscopy; Herzberg-Teller Contributions. Journal of Chemical Physics 84, 4174-4180 (1986).

[26] Cai, W. et al. Investigation of Surface-Enhanced Raman Scattering from Platinum Electrodes using a Confocal Raman Microscope: Dependence of Surface Roughening Pretreatment. Surface Science 406, 9-22 (1998).

[27] Xie, Y. et al. Adsorption and Photon-Driven Charge Transfer of Pyridine on a Cobalt Electrode Analyzed by Surface Enhanced Raman Spectroscopy and Relevant Theories. Journal of Electroanalytical Chemistry 554, 417-425 (2003).

[28] Haynes, C. & Van Duyne, R. Plasmon-Sampled Surface-Enhanced Raman Excitation Spectroscopy. Journal of Physical Chemistry B 107, 7426-7433 (2003).

[29] Bhandari, D., Wells, S. M., Retterer, S. T. & Sepaniak, M. J. Characterization and Detection of Uranyl Ion Sorption on Silver Surfaces Using Surface Enhanced Raman Spectroscopy. Analytical Chemistry 81, 8061-8067 (2009).

[30] Oran, J., Hinde, R., Abu Hatab, N., Retterer, S. & Sepaniak, M. Nanofabricated Periodic Arrays of Silver Elliptical Discs as SERS Substrates. Journal of Raman Spectroscopy 39, 1811-1820 (2008).

[31] Sylvia, J., Janni, J., Klein, J. & Spencer, K. Surface-Enhanced Raman Detection of 1,4-Dinitro Toluene Impurity Vapor as a Marker to Locate Landmines. Analytical Chemistry 72, 5834-5840 (2000)

[32] Cinta-Pinzaru, S. et al. FT-Raman and NIR-SERS Characterization of the Antimalarial Drugs Chloroquine and Meoquine and their Interaction with Hematin. Journal of Raman Spectroscopy 37, 326-334 (2006)

[33] Binoy, J., Joe, I., Jayakumar, V., Nielsen, O. & Aubard, J. DFT Based Relaxed PES Scan Studies and SERS of Anti Cancer Drug, Combretastatin A-4. Laser Physics Letters 2, 544-550 (2005)

[34] Szeghalmi, A. et al. Adsorption of 6-Mercaptopurine and 6-Mercaptopurine Riboside on Silver Colloid: a pH Dependent Surface Enhanced Raman Spectroscopy and Density Functional Theory Study. Part I. 6-Mercaptopurine. Journal of molecular structures 735, 103-113 (2005)

[35] Szeghalmi, A. et al. Adsorption of 6-Mercaptopurine and 6-Mercaptopurine-Riboside on Silver Colloid: A pH-Dependent Surface-Enhanced Raman Spectroscopy and Density Functional Theory Study. II. 6-Mercaptopurine-Riboside. Biopolymers 78, 298-310 (2005)

[36] Alvarez-Puebla, R. A., dos Santos, D. S., Jr. & Aroca, R. F. SERS Detection of Environmental Pollutants in Humic Acid-Gold Nanoparticle Composite Materials. Analyst 132, 1210-1214 (2007)

[37] Camden, J. P., Dieringer, J. A., Zhao, J. & Van Duyne, R. P. Controlled Plasmonic Nanostructures for Surface-Enhanced Spectroscopy and Sensing. Accounts of Chemical Research 41, 1653-1661 (2008)

[38] Yonzon, C. R., Lyandres, O., Shah, N. C., Dieringer, J. A. & Van Duyne, R. P. Glucose Sensing with Surface-Enhanced Raman Spectroscopy. In Surface-Enhanced Raman Scattering: Physics and Applications, vol. 103 of Topics in Applied Physics, 367-379 (2006)

[39] Lyandres, O. et al. Real-Time Glucose Sensing by Surface-enhanced Raman Spectroscopy in Bovine Plasma Facilitated by a Mixed Decanethiol/Mercaptohexanol Partition Layer. Analytical Chemistry 77, 6134-6139 (2005)

[40] Leona, M. Microanalysis of Organic Pigments and Glazes in Polychrome Works of Art by surface-enhanced Resonance Raman Scattering. Proceeding of the National Academy of Sciences of the United States of America 106, 14757-14762 (2009)

[41] Lau, D., Livett, M. & Prawer, S. Application of Surface-Enhanced Raman Spectroscopy (SERS) to the Analysis of Natural Resins in Artworks. Journal of Raman Spectroscopy 39, 545-552 (2008)

[42] Chen, K., Leona, M. & Vo-Dinh, T. Surface-enhanced Raman Scattering for Identification of Organic Pigments and Dyes in Works of Art and Cultural Heritage Material. Sensor Review 27, 109-120 (2007)

[43] Feng, S. et al. Gold Nanoparticle Based Surface-Enhanced Raman Scattering Spectroscopy of Cancerous and Normal Nasopharyngeal Tissues Under Near-Infrared Laser Excitation. Applied Spectroscopy 63, 1089-1094 (2009)

[44] Han, X. X., Zhao, B. & Ozaki, Y. Surface-enhanced Raman Scattering for Protein Detection. Analytical and Bioanalytical Chemistry 394, 1719-1727(2009)

[45] Han, X. X., Huang, G. G., Zhao, B. & Ozaki, Y. Label-Free Highly Sensitive Detection of Proteins in Aqueous Solutions Using Surface-Enhanced Raman Scattering. Analytical Chemistry 81, 3329-3333 (2009)

[46] Chowdhury, M. H., Ray, K., Gray, S. K., Pond, J. & Lakowicz, J. R. Aluminum Nanoparticles as Substrates for Metal-Enhanced Fluorescence in the Ultraviolet for the Label-Free Detection of Biomolecules. Analytical Chemistry 81, 1397-1403 (2009)

[47] K. W. Kho , C. Y. Fu , U. S. Dinish , M. Olivo , *J. Biophoton.* **2011** , *4* ,667 – 684

[48] S. Kita , S. Otsuka , S. Hachuda , T. Endo , Y. Imai , Y. Nishijima , H. Misawa , T. Baba , *IEICE Trans. Electron.* **2012** , E95-C , 188 – 198

[49] S. Kita , S. Otsuka , S. Hachuda , T. Endo , Y. Imai , Y. Nishijima ,H. Misawa , T. Baba , *Opt. Express* **2011** , *19* , 17683 – 17690

[50] S. Shanmukh , L. Jones , J. Driskell , Y. Zhao , R. Dluhy , R. A. Trippet ,*Nano Lett.* **2006** , *6* , 2630 – 2636

[51] E. Zachariah , A. Bankapur , C. Santhosh , M. Valiathan , D. Mathur ,*J. Photochem. Photobiol. B: Biol.* **2010** , *100* , 113 – 116

[52] A. J. Hobro , A. Konishi , C. Coban , N. I. Smith , *Analyst* **2013** , *138* , 3927 – 3933

[53] J.A. Creighton, in: *Spectroscopy of Surfaces,* R.J.H. Clark and R.E. Hester (eds), Wiley, 1998, p. 27

Chapter 3: SERS Substrates: State of the art

3.1 SERS substrates: generalities

Any nanostructured metallic platform that supports plasmon resonance and amplifies Raman signals to some extent are generally denominated as "SERS substrates". The ambition for fabricating SERS substrates have changed over the years and goes from the early efforts involving roughening metal surfaces obtained by a repeatition of chemical oxidation-reduction cycles to the nowadays goal in developing fabrication methods for reliable, reproducible and inexpensive SERS substrates.

When SERS was invented, it turned out that only a few 'free-electron-like' metals, mainly Ag, Au and Cu could provide a large SERS effect for roughened metal surfaces and colloidal metal particles with dimensions in the order of nanometres. As the SERS activity strongly depends on the nature of the substrates to be used for SERS effect, lack of suitable SERS substrates other than those mentioned above gave rise to lack of 'substrate generality' of SERS in the early 1990s. This means transition metals such as Ni, Pd, Pt, Ti, Co cannot be used as SERS substrates. To meet the conditions of good SPR, infact, the metal usually should have a low value of the imaginary component of the dielectric constant: this is impossible for a transition metal because in the visible light region the value of the imaginary part of the dielectric constant is large and interband excitation occurs as the Fermi level is located at the d-band. In addition, there is coupling between conduction electrons and interband electronic transitions. This can depress considerably the quality of the SPR of transition metals. Accordingly, the SERS activity of electrochemically roughened transition metal surface is in general quite low, with typical surface enhancement factor ranging from 10 to 10^3 [1]. In the early stages of SERS, most substrates were made using randomly deposited metal films or electrochemically roughened electrodes with ill-defined surface morphology [2]. For example, a thin layer of gold or silver, typically between 5 and 10 nm, was vapor deposited onto a slide, resulting in a collection of thin island films capable of supporting surface plasmons. Although a small amount of tunability is possible through the modification of film thickness and solvent annealing, variations and a lack of information regarding the SERS active sites prevented a quantitative application of SERS [3-5]

SERS has become an important branch of nanoscience and nanotechnology. It has been found that SERS activity depends on the size, shape and aggregation of nanoparticles. Several

techniques of nanoscience have been employed to fabricate and characterize SERS- related nanoparticles or nanostructures in a well- controlled fashion. Such efforts have led to the significant progress in this versatile field. High-quality SERS spectra from a single molecule adsorbed on well-characterized Au and Ag nanoparticles have been obtained with a high signal enhancement up to 10^{14} [6-8]. The high-quality single molecular SERS spectra have improved the molecule generality and made SERS a promising tool for trace analysis in life and medical sciences as well as security and environment protection. [1]

3.2   SERS substrates: an overview

SERS-active substrate fabrication is an important field in SERS research. Many years of research have been devoted to creating and optimizing SERS substrates in order to provide the largest enhancements possible [9-12]. The fundamental metric for SERS activity is the enhancement factor (EF), which quantifies the increase in signal intensity (counts s^{-1} mW^{-1}) per molecule. Commonly, EFs range from 10^3-10^7, with a few highly enhancing substrates achieving EFs >10^8 [12-14]

Over time, SERS substrates have had many iterations and forms, beginning with roughened silver electrodes [15-16], then moving onto silver and gold colloids [17-18]. Later, as the SERS research community continued to grow, metal films with various thicknesses and nanostructured features were investigated as possible substrates [18-21]. The recent advancement of nanotechnology has been utilized to fabricate various nanostructures from nanoparticles to nanowires, and more recently, combinations of both colloidal and film fabrication strategies have been developed to form SERS substrates [22-24].

Comparison of various SERS substrates is challenging because rigorous characterization of substrates is frequently overlooked for reasons of complexity. This prevents the determination of analytical parameters such as sensitivity and reproducibility.

The SERS substrates can be classified in three categories: (1) Metal nanoparticles (MNPs) in suspension; (2) MNPs immobilized on solid substrates; (3) Nanostructures fabricated directly on solid substrates, which includes nanolithography and template synthesis of nanostructures.

Although nanoparticles and nanoparticle film electrodes show good surface uniformity, it is difficult to control the spacing of the nanoparticles to optimize the SERS activity. Template methods can provide highly ordered SERS substrates with controlled interparticle spacing [25, 1].

3.2.1 Bottom-up methods

In Bottom-up methods small building units are used to fabricate a hierarchical structure [26]. More precisely, bottom-up approaches are common in colloidal science for rationally designed synthesis [10] and assembly [25, 27-30] of nanoparticles. The control achievable by bottom-up techniques in the size [10, 31], shape [32-39] and composition [40-44] of metallic nanoparticles, as well as their organization in clusters [45-47] or interfaces [48, 49] to create high local electromagnetic (EM) field enhancement or "hot spots" are particularly relevant for SERS [12, 50, 51]. Bottom-up synthesis methods for nanoparticles involve creating larger systems from smaller units, including atoms, molecules, polymers, and/or nanoparticles. Some techniques used are chemical synthesis, laser trapping, self-assembly, and colloidal aggregation [12, 25, 52]. Regardless, both gold and silver have been extensively used for SERS substrates. Historically, the synthesis of chemically stable silver nanoparticles with high size and shape tunability, as well as monodispersity, has been more arduous than for gold. During the last few years, silver and gold nanoparticles have been prepared in very diverse shapes, including sphere [53-55], cubes [56, 57], tetrahedra [58], bipyramids [59-61], decahedra [62], prisms [63-65], nanorods and wires [31, 66], nanoshells [32], stars [38, 67], laces [39], and other polyhedral shapes [39, 56, 60, 68, 69] (*Fig. 3.1*).
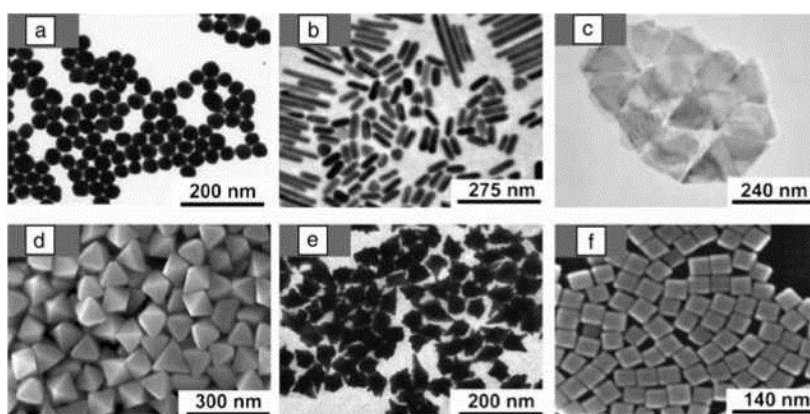
Fig. 3.1. Various types of nanoparticles synthesized using bottom-up approaches. (a) Transmission electron microscopy (TEM) image of Au nanospheres [54] (b) TEM image of Au nanorods and (c) Au nanoprisms. [64] (d) SEM image of Au bipyramids [68] (e) TEM image of Au nanostars [38] (f) SEM image of Ag polyhedra [39]

3.2.2 Top-down methods

Top-down synthetic techniques are used to modify larger structures through milling, etching, or molding into smaller substrate components. Among various templates tecnique,

nanosphere lithography (NSL) and anodic aluminum oxide (AAO) films have been most widely used for the fabrication of SERS-active substrates. In addition, Langmuir-Blodgett (LB) technique can be used to fabricate highly-ordered SERS active substrates. On the other hand, the development of lithography techniques - such as electron beam lithography, focused ion beam milling - have allowed the fabrication of ordered nanostructures due to the possibility of large-scale fabrication and a high degree of reproducibility that can produce reasonably reproducible SERS intensities. However, the equipment for these techniques is expensive and the process requires multiple manufacturing steps thus lithography techniques are somewhat scarce in conventional laboratories.

At the current development state of electron- and ion-beam lithography (EBL and IBL), 2–20 nm wide nano-gaps can be milled between nanoparticles or inscribed on their arrays with high fidelity down to sub-1 nm precision [70-73] using a top down approach [74]. Thus, Electron beam lithography (EBL) and focused ion beam (FIB) milling are considered the best for making reproducible SERS substrates with nanoscale resolution [75, 77]. Both of these techniques have been mostly used to study the SERS effect and its variations due nanoparticle geometry and interparticle distance.

Nanosphere lithography

NSL technique has been well developed by various groups [79, 79]. It involves the deposition of a layer of closely packed polystyrene beads on the surface followed by vapor deposition of a thin silver nanoparticle film over the surface. The interstices between the polystyrene beads serve as a mask and as the beads are chemically lifted off the surface only the silver particles that fell through the interstices remain on the surface forming a single-layered periodic array of triangle shaped nanoparticles (*Fig. 3.2*) As the solvent evaporates, nanospheres get closer due to the capillary action and finally forms a hexagonally close-packed pattern or mask on the substrate (*Fig. 3.2, left*). Following the evaporation of metal thin film on NSL mask, nanospheres are lifted-off leaving behind the arrays of metallic nanostructures (truncated tetrahedrons) on the interstitial sites (*Fig. 3.2, right*) [80].
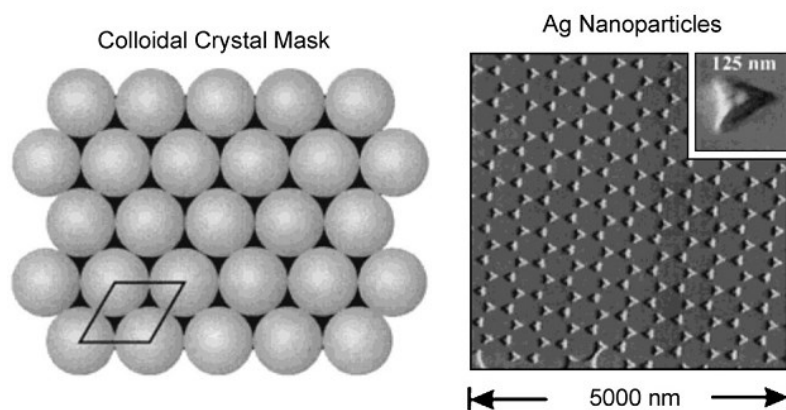
Fig. 3.2: Ag NPs fabricated through the NSL technique [79] left: single layer mask particle arrays; right: AFM image of the Ag triangles fabricated

Haynes et al reported SERS amplification factors of 10^8 using this technique [81]. The technique has been shown to be reasonably inexpensive and easy to produce nanoparticles array with somewhat controlled shape, size, and spacing.

Templated-based method: Ag/AAO systems for chemical and bio-sensing

Wang *et al.* [82] utilized porous anodized aluminum oxide (AAO) film as template to electrochemically deposit arrays of silver (Ag) nanoparticles with a precisely controlled gap up to 5 nm. This Ag/ AAO system with tunable sub-10 nm interparticle gap can be used as a uniform SERS-active substrate with large enhancement factor (~10^8). The 'hot junction' present at the interparticle gap of this nanostructure-based SERS substrates can increase the SERS sensitivity (a key factor for large electromagnetic field enhancement and increased SERS sensitivity). This Ag/AAO-based SERS substrate with highly uniform and reproducible SERS signals can be used as bio/chemical sensor and concentrations up to picomolar level have been detected. This excellent SERS substrate can be further extended into single molecular regime increasing the detection limit and SERS sensitivity.

Langmuir-Blodgett technique

Chemical assembly of metal nanoparticles on solid substrates like glass, silicon and ITO can be used as ordered SERS substrates through electrostatic or chemical interaction to form an ordered layer of nanoparticles. However, this method still cannot provide totally defect-free SERS substrate over a large area of a few hundred square centimetres.

The LB technique can potentially solve this problem. The method was originally used to prepare a large-area surface film of amphiphilic molecules on solid substrates. In this method, the amphiphilic molecules are dissolved in a volatile solvent immiscible with water, and dispersing the solution on the surface of the water phase, a monolayer of the amphiphilic molecules will form at the air/water interface after evaporation of the volatile solvent. By changing the position of the movable barrier in the LB trough, one can change the density of the monolayer film. The film can then be deposited on the substrate by the dipping and pulling method. Similarly, a nanoparticle film can be fabricated by the LB method. At first, the nanoparticles should be modified with hydrophobic molecules and dispersed into highly volatile solvent, which is immiscible with water. By dispersion of the solution into the water phase, a layer of randomly distributed nanoparticles will be left at the interface after evaporation of the solvent. As a result of compression of the layer on moving the barrier, an ordered layer of nanoparticles will be formed on the surface. The LB technique has been shown to be a high-throughput, low- cost, rapid and easily integrated method for the controlled assembly and patterning of nanoparticles and nanowires.

Yang and his group had carried out systematic SERS studies using SERS substrate fabricated by the LB technique [83]. At present, the LB technique has been successfully utilized to fabricate most uniform SERS substrates of films of nanorods, nanowires, and spherical, cubic, cuboctahedral and octahedral Ag nanoparticles [83]. Among these, the Ag nanocube exhibits the lowest enhancement, and the octahedral nanoparticle shows the highest enhancement, up to 10^7-10^8. [1]

Focused Ion beam Litography

Recently, focused ion beam direct writing (FIBDW) technology has been an increasingly important nano-fabrication technique, which has been used in the SERS substrate's development (*Fig. 3.3*) [84-86]. However, thin gold film which is coated on the Si substrate or quartz glass is soft, so it has unstable properties during the FIB processing. It is difficult to obtain nanostructures with spacing less than 20nm [87]. FIB system combines ultra-high resolution field emission SEM and precise focused ion beam etch, and could be used for nano scale prototyping, machining, and on-line high resolution SEM measurements (*Fig. 3.4*) [88]
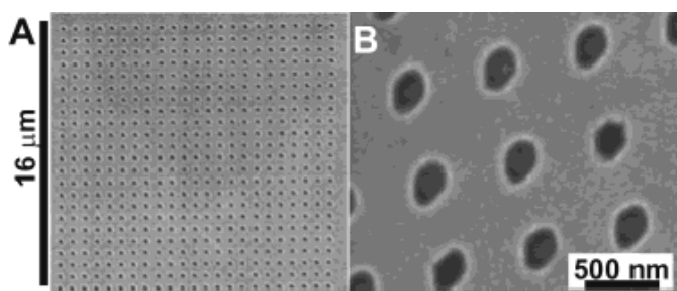
Fig. 3.3 SEM images of a typical array of sub-wavelength holes obtained by FIB technique. The image in part B is an enlargement of the array presented in part A [84]
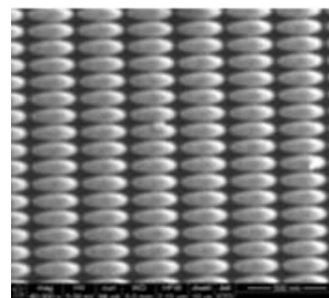
Fig. 3.4 SEM images of elliptical nanostructures coated with Au [88]

Electron-beam lithography

EBL, described in details in *Chapter 5* uses focussed electron beam to create patterns on electron-sensitive resist such as polymethyl methacrylate (PMMA), Zep 520A, etc. Due to the shorter wavelength possessed by energetic electrons (order of 1 A) it offers higher patterning resolution down to ∼ 10 nm [89].

In SERS study, EBL has been conjugated with processes like reactive ion etching (RIE) and lift-off to fabricate various nanostructures for SERS detection (*Fig 3.5*). Shown in *Fig. 3.6* are some EBL/RIE created patterns. The most important advantage of the EBL approach is the possibility of control the MNPs size and shape and the interparticle distance with great accuracy, Gunnarsson et al. explored the distance control in the evaluation of the distance-dependent for periodic structures[90].
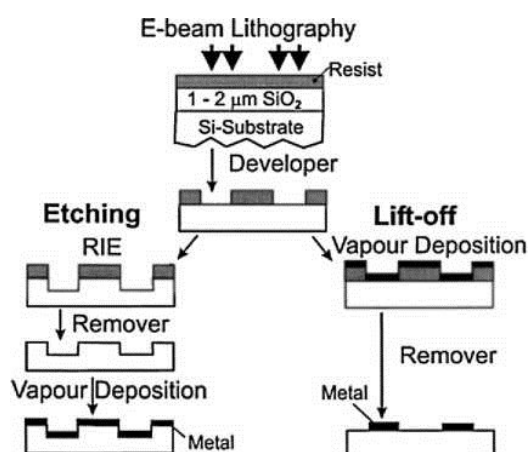
Fig. 3.5 Schemes for two fabrication strategies for SERS substrates using EBL. Two processes are presented. The left hand side process consists in an chemical etching that follows the electron beam exposing, the dissolution of the remaining PMMA layer, and deposition of metal. The substrate ends up with metal over the whole surface. The right hand side shows a metal deposition immediately afterthe e-beam exposition. After removal of the photoresistor layer, the substrate will present a series of isolated NPs, separated by regions where only bare Si substrate is exposed. From Kahl et al. [91].

Aperiodic nanostructures obtained by EBL with additional nanostructures of dimensions around 30 nm have been investigated [92]. The modification was directed by the local field enhancement, and resulted in 30 nm nanostructures connected to the 200 nm features obtained by FIB. The claimed spatially- averaged SERS-EF on these substrates was *ca.* 10^8, 3 orders of magnitude higher than the original nanostructures. The increase in SERS performance may be attributed to the coupling of the additional nanostructures with the neighboring nanostructures, as suggested by FDTD numerical calculations reported by the authors. The approach of EBL-constructed aperiodic arrays of SERS-active MNPs was also used for the creation of matrices of randomly distributed MNPs with several shapes and sizes [93].

Despite the impressive resolution, EBL has certain limitations in SERS research. The existing pattern resolution of EBL is good enough for the fabrication of isolated particles of different shape and size. However, there still remains challenge in fabricating precisely controlled nanogap of less than 5 nm and is obligatory to understand the gap-plasmon effects.
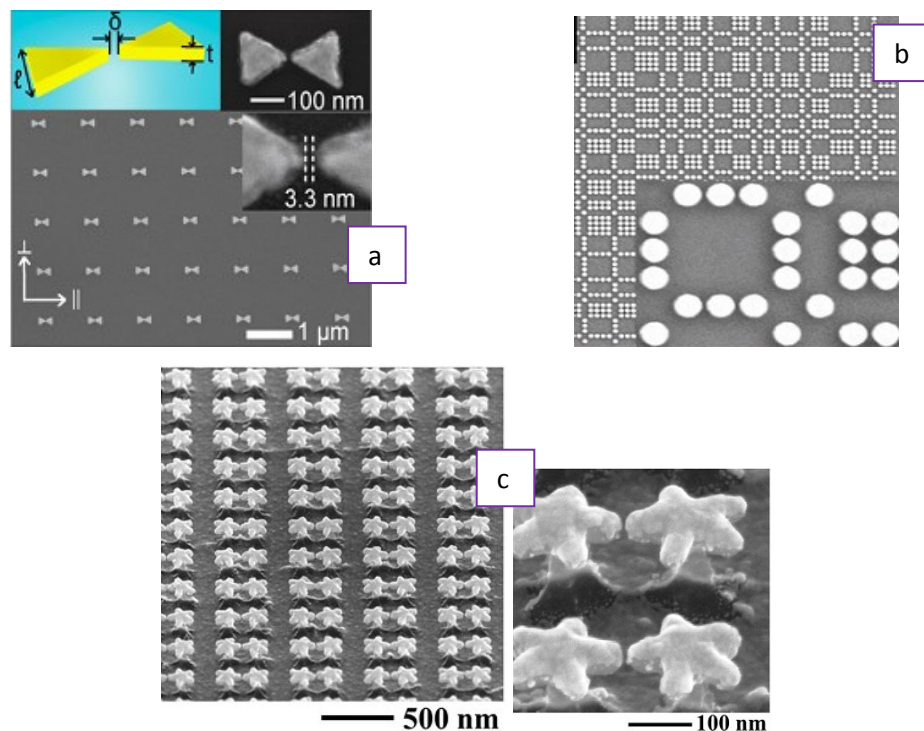
Fig. 3.6 Some patterns suitable to become engineered SERS substrates, realized by EBL: a) Bowtie antennas [94]; b)Rudin-Shapiro arrangement of gold nanoparticles [92]; c) Gold Nanostars [95]

References

[1] Ujjal Kumar Sur and Joydeep Chowdhury , *Surface-enhanced Raman scattering: overview of a versatile technique used in electrochemistry and nano science*, *CURRENT SCIENCE*, **VOL. 105, NO. 7, 10 OCTOBER 2013** (2013)

[2] Moskovits M. *Surface-enhanced spectroscopy*. ***Rev.Mod. Phys***. 57:783–826 (1985)

[3] Doron-Mor I, Barkay Z, Filip-Granit N, Vaskevich A, Rubinstein I, *Ultrathin gold island films on silanized glass: morphology and optical properties.* ***Chem. Mater***. 16:3476–83 (2004)

[4] Pieczonka NPW, Aroca RF., *Inherent complexities of trace detection by surface-enhanced Raman scattering.* ***Chemphyschem*** 6:2473–84 (2005)

[5] Bhavya Sharma, M. Fernanda Cardinal, Samuel L. Kleinman, Nathan G. Greeneltch, Renee R. Frontiera, Martin G. Blaber, George C. Schatz, and Richard P. Van Duyne, *High-performance SERS substrates: Advances and challenges*, ***MRS Bullettin. 38***, (2013)

[6] K. Kneipp, Y. Wang, H. Kneipp, L. T. Perelman, I. Itzkan, R. R. Dasari and M. S. Feld, *Single molecule detection using surface-enhanced Raman scattering (SERS).***Phys. Rev. Lett**., 78, 1667 (1997)

[7] S. R. Emory, W. E. Haskins and S. Nie, *Direct Observation of Size-Dependent Optical Enhancement in Single Metal Nanoparticles*, ***J. Am. Chem. Soc***., 120, 8009 (1998)

[8] K. Kneipp, H. Kneipp, I. Itzkan, R. R. Dasari, M. S. Feld and M. S. Dresselhaus, *Nonlinear Raman probe of single molecules attached to colloidal silver and gold clusters*, ***Top. Appl. Phys***., 82, 227(2002)

[9] S. Abalde-Cela, P Aldeanueva-Potel, C. Mateo-Mateo, L. Rodríguez-Lorenzo, R.A. Alvarez-Puebla, L.M. Liz-Marzán, *Surface Ehanced Raman Scattering biomedical application of plasmonic colloidal particles*, ***J. R. Soc. Interface*** 7, S435 (2010)

[10] Banholzer, M. J.; Millstone, J. E. ; Qin, L. ; Mirkin, C. A., *Rationally Designed Nanostructures for Surface-Enhanced Raman Scattering*, ***Chem. Soc. Rev***. 37, 885 (**2008)**

[11] A.J. Haes, C.L. Haynes, A.D. McFarland, G.C. Schatz, R.P. Van Duyne, S. Zou, *Plasmonic materials for surface-enhanced sensing and spectroscopy*, ***MRS Bull***. 30, 368 (2005)

[12] S.L. Kleinman, R.R. Frontiera, A.I. Henry, J.A. Dieringer, R.P. Van Duyne, „*Creating, characterizing, and controlling chemistry with SERS hot spots*", ***Phys. Chem. Chem. Phys***. 15, 21 (2013)

[13] S S.L. Kleinman, B. Sharma, M.G. Blaber, A.-I. Henry, N. Valley, R.G. Freeman, M.J. Natan, G.C. Schatz, R.P Van Duyne, "*Structure Enhancement Factor Relationships in Single Gold Nanoantennas by Surface-Enhanced Raman Excitation Spectroscopy,*" ***J. Am. Chem. Soc.*** 135, 301 (2013)

[14] N.G. Greeneltch, M.G. Blaber, A.-I. Henry, G.C. Schatz, R.P Van Duyne, *Immobilized nanorod assemblies: fabrication and understanding of large area surface-enhanced Raman spectroscopy substrates.* ***Anal. Chem.*** (2013), doi:10.1021/ac303269w

[15] M. Fleischmann, P.J. Hendra, A.J. McQuillan, *Raman spectra of pyridine adsorbed at a silver electrode*, ***Chemical Physics Letters*** 26, 163 (1974)

[16] D.L. Jeanmaire, R.P. Van Duyne, *Surface Enhanced Elecrochemistry Part I.* Heterocyclic, aromatic, and aliphatic-amines adsorbed on *anodized silver electrode,* ***J. Electroanal. Chem. Interfacial Electrochem***. *84* 1 (1977)

[17] J.A. Creighton, C.G. Blatchford, M.G. Albrecht, *Plasma resonance enhancement of Raman scattering by pyridine adsorbed on silver or gold sol particles of size comparable to the excitation wavelength*, ***J. Chem. Soc., Faraday Trans. II*** 75, 790 (1979)

[18] PC. Lee, D. Meisel, *Adsorption and surface-enhanced Raman of dyes on silver and gold sols,* ***J. Phys. Chem***. 86, 3391 (1982)

[19] M. Jin, H. van Wolferen, H. Wormeester, A. van den Berg, E.T. Carlen, *Large-area nanogap plasmon resonator arrays for plasmonics applications*, ***Nanoscale*** 4, 4712 (2012)

[20] Y. Qiuming, B. Scott, C. Brian, X. Jiajle, M.W. Paul, G. Heng, K. Dmitry, *Surface-enhanced Raman scattering on gold quasi-3D nanostructure and 2D nanohole arrays*, **Nanotechnology** 21, 355301 (2010)

[21] R.P Van Duyne, J.C. Hulteen, D.A. Treichel, "*Atomic Force Microscopy and Surface-Enhanced Raman Spectroscopy. I. Ag Island Films and Ag Film Over Polymer Nanosphere Surfaces Supported on Glass*" ***J. Chem. Phys***. 99, 2101 (1993)

[22] J.R. Anema, J. F. Li, Z. L. Yang, B. Ren, Z. Q. Tian, *Shell-isolated nanoparticle-enhanced Raman spectroscopy: expanding the versatility of surface-enhanced Raman scattering,* ***Annu. Rev. Anal. Chem***. 129 (2011)

[23] S.J. Barcelo, A. Kim, W. Wu, Z. Li, *Fabrication of deterministic nanostructure assemblies with sub-nanometer spacing using a nanoimprinting transfer technique*, ***ACS Nano*** 6, 6446 (2012)

[24] K.D. Osberg, M. Rycenga, N. Harris, A.L. Schmucker, M.R. Langille, G.C. Schatz, C.A. Mirkin, *Dispersible gold nanorod dimers with sub-5 nm gaps as local amplifiers for surface-enhanced Raman scattering*, ***Nano Lett.*** 12, 3828 (2012)

[25] M. Fan, G.F.S. Andrade, A.G. Brolo, *A review on the fabrication of substrates for surface enhanced Raman spectroscopy and their applications in analytical chemistry,* ***Anal. Chim. Acta*** 693, 7 (2011)

[26] H. Skaff, T. Emrlck, In ***Nanoparticles:Building Blocksfor Nanotechnology,*** V. Rotello, Ed. (Springer, NY, 2004), p. 29

[27] J. Vermant, E.M. Furst, L.M. Liz-Marzán, *Directed self-assembly of nanoparticles*, **ACS Nano** 4, 3591 (2010)

[28] J. Song, J. Zhou, H. Duan, *Self-assembled plasmonic vesicles of SERS-encoded amphiphilic gold nanoparticles for cancer cell targeting and traceable intracellular drug delivery*, **J. Am. Chem. Soc.** 134, 13458 (2012)

[29] L. Wang, L. Xu, H. Kuang, C. Xu, N.A. Kotov, *Dynamic nanoparticle assemblies*, **Acc. Chem. Res.** 45, 1916 (2012)

[30] T. Wang, D. LaMontagne, J. Lynch, J. Zhuang, YC. Cao, *Colloidal superparticles from nanoparticle assembly*, **Chem. Soc. Rev. 7, 42** (2013), doi:10.1039/C2CS35318k

[31] X. Ye, C. Zheng, J. Chen, Y Gao, C.B. Murray, *Seeded growth of monodisperse gold nanorods using bromide-free surfactant misture*, **Nano Lett**. 13 (5), 2163 (2013)

[32] B.E. Brinson, J.B. Lassiter, C.S. Levin, R. Bardhan, N. Mirin, N.J. Halas, *Nanoshells made easy: improving Au layer growth on nanoparticle surfaces*, **Langmuir** 24, 14166 (2008)

[33] M. Grzelczak, J. Pérez-Juste, P Mulvaney, L.M. Liz-Marzán, *Shape control in gold nanoparticle synthesis*, **Chem. Soc. Rev**. 37 1783 (2008)

[34] M.R. Langille, M.L. Personick, J. Zhang, C.A. Mirkin, *Defining rules for the shape evolution of gold nanoparticles*, **J. Am. Chem. Soc.** 134, 14542 (2012)

[35] X.M. Lu, M. Rycenga, S.E. Skrabalak, B. Wiley, YN. Xia, *Chemical synthesis of novel plasmonic nanoparticles*, **Annu. Rev. Phys. Chem**. 60, 167 (2009)

[36] C.J. Murphy, T.K. Sau, A.M. Gole, C.J. Orendorff, J. Gao, L. Gou, S.E. Hunyadi, T. Li, *Anisotropic metal nanoparticles: Synthesis, assembly, and optical applications*, **J. Phys. Chem. B** 109, 13857 (2005)

[37] T.K. Sau, A.L. Rogach, M. Döblinger, J. Feldmann, *One-step high-yield aqueous synthesis of size-tunable multispiked gold nanoparticles*, **Small** 7, 2188 (2011)

[38] X. Xia, J. Zeng, Q. Zhang, C.H. Moran, Y Xia, *Recent Developments in Shape-Controlled Synthesis of Silver Nanocrystals*, **J. Phys. Chem. C** 116, 21647 (2012)

[39] M. Yang, R.A. Alvarez-Puebla, H.-S. Kim, P Aldeanueva-Potel, L.M. Liz-Marzán, N.A. Kotov, *SERS-active gold lace nanoshells with built-in hotspots*, **Nano Lett.** 10, 4013 (2010)

[40] PD. Cozzoli, T. Pellegrino, L. Manna, *Synthesis, properties and perspectives of hybrid nanocrystal structures*, *Chem. Soc. Rev.* 35, 1195 (2006)

[41] M.F. Cardinal, B. Rodríguez-González, R.A. Alvarez-Puebla, J. Pérez-Juste, L.M. Liz-Marzán, *Modulation of Localized Surface Plasmons and SERS Response in Gold Dumbbells Through Silver Coating*, **J. Phys. Chem. C** 114, 10417 (2010)

[42] M. Gühlke, S. Selve, J. Kneipp, *Magnetic separation and SERS observation of analyte molecules on bifunctional silver/iron oxide composite nanostructures*, **J. Raman Spectrosc**. 43, 1204 (2012)

[43] J. Pérez-Juste, I. Pastoriza-Santos, L.M. Liz-Marzán, *Multifunctionality in metal@microgel colloidal nanocomposites*, **J. Mater. Chem. A** 1, 20 (2013)

[44] M. Spuch-Calvar, L. Rodríguez-Lorenzo, M.P Morales, R.A. Álvarez-Puebla, L.M. Liz-Marzán, *Bifunctional Nanocomposites with Long-Term Stability as SERS Optical Accumulators for Ultrasensitive Analysis*, **J. Phys. Chem. C** 113, 3373 (2008)

[45] S. Xie, M. Jin, J. Tao, Y. Wang, Z. Xie, Y Zhu, Y Xia, *Synthesis and Characterization of Pd@M_xCu$_{1-x}$ (M=Au, Pd, and Pt) Nanocages with Porous Walls and a Yolk–Shell Structure through Galvanic Replacement Reactions*, **Chem. Eur. J.** 18, 14974 (2012)

[46] G. Chen, Y. Wang, L.H. Tan, M. Yang, L.S. Tan, Y Chen, H. Chen, *High-purity separation of gold nanoparticle dimers and trimers*, **J. Am. Chem. Soc**. 131, 4218 (2009)

[47] G. Chen, Y Wang, M. Yang, J. Xu, S.J. Goh, M. Pan, H. Chen, *Measuring ensemble-averaged surface-enhanced Raman scattering in the hotspots of colloidal nanoparticle dimers and trimers*. **J. Am. Chem. Soc.** 132, 3644 (2010)

[48] N.P.W. Pieczonka, G. Moula, R.F. Aroca, *SERRS for single-molecule detection of dye-labeled phospholipids in Langmuir-Blodgett monolayers*, **Langmuir** 25, 11261 (2009)

[49] M. Rycenga, PH.C. Camargo, Y Xia, *Template-assisted self-assembly: a versatile approach to complex micro- and nanostructures*, **Soft Matter** 5, 1129 (2009)

[50] E.C. Le Ru, M. Meyer, E. Blackie, PG. Etchegoin, *Advanced aspects of electromagnetic SERS enhancement factors at a hot spot*, **J. Raman Spectrosc**. 39, 1127 (2008)

[51] A. Otto, *What is observed in single molecule SERS, and why?*, **J. Raman Spectrosc**. 33, 593 (2002)

[52] H. Skaff, T. Emrlck, In **Nanoparticles: Building Blocks for Nanotechnology**, V. Rotello, Ed. (Springer, NY, 2004)

[53] PC. Lee, D. Meisel, *Adsorption and surface-enhanced Raman of dyes on silver and gold sols*, **J. Phys. Chem**. 86, 3391 (1982)

[54] N.G. Bastús, J. Comenge, V.C. Puntes, *Kinetically Controlled Seeded Growth Synthesis of Citrate-Stabilized Gold Nanoparticles of up to 200 nm: Size Focusing versus Ostwald Ripening*, **Langmuir** 27, 11098 (2011)

[55] J. Rodríguez-Fernández, J. Pérez-Juste, FJ. García de Abajo, L.M. Liz-Marzán, Seeded *Growth of Submicron Au Colloids with Quadrupole Plasmon Resonance Modes*, **Langmuir** 22, 7007 (2006)

[56] M. Rycenga, X. Xia, C.H. Moran, F. Zhou, D. Qin, Z.-Y. Li, Y. Xia, *Generation of hot spots with silver nanocubes for single-molecule detection by surface-enhanced Raman scattering*, **Angew. Chem. Int.** *Ed.* 50, 5473 (2011)

[57] L.J. Sherry, S.-H. Chang, G.C. Schatz, R.P. Van Duyne, B.J. Wiley, Y. Xia, *Localized surface plasmon resonance spectroscopy of single silver nanocubes*, **Nano Lett**. 5, 2034 (2005)

[58] F. Kim, S. Connor, H. Song, T. Kuykendall, P Yang, *Platonic gold nanocrystals*, **Angew. Chem. Int.** *Ed.* 43, 3673 (2004)

[59] M.R. Langille, M.L. Personick, J. Zhang, C.A. Mirkin, *Defining rules for the shape evolution of gold nanoparticles*, **J. Am. Chem. Soc**. 134, 14542 (2012)

[60] X.M. Lu, M. Rycenga, S.E. Skrabalak, B. Wiley, YN. Xia, *Chemical synthesis of novel plasmonic nanoparticles*, **Annu. Rev. Phys. Chem**. 60, 167 (2009)

[61] M.Z. Liu, P Guyot-Sionnest, *Mechanism of silver(I)-assisted growth of gold nanorods and bipyramids*, **J. Phys. Chem. B** 109, 22192 (2005)

[62] A. Sánchez-Iglesias, I. Pastoriza-Santos, J. Pérez-Juste, B. Rodríguez-González, FJ. García de Abajo, L.M. Liz-Marzán, *Synthesis and Optical Properties of Gold Nanodecahedra with Size Control*, **Adv. Mater**. 18, 2529 (2006)

[63] T.H. Ha, H.-J. Koo, B.H. Chung, *Shape-Controlled Syntheses of Gold Nanoprisms and Nanorods Influenced by Specific Adsorption of Halide Ions*, **J. Phys. Chem**. *C* 111, 1123 (2006)

[64] J.E. Millstone, W. Wei, M.R. Jones, H. Yoo, C.A. Mirkin, *Iodide Ions Control Seed-Mediated Growth of Anisotropic Gold Nanoparticles*, **Nano Lett.** 8, 2526 (2008)

[65] I. Pastoriza-Santos, L.M. Liz-Marzán, *Synthesis of Silver Nanoprisms in DMF*, **Nano Lett**. 2, 903 (2002)

[66] C.J. Murphy, T.K. Sau, A.M. Gole, C.J. Orendorff, J. Gao, L. Gou, S.E. Hunyadi, T. Li, *Anisotropic metal nanoparticles: Synthesis, assembly, and optical applications*, **J. Phys. Chem. B** 109, 13857 (2005)

[67] L. Rodríguez-Lorenzo, R.A. Álvarez-Puebla, F.J. García de Abajo, L.M. Liz-Marzán, *Surface Enhanced Raman Scattering Using Star-Shaped Gold Colloidal Nanoparticles*, **J. Phys. Chem. C** 114, 7336 (2009)

[68] W. Niu, S. Zheng, D. Wang, X. Liu, H. LI, S. Han, J. Chen, Z. Tang, G. Xu, *Selective Synthesis of Single-Crystalline Rhombic Dodecahedral, Octahedral, and Cubic Gold Nanocrystals*, **J. Am. Chem. Soc.** 131, 697 (2008)

[69] D. Seo, C.I. Yoo, I.S. Chung, S.M. Park, S. Ryu, H. Song, *Shape Adjustment between Multiply Twinned and Single-Crystalline Polyhedral Gold Nanocrystals: Decahedra, Icosahedra, and Truncated Tetrahedra*, **J. Phys. Chem. C** 112, 2469 (2008)

[70] K. Ueno , S. Juodkazis , V. Mizeikis , K. Sasaki , H. Misawa, *Inhibition of multipolar plasmon excitation in periodic chains of gold nanoblocks*, **J. Am.Chem. Soc**. 2006 , *128* , 14226 – 14227 (2006)

[71] K. Ueno , S. Juodkazis , V. Mizeikis , K. Sasaki , H. Misawa, *Clusters of Closely Spaced Gold Nanoparticles as a Source of Two-Photon Photoluminescence at Visible Wavelengths*, **Adv. Mater**. 2008 , 20 , 26 – 29 (2008)

[72] L. Rosa , K. Sun , J. Szymanska , F. E. Hudson , A. Dzurak , A. Linden ,S. Bauerdick , L. Peto , S. Juodkazis, *Tailoring spectral position and width of field enhancement by focused ion-beam patterning of plasmonic nanoparticles*, **Phys. Status Solidi – RRL**,*4* , 262 – 264 (2010)

[73] G. Gervinskas , G. Seniutinas , L. Rosa , S. Juodkazis , *Arrays* of *arbitrarily shaped nanoparticles*: *Overlay-errorless* direct ion *write*, **Adv. Opt. Mater.**, *1* , 456 – 459 (2013)

[74] Yoshiaki   Nishijima, Yoshikazu Hashimoto, Lorenzo Rosa, Jacob B. Khurgin, and Saulius Juodkazis, *Scaling rules of Sers intensity*, **Advanced optical materials** (2014) DOI: 10.1002/adom.201300493

[75] R. J. C. Brown, M. J. T. Milton, Nanostructures and nanostructured substrates for surface—enhanced Raman scattering (SERS), **J. Raman Spectrosc.** 39, 1313 (2008)

[76]R. A. Tripp, R. A. Dluhy, Y. P. Zhao, *Novel nanostructures* for *SERS biosensing,* **Nano Today**, 3, 31 (2008)

[77] G. Das, M. Chirumamilla, A. Toma, A. Gopalakrishnan, R. Proietti Zaccaria, A. Alabastri, M. Leoncini, E. Di Fabrizio, *Plasmon based biosensor for distinguishing different peptides mutation states*, **SCIENTIFIC REPORTS** | 3 : 1792 (2013)

[78] Willets, K. A. and Van Duyne, R. P., *Localized surface plasmon resonance spectroscopy and sensing. **Annu. Rev. Phys. Chem.**,* 58, 267-297 (2007)

[79] Haynes, C. L. and Van Duyne, R. P., *Nanosphere lithography: a versatile nanofabrication tool for studies of size-dependent nanoparticle optics. **J. Phys. Chem. B***, 105, 5599-5611 (2001)

[80] J. C. Hulteen, D. A. Treichel, M. T. Smith, M. L. Duval, T. R. Jensen, R. P. Van Duyne, *Nanosphere Lithography: Size-Tunable Silver Nanoparticle and Surface Cluster Arrays*, **J. Physhem. B** 103, 3854 (1999)

[81] C. L. Haynes, R. P. Van Duyne, *Plasmon-Sampled Surface-Enhanced Raman Excitation Spectroscopy*, **J. Phys. Chem. B**, 107, 7426 (2003)

[82] Wang, H. H. *et al., Highly Raman-enhancing substrates based on silver nanoparticle arrays with tunable sub-10 nm gaps. **Adv. Mater.**,* 18, 491-495 (2006)

[83] Tao, A. *et al., Langmuir-Blodgett silver nanowire monolayers for molecular sensing using surface-enhanced Raman spectroscopy. **Nano Lett.**,* 3, 1229-1233 (2003)

[84] Brolo et al. *Surface Plasmon Sensor Based on the Enhanced Light Transmission through Arrays of Nanoholes in Gold Film*, **Langmuir**, 20, 4813 4815 (2004)

[85] Min Q, Santos MJL, Girotto EM, Brolo AG, Gordon R: *Localized Raman enhancement from a double-hole nanostructure in a metal film. **Phys Chem Lett**, 112:15098–1510 (2008)

[86] Bahns JT, Imre A, Vlasko-Vlasov VK, Pearson J, Hiller JM, Chen LH, Welp U: *Enhanced Raman scattering from focused surface plasmons. **Appl Phys Lett**, 91:081104. (2004)

[87] Naik JP, Prewett PD, Das K, Raychaudhuri AK: *Instabilities in focused ion beam-patterned Au nanowires. **Microelectron Eng**, 88:2840–2843 (2011)

[88] Gao et al. *High performance surface-enhanced Raman scattering substrates of Si-based Au film developed by focused ion beam nanofabrication*, **Nanoscale Research Letters**, 7:399 (2012)

[89] Wang, H. et al. *Low temperature ZEP-520A Development Process for Enhanced Critical Dimension Realization in Reactive Ion Etched Polysilicon. **Journal of Vacuum Science & Technology B** 25, 102-105 (2007)

[90] L. Gunnarsson, E.J. Bjerneld, H. Xu, S. Petronis, B. Kasemo, M. Kall, **Applied Physics Letters** 78, 802 (2001)

[91] M. Kahl, E. Voges, S. Kostrewa, C. Viets, W. Hill, *Periodically structured metallic substrates for SERS*, **Sensors and Actuators B-Chemical** 51, 285 (1998)

[92] A. Gopinath, S.V. Boriskina, W.R. Premasiri, L. Ziegler, B.r.M. Reinhard, L. Dal Negro, *Plasmonic Nanogalaxies: Multiscale Aperiodic Arrays for Surface-Enhanced Raman Sensing*, **Nano Letters** 9, 3922 (2009)

[93] S.M. Wells, S.D. Retterer, J.M. Oran, M.J. Sepaniak, *Controllable Nanofabrication of Aggregate-like Nanoparticle Substrates and Evaluation for Surface-Enhanced Raman Spectroscopy*, **ACS Nano** 3, 3845 (2009)

[94] Stephanie Dodson, Mohamed Haggui, Renaud Bachelot, Jerome Plain, Shuzhou Li, and Qihua Xiong, *Optimizing Electromagnetic Hotspots in Plasmonic Bowtie Nanoantennae*, **J. Phys. Chem. Lett.**, 4, 496–501 (2013)

[95]Di Fabrizio et Al., *3D Nanostar Dimers with a Sub-10-nm Gap for Single-/Few-Molecule Surface-Enhanced Raman Scattering*, **Adv. Mater**. (2014) DOI: 10.1002/adma.201304553

Chapter 4: Photonic Crystals and Photonic Quasi-Crystals

4.1 Metamaterials

From the early age of optical science and engineering, scholars and opticians have devised many ways to control light by constraining, shaping and directing it via all kinds of devices using the "bulk" optical properties of the materials at hand. To further extend our level of control over light, scientists now envision the creation of artificial materials specially designed on the microscale (and nanoscale) level to exhibit new and unusual electromagnetic properties at the macro-scale. Proponents of these human-made "***meta***-materials" anticipate that their continuing development will impact every area of optics in the near future. This optical revolution would be made possible by taking advantage of the unique exotic effects displayed by metamaterials such as invisibility cloaking, negative refraction, slow light and superlensing. [1-3]. Some of these feats could purposely "beat" classical limits of physics previously believed to be unwavering. No wonder some investigators go as far as saying metamaterials open up a new "magical world" for photonics [4, 5]. The prefix "meta" comes from Greek and means "after" or "beyond". Thus with that in mind, Metamaterials are defined as a class of ordered composites that exhibit exceptional properties that arise from qualitatevely new response functions, that are not observed in the constituent materials [6] and result from the inclusion of artificially fabricated, extrinsic, low dimensional inhomogeneities. This means that if properly engineered, metamaterials can exhibit tailored values of response functions such as the dielectric function ε or the magnetic permeability μ. Tuning the optical properties in this way, metamaterials can be used to control electromagnetic waves and structures that can even cloak an object from incident radiations can be fabricated.[7]. Modifying the values of ε and μ has as a direct consequence the modification of the value of the index of refraction n of the metamaterial, which in turn is another response function that can be tuned in this particular class of materials [8; 9]. It has to be noted though that the index of refraction *n* can be tuned without varying the values of ε and μ throughout the entire structure, but also simply using two (or more) constituent materials with different response function, ordered in a lattice. This is precisely what happens in photonic crystals, ordered structures made of dielectric or metals, that can be realized in one, two or three dimensions [10].

4.2 Photonic crystals

The advances in photonics especially in the last decade makes it necessary to have suitable ways for generating and managing electromagnetic energy for various applications. It is important to engineer the properties of the materials which can respond to light waves of the desired frequency to confine, filter or guide the electromagnetic radiation. Photonic crystals (also known as photonic band gap materials) are optical materials with periodic changes in the dielectric constant and able to control the light propagation. As demonstrated several years ago, this phenomena has similar influence on the propagation of light as atomic crystalline potentials have on electrons [10]. A crystal is a periodic arrangement of atoms or molecules; therefore it presents a periodic potential to an electron propagating through it, and the geometry of the crystal dictates many of the conduction properties of the crystal. In particular, the lattice might introduce gaps into the energy band structure of the crystal, so that electrons are forbidden to propagate with certain energies in certain directions. The optical analogy is the photonic crystal, in which the periodic potential is due to a lattice of dielectric media instead of atoms. Yablonovitch [11] showed that if the dielectric constants of the two materials are sufficiently different, the photonic crystals can also possess a photonic band-gap (PBG), so that a certain range of frequencies are not passed through the crystal, just like an electronic semi-conductor.

The position and width of the photonics band-gap plays an important role in case of most of the applications of photonic crystals (PCs). In this way, we can design and construct photonic crystals with photonic band gaps, preventing light, with specified energies, from propagating in certain directions. Intentionally introduced defects in the crystal (analogous to electronic dopants) give rise to localized electromagnetic states: linear waveguide and point-like cavities. Electromagnetic wave propagation in periodic media was first studied by Lord Rayleigh in 1887, in connection with the peculiar reflective properties of a crystalline mineral with period "twinning" planes. These correspond to one-dimensional photonic crystals, and he identified the fact that they have a narrow band gap prohibiting light propagation through the planes and that this band gap is angle-dependent.

A similar effect is responsible for many other iridescent colors in nature, where more or less ordered photonic crystals have been recognized in recent years to be largely diffused: they provide an immense variety of structural colorations to coleopters, butterfly wings, opals, abalone shells, [12-14] and a source of inspiration for novel bio-mimetic nanotechnologies for color engineering and photonic devices. [15]
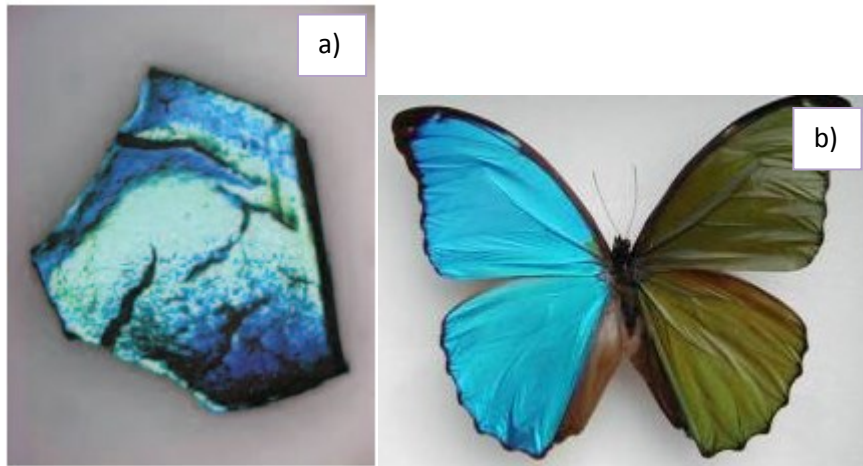
Fig. 4.1: Light reflected from a) a photonic crystal, titania inverse opal [16]; b) wings of a butterfly

Order with periodicity

Structural order is often exclusively associated with the concept of *spatial periodicity.* Humans can easily recognize periodic patterns even in the presence of substantial noise or perturbations, and many of the beautiful regularity of natural phenomena are manifestations of periodic systems. In his book "An introduction to mathematics", published in 1911, the English mathematician Alfred North Whitehead remarked that [17]: *"The whole life of nature is dominated by the existence of periodic events… The presupposition of periodicity is fundamental to our very conception of life".* Periodic patterns repeat a basic motif or building block in three-dimensional space. In general, any vector function of position vector *r* satisfying the condition *Φ(r + R₀) = Φ (r)* describes spatially periodic patterns because it is invariant under the set of translations generated by the vector *R₀*. As a result, we say that periodic structures display *a specific kind of long-range order* characterized by *translational invariance symmetry* along certain spatial directions. The beautiful regularity of inorganic crystals best exemplifies periodically ordered patterns where a certain atomic configuration, known as the *base,* repeats in space according to an underlying periodic lattice, thus defining *a crystal structure.* One of the most fundamental results of classical crystallography states that the combination of translation and rotation operations restricts the total number of rotational symmetries to only the ones compatible with the periodicity of the lattice. This important result is known as the *crystallographic restriction.* We say that a structure possesses an **n-fold** rotational symmetry if it is left unchanged when rotated by an angle *2π/n*, and the integer *n* is called the *order* of the rotational symmetry (or the order of the symmetry axis). It can be shown that only rotational symmetries of order *n* = 2,3,4 and 6 can match the translational

symmetry of 2D and 3D periodic lattices in Euclidean space [18-20] A fundamental feature of the diffraction patterns of all types of periodic lattices is the presence of well defined and sharp peaks corresponding to the presence of periodic long-range order. As a result, the reciprocal Fourier space of periodic and multi-periodic lattices is discrete (i. e., pure-point), with Bragg peaks positioned at rational multiples of primitive reciprocal vectors. As an example, we show in *Fig. 4.2* the square and hexagonal lattices (*Fig. 4.2 a,c*) with their corresponding diffraction spectra (*Fig. 4.2 b,d*), or reciprocal spaces, obtained by calculating the amplitudes of the lattice Fourier transforms (i. e., the Fraunhofer regime). Bright diffraction spots arranged in patterns with square and hexagonal symmetries are clearly visible in *Figs. 4.2(b,d)*. Their intensities progressively decrease away from the centers of the diffraction diagrams due to the contributions of the circular shape of finite-size particles, which filter the diffraction pattern according to the envelope of a Bessel function, and the size of the entire arrays, which determines the shape/size of individual diffraction spots.
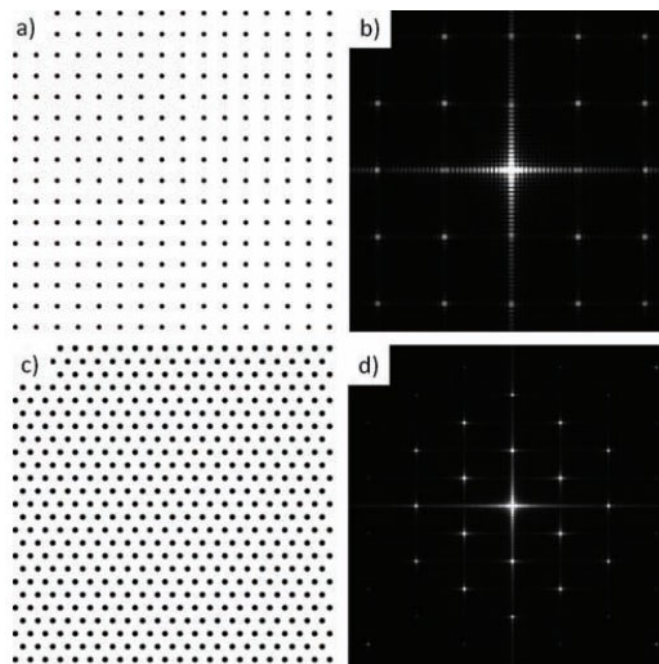
Fig 4.2: (a) Periodic square lattice. (b) Reciprocal space of the square lattice calculated via its. Fourier transform amplitude. (c) Periodic hexagonal lattice. (d) Reciprocal space of the hexagonal lattice calculated via its Fourier transform amplitude [21]

This picture best exemplifies the notion of periodic arrangement of atoms which is at the origin of the traditional classification scheme of materials into the two broad categories of *crystalline* and *amorphous* structures. According to this simple classification scheme, *long-range structural order* and *periodicity* are considered identical, leading to the widespread

conception of crystalline materials as the *paradigm of order* in solid state electronics and optics (e. g., photonic crystals).
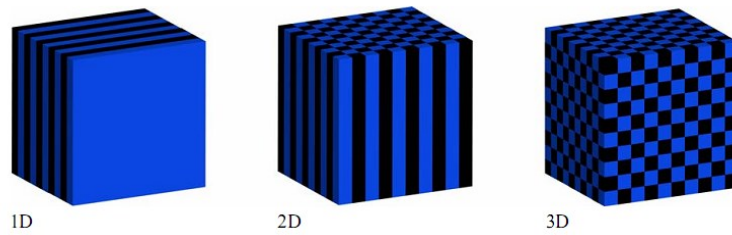
Fig. 4.3: Simple example of one-, two-, three-dimensional Photonic Crustals.
Different colors represent materials with different dielectric constant

An important application of photonic crystals is in the localization of electromagnetic field. This is usually done by intentionally introducing some defect in the periodic structure. If radiation of frequency corresponding to the photonic band gap is then introduced to a point defect, the field will be trapped inside the defect since the propagation is prohibited inside the crystal. This effect can be exploited to design *cavity resonators*. The same effect can be used to create waveguides by introducing linear defects which can confine and guide the radiation without loss in the preferred path. Another important application of photonic crystals is their ability to have lasing close to the band-edge because of the anomalous reduction of group velocity near the band-edge which induces an enhanced spontaneous thereby reducing the threshold for lasing. There had been several investigations in this direction [22-26].

4.2.1 Electromagnetism as an eigenvalue problem

In order to study the propagation of light in a photonic crystal, we begin with the Maxwell equations. After specializing to the case of a mixed dielectric medium, we cast the Maxwell equations as a linear Hermitian eigenvalue problem. This brings the electromagnetic problem into a close analogy with the Schrödinger equation, and allows us to take advantage of some well-established results from quantum mechanics, such as the orthogonality of modes, the variational theorem, and perturbation theory. One way in which the electromagnetic case differs from the quantum-mechanical case is that photonic crystals do not generally have a fundamental scale, in either the spatial coordinate or in the potential strength (the dielectric constant). This makes photonic crystals scalable in a way that traditional crystals are not.

All of macroscopic electromagnetism, including the propagation of light in a photonic crystal, is governed by the four macroscopic **Maxwell equations**. In SI units, they are:

$$\nabla \cdot \boldsymbol{B} = 0 \qquad\qquad \nabla \times \boldsymbol{E} + \frac{\partial \boldsymbol{B}}{\partial t} = 0 \qquad\qquad (4.1)$$

$$\nabla \cdot \boldsymbol{D} = \rho \qquad\qquad \nabla \times \boldsymbol{H} - \frac{\partial \boldsymbol{D}}{\partial t} = \boldsymbol{J} \qquad\qquad (4.2)$$

where (respectively) **E** and **H** are the macroscopic electric and magnetic fields, **D** and **B** are the displacement and magnetic induction fields, and p and **J** are the free charge and current densities. An excellent derivation of these equations from their microscopic counterparts is given in Jackson (1998).

Considering a homogenous dielectric material, in which light propagates but there are no sources of light, we can set $\rho = 0$ and $\boldsymbol{J} = 0$.

For many dielectric materials, it is a good approximation to assume the material is macroscopic and isotropic, so that $\boldsymbol{E(r, \omega)}$ and $\boldsymbol{D(r, \omega)}$ are related by ε_0 multiplyed by a scalar **dielectric function** $\varepsilon(r, \omega)$, also called the **relative permittivity**. Moreover, we can ignore any explicit frequency dependence (**material dispersion**) of the dielectric constant, simply choosing the value of ε appropriate to the frequency range of the physical system we are considering. Finally, if we focus primarily on **transparent materials**, which means we can treat $\varepsilon(r)$ as purely real and positive.

Assuming these four approximations to be valid, we have:

$$\boldsymbol{D(r)} = \varepsilon_0 \varepsilon(r) E(r) \qquad\qquad \boldsymbol{B(r)} = \mu_0 \mu(r) H(r) \qquad\qquad (4.3)$$

where $\mu_0 = 4\pi \times 10^{-7}$ Henry/m is the vacuum permeability, but for most dielectric materials of interest the relative magnetic permeability $\mu(r)$ is very close to unity and we may set $\boldsymbol{B} = \mu_0 \boldsymbol{H}$ for simplicity. In that case, ε is the square of the **refractive index** n that may be familiar from Snell's law and other formulas of classical optics. In general $n = \sqrt{\varepsilon \mu}$.

With all of these assumptions in place, the Maxwell equations (4.1)-(4.2) become

$$\nabla \cdot \boldsymbol{H(r, t)} = 0 \qquad\qquad \nabla \times \boldsymbol{E(r, t)} + \mu_0 \frac{\partial \boldsymbol{H(r, t)}}{\partial t} = 0 \qquad\qquad (4.4)$$

$$\nabla \cdot \varepsilon(r) E(r, t) = 0 \qquad\qquad \nabla \times \boldsymbol{H(r, t)} - \varepsilon_0 \varepsilon(r) \frac{\partial \boldsymbol{E(r, t)}}{\partial t} = 0 \qquad (4.5)$$

Since Maxwell equations are linear, however, we can separate the time dependence from the spatial dependence by expanding the fields into a set of **harmonic modes**. We thus need solutions of the form:

$$\boldsymbol{H(r, t)} = \boldsymbol{H(r)} e^{i\omega t} \qquad\qquad\qquad (4.6)$$

$$E(r, t) = E(r)e^{i\omega t}$$

Substitution of (4.6) into (4.4) gives:

$$\nabla \cdot H(r) = 0 \qquad\qquad \nabla \cdot D(r) = 0 \qquad\qquad (4.7)$$

Thus the fields are built up of waves that are *transverse.*

Substitution of (4.6) into (4.6) gives:

$$\nabla \times E(r) - i\omega\mu_0 H(r) = 0$$
$$\nabla \times H(r) + i\omega\varepsilon_0\varepsilon(r)E(r) = 0 \qquad\qquad (4.8)$$

Combining the two equations (4.8) and taking into account that the constants ε_0 and μ_0 can be combined to yield the vacuum speed of light, $c = 1/\sqrt{\varepsilon_0\mu_0}$, the result is an equation entirely in *H(r):*

$$\nabla \times \left(\frac{1}{\varepsilon(r)}\nabla \times H(r)\right) = \left(\frac{\omega}{c}\right)^2 H(r) \qquad\qquad (4.9)$$

This is the **Master Equation.** Once we know $\varepsilon(r)$ for a given photonic crystal, we can solve the master equation to find the *H(r)* for a given frequency. Then using the second of (4.8), it is possible to recover *E(r):*

$$E(r) = \left(\frac{-ic}{\omega\varepsilon(r)}\right)\nabla \times H(r) \qquad\qquad (4.10)$$

Note that (4.9) is just an *eigenvalue problem.* In this situation, when the result of an operation on a function is just the function itself, multiplied by some constant, the function is called an *eigenfunction* of that operator, and the multiplicative constant is called the *eigenvalue* [27].

In this case we identify the operator $\theta \equiv \nabla \times \frac{1}{\varepsilon(r)}\nabla \times$, acting on *H(r) and making it look explicitly like an eigenvalue problem:*

$$\theta H(r) = \left(\frac{\omega}{c}\right)^2 H(r) \qquad\qquad (4.11)$$

One important thing to notice is that the operator θ is a linear *Hermitian* operator and thus reminiscent of the Hamiltonian for electrons.

4.2.2Photonic band structures

Photonic crystals, like the familiar crystals of atoms, do not have continuous symmetry; instead, they have *discrete* translational symmetry. Thus they are not invariant under translations of any distance, but only under distances that are multiple of a fixed step length. This basic step length is the so called *lattice constant A,* and the basic step vector is called *primitive lattice vector* **a**. Because of this symmetry, *ε(r) = ε(r+A).* By repeating this translation, we can see that *ε(r) = ε(r+R)* for any **R** that is integral multiple of **a**. The dielectric unit that we consider to be repeated over and over, is known as the *unit cell.*

The discrete periodicity in a certain direction leads to a dependence of **H** for that direction, that is simply the combination of plane waves, modulated by a periodic function because of the periodic lattice:

$$H(r) = e^{ik_r r} u_k(r) \tag{4.12}$$

where $u_k(r)$ is periodic in the real space lattice.

This result is commonly known, from the solid-state physics, as ***Bloch's theorem,*** and the form of (4.12) is known as a *Bloch state* [28]. The wave vectors k_r that differ by integral multiples m of $2\pi/A$ are not different from a physical point of view. In fact, all the modes with wave vector of the form $k_r + m(2\pi/A)$, where m is an integer, form a degenerate set and leave the state unchanged. Thus the mode frequencies must also be periodic in k_r: $\omega(k_r) = \omega\left(k_r + m \cdot \frac{2\pi}{A}\right)$. In fact we only need to consider k_r to exist in the range - $\pi/A < k_r \le \pi/A$. This region of non-redundant values of k_r is called the ***Brillouin zone.*** Substitution of Bloch state (4.12) into Master Equation (4.9) gives a reduced form of master equation:

$$(i\boldsymbol{k} + \nabla) \times \left(\frac{1}{\varepsilon(\boldsymbol{r})} (i\boldsymbol{k} + \nabla) \times u_k(\boldsymbol{r})\right) = \left(\frac{\omega(\boldsymbol{k})}{c}\right)^2 u_k(\boldsymbol{r}) \tag{4.13}$$

that can be solved numerically for all **k** in the first Brillouin zone, resulting in an infinite set of modes with discretely spaced frequencies, which we can label with the band index *n*. In this way we arrive at the description of the modes of the photonic bands, *ωₙ(k),* of the crystal: they are a family of continuous functions, indexed in order of increasing frequency by the band number. The information contained in these functions is called the ***band structure*** of the photonic crystal. Studying the band structure of a crystal, allows us to predict its optical properties.

1. One dimensional Photonic Crystals

The simplest possible photonic crystal, shown in *Fig. 4.4*, consists of alternating layers of dielectric material, the familiar "***quarter-wave-stack***".

This photonic crystal acts as a perfect mirror: light of the proper wavelength, when incident on such a layered material, is completely reflected. The reason is that the light wave is scattered at the layer interfaces, and if the spacing is just right, the multiply-scattered waves interfere destructively inside the material. This effect is well known, and is at the basis of many widely used optical devices, including dielectric mirrors and dielectric Fabry-Perot filters. All contain low-loss dielectrics that are periodic in one dimension, so they are defined *one-dimensional photonic crystals.*

However, such mirrors only reflect light at normal or near-normal incidence to the layered material. To understand this system we need to take into account a plane wave to propagate through the material and to consider the multiple reflections that take place at each interface. The material is periodic in *z*-direction, and homogeneous in the *xy*-plane. This allows us to index the modes using $\boldsymbol{k}_{//}$, k_z and n: the wave vector in the plane, the wave vector in the *z*-direction and the number. We can write the modes in the Bloch form:

$$\boldsymbol{H}_{n,k_z,\boldsymbol{k}_{//}}(\boldsymbol{r}) = e^{ik_{//}\cdot\rho}e^{ik_z\cdot z}\boldsymbol{u}_{n,k_z,\boldsymbol{k}_{//}}(z) \tag{4.14}$$

u(z) is a periodic function, so that *u(z)* =*u(z+R)* whenever R is an integral multiple of *A,* the layer spacing. However we restrict k_z to a finite interval, the onedimensional Brillouin zone (-$\pi/A < k_z \le \pi/A)$, because the crystal has discrete translational symmetry in the *z*-direction. The crystal has continuous translational symmetry in the *xy*-plane, so the wave vector $\boldsymbol{k}_{//}$ can assume any value.

Let's consider light that propagate entirely in the *z*-direction, crossing the sheets of dielectric at normal incidence. In this case, $k_{//} = 0$, so only the wave vector component k_z is important. In *Fig. 4.5* $\omega_n(k)$ is plotted for three different multilayer films.
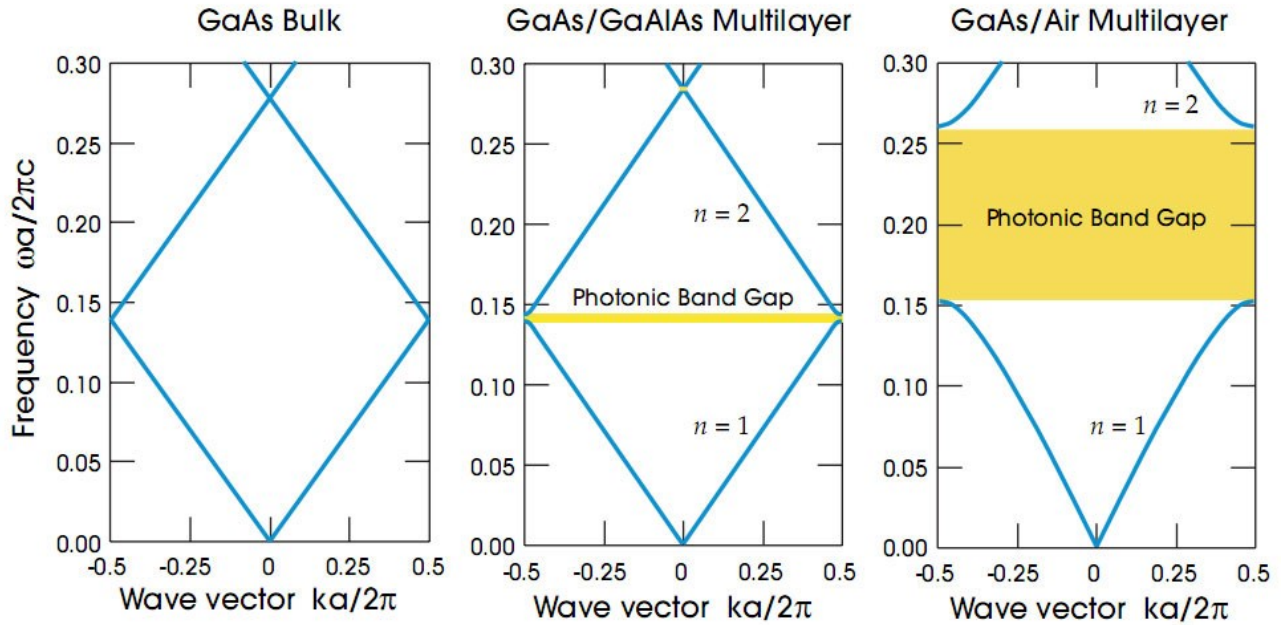
Fig. 4.5: The photonic band structure for on-axis propagation, as computed for three different multiplayer films. In all cases each layer has a widht 0.5 a . Left: every layer has the same dielectric constant ε=13. Center: layers alternate between ε of 13 and 12. Right: layers alternate between ε of 13 and 1

For an infinite stack of dielectric layers with all the layers having the same dielectric constant (*Fig. 4.5 a*), the dispersion relationship gives two straight lines with slope *Δω/Δk = |1|* in the extended zone. In the reduced zone, the folded bands either at the zone center or the zone edge. As a result, there is no band gap with a range of forbidden frequency for photons. If we introduce a small effect of index contrast, a gap in frequency appears between the upper and the lower branches of lines (*Fig. 4.5 b*), a frequency gap in which no mode, regardless of *k*, can exist in the crystal. We call such a gap a ***photonic band gap***. As the dielectric contrast increases, the gap widens considerably, as we can see in *Fig. 4.5 c*.

The effect of index contrast on band gaps can be explained with the electromagnetic variation theorem, which is analogous to the variational method of quantum mechanics. The equation gives the dependence of the energy bands on the refractive index and the result is that the low-frequency modes concentrate their energy in the high-ε regions, and the high frequency modes concentrate their energy in the low-ε regions (*Fig. 4.6*). This is worked out in detail in reference [10, 29].
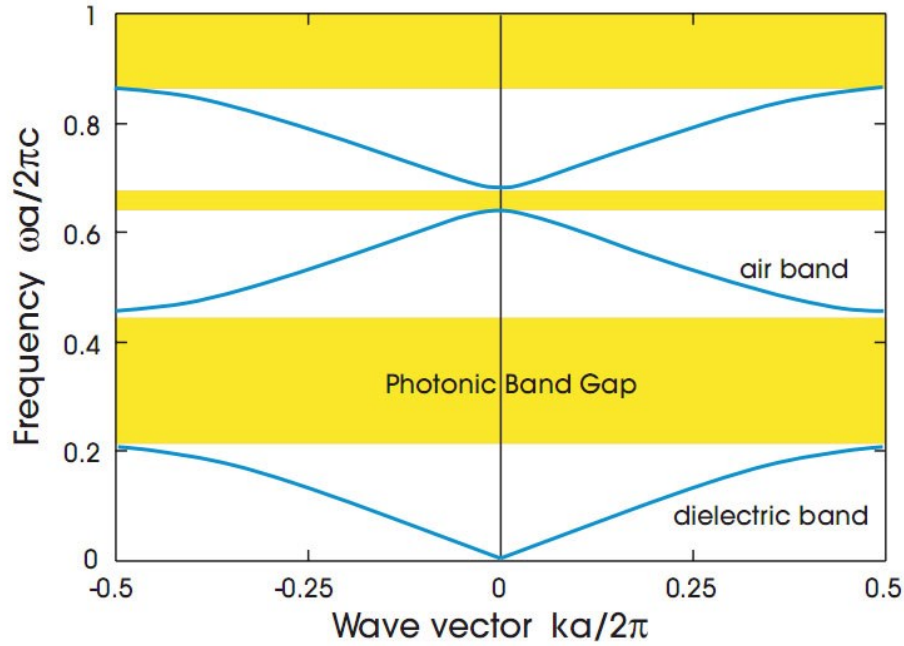
Fig. 4.6: The photonic band structure of a multilayer film with lattice constant a and alternating layers of different widths. The width of the ε=13 layer is 0.2a, and the width of the ε=1 layer is 0.8a

The modes that have frequency in the gap become evanescent, meaning that their wave vector becomes imaginary in the direction of the periodicity.

Untill now we just considered modes which happen to have $\mathbf{k}_{//}$ = 0, that means modes that propagate only in *z*-direction. The most important difference between on-axis and off-axis propagation is that there are no band gaps for off-axis propagation. This is always the case for a multilayer film, because the off-axis direction contains no periodic dielectric regions to coherently scatter the light and split open a gap.

2. Two dimensional Photonic Crystals

After the identification of one-dimensional band gaps, it took a full century to add a second dimension, and three years to add the third.

So now we can see how the situation changes when the crystal is periodic in two directions and homogeneous in the third. The key for understanding photonic crystals in two dimensions is to realize that the field in every two-dimensional photonic crystals can be divided into two polarizations by symmetry: *TM* (transverse-magnetic), in which the magnetic field is in the (*xy*) plane and the electric field is perpendicular (*z*); and the *TE* (transverse-electric), in which the electric field is in the plane and the magnetic field is perpendicular. Starting from Bloch's theorem, and considering that the system has discrete

66

translational symmetry in the *xy*-plane, we can index the modes of the crystal by k_z and $\mathbf{k}_{//}$ and n (band number):

$$H_{n,k_z,k//}(\boldsymbol{r}) = e^{i\boldsymbol{k}//\cdot\rho}e^{ik_z\cdot z}\boldsymbol{u}_{n,k_z,k//}(\rho) \tag{4.15}$$

where $\boldsymbol{u}(\rho)$ is a periodic function, $\boldsymbol{u}(\rho) = \boldsymbol{u}(\rho + \boldsymbol{R})$, for all lattice vectors $\boldsymbol{R}$. The modes of this system look similar to those of the multilayer film that we saw in equation (4.14), of previous section. The key difference is that in the present case, $\mathbf{k}_{//}$ is restricted to the Brillouin zone and k_z is unrestricted. In the multilayer film, the roles of these two vectors were reversed. Also $\boldsymbol{u}$ is now periodic in the plane.

If $k_z = 0$, so that light is propagating strictly in the *xy*-plane, than the system is invariant under reflections through the *xy*-plane. This mirror symmetry allows us to classify the modes into transverse-electric (*TE*) and transverse-magnetic (*TM*) modes.

The band structures for TE and TM modes can be completely different, in particular there can be photonic band gaps for one and not the other.

Corresponding to the polarizations, there are two basic topologies for two-dimensional photonic crystal, as depicted in *Fig. 4.7*: in the top view high refractive index rods surrounded by low index, and in the bottom view low-index holes in high index medium.
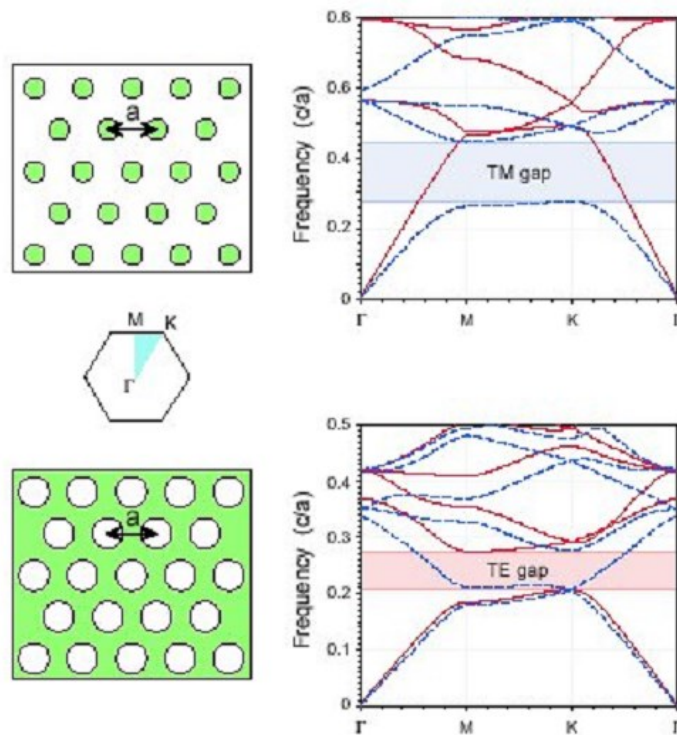
Fig.4.7: Band diagrams and photonic band gaps for hexagonal lattices of high dielectric rods
(ε = 12, r=0.2a) in air (top), and air holes (r=0.3a) in dielectric (bottom), where a is the
center-center periodicity.

The rods, dielectric columns of high-ε, are best suited to *TM* light (**E** parallel to the rods), and the holes are best suited to *TE* light (**E** running around the holes). The reason for that is due to the fact that a photonic band gap requires electric field lines running along veins (for demonstrations see [10]); this preference is reflected in the band diagrams of *Fig. 4.7* in which the rods/holes (top/botton) have a strong *TM/TE* band gap. It is conventional to give the frequencies ω in units of *2πc/a*, which is equivalent to *a/λ* (λ being the vacuum wavelength), because Maxwell's equations are scale-invariant, and the same solution can be applied to any wavelength simply by choosing the appropriate *a*. The photonic band structure for the modes of a triangular array of air columns drilled in a dielectric substrate *(ε = 13)* with a radius *r/a*=0.48 is shown in *Fig. 4.8*. The blue lines represent TM bands and the red lines represent TE bands. The inset shows the point of the irreducible Brillouin zone.
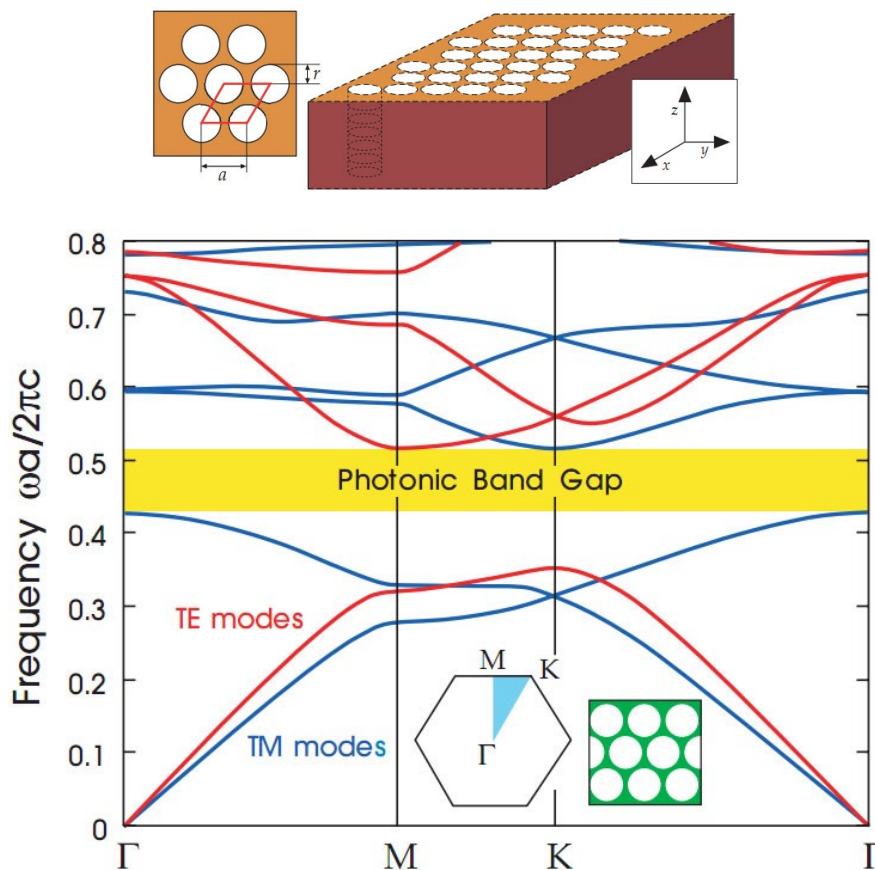
Fig.4.8: Photonic band structure for a triangular array of air columns drilled in a ε = 13 dielectric substrate

Until now we focused exclusively on modes that propagates on plane of periodicity, so that k_z = 0. However, in the out-of-plane band structure there are no band gaps for propagation in the z-direction, simply because the crystal is homogeneous in that direction.

3. Three-dimensional photonic crystals

If, for some frequency range, a photonic crystal reflects light of any polarization incident at any angle, we say that the crystal has a *complete photonic band gap.* In such a crystal, no light modes can propagate if they have a frequency within that range. A simple dielectric mirror cannot have a complete photonic band gap, we must arrange the contrasting dielectrics in a lattice that is periodic along three axes. A possibility, that is under development in these last years, is the creation of a crystal of a three-dimensional lattice of dielectric spheres. Once again, the band gaps tend to appear in structures with a high dielectric contrast.

Ho, Chan and Soukoulis [30] were the first theorists to correctly predict that a particular three-dimensional photonic crystal would have a complete band gap. They found that a complete photonic band gap exists whether one embeds dielectric spheres in air or air spheres in a dielectric medium, as long as the spheres radius is chosen appropriately. Therefore, three-dimensional photonic crystals are the only ones which may possess a truly complete band gap [10, 31], yet their fabrication at sub-micrometric scales is hard to achieve and not flexible enough to allow for the controlled introduction of line and point defect.

4.3 Photonic quasi-crystals

Periodicity, or the lack of it, is of fundamental importance in a broad range of science and engineering disciplines. In particular, two-dimensional (2D) arrays can be described in terms of long-range order, short-range order, and local rotational symmetry that may be revealed in the Fourier transform structure factor. Several 2D array classes exist, including:

(1) **periodic lattices** having both long-range and short-range order, and discrete Fourier transform vectors, but their n-fold rotational symmetry in real and reciprocal space is limited to n= 2, 3, 4 and 6;

(2) **quasicrystals** with long-range order but no short-range order, but their discrete Fourier transform vectors possess unusual *n*-fold rotational symmetry with *n*= 5, 8, 12, and so on;

(3) **aperiodic structures** having no long-range or short-range order, but their structure factor may contain a number of discrete Fourier transform vectors with even more unusual n-fold rotational symmetry;

(4) **randomly distributed structures** with no discrete Fourier transform vectors at all. Patterns that fall into categories (2) and (3) can be referred to generically as deterministic

aperiodic structures, although quasicrystals are unique in that their patterns can be developed using well-defined algorithms. The lack of periodicity in these two categories excludes the possibility of describing them using well-established analytical tools (such as Brillouin zones and the Bloch theorem) that are unique to Bravais lattices.

Thus, photonic quasicrystals (PQCs) are structures exhibiting long-range aperiodic order and rotational symmetry [32, 33]. A quasi-lattice can fill up the entire space to form an infinite structure with forbidden rotational symmetry for periodic crystals. The unit cells overlap each other in a complex manner repeating along the symmetry axis [32]. Although lacking an overall absolute translational symmetry, this local overlapping periodicity acts as a superimposed Bragg grating and gives rise to multiple forbidden photonic band-gap (PBG) frequencies.

PQCs may exhibit PBG [34, 35] that are more isotropic than in conventional photonic crystals, permitting the existence of forbidden frequency ranges even in materials possessing very low dielectric contrast. The photonic quasi-lattices are artificial dielectric inhomogeneous media, where scattering centers are usually located in the vertices of the tiles [36]. The quasiperiodic order gives rise to many nonequivalent defect sites, increasing the flexibility of these materials for different photonic applications and leading to interesting properties for confining and guiding electromagnetic energy [37, 38]. Superlensing effect, directive emission, and mode confinement [39-41] are examples of the quasicrystal features that have recently attracted tremendous interest because of their potential impact in optical components. Typically, a complete PBG in photonic crystals can be achieved by using materials with a refractive index contrast substantially higher than zero. Recent studies on quasicrystals with 8-fold (octagonal point group) [34], 10-fold (decagonal), and 12-fold (dodecagonal) [39] rotational symmetries have shown that, in general, most of the PQCs have wide complete bandgaps even for low-threshold values of the refractive index contrast. This characteristic entails the possibility of using a flexible and versatile low-cost technology combined with holographic or lithographic fabrication techniques able to realize both large-area and high quality structures in novel soft matter-based and silicon-based devices.

The concept of quasicrystal as a nonperiodic structure with perfect long-ranged order was brought in solid-state physics by Levine and Steinhardt in 1984 [33]. At present it has become clear that, in addition to crystalline and amorphous materials, there exists a third form of solids which unexpectedly fills the gap between the two well-defined condensed-matter states. This intermediate class called *deterministic aperiodic structures* (DAS) which can be

generated by a substitution rule based on two building blocks that exhibit long range order but lack translational symmetry, can be further divided into two groups: quasicrystals and all other deterministic aperiodic structures; quasicrystals therefore represent a special class of deterministic aperiodic structures. A more precise definition of quasicrystals with dimensionality n_D (n = 1, 2 or 3) is that in addition to their possible generation by a substitution process, they can also be formed from a partial projection of an appropriate periodic structure in a higher dimensional space m_D, where m > n. In contrast, all other DAS cannot be constructed in such a manner. Examples of aperiodic structures that differ from quasicrystals include Thue–Morse [42, 43]. Rudin–Shapiro [44] and period-doubling sequences [45]. All DAS show discrete Fourier components, although structures such as the Thue Morse or Rudin Shapiro exhibit much more complex Fourier properties than quasi-crystals.

DAS are optical structures in which the refractive index varies over length scales comparable or smaller than the wavelength of light. They include dielectric and metallic structures, metallo-dielectric nanostructures and metamaterials. In all cases, DAS are designed by mathematical algorithms that interpolate in a tunable fashion between periodicity and randomness, thus providing novel opportunities to explore and manipulate light-matter interactions at the nanoscale. DAS can be conveniently fabricated using conventional nanolithographic techniques while displaying unique transport and localization properties akin to random systems. Differently from well-investigated fractal structures, DAS may not possess self-similarity in direct space although they exhibit a far richer complexity in Fourier space resulting in distinctive diffraction patterns. Most importantly, the Fourier space of DAS can be simply designed to range from a pure-point discrete spectrum, such as for periodic and quasiperiodic crystals, to a diffused spectrum with short-range correlations, as for disordered amorphous systems. In addition, DAS diffraction patterns can display non-crystallographic point symmetries of arbitrary order as well as more abstract mathematical symmetries [46]. The structural complexity of DAS profoundly influences the character of photon transport in the multiple scattering regime, and results in a high density of discrete resonances, known as critical modes, with multi-fractal spatial patterns and large fluctuations of their photonic mode density (LDOS). As we will discuss, these are key attributes to boost the frequency bandwidth and the strength of light-matter coupling in photonic-plasmonic structures, offering yet unexplored avenues to advance fundamental optical sciences and device technology.

4.3.1 Order without periodicity in quasicrystals

One of the great intellectual triumphs of the twentieth century is the discovery of aperiodic order in the mathematical and physical sciences. In mathematics, quasiperiodic order was originally investigated by Harald Bohr who developed in 1933 a general theory of almost periodic functions, including quasiperiodic functions strictly as a subset [46, 19]. However, it was not until 1974 when the mathematician Roger Penrose discovered the existence of two simple polygonal shapes capable of tiling the infinite Euclidean plane without spatial periodicity [47]. It was realized in the early 1980s that the diffraction patterns of aperiodic point sets consist of sharp diffraction peaks with icosahedral point-group symmetry, which includes the "forbidden" pentagonal symmetry. While for periodic arrays all the information contained in their reciprocal space can be compressed into periodic Brillouin zones, aperiodic arrays have non-periodic diffraction diagrams and therefore Brillouin zones cannot uniquely be defined. As a result, when comparing diffraction patterns of different types of aperiodic arrays, it is important to adopt an approach that guarantees a homogeneous sampling of their aperiodic spectral features. This can be done by restricting their reciprocal spaces to the so-called *pseudo-Brillouin zones*, which contain spatial frequencies in the compact interval 1Δ, where Δ is the minimum or the average inter-particle separation for the specific type of aperiodic array. In 1984, Dan Shechtman et al [48] were the first to experimentally demonstrate the existence of physical structures with non-crystallographic rotational symmetries. When studying the electron diffraction spectra from certain metallic alloys $(Al6Mn)$, they discovered sharp diffraction peaks arranged according to the icosahedral point group symmetry (i. e., consisting of 2-, 3-, 5-, and 10-fold rotation axes for a total of 120 symmetry elements). The sharpness of the measured diffraction peaks, which is related to the coherence of the spatial interference, turned out to be comparable with the one of ordinary periodic crystals. Stimulated by these findings, Dov Levine and Paul Steinhardt promptly formulated the notion of quasicrystals in a seminar paper titled [32]: "Quasicrystals: a new class of ordered structures". Aperiodic structures possess a *rich and novel type of long-range order,* described by more abstract symmetries than simple translational invariance.

In optics and electronics, an alternative approach to generate deterministic aperiodic structures with controlled Fourier spectral properties relies on symbolic substitutions [46, 49-51]. Not surprisingly, profound connections exist between the theory of substitutional sequences, dynamical systems, and number theory. Substitutions are an essential component of every recursive *symbolic dynamical system* formally defined on a finite symbolic alphabet

G= {A, B, C,...}. In physical realizations, each letter corresponds to a different type of building block (e. g., nanoparticle, dielectric layer, etc). A specific substitution rule *a* replaces each letter in the alphabet by a finite word, starting from a given letter called an *axiom* or *initiator.* An aperiodic (deterministic) sequence is then obtained by iterating the substitution rule *a*, resulting in a symbolic string of arbitrary length. Until recently, patterns were simply classified as either periodic or non-periodic, without the need of further distinctions. However, it should now be sufficiently clear that the word "non-periodic" encompasses a very broad range of different structures with varying degrees of order and spatial correlations, ranging from quasiperiodic crystals to more disordered "amorphous" materials with diffuse diffraction spectra. One of the most fascinating questions in quasicrystals theory is whether there exist tilings with absolutely continuous diffraction spectra, as opposed to mixed ones [19].

4.3.2 Thue-Morse quasicrystals

Aperiodic structures can be rigorously distinguished according to the nature of their diffraction patterns and energy spectra, which correspond to mathematical spectral measures [46, 50]. In optics and electronics, these spectral measures are often identified with the characteristics of the transmission/energy spectra of the structures. A spectral measure is also associated with the Fourier transforms of the structures, or *lattice spectrum,* providing information on the nature of the corresponding diffraction patterns. The chief example of a deterministic sequence with singular continuous diffraction and energy spectra is the Thue-Morse sequence [50, 52-59].

A Thue Morse pattern can be realized by means of binary symbols (0 and 1) starting from one of the two (1, for example), and proceeding with the *Boolean complement* of the so far obtained sequence (*Fig. 4.9*):

<div align="center">

1

1 0

10 01

1001 0110

10010110 01101001

1001011001101001 0110100110010110

</div>
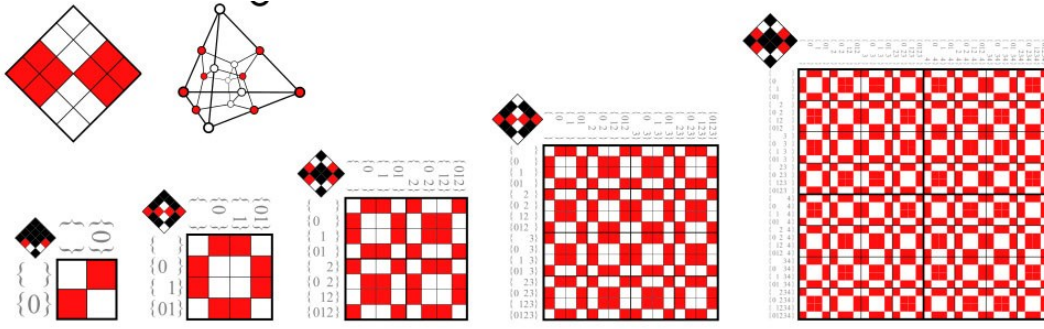
Fig. 4.9: Construction of Thue-morse tiling

This binary sequence was first studied by Eugene Prouhet in 1851, who applied it to number theory [60]. Axel Thue in 1906 used it to found the study of combinatorics on words. The sequence was successively brought to worldwide attention by the differential topology work of Marston Morse in 1921, who proved that the complex trajectories of dynamical systems whose phase spaces have negative curvature can be mapped into a discrete binary sequence, the Thue-Morse sequence [61]. More recently, in the context of the algorithmic theory of finite automata, a number of results have been demonstrated that connect the existence of palindromes of arbitrary length in the Thue-Morse and similar binary sequences with singular continuous Fourier spectra [49]. In other words it is generetad by the substitution ω_{TM}: A →AB, B → BA following the rule: given an arbitrary sequence of two symbols, A = 0 and B = 1, a new sequence is formed by replacing each occurrence of A with the pair AB and any occurrence of B with the pair BA [62].

To realize an experimental dielectric structure for photonic application the elements A and B will correspond to particular regions of different dielectric materials. The sequence of order N is then consisting of 2N elements. By assuming A = 1 and B =−1 (that is a π phase jump between adjacent different dielectric elements), the intensity of the Fourier transform of the 1D ThMo sequence of order N is given by

$$\left| f_N^{(1)}(k) \right|^2 = 2^{2N} \prod_{j=0}^{N-1} sin^2 \left(2^j \pi k \right) \tag{4.16}$$

where k is the magnitude of the reciprocal vector. Finite realizations of the ThMo lattice give rise to essentially discrete spectra (or diffraction patterns) giving evidence of the aperiodic nature of the crystal (*Fig. 4.10*). By the inflation rule the one-dimensional aperiodic lattice can be generalized to the two-dimensional space introducing a substitutional matrix obtained as Cartesian product of 1D ThMo sequences [62, 63].

The Thue Morse structure is generated by two symbols, A and B, following the inflation rule: A→AB and B→BA. The successive ThMo strings are A, AB, ABBA, ABBABAAB, etc. Recently the

ThMo inflation method has been generalized from one-dimensional sequence to two dimensional (2D)$A \to \begin{pmatrix} A & B \\ B & A \end{pmatrix}$, and $B \to \begin{pmatrix} B & A \\ A & B \end{pmatrix}B$ [57-59, 62]. A (or B) stands for the presence (or absence) of a dielectric scatterer on a 2D square lattice.

The 2D ThMo structures used in this work have been experimentally obtained by removing scatterers, namely A and B, from a regular square array with a lattice constant A by EBL following the ThMo inflation rule. This forms a pattern of air filled square/circular rods whose centres are located at the vertices of a 2D ThMo lattice of order N=8,10.

We designed and fabricated different 2D ThMo-PQCs with either square or circular rods of side/diamater size and lattice constant reported in the table below (*Tab. 4.1*).

The experimental ThMo-PQCs realized have been characterized in the direct space through SEM metrological measurements, whereas in the reciprocal space interesting properties of the aperiodic ThMo array can be provided through the experimental determination of the Fourier spectra of the sample.

Thue Morse STRUCTURES					
SHAPE	ARRANGEMENT	SIZE (d)	Lattice Constant (G)	Minimum Interparticle Separation (s)	FILLING FACTOR (*FF*)
Square	Thue-Morse	100nm	144nm	44nm	0,26
Square	Thue-Morse	150nm	216nm	66nm	0.26
Square	Thue-Morse	185nm	264nm	79nm	0,27
Square	Thue-Morse	200nm	288nm	88nm	0,26
Square	Thue-Morse	250nm	360nm	110nm	0.26
Square	Thue-Morse	500nm	710nm	210nm	0.26
Cylinder	Thue-Morse	100nm	144nm	44nm	0.19
Cylinder	Thue-Morse	150nm	216nm	66nm	0.19
Cylinder	Thue-Morse	250nm	360nm	110nm	0.20

Tab. 4.1: Summary of Thue Morse nanostructures realized for this PhD research activity

The theoretical Fourier spectrum of a two-dimensional Thue-Morse structure has been calculated. Starting from the one-dimensional formulation of the Fourier spectrum given in equation (4.16) for a Thue-Morse sequence of order *N*, we have generalized this result to the case of a two-dimensional aperiodic crystal. Let us indicate by *s* the thickness of the sample

and by Δn the refractive index difference between different dielectric elements, that is between the air rods and the polymeric substrate of index n_p=1.5 and the air rods of index n_a=1. For a laser beam of wavelength λ, the optical phase mismatch ϕ experienced between adjacent elements is given by $\phi = 2\pi \Delta n s / \lambda$.

To calculate the diffraction pattern produced by a two-dimensional Thue-Morse structure, orthogonally oriented with respect to the impinging light, is convenient to separate the contributions of the dielectric circular rods of radius *r=d/2* from the homogeneous environment of polymer in which the rod is embedded. If we consider a 2D Thue-Morse structure of order N, then the overall Fourier spectrum can be calculated considering that the whole pattern can be divided into $2^N \times 2^N$ equally sized square cells of two kinds as schematically represented in *Fig. 4.10(a)* for the particular case N=2, that is one consisting of a circular rod into a square environment of different refractive index (grey cell on the left in *Fig. 4.10(a)*), and one consisting of a homogenous square element (grey cell on the right of *Fig. 4.10(a)*). The latter is a homogenous square dielectric region of side size a, hence the amplitude of the Fourier transform of such cell (corresponding to the polymer in the experimental sample), say $f_p(k_x, k_y)$, is simply given by

$$f_p(k_x, k_y) = \frac{\sin(\pi k_x a)\sin(\pi k_y a)}{\pi^2 k_x k_y} \tag{4.17}$$
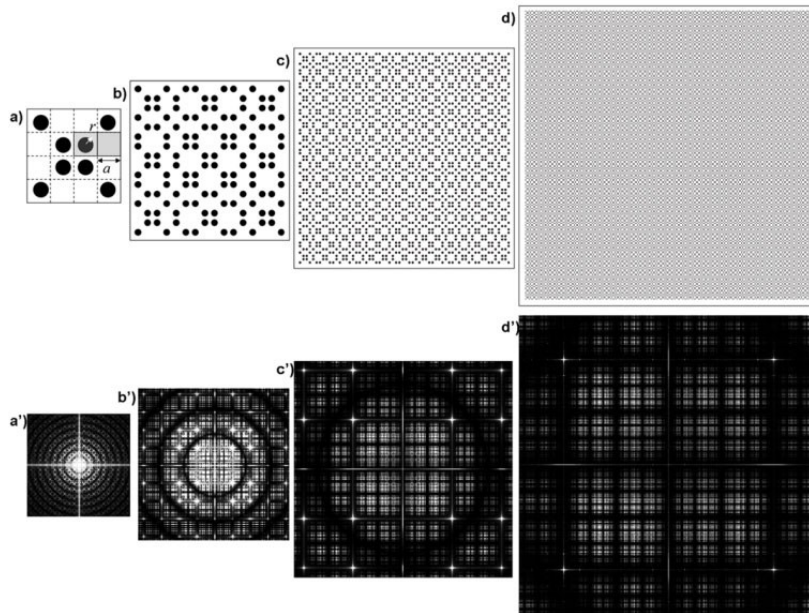
Fig. 4.10: (a)–(d) Schematic representation of 2D Thue–Morse patterns of order N = 2, 4, 6, 8, respectively. Inset (a) shows the schematization of the ThMo basic elements: top view of circular rod of radius r inscribed into a square region of side size a. (a')–(d') Theoretical far field diffraction patterns of the corresponding ThMo lattices of order N = 2, 4, 6, 8, respectively.

On the other hand, each region consisting of a circular rod of radius r of index n_r inscribed into a square cell of side size a and index n_p (left cell in *Fig. 4.10(a)*), gives an overall contribution to the diffraction pattern, say $f_{r,p}(k_x, k_y)$, expressed by

$$f_{r,p}(k_x, k_y) = (1 - e^{i\varphi})r \frac{J_1\left[2\pi r \sqrt{k_x^2 + k_y^2}\right]}{\sqrt{k_x^2 + k_y^2}} + e^{i\varphi} f_p(k_x, k_y) \tag{4.18}$$

in which the first term containing the Bessel function of first order J_1 is associated to the circular rod, whereas the second term to the polymer environment of the same square cell. The two terms have a phase mismatch ϕ. For the sake of simplicity let us indicate

$$u = e^{-2i\pi k_x a}, v = e^{-2i\pi k_y a} \tag{4.19}$$

as the basic Fourier spectral components. The two contributions to the ThMo spectrum of equations (4.17) and (4.18) must be properly combined in order to represent the diffraction pattern of the whole Thue-Morse structure. The total amplitude $f(k_x, k_y)$ of the Fourier spectrum can be written according to the following linear combination

$$f(k_x, k_y) = \alpha(k_x, k_y) f_{r,p}(k_x, k_y) + \beta(k_x, k_y) f_p(k_x, k_y) \tag{4.20}$$

where we have introduced the spatial frequencies dependent coefficients $\alpha(k_x, k_y)$ and $\beta(k_x, k_y)$. The coefficients $\alpha(k_x, k_y)$ and $\beta(k_x, k_y)$ are determined by taking into account that the coordinates of the centres of the circular rods are coincident with the spatial positions of the Thue-Morse lattice points. Following the ThMo inflation rule and using the spectrum of a 1D ThMo sequence given in equation (4.16), it is possible to verify that the coefficients of equation (4.20) for a 2D Thue-Morse quasicrystal of order N can be written according to the following relations:

$$\alpha(k_x, k_y) = \frac{uv}{2} \prod_{j=0}^{N-1} \left(1 + u^{2^j}\right)\left(1 + v^{2^j}\right) + \frac{uv}{2} \prod_{j=0}^{N-1} \left(1 - u^{2^j}\right)\left(1 - v^{2^j}\right) \tag{4.21}$$

$$\beta(k_x, k_y) = \frac{uv}{2} \prod_{j=0}^{N-1} \left(1 + u^{2^j}\right)\left(1 + v^{2^j}\right) - \frac{uv}{2} \prod_{j=0}^{N-1} \left(1 - u^{2^j}\right)\left(1 - v^{2^j}\right) \tag{4.22}$$

Thue-Morse quasicrystals of order N=2, 4, 6, 8, respectively, are schematically represented in *Fig 4.10(a), 4.10(b), 4.10(c) and 4.10(d)*, respectively. *Fig. 4.10* also displays the corresponding theoretical Fourier spectra calculated from the spectral distribution given by equation (4.20). It is clearly seen that the spectra becomes more structured with increasing the order of the Thue-Morse quasicrystal and it is difficult to recognize fine details even at relatively low orders. *Fig. 4.11* shows an example of a Thue-Morse quasicrystal of order N=10 with squared air rods realized by e-beam lithography.
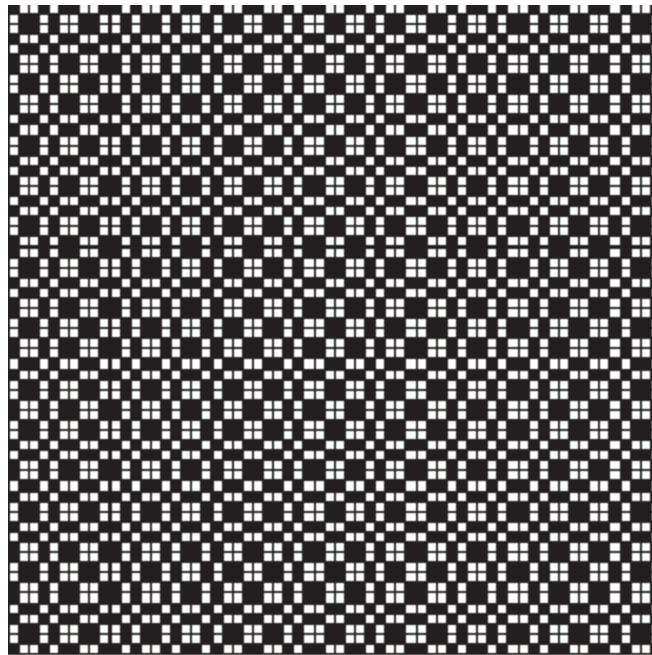
Fig. 4.11: Example of a designedThue Morse of squares

4.3.3 8-Fold Quasi-crystals

Recently, the importance of tiling geometry in the arrangement of the octagonal quasicrystal was discussed [64]. The octagonal tiling gives (*Fig. 4.12*) rise to a wide photonic band-gap for low refractive index difference as low as 0.5 with an attenuation of the transmittance signal up to 50dB [65]. Therefore, optoelectronics and photonics devices based on such octagonal photonic quasicrystal promise to be realized even in soft materials like polymer. The spatial tiling of the quasi-lattice can be determined point-by-point by geometric rules or inflation algorithms.
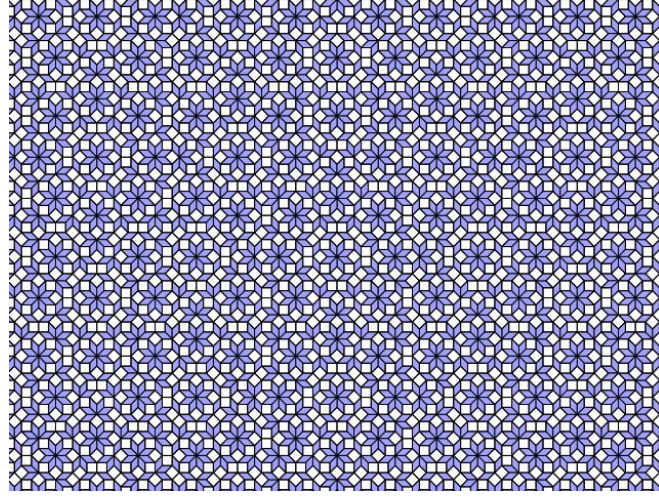
Fig. 4.12: 8-fold Ammann-Beeker tiling

The fabricated octagonal structure analyzed in this PhD thesis (*Tab. 4.2*) was determined by simulating the quasiperiodic transverse irradiance distribution given by 8-beam interference process [66].

8-fold STRUCTURES					
SHAPE	ARRANGEMENT	SIZE (d)	Lattice Constant (G)	Minimum Interparticle Separation (s)	FILLING FACTOR (ϕ)
Cylinder	8-Fold	100nm	/	25nm	0.14
Cylinder	8-Fold	125nm	/	30nm	0,18
Cylinder	8-Fold	150nm	/	35nm	0.16
Cylinder	8-Fold	250nm	/	70nm	0.18

Tab. 4.2: Summary of 8-fold nanostructures realized for this PhD research activity

In fact, the interference irradiance profiles *I (r)*, according to [67, 68]

$$I(r) = \sum_{m=1}^{N} \sum_{n=1}^{N} A_m A_n^* e^{[i(\boldsymbol{k}_m - \boldsymbol{k}_n) \cdot \boldsymbol{r} + i(\phi_m - \phi_n)]}$$

(4.23)

where A_m, $\boldsymbol{k}_m$, and φ_m are the amplitudes, the wavevectors and the initial phases of the interfering beams, respectively, give quasiperiodic distributions of the dielectric material in the recording medium. Depending on the threshold level of the photosensitive matter and the exposure time, the filling factor may have different values. Typically, the maxima positions of the light pattern correspond to the high dielectric regions, that, usually, can be approximated

with a structure of dielectric rods in air (or other materials). The number N of the interfering beams determines the order of the rotational symmetry of the quasicrystal pattern [69]. The wavevectors of the interfering beams are given by [68]:

$$\boldsymbol{k}_m = \frac{2\pi n}{\lambda}\left(\sin\left(\frac{2\pi m}{N}\right)\sin\theta, \cos\left(\frac{2\pi m}{N}\right)\sin\theta, \cos\theta\right)$$

(4.24)

where the $\boldsymbol{k}_m$, $m = (1,..., N)$, are oriented at angle θ with respect to the longitudinal z-direction, and are equally distributed along the transverse (x, y)-plane; n is the average refractive index of the photosensitive mixture, and λ is the common wavelength of the beams. By adjusting the parameters in equation (4.23), different interference patterns can be obtained (*Fig. 4. 13*).
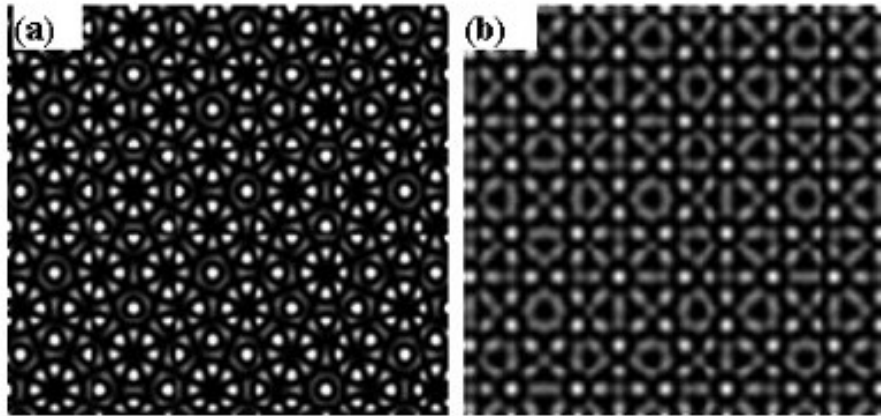
Fig. 4.13 (a) Calculated quasiperiodic irradiance profile (IP) with 8-fold rotational symmetry obtained from phase values $\phi_i = 0$, for i =-1,..., 8}, say, 8-fold(A) pattern; (b) calculated 8-fold IP from phase values $\phi_1 = \phi_5 = 0$, $\phi_2 = \phi_4 = \phi_6 = \phi_8 = \pi/2$, $\phi_3 = \phi_7 = \pi$, say, 8-fold(B) pattern [70].

By changing the relative initial phases of the beams, different spatial arrangements of the rods in air may be realized, depending on the resulting interferential profiles. We compared the octagonal pattern with the 8-fold interferential structures obtained for two different sets of the initial phases. For the first pattern, say, *8-fold (A)*, the phases were supposed to be all equal, that is $\phi_1 = \cdots = \phi_8 = 0$, whereas for the second pattern, say, *8-fold (B)*, the phases were periodically shifted of $\pi/2$, that is $\phi_1 = \phi_5 = 0$, $\phi_2 = \phi_4 = \phi_6 = \phi_8 = \pi/2$, $\phi_3 = \phi_7 = \pi$.

The intensity profiles calculated for both the *8-fold (A)* and *8-fold (B)* structures are shown in *Fig. 4.13 (a)* and *(b)* respectively. The corresponding patterns of rods are shown in *Fig. 4.14 (a)* and *(b)*, respectively. These structures are obtained by positioning circular dielectric rods of radius r in the maxima of the interferential intensity pattern *IP* of *Fig. 4.13(a)* and *(b)*, respectively. In *Fig. 4.14 (c)*, the octagonal structure of rods with the Ammann–Beenker tiling

of space (*Fig. 4.12*) is depicted. The side length of the unit-tile of space is *a* for the octagonal patternin *Fig. 4.14 (c)*.
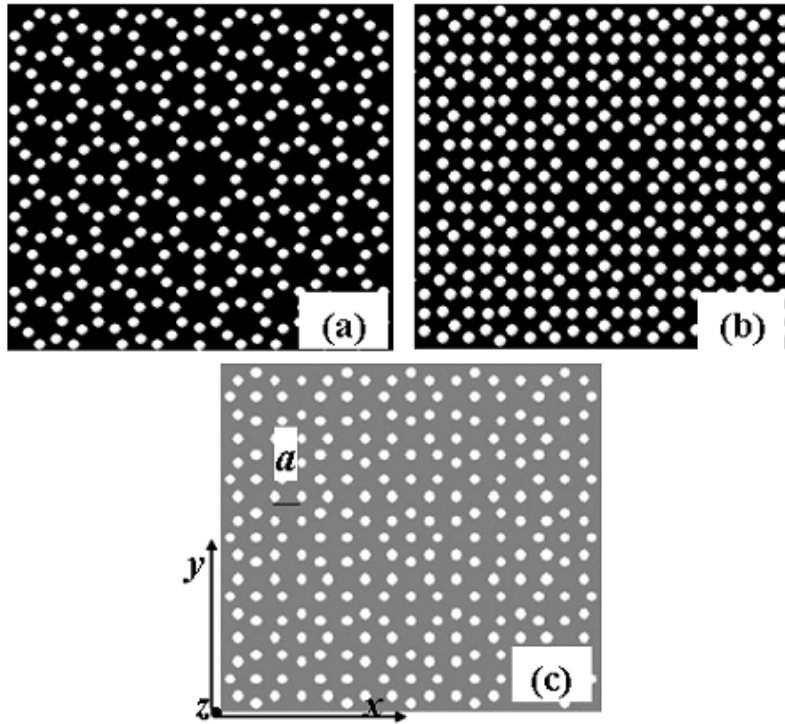
Fig. 4.14: (a) Dielectric structure of rods from 8-fold (A) pattern; (b) dielectric structure of rods from 8-fold (B) pattern; (c) octagonal structure of rods with 'square-rhombus' tile of equal side length a.

The fabricated octagonal structure (see *Fig. 4.14b*) was determined by simulating the quasiperiodic transverse irradiance distribution given by 8-beam interference process and was theoretically analyzed through finite difference time domain (FDTD) simulations of the transmittance spectra (*Fig. 4.15-4.16*) [71, 72].
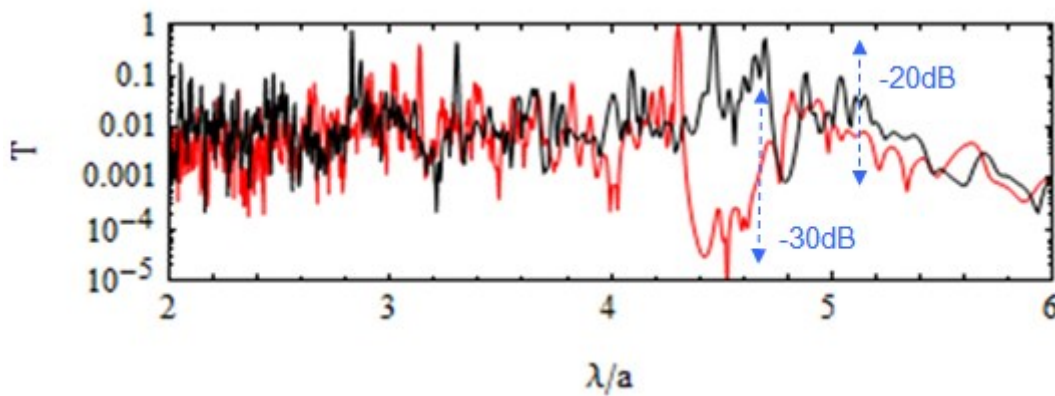
Fig. 4.15: FDTD simulations of the transmittance spectra for 2D Octagonal QC (air rods embedded in polymer matrix) for TM (red curves) and TE (black curves) polarizations for refractive index n = 1.7
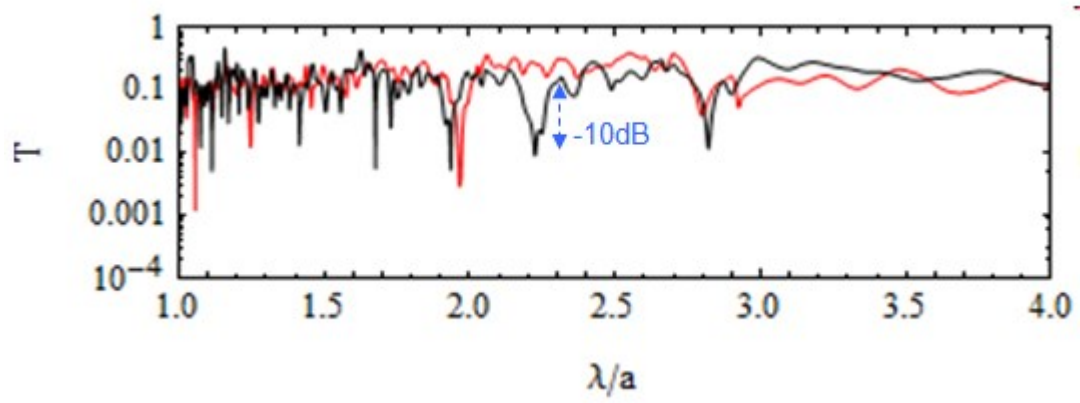
Fig. 4.16: FDTD simulations of the transmittance spectra for 2D Octagonal QC (air rods embedded in polymer matrix) for TM (red curves) and TE (black curves) polarizations for refractive index n = 0.5

References

[1] J. Yao, Z. Liu, Y. Liu, Y. Wang, C. Sun, G. Bartal, A. M. Stacy and X. Zhang, "Optical Negative Refraction in Bulk Metamaterials of Nanowires," Science 321, 930 (2008)

[2] V. M. Shalaev, "Optical negative-index metamaterials," Nature Photon. 1, 41-48 (2007)

[3] J. B. Pendry, "Negative Refraction Makes a Perfect Lens," Phys. Rev. Lett. 85, 3966-3969 (2000)

[4] E. Ozbay, "The Magical World of Photonic Metamaterials," Optics Photonics News, November, 22–27 (2008)

[5] B. Ung, "Metamaterials: a mata-review"; N. M. Litchinitser and V. M. Shalaev, "Metamaterials move beyond nature's limits," Opt. Lasers Eur. 14–16 (2008)

[6] Defense Advanced Research Projects Agency. [cited 2008/11/11] http://www.darpa.mil/DARPATech2002/presentations/dso_pdf/speeches/BROWNING.pdf

[7] D. Schurig, J. J. Mock, B. J. Justice, S. A. Cummer, J. B. Pendry, A. F. Starr, and D. R. Smith, Science 314, 977 (2006)

[8] A. Sihvola, "Metamaterials in electromagnetics," Metamaterials 1, 2-11 (2007)

[9] V. G. Veselago and E. E. Narimanov, "The left hand of brightness: past, present and future of negative index materials " Nature Mat. 5, 759-762 (2006)

[10] [J. D. Joannopoulos, S. G. Johnson, R. D. Meade, and J. N. Winn, Photonic Crystals: Molding the Flow of Light - Second Edition (Princeton University Press, Princeton, 2008)

[11] E. Yablonovitch, "Inhibited Spontaneous Emission in Solid state Physics and Electronics", Phy. Rev. Lett., vol.58, p.2059, 1987

[12] J. P. Vigneron, J. F. Colomer, N. Vigneron, and V. Lousse, Phys. Rev. E 72, 061904 (2005)

[13] J. P. Vigneron, J. F. Colomer, M. Rassart, A. L. Ingram, and V. Lousse, Phys. Rev. E 73, 021914 (2006)

[14] M. Rassart, P. Simonis, A. Bay, O. Deparis, and J. P. Vigneron, Phys. Rev. E 80, 031910 (2009)

[15] J. Aizpurua and J. P. Vigneron, in Bio-Inspired Photonic Structures: Photonic Science and Engineering in the Living and Artificial Worlds, Donostia International Physics Center (Abstract Book Editions, Donostia - San Sebasti´an, 2009)

[16] A.F. Koenderink, L. Bechger, H.P. Schriemer, A. Lagendijk, andW.L. Vos, Broad-band fivefold reduction of vacuum fluctuations probed by dyes in photonic crystals, Phys. Rev. Lett. 88, 143903 1-4 (2002)

[17] A.N. Whitehead, An Introduction to Mathematics (H. Holt and Company, New York, T. Butterworth, Ltd., London, 1939)

[18] M. Senechal, Quasicrystals and geometry (Cambridge Univ.Press, Cambridge, 1996)

[19] T. Janssen, G. Chapuis, and M. De Boissieu, Aperiodic crystals: from modulated phases to quasicrystals (Oxford University Press, Oxford, 2007)

[20] ; M. DeGraef,M. E.McHenry, and V. Keppens, J. Acoustical, Soc. Am. 124, 1385–1386 (2008)

[21] L. Dal Negro and S. Boriskina, Deterministic aperiodic nanostructures for photonics and

plasmonics applications, Laser Photonics Rev., 1–41 (2011) /DOI 10.1002/lpor.201000046

[22] Luo, X. W. Sun, H. T. Dai, H. V. Demi, H. Z. Yang, and W. Ji, "Electrically tunable lasing from a dye-doped two-dimensional hexagonal photonic crystal made of holographic polymer-dispersed liquid crystals", Appl. Phys. Lett., vol. 97, p.081101, 2010

[23] Masayuki Fujita *et al* Simultaneous Inhibition and Redistribution of Spontaneous Light Emission in Photonic Crystals *Science* 308, 1296 (2005); DOI: 10.1126/science.1110417

[24] Aurelien David, Henri Benisty and Claude Weisbuch, Photonic crystal light-emitting sources, Rep. Prog. Phys. 75 (2012) 126501 (38pp) doi:10.1088/0034-4885/75/12/126501

[25] Mang Hin Kok, Weixin Lu, Wing Yim Tam and George K. L. Wong, Lasing from dye-doped icosahedral quasicrystals in dichromate gelatin emulsions, Vol. 17, No. 9 / OPTICS EXPRESS 7275

[26] Susumu Noda, Seeking the Ultimate Nanolaser, *Science* 314, 260 (2006);

[27] R. Shankar. "Principles of quantum mechanics", Plenum Press (New York) 1983

[28] C. Kittel, "Solid State Physics", Jhon Wiley & Sons, New York (1986)

[29] J. J. Sakurai, "Modern Quantum Mechanics", *Addison-Wesley, Mass.* (1985).

[30] K. M. Ho, C. T. Chan, C. M. Soukoulis "Existence of photonic gaps in periodic dielectric structures" *Phys. Rev. Lett.* 65, 3152 (1990)

[31] K. Sakoda, "Optical properties of photonic crystals" *Springer, Berlin* (2001)

[32] D. Levine and P.J. Steinhardt, Quasicrystals: A new class of ordered structures, Phys Rev Lett 53 (1984), 2477–2480

[33] Z.M. Stadnik, Physical properties of quasicrystals, Springer, New York, NY, 1999

[34] Y.S. Chan, C.T. Chan, and Z.Y. Liu, Photonic band gaps in two-dimensional photonic quasicrystals, Phys Rev Lett 80 (1998), 956–959

[35] X. Zhang, Z.Q. Zhang, and C.T. Chan, Absolute photonic band gaps in 12-fold symmetric photonic quasicrystals, Phys Rev B 63 (2001), 0811051–0811054

[36] J.B. Suck, M. Schreiber, and P. Haussler, Quasicrystals, Springer, Berlin, 2002

[37] S.S.M. Cheng, L. Li, C.T. Chan, and Z.Q. Zhang, Defect and transmission properties of two-dimensional quasiperiodic photonic band-gap systems, Phys Rev B 59 (1999), 4091–4099

[38] C. Jin, B. Cheng, B. Man, Z. Li, D. Zhang, S. Ban, and B. Sun, Bandgap and wave guiding effect in a quasiperiodic photonic crystal, Appl Phys Lett 75 (1999), 1848–1850

[39] M.E. Zoorob, M.D.B. Charlton, G.J. Parker, J.J. Baumberg, and M.C.Netti, Complete photonic bandgaps in 12-fold symmetric quasicrystals, Nature 13 (2000), 404,

[40] E. Di Gennaro, S. Savo, A. Andreone, V. Galdi, G. Castaldi, V. Pierro, and M.R. Masullo, Mode confinement in photonic quasicrystal point-defect cavities for particle accelerators, Appl Phys Lett 93 (2008), 164102

[41] E. Di Gennaro, C. Miletto, S. Savo, A. Andreone, D. Morello, V. Galdi, G. Castaldi, and V. Pierro, Evidence of local effects in anomalous refraction and focusing properties of dodecagonal photonic quasicrystals, Phys Rev B 77 (2008), 193104

[42] Cheng, Z., Savit, R. & Merlin, R. Structure and electronic properties of Thue–Morse lattices. Phys. Rev. B 37, 4375–4382 (1988);

[43] Liu, N. Propagation of light waves in Thue–Morse dielectric multilayers. Phys.Rev. B 55, 3543–3547 (1997)

[44] Dulea, M., Johansson, M. & Riklund, R. Localization of electrons and electromagnetic waves in a deterministic aperiodic system. Phys. Rev. B 45, 105–114 (1992)

[45] Steurer, W. & Sutter-Widmer, D. Photonic and phononic quasicrystals. J. Phys. D 40, R229–R247 (2007)

[46] E. Macia, Aperiodic structures in condensed matter: Fundamentals and applications (CRC Press Taylor & Francis, Boca Raton, 2009)

[47] R. Penrose, Inst. Math. Appl. 7, 10 (1974)

[48] D. Shechtman, I. Blech, D. Gratias, and J.W. Cahn, Phys. Rev. Lett. 53, 1951 (1984)

[49] J. P. Allouche and J.O. Shallit, Automatic Sequences: Theory, Applications, Generalizations (Cambridge University Press, New York, 2003)

[50] M. Queffèlec, Substitution dynamical systems-spectral analysis (Springer Verlag, Berlin, 2010)

[51] L. Dal Negro, N.N. Feng, and A. Gopinath, J. Opt. A, Pure Appl. Opt. 10, 064013 (2008)

[52] M. Kolar, M.K. Ali, and F. Nori, Phys. Rev. B 43, 1034 (1991)72

[53] M. Rippa, R. Capasso, P. Mormile, S. De Nicola, M. Zanella, L. Manna, G. Nenna and L. Petti. Bragg Extraction of Light in 2D Photonic Thue Morse Quasicrystal patterned in Active CdSe/CdS Nanorods-Polymer Nanocomposites, **Nanoscale**, 2013, 5, 331. ISSN: 20403364. DOI: 10.1039/c2nr31839c

[54] L. PETTI, M Rippa, R Capasso, M Zanella, L Manna, and P Mormile, CdSe/CdS nanorods-polymer nanocomposites patternable by e-beam lithography: A novel active 2D photonic quasicrystal simulated, designed, fabricated and characterized, **AIP Conf. Proc**. 1459, pp. 154-156 (2012); doi:http://dx.doi.org/10.1063/1.4738428

[55] Feng, Y.-P., Zhou, J., Petti, L., Yang, M.-Y., Zhang, L.-F., Ma, Y.-Q. Guangdian Gongcheng, The effect of lattice shapes of Thue-Morse crystals on the diffraction pattern, **Opto Engineering** 38 (11), pp. 130-135 (2011)

[56] Feng, Y.-P., Zhou, J., **Petti, L.**, Yang, M.-Y., Hao, L., Haifang D., Fabrication and Optical Properties of Two-dimensional Thue-Morse Quasicrystals, **Acta Optica Sinica** 31 (4) , pp. 0423001-1 (2011)

[57] Mingyang Yang, Jun Zhou, L Petti, S De Nicola , P Mormile, Fractals characteristics of far-field diffraction patterns for two-dimensional Thue-Morse quasicrystals, **Optoelectronics Letters**, 7, 5 (2011). DOI 10.1007/s11801-011-1057-0

[58] Jun Zhou, Mingyang Yang, L Petti, P Mormile, A non-iterative image reconstruction method based on the subtraction of diffraction-intensity pattern, **Optical Engineering** 50, 11 (November 2011).

[59] V. Matarazzo, S. De Nicola, G. Zito, P. Mormile, M. Rippa, G. Abbate, J. Zhou, and L. Petti, Spectral characterization of two-dimensional Thue-Morse quasicrystals realized with high resolution lithography, **Journal of Optics**, 13, 015602 (2011). DOI: 10.1088/2040-8978/13/1/015602.

[60] M. E. Prouhet, CR Acad. Sci. Paris 33, 225 (1851)

[61] H.M. Morse, J. Math. 42 (1920)

[62] Moretti L and Mocella V, Two-dimensional photonic aperiodic crystals based on Thue–Morse sequence, Opt. Express 15 15314–23 (2007)

[63] Zito G, Piccirillo B, Santamato E, Marino A, Tkachenko V and Abbate G 2008 Two-dimensional photonic quasicrystals by single beam computer-generated holography Opt. Express 16 5164–70 (2008)

[64] Marian Florescu, Salvatore Torquato, and Paul J. Steinhardt, "Complete band gaps in two-dimensional photonic quasicrystals", PHYSICAL REVIEW B 80, 155112, (2009)

[65] Zito, G., Rose, T. P., Di Gennaro, E., Andreone, A., Santamato, E. and Abbate, G., "Bandgap properties of low-index contrast aperiodically ordered photonic quasicrystals", Micro. and Opt. Tech. Letters, 51: 2732, (2009)

[66] Petti et al. Nanoscale Research Letters 2011, 6:371, Novel hybrid organic/inorganic 2D quasiperiodic PC: from diffraction pattern to vertical light extraction

[67] Wang X, Ng C Y, Tam W Y, Chan C T and Sheng P 2003, Large-area two-dimensional mesoscale quasicrystals, Adv. Mater. 15 1526–8,

[68] Yang Y, Zhang S and Wang G P 2006 Fabrication of two-dimensional metallo-dielectric quasicrystals by single-beam holography Appl. Phys. Lett. 88 251104

[69] Mao W, Liang G, Zou H, Zhang R, Wang H and Zeng Z 2006 Design and fabrication of two-dimensional holographic photonic quasi crystals with high-order symmetries J. Opt. Soc. Am. B 23 2046–50

[70] Zito et al. *J. Opt. A: Pure Appl. Opt. 11 (2009) 024007*

[71] Petti, L., Matarazzo, V., Rippa, M., Zito, G., De Nicola, S., Abbate, G., and Mormile, P., "High resolution lithography as a Tool to Fabricate Quasiperiodic Crystals" AIP Conference Proceedings, Vol.1176: 146-148, (2009)

[72] Lucia Petti ; Massimo Rippa ; Rossella Capasso ; Marco Zanella ; Liberato Manna, et al."Novel hybrid organic/inorganic 2D photonic quasicrystals with 8-fold and 12-fold diffraction symmetries", *Proc. SPIE* 8409, Third International Conference on Smart Materials and Nanotechnology in Engineering, 84091E (April 2, 2012); doi:10.1117/12.923183

Chapter 5: Experimental apparatus EBL litography

5.1 Electron Beam Lithography (EBL) vs Optical Lithography

Lithography is the most critical procedure of defining dimensions of photonic structures. When the dimensions of the structures required approach the wavelength of the light, optical lithography suffers from the diffraction limit. The progress of new fabrication technologies has enabled the miniaturization of the dimensions of the devices smaller than the wavelength of the light. Therefore, new types of lithography systems with higher resolution are desired including electron beam direct writing. Electron beam direct writing is a maskless lithography which offers the great flexibility in design and process and allow to create the extremely fine patterns required by the modern electronic industry for integrated circuits. The technique consists of a scanning beam of electrons across a surface covered with a resist film sensitive to those electrons, thus depositing energy in the desired pattern. In this way, using the scheduled scans, managed by an appropriate design software, we can create any pattern in the resist deposited on our sample. Electrons generated in a standard Scanning Electron Microscope (SEM) column and accelerated to tens of keV, can efficiently expose specialized electron beam resist, with a great advantage over light: they don't suffer from optical thin-film interference. Their wavelengths are short compared to the wavelengths of optical radiation used for lithography: the De Broglie wavelength of the electron is expressed by

$$\lambda = h/(\sqrt{2mE_0}) = 1.24/\sqrt{E_0} \tag{5.1}$$

where E_0 is the energy of the electron in electron volts and λ is in nanometer. A 10 keV electron has a wavelength of 0.012nm, and more energetic electrons have correspondingly shorter wavelengths. The shortness of the wavelength means that any diffractive spreading of the electron beam image can be ignored. The only phenomena limiting the resolution of electron beam lithography is the electron scattering in the resist layer and various aberrations of electron optics, that will be treated in detail in this chapter.

The electron beam lithography technique:

- allows very high resolutions, up to the level of a single atom;
- it is a very flexible technique that allows to work with a wide variety of materials and with an "infinite" number of patterns;
- it is much slower than optical lithography techniques, with execution times of several orders of magnitude larger;

• it is a very complicated technique to use with very substantial costs.

This technique is applied in the industrial field for the realization of integrated circuits, where it is used for the construction of masks, for optical lithography, typically obtained using chromium on glass. Furthermore, it is of fundamental importance in the research due to the fact that it could be used for the construction of nanostructures or nanodevices of any type, such as recognizing as the only real fabrication limit the fantasy in design of the researcher. In Fig. 5.1 a few examples of nanofabbricated structures through the EBL technique are reported.
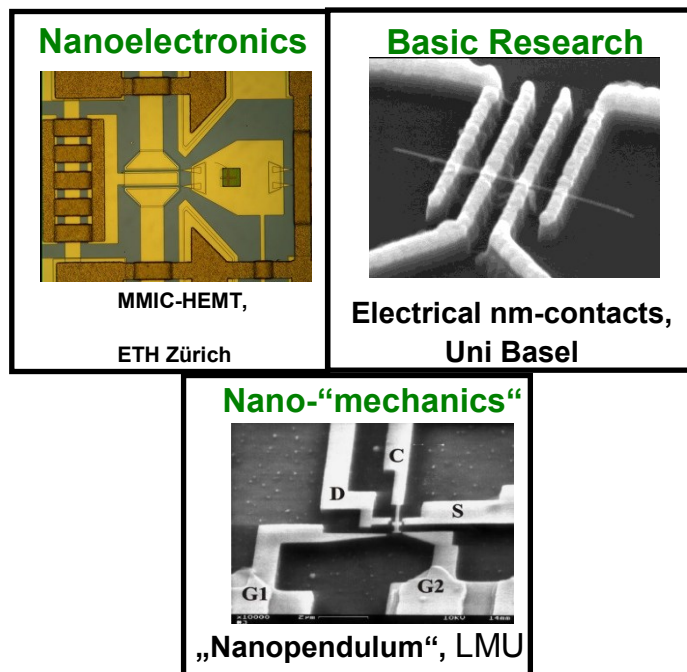
Fig.5.1 Some examples of structures nanofabricated by means of EBL technique

The Cybernetics Institute of C.N.R. (Pozzuoli) "E. Caianiello" has among its facilities an E.B.L. RAITH 150. This facility allows to write patterns of arbitrary geometry with minimal structures size of 17 nm. The system Raith 150 is a commercial tool based on a column SEM Leo, it has an acceleration voltage ranging from 1-30 keV and a beam diameter of approximately 3 nm for low currents. The pattern generator can deflect the beam to effective rate of approximately 1 MHz and can write fields with dimensions from 50 to 800 microns. This tool has written 17 nm isolated lines and patterns with a pitch of <70 nm (ie, lines spaced 35nm and 35nm).

5.2 Description of the SEM column

The most important component within an EBL system is certainly the S.E.M. (Scanning Electron Microscope) column shown in *Fig. 5.2 a-b*. It consists essentially of an electron source, two or more lenses, a beam deflection mechanism, a blanker to obscure the beam diverting it completely from its direction, an astigmator to correct astigmatism of the beam, an opening that determines the size of the beam, an alignment system that allows to center the beam in the column, and finally an electronic detector that allows to observe the illuminated area by the electron beam with a high level of magnification, in our case we arrive at a magnification of 974000 x. The E.B.L. RAITH 150 is equipped with two detectors, the second one is used only in the case in which the electrons of the beam are brought to an energy greater than 20 KeV.
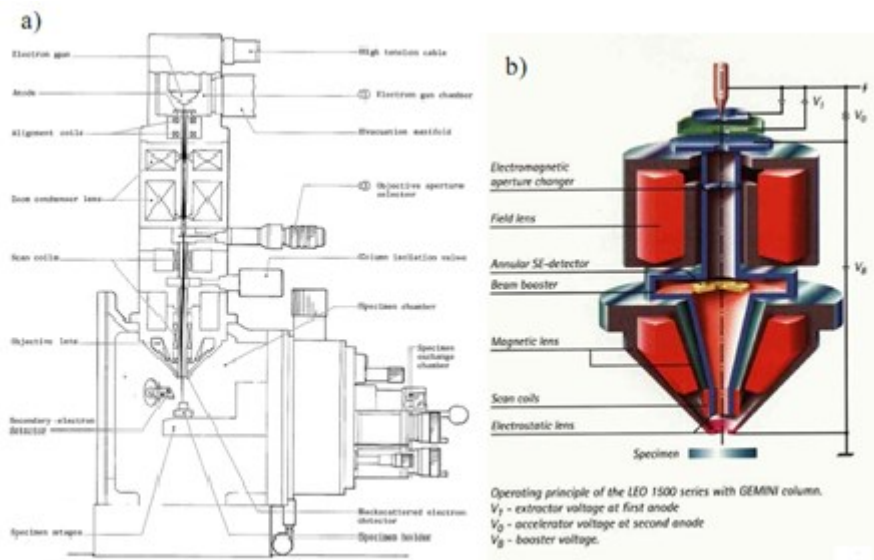
Fig.5.2 a)Cross-section of a S.E.M. column b) Detail of a LEO 1500 column of the GEMINI series on an E.B.L. RAITH 150.

The electronic source. The electrons are extracted by thermionic effect from the tip of a thin filament of tungsten, brought to a temperature of 1800 ° K. The filament is coated with a layer of zirconium oxide to decrease the work of extracting the electrons. This system requires a high vacuum of the order of 10^{-9} Torr. To accelerate the electrons is used a cylinder of Wehlnet, schematized in Fig. *Fig.5.3*.
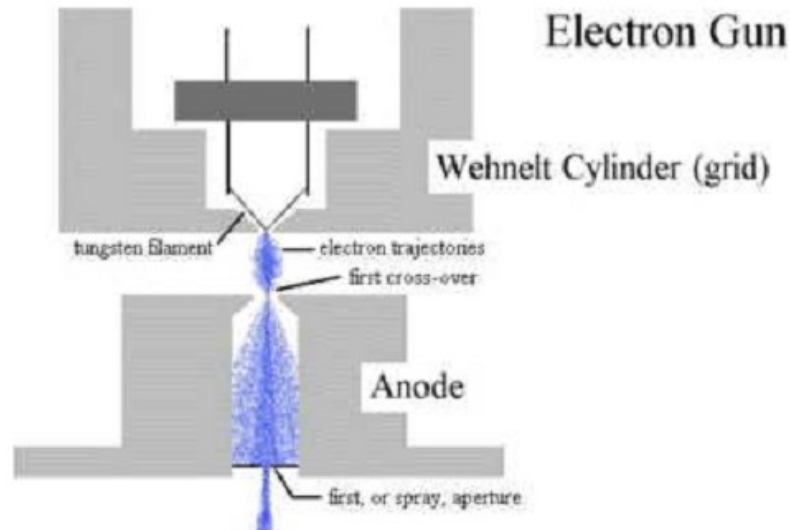
Fig. 5.3 Cross section of the electron gun.

The filament and the Wehnelt cylinder are held at a negative high voltage and they repulse electrons. The anode, that is in front of the filament, is a positively charged plate grounded to the microscope column that serves to pull the electrons from the filament and accelerate them down the column. The speed of the electrons emitted from this gun is controlled by the amount of potential (accelerating voltage) applied to the cathode and anode plates; in the RAITH 150 system it can range between 0,2 a 30 kV. So the instrument is equipped with an oil rotary pump and two oil diffusion pumps.

The electron lenses: they are electromagnetic lenses that can govern the focusing of beam on the specimen surface and the beam current that corresponds to the beam spot size. By applying current to wire coiled around an iron cylindrical core, a magnetic field is created which acts as a lens. The advantage that an electromagnetic lens in an electron microscope has over its glass counterparts in a light microscope is that by varying the current through the wires, the lens can have a variable focal length.

The apertures: they represent small holes through which passes the electron beam. In our system, it is adjustable to different values ranging from a minimum of 7.5 μm to a maximum of 120 μm. A beam limiting aperture has the effect to set the beam convergence angle and to control the effect of lenses aberration improving the resolution.

The deflecting mechanism : it is made up of two magnetic coils, located just after the last lens and is used to scan the beam across the surface of the sample.

$$F = q \cdot (E + v \times B)$$

-I ⎰⎱ ⎰⎱ +I
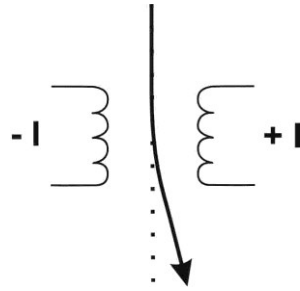
The beam blanker: consisting in a pair of metal plates facing each other (a plate capacitor) placed within the column, and connected to an electric circuit with an amplified high frequency response of the order of MHz. In order to turn the beam off it is necessary to apply a voltage, of the order of 200 V, to the plates which sweeps the beam off axis, while the other is kept at ground potential.

Beam-blanker off **Beam-blanker on**

Filament

Anode

Beam-blanker +250V GND

Aperture
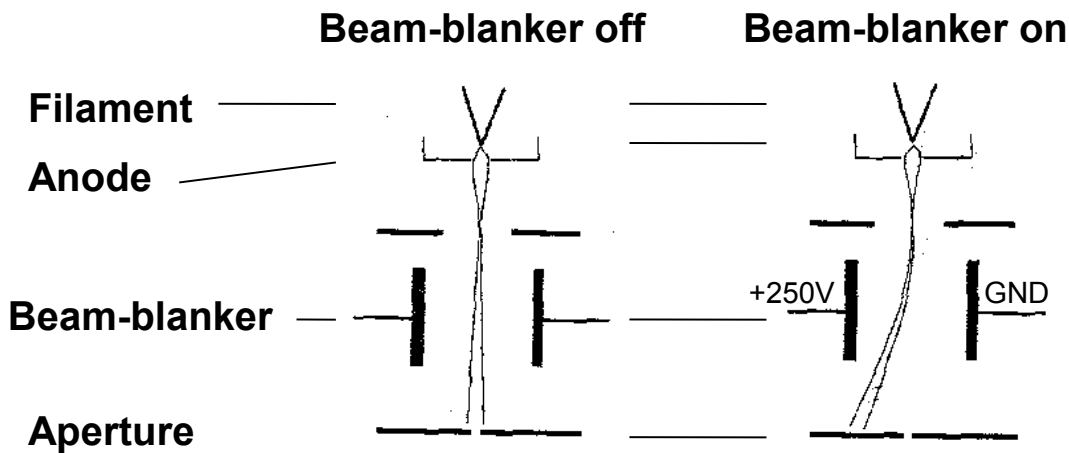
The stigmator: These are special lenses used to compensate for the imperfections of alignment of the electron beam. The astigmatism tends to make the elliptical cross section of the beam on its way up to the sample (*Fig. 5.4*). The stigmator erases these effects, forcing the beam to return to its optimum shape.
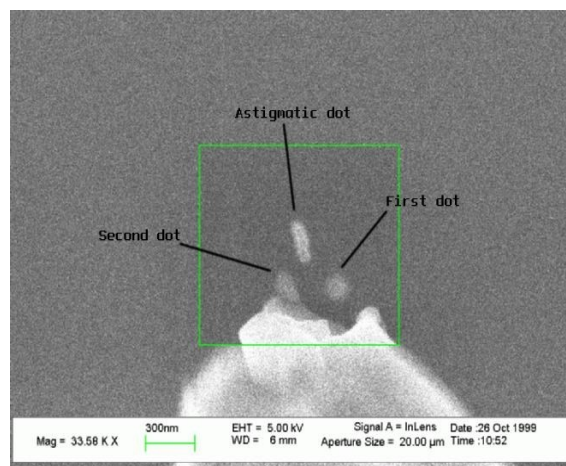
Fig.5.4 An astigmatism example (Courtesy of KTH Stocholm-Sweden.)

The detector. Secondary electrons emitted from the sample due to the collisions of the electrons of the beam are detected by means of a scintillator. It consists in a solid state detector that collects these electrons in the silicon, producing a light signal. Subsequently a photomultiplier amplifies and converts the light signal into an electrical signal. We emphasize that the secondary electrons have very small energies, and therefore before they can be detected must be suitably accelerated with a potential of the order of 10 kV.

All the parts of an electron beam column exposed to the beam must be conductive or charging will cause unwanted displacements of the beam. It has also two isolation valves: one between the chamber and the specimen exchange chamber, that allows the specimen exchange maintaining the chamber under vacuum, and the other one between the gun and the chamber, allowing the chamber to be vented while the gun is still under vacuum.

5.3   Main features of Raith150 system

The main features of the EBL RAITH 150 are:

- Ultra-high resolution, thermal field emission source consisting in a Tungsten filament covered by zirconium oxide (ZrO/W) (see *Fig. 5.5*);
- GEMINI electron optics: beam energy selectable between 200eV- 30keV;
- 6" laser interferometer stage with automated sample leveling using 3-point contact with piezo electric devices;
- Wide range of selectable writing field sizes (0.5µm - 800 µm);
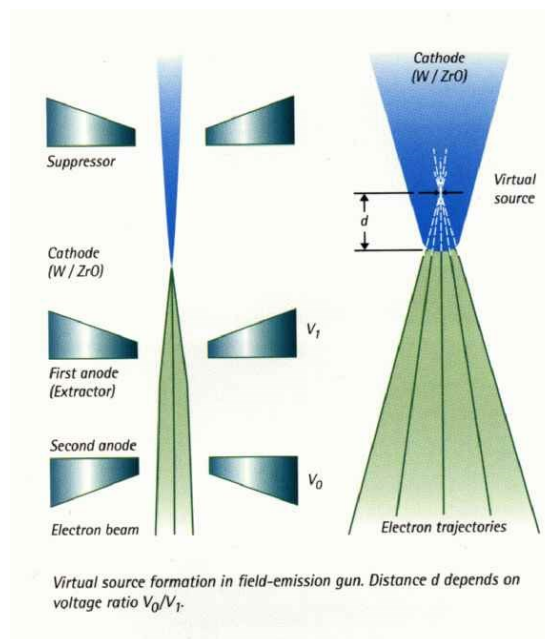
Fig. 5.5 Thermal field emitter source

- Fast Pattern Generator with up to 10Mhz writing speed;

- Patterns are generated by a GDSII hierarchical editor with dose assignment.

- Metrology functions and SEM inspection @ 0°, 45°, 90°;

- Full 6 inch wafer handling compatibility;

- Beam current range: Selectable between 5pA-5nA;

- Beam Size: 1,6nm@ 20kV, 2,5nm @ 1kV (Gaussian beam);

- Beam current drift: < 0.5%/hr;

- Lithography resolution: ≤ 20nm minimum feature size ;

- Field stitching: 10,6nm;

- Exposure of all types of arbitrary shaped areas in fast vector scan mode;

- Exposure of single pixel lines and dot arrays;

- Step size: freely selectable, but minimum is 1nm;

- Writing speed: 2Hz to 10MHz pixel frequency in area mode;

- FBMS (Fixed Beam Moving Stage) module to write gratings or millimetric sizes waveguides with an extremely reduced stitching. This module allows to create extremely long lines, regular and continuous.

5.4 Electron-solid interaction

Electrons, penetrating firstly in the resist and then in the substrate, can interact with electrons or with the core of the particles of the resist or of the substrate, giving rise to electron-electron or electron – nucleus interactions.

The *electron-electron* interaction is inelastic, then the energy of the electron beam is transferred to the electrons belonging to the atoms or molecules of the resist. If the energy transferred to the bound electron is sufficient, a new free electron is generated, the so-called *secondary electron*. These electrons are proving to have a very low energy level, ranging from 2 and 50 eV. In the resist are just the secondary electrons to be responsible for the reactions that determine the chemical reactions underlying the behavior of the resist itself as a positive resist or negative. Such reactions, however, also have effects on the electron beam. They, in fact, deviate the electrons from their initial direction, producing an effective enlargement of the beam. These diffusion processes are described with the so-called *forward scattering* (*Fig. 5.6*)
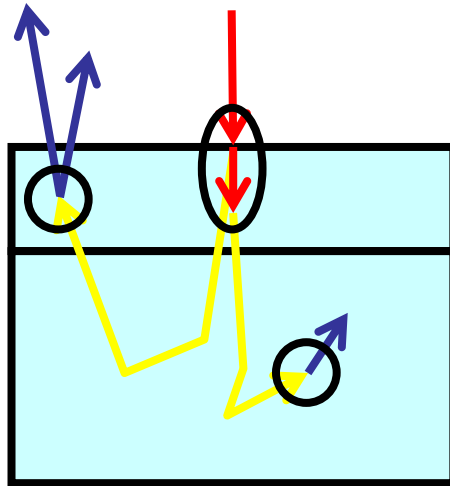
Fig. 5.6: Forward scattering effect

These diffusion processes are very weak and it is shown that the increase of the beam diameter, expressed in nanometers, produced by forward scattering is given by:

$$d_f = 0.9 \left(\frac{R_t}{V_b}\right)^{1.5} \tag{5.2}$$

where R_t is the thickness of the resist and V_b is the voltage, expressed in kV, at which the beam is accelerated.

Therefore, to minimize the effects of beam spread we must work at high voltages and with very small resist thicknesses.

The *electron-nucleus* interaction is instead an elastic process, here the deviation imprinted to the electrons is very large and sometimes it's able to bounce back the electrons of the beam. This deviation, referred to as *backscattering* (*Fig. 5.7*), is greater the higher is the atomic number of the substance with which the electron itself interacts. For this reason it is much more important the contribution from the substrate compared to that of the resist.

Also this phenomenon is responsible for an enlargement of the electron beam on sizes larger than those obtained for forward scattering, and the differences are approximately of one order of magnitude. Obviously the phenomena of enlargement of the beam are to be avoided, or at least to be limited as they may compromise the minimum achievable resolution.
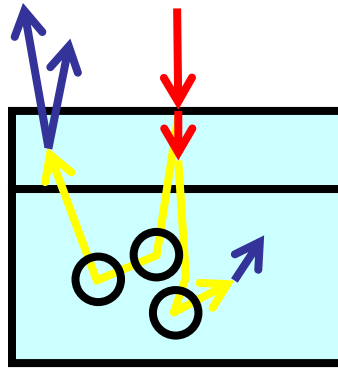
Fig. 5.7 Back scattering effect

5.5 Proximity effect

For electron beam lithography (EBL), it is most important to determine the clearing dose of the resist material. This is the parameter that governs the position that the beam moves from one position to its next position. The step size parameter has a huge impact on the proximity effect.

Dose definition

The Raith150 electron beam has a Gaussian profile, and a circular cross section. The exposure of any geometric shape will be obtained covering uniformly the shape itself with circles, said pixels, the size of which will coincide with the cross section of the beam, as shown in the Fig.. We define:

- *dwell time* t_S as the time in which the beam is stopped on the single pixel;
- *beam current* I_B to the electric current associated with the electron beam;
- *step size* s the minimum distance between two successive pixels.

The resist thickness, after the development process, depends on the energy deposited in the resist itself. From the operational point of view it is very difficult to work referring to such energy, as it is connected to the beam parameters, defined before, by means of extremely complex relations.
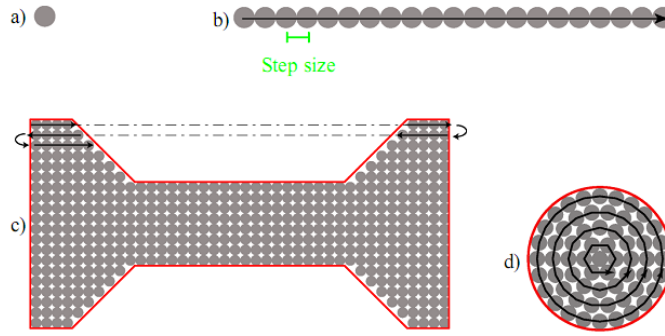
Fig. 5.8 a) Single point exposure. b) Single pixel line. c) Non trivial geometric shape exposure. d) Circular element exposure. In all the Fig.s balck arrow underlines the electron beam scan paths.

It is therefore appropriate to define a new quantity called "***dose***" that takes into account the energy that is deposited within the resist and that it is connected in a simple way with t_S, I_B and s.

The product of the *beam current I_B* by the *dwell time t_S* rapresents the charge that passes through the sample per unit area. This quantity is proportional to the number of electrons that pass through the resist per unit area and so it is definitely connected to the energy deposited in the resist by the beam. It is therefore natural, in the case of a single pixel exposure, to choose this amount as a dose of the single point exposed, d_D:

$$d_D = I_B t_S \Rightarrow d_D \rightarrow [pA \cdot s] \tag{5.4}$$

in the formula, we also referred to the unit of measurement of d_D.

In the case of the exposure of a line made by single pixels, as shown in *Fig. 5.8 b* we have to multiply the product I_B t_S by *1/s* which represents the linear density of the pixels in the exposed line. We define a ***linear dose*** L_D, related to the exposures of single pixel lines given by:
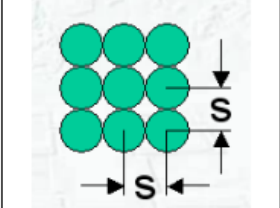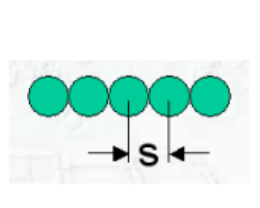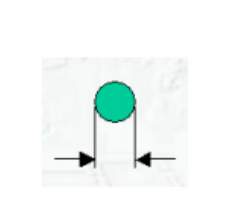
$$L_D = \frac{I_B t_S}{s} \Rightarrow L_D \rightarrow \left[\frac{pA \cdot s}{cm} \right] \tag{5.5}$$

It remains to consider the case of an exposure of a general area, as shown in *Fig. 5.8 c-d*. In this case we must multiply the product I_B t_S by *1/s²* that represents the surface density of the pixels in the exposed area. So we define a dose of surface A_D given by:

$$A_D = \frac{I_B t_S}{s^2} \Rightarrow L_D \rightarrow \left[\frac{\mu A \cdot s}{cm^2} \right] \tag{5.6}$$

In *Fig. 5.8* is also shown the scan mode of the electron beam, called **vector scan**. We emphasize how, in the case of a circular element, the scanning of the electron beam is made by

placing the pixels at the vertices of concentric polygons so as to cover the entire surface of the circumference considered, as shown in *Fig 5.8 d*.

Area dose (AD)	SPL dose (LD)	Dot dose (DD)
$AD = I_{beam} \cdot T_{dwell} / s^2$ ($\mu As/cm^2$)	$LD = I_{beam} \cdot T_{dwell} / s$ (pAs/cm)	$DD = I_{beam} \cdot T_{dwell}$ (pAs)

Tab. 5.1: Useful formulas summary to determine exposure Dose

Exposure dose Effect on resist profile

Assuming that our exposure involves areas, we have to optimize the dose identifying the particular one A_D^C, called ***clearing dose***, such that applied in the exposing process and as a result of the development process leads to a complete removal of the resist . This dose will depend on the resist used, its thickness, the type of substrate and the time of development. Using too low doses prevent the complete removal of the resist layer Increasing the exposure dose we can completely remove the resist getting closer to the ideal situation. Using even higher doses can cause excessive removal of the resist in the vicinity of the substrate, and can be pushed so as to cause the complete removal of the base of the wall and therefore the detachment from the substrate that determines the collapse of the structure under examination.

It is defined as ***proximity effect*** (*Fig. 5.9*, *Fig. 5.10*) the alteration of doses than those laid down in a process of exposure due to the scattering of electrons in the resist and the substrate. Such disclosure concerns the regions adjacent to those reached by the electron beam.
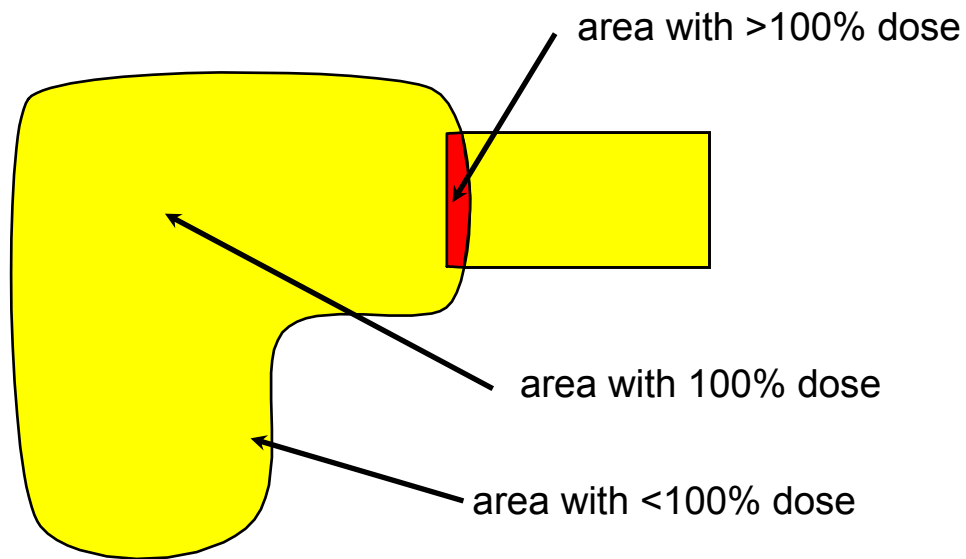
Fig. 5.9 Proximity effect schemeatization
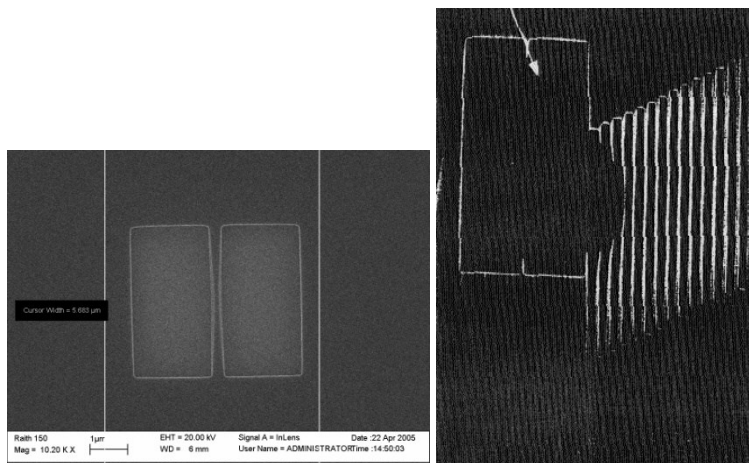
Fig. 5.10 Examples of proximity effect

The proximity effect can be classified into two categories:

- **Intrashape proximity effect.** In the exposure of a single element the electronic distribution changes the dose of the element itself. This effect is less than the smaller is the exposed elements.

- **Intershape proximity effect.** In the realization of a pattern consisting in different elements, in the single element exposure the electronic distribution changes the exposure doses of the elements adjacent to the one exposed. This effect is greater the larger is the packing density of the elements in the pattern.

In both cases, after the development procedures we have a structure that does not reflect the original desired pattern. The processes of forward scattering and backscattering, explained in advance, are both responsible for proximity effects. In principle, the processes of forward

scattering contribute to the generation of secondary electrons whose effects are felt on a distance of the order of 20 nm, and in the case of secondary electrons with a high energy, that is with an energy of the order of 1keV, they can reach up to a distance of the order of hundreds of nanometers. The processes of backscattering, however, have a much wider range of action coming to distances in the order of several microns. These distances are only indicative and their value depends on the materials used (the resist and the substrate), the geometry of the exposed structures and finally the electron beam energy used.
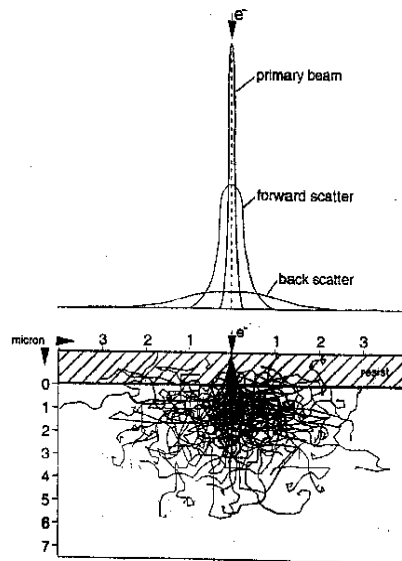
Fig. 5.11 Electron path simulation:

- *Resist tickness=1.5 μm on a silicon wafer*
- *50 path, beam Energy= 25 keV.*

The proximity effect increases with increasing energy of the beam (*Fig. 5.12*):
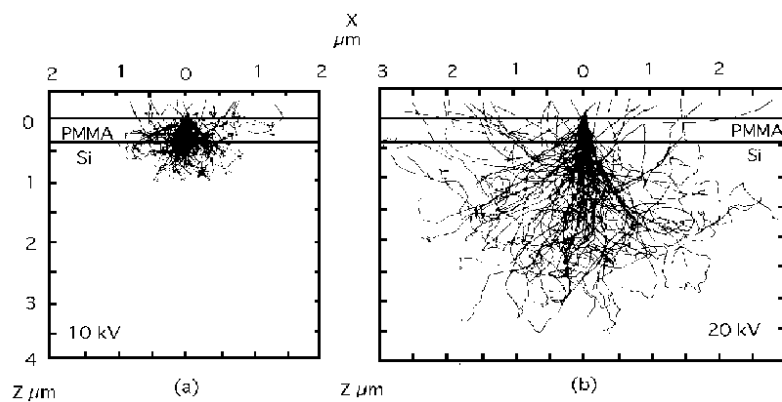
Fig. 5.12 (D. F. Kyser and N. S. Viswanathan, "Monte Carlo simulation of spatially distributed beams in electron-beam lithography", J. Vac. Sci. Technol. 12(6), 1305-1308 (1975))

Correction of these effects occurs modulating the exposure doses of the single objects that make up our pattern. We compare two images of the same pattern on a resist exposed to 30KV PMMA often 350nm: in the first case proximity effects have not been corrected (*Fig. 5.13 a*), in the second case was properly defined a correction methodology (*Fig. 5.13 b*).
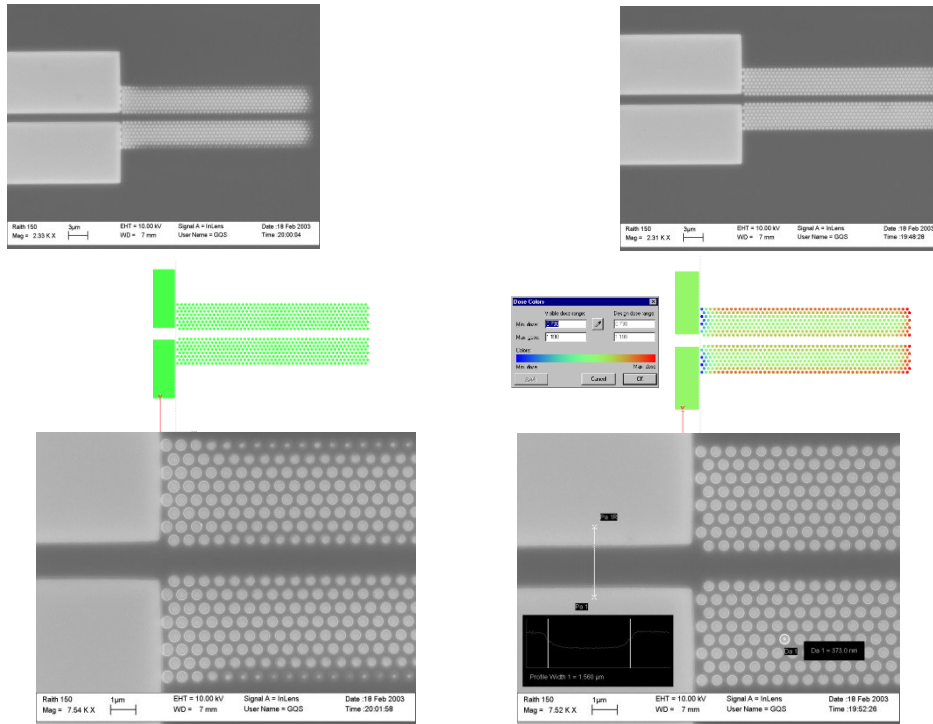
Fig.5.13 a) Without Proximity correction   Fig.5.13 b) With Proximity correction

5.6 Resist interaction

Inside the lithographic process is of fundamental importance the resist used. The resists at our disposal are different but categorized into two large families:

- positive resists that behave like the one now described;
- negative resists that have a complementary behavior, in the sense that the areas exposed to the scanning of the electron beam will cross-link, while those not reached by the beam will be pruned away in the development process.

The use of either resists depends on the specific manufacturing needs.

Resists are most commonly liquid solutions composed of organic polymers dissolved in a solvent. They are deposited on a substrate by spin coating to form a film of uniform thickness. Following spin casting, the casting solvent is evaporated by baking through an oven or an hot stage (generally is a soft baking). After this operation the sample is covered by a durable polymer film and it is ready for electron beam exposure. Often resist is applied to the

substrate in multiple layers or in layered combinations with inorganic materials or other organic materials that are not sensitive to electron-beam exposure. The purposes of multi-layer resist are varied and include planarization, improvement of pattern transfer, reduction of backscatter, and creation of specific feature cross-sections. The electron-beam pattern exposure deposits energy in the resist and modifies it to create the latent pattern image. Development by specific solvents completes the transformation of the resist coating into the desired pattern. For a positive resist, the exposed regions are made more soluble and are selectively removed by the developer. For a negative resist, the exposed regions are rendered insoluble in developer and the unpatterned area is removed by the developer.

Exposure of the resist results in chain scission or cross-linking. For high-resolution e-beam lithography, high-sensitivity resists are preferred.
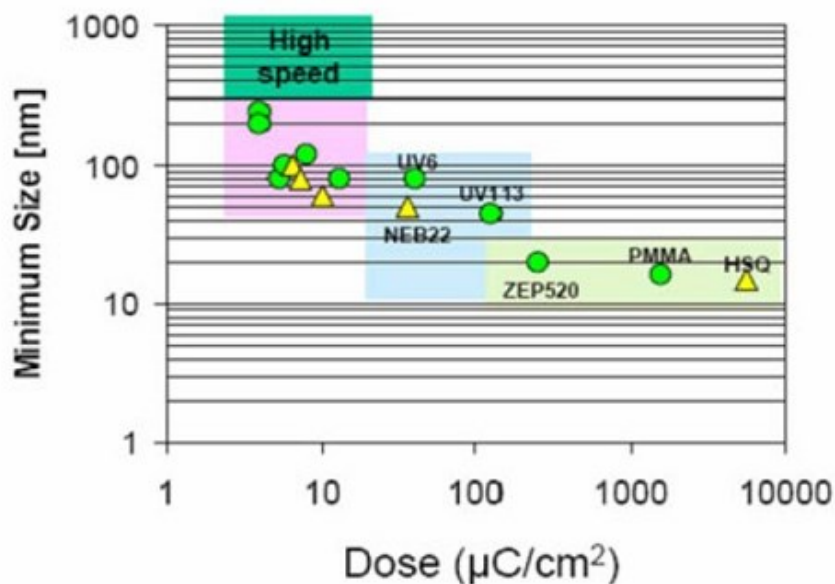
Fig. 5.14 Comparison of performance for different positive and negative electron beam resists exposed at 100 keV. Representation of sensitivity in function of resolution. PMMA has high resolution, but requires higher doses than ZEP520.

PMMA

For many years, PMMA (*Fig. 5.15*) has remained the resist of choice for very high resolution electron beam lithography since its introduction into electron-beam lithography in 1968. It has extremely high resolution (below 10 nm), excellent shelf life, and does not suffer from swelling or post-exposure latency effects. Its biggest drawbacks are its poor sensitivity, poor dry etch resistance, and poor thermal stability. Historically cast in chlorobenzene, it is now commercially available cast in safer anisole solvent. It is available in molecular weights from

50 to 950K, with slightly decreasing sensitivity and higher resolution capability with increasing molecular weight.
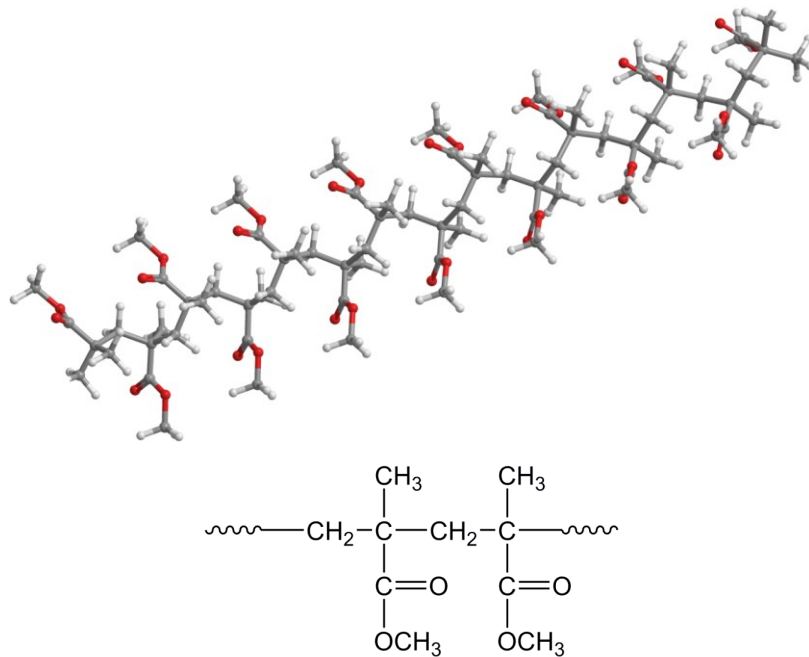
Fig. 5.15 PMMA chemical structure

PMMA is also sensitive to exposure by deep ultraviolet light and x-rays, permitting hybrid exposure strategies. A hybrid exposure exposes the finest features of a given lithography level by electron beam with coarser features of the same lithography level exposed separately by a high-throughput optical or x-ray technique, all in the same resist and with a common development. The primary exposure mechanism for PMMA is by scission of the polymer chain (*Fig. 5.16*). Scission in the exposed region reduces the molecular weight, with the lighter weight fragments selectively removed by MIBK:IPA (methyl isobutyl ketone : isopropyl alcohol) developer.
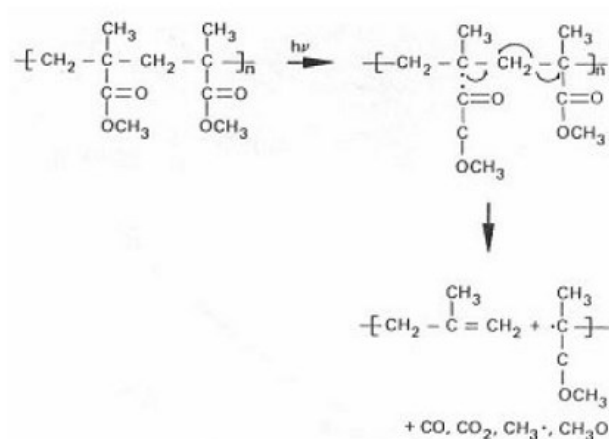
Fig.5.16 PMMA breaking chain mechanism through a radiation-induced scission

ZEP520A

ZEP520A (ZEONREX® Electronic Chemicals) is a positive-tone electron- beam resist with comparable resolution to PMMA. Chemical structure of this resist is alternating a-copolymer of α-chloromethacrylate and α-methylstyrene (*Fig. 5.17*). This resist has a better sensitivity (requires less dose) and resistance to dry etching processing compared with PMMA but is need to be completely shielded from sun light. Zep-made nanostructures show an intrinsic undercut profile, this represent an enormous advantage for the lift-off post-processing tecnique. On the other hand it often show a poor adhesion to the substrate requiring the need for a preventive layer of hexamethyldisilazane (HDMS) to be used as primer.
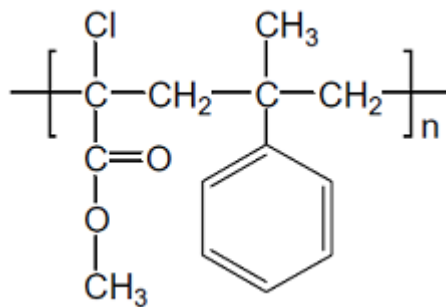
Fig 5.17. ZEP Chemical structure.

Development is accomplished with n-hexyl acetate, ZED50 (n-amyl acetate), or ZEP-RD (xylene), and is immediately followed by a rinse of isopropanol or methyl isobutyl ketone.

References

[1] S.Y. Chou, H.I. Smith and D.A. Antoniadis, "*Sub-100nm channel-length transistors fabricated using x-ray lithography*", ***J. Vac. Sci. Technol***. **B4** (1), 253-255, 1986.

[2] R. Viswanathan, D. Seeger, A. Brigth, T. Bucelot, A. Pomerene, K. Petrillo, P. Blauner, P. Agnello, J. Warlaumont, J. Conway, and D. Patel, "*Fabrication of high performance 512k static-random access memories in 0.25 µm complementary metal-oxide semiconductor technology using x-ray lithography*", ***J. Vac. Sci. Technol***. **B11** (6), 2910-2919, 1993.

[3] H.-S. Kitzerow and K. Busch, "***Nanophotonic Materials***" edited by R.B. Wehrspohn, , Wiley-VCH, 2008.

[4] "***Handbook of Microlithography, Micromachining, and Microfabrication***", **Vol.1**, edited by P. Rai-Choudhury, IEE Materials and Devices series, 1997.

[5] A.A. Tseng, K. Chen, C.D. Chen, and K.J. Ma, "*Electron beam lithography in nanoscale fabrication: recent development*", ***IEEE Transaction on Electronics packaging manufacturing*** **26** (2), 141- 149 (2003)

[6] D. J. Grant, "***Electron beam lithography: from past to present***", University of Waterloo (2003)

[7] D.K. Ferry, M. Khoury, D.P. Pivin, K.M. Connolly, T.K. Whidden, M.N. Kozicki, and D.R. Allee, "*Nanolitography*", ***Semiconductor Science and Technology*** **11** (11), 15552-1557 (1996)

[8] D.M. Tennant, "***Nanotechnology***", Springer NY (1999)

[9] A.N. Broers, "*Fabrication limits of electron beam lithography and of UV, X-ray and ion-beam litographies*", Philosophical Transactions of the Royal Society of London Series a-Mathematical Physical and Engeneering Science, **353** (1703), 291-311 (1995)

[10] A.N. Broers, A.C.F Hoole, and J.M.Ryan, "*Electron beam lithography –Resolution limits*" Microelectronic Engineering **32** (1-4), 131-142 (1996)

[11] T.H.P Chang, M.G.R. Thomson, M.L. Yu, E. Kratschemer, H.S. Kim, K.Y. Lee, S.A. Rishton, and S. Zolgharnain, "*Electron Beam technology – SEM to microcolumn*", Microelectronic Engineering **32** (1-4), 113-130 (1996)

[12] E. Chen, "*Introduction to nanofabrication*", Applied Physics **294r** (Harvard University) (2004)

[13] E. Gipstein, A.C. Ouano, D. E. Johnson, and O. U. Need, "*Parameters affecting sensitivity of PolyMethylMethacrylate as a positive litoghraphic resist*", Polymer Engeneering and science **17**(6), 396-401 (1977)

[14] ***Handbook of Nanotechnology***, edited by Bharat Bhushan, Springer (2004)

[15] James W. Conway , "*E-beam Process for ZEP – 520 to be used for Metal Liftoff and RIE*", Stanford Nanofabrication Facility - Stanford University (2002)

[16] Hector M Saavedra, Thomas J Mullen, Pengpeng Zhang, Daniel C. Dewey, Shelley A Claridge, and Paul S Weiss, "*Hybrid strategies in nanolithography*", Rep. Prog. Phys. **73** (2010) 036501 (40pp)

Chapter 6: Realization of SERS substrates

As both bottom-up and top-down synthesis methods have their advantages and disadvantages, we used both techniques to realize SERS substrates and to compare them.
An effective and facile method for the fabrication of a SERS-active film with Silver nanowires (AgNWs) is proposed by drop casting of AgNWs on glass with ethanol as the inducer. Alternatively, Au photonic crystals (PCs) and photonic quasi crystals (PQCs) realized by EBL are proposed as engineered and reproducible SERS substrates.

6.1 Silver Nano-Wires based substrates by Bottom up approach

An effective and facile method for the fabrication of a SERS-active film with Silver Nanowires (AgNWs) is proposed by drop casting of AgNWs on glass with ethanol as the inducer. We adopted a very simple drop casting process to fabricate Ag NW films (with areas over 2 cm^2) on glass from a dispersion of silver nanowires (provided by Prof. W. Song group from Ningbo Institute of Material Technology and Engineering (NIMTE), China) that are ~190 nm in diameter and 7-15 μm in length diluted with ethanol. The samples were allowed to dry on a Hot Stage (Cee 1100FX by Brewer Science, see *Fig. 6.6*) set at 150°C for 5 minutes (*Fig. 6.1*). Ag NWs in ethanol showed a very good dispersibility and were easier to redispersion. *Fig 6.2 a-b* show the SEM and TEM images of the Ag NWs on glass.
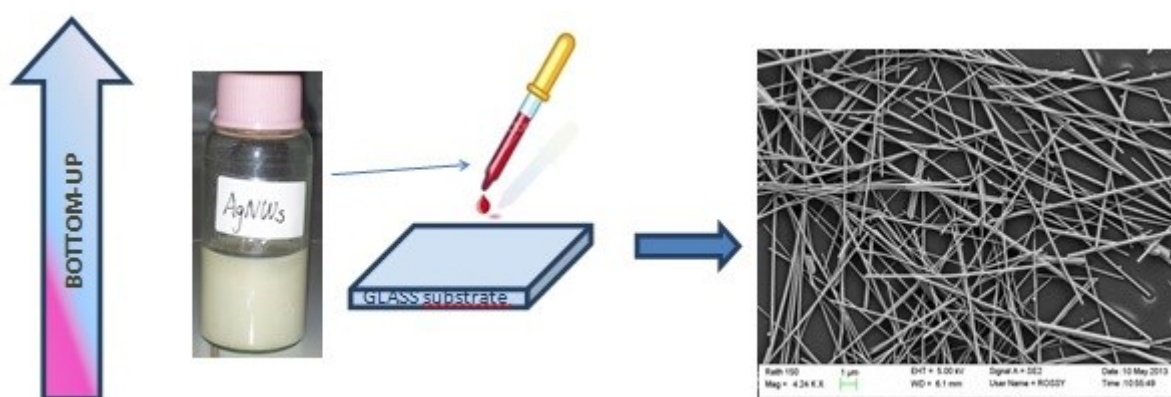
Fig. 6.1 Fabrication process of a AgNWs based SERS substrate
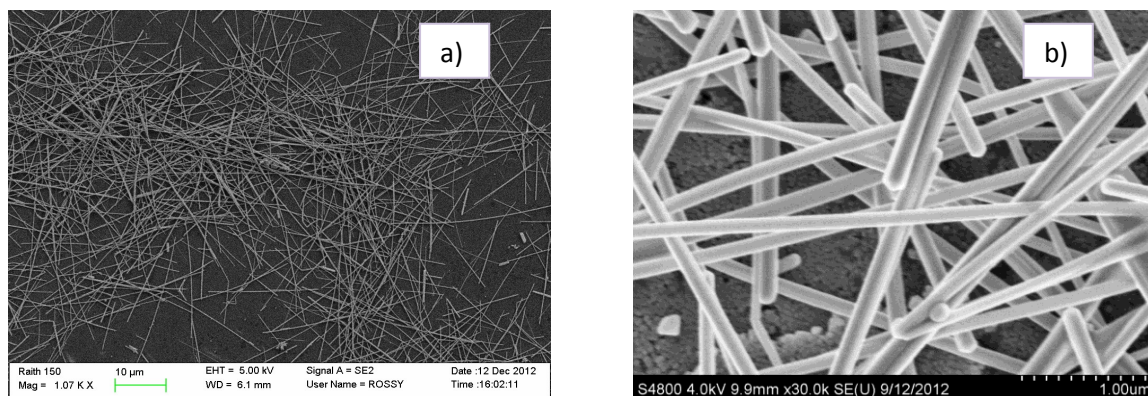
Fig. 6.2 a) Scanning electron microscopy (SEM) and b) and TEM images of the Ag NW film deposited on a glass substrate: d~190nm and L=7-15µm.

6.2 Engineered SERS substrates by top-down approach: EBL technique

As described in details in *Chapter 5*, the basic idea behind electron beam lithography is identical to optical or any other lithographies. The substrate is coated with a thin layer of resist (in analogy with photoresist we use the word *e-resist*), which is chemically changed under exposure to the electron beam, so that the exposed (non-exposed) areas can be dissolved in a specific solvent (positive (negative) lithography). This process is called *development* (in analogy with development of photographic films) In this way, we can create any pattern in the resist deposited on our sample (*Fig. 6.3*). After the removal of the exposed resist, a thin metallic layer is deposited on the substrate. On the areas exposed to the electron beam the deposited metal sticks to the substrate, while on the unexposed areas the metal sticks to the resist surface. After metal deposition the remaining (unexposed) e-resist is dissolved in an aggressive solvent (lift off). The metal sticking to the resist looses "footing" and so only the metal sticking to the substrate remains.
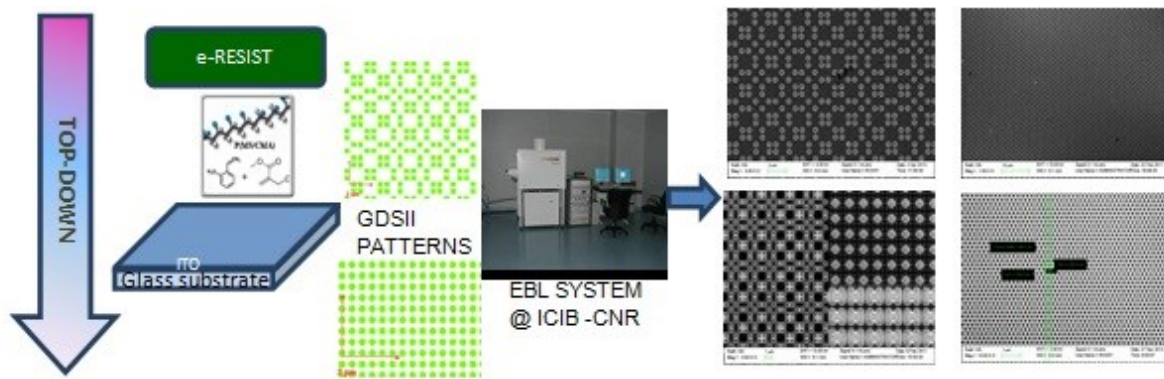
Fig 6.3 Ebl Fabrication process (cloackwise: Thue Morse QCs (d=500nm, G=510nm), Hexagonal periodic arrays (d=500, A=1μm), hybrid Thue Morse/Serpinsky carpet/periodic H structures, Honey periodic arrays (d=200nm, A=250nm))

6.2.1 Fabrication steps

The main part of the PhD research activity held at the Institute of Cybernetics "E. Caianiello "CNR of Pozzuoli, and useful for the purposes of this PhD thesis, was the acquisition of a sample preparation technique suitable to the exposure processes by electron beam lithography. About 70 samples were realized by spin coating a layer of ZEP520A (ZEONREX® Electronic Chemicals), with thickness of about 180-200nm, on glass substrates (BK7 by Sigma Aldrich) covered with a 15-30nm thick ITO (Indium Thin Oxide) layer, in order to obtain, after exposure by EBL and pattern transfer on Gold by a Lift-off post-processing, the desired patterns previously realized by a GDSII 2D CAD software.

Below the realization process of a single nanostructure is presented in detail.

As part of the manufacturing process and characterization we can generally distinguish the following steps:

1. cleaning of the substrate and spin coating of the chosen resist;

2. evaluation of the thickness of the obtained film with a profilometer;

3. design of the desired pattern through a GDSII editor;

4. exposure of the sample with EBL;

5. development of the sample;

6. evaporation of a metal;

7. lift-off process.

1. Substrate cleaning and Thin films deposition: resist spin-coating

The first and fundamental operation is the cleaning of the substrate using suitable solvents: first of all with a mechanical cleaning, and then through an ultrasonic bath. In particular, for glass + ITO substrates ultrasonic bath is carried out in a solution of distilled water and soap for about 2 hours, and the rinsing is done by running water. Scrupulous and accurate cleaning operations are of fundamental importance, as a substrate not clean in a timely manner can affect the uniformity of the layer of resist that will spin-coated on the substrate.

The spin-coater used is Karl Suss RC Spin coaters CT62 V08 (*Fig. 6.4*)

Fig. 6.4: Karl Suss RC Spin coaters CT62 V08 @Cybernetic Institute of CNR (Pozzuoli-Italy).

It allows to program an arbitrary spin-coating cycle as that represented in *Fig. 6.5* in which we can distinguish two spin-coats at two different speeds: the first one determines a uniform distribution of the resist on the sample, while the second one provides to the thickness of the resist layer.
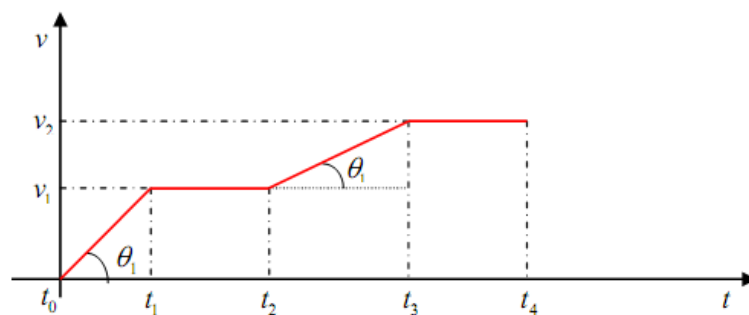
Fig 6.5: An example of Spin-coating cycle by Karl Suss RC Spin coaters CT62 V08

The resist used to realize the substrates object of this dissertation is ZEP520A. It has been useful to characterize the thickness of ZEP520A supplied at the "Nanocomposites and Soft Matter Laboratory" of the Cybernetic Institute of CNR at different spin-coating speeds. After

spin-coating a soft-bake operation is needed: in our case we used a Hot Plate (*Fig 6.6*) (Cee 1100FX by Brewer Science) set at 170° for 5 minutes in order to evaporate solvents [1].

Fig.6.6: Hot Plate Cee 1100 FX by Brewer Science @Cybernetic Institute of CNR
(Pozzuoli-Italy).

2. *Resist Thickness evaluation*

To obtain a correct evaluation of the film thickness obtained we used a profilometer "Alpha-step 200" (*Fig. 6.7*) by *Tencor Instruments* to evaluate the thickness of the layer obtained.

Fig .6.7: " Alpha Step 200" Profilometer by Tencor Instruments @ Cybernetic Intitute –CNR
(Pozzuoli)

In the following Fig. (*Fig. 6.8*) we show an example of a tipical resist profile taken on a realized sample.
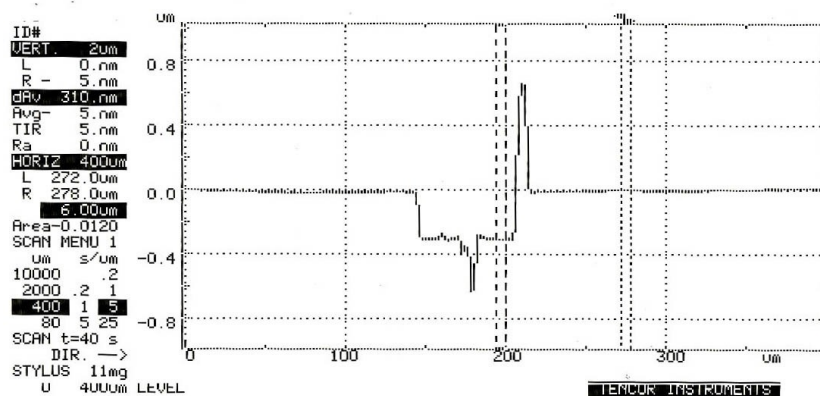
Fig. 6.8: Glass/ITO/ZepCut (50% in Anisole) spin speed: 2000 r.p.m, Thickness: t=310nm

Thanks to this procedure we calibrated each concentration of the solution used to make the resist film, in order to get a precise knowledge of the proper spinner parameters to be set to obtaina specific thickness of the film for each concentration used (*Fig. 6.9 a-b-c-d*). Each graph shows the resist thickness measured by profilometer as a function of rounds per minute (rpm) set on the spinner. Each curve has been obtained for a specific concentration of the material used and with four different measurements changing rpm.
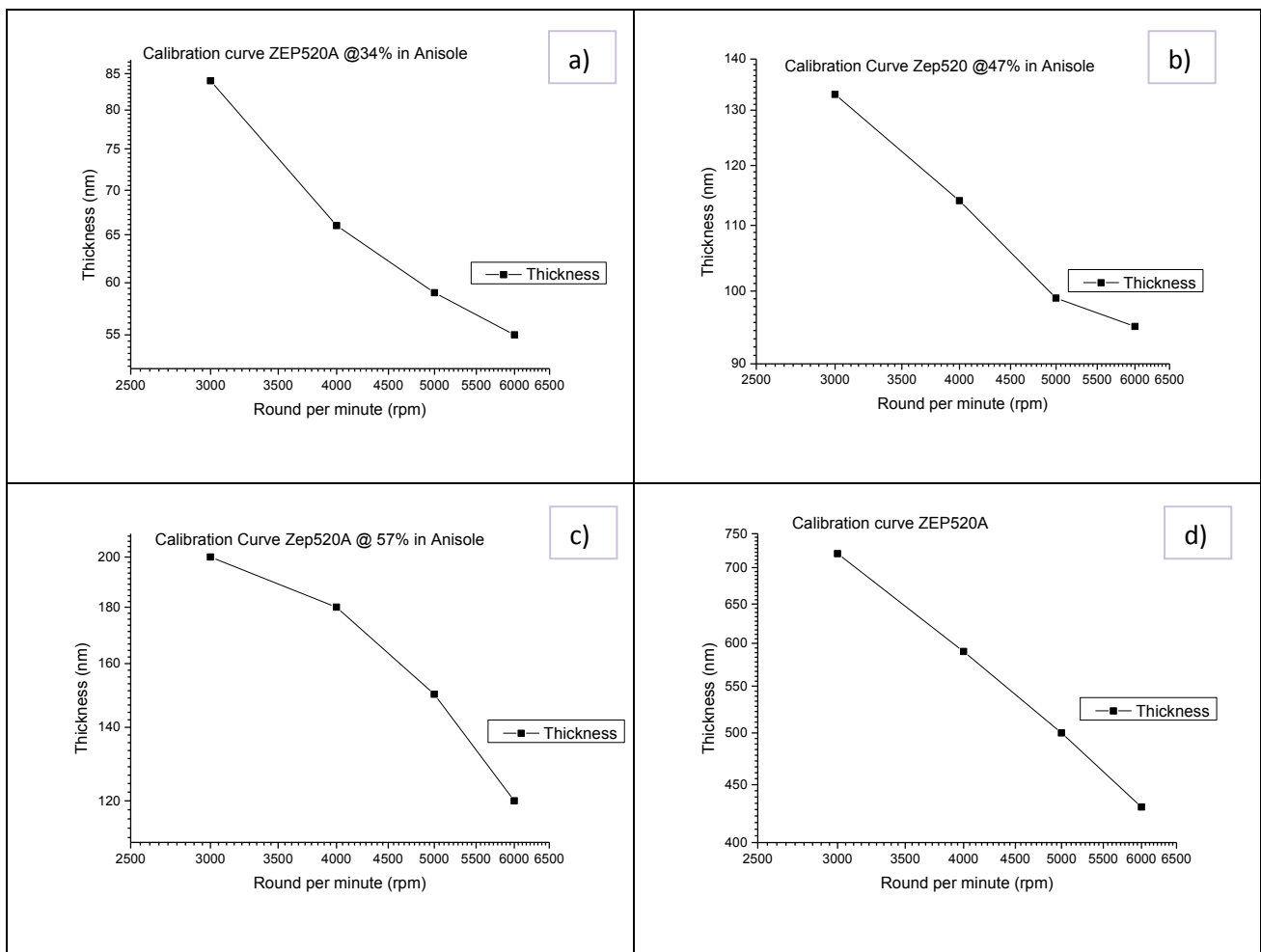
Fig. 6.9: Some Zep520A with different concentrations in Anisole calibration curves. a)Zep520A 36% in Anisole; b) Zep520A 47% in Anisole; c)Zep520A 57% in Anisole; d)Zep520A not diluted

These operations allowed us to set the right parameters to make a thin layer (200nm) of the "*electrosensitive*" polymer (ZEP520A) spin coated upon a conductive glass substrate (a 15nm Indium-Tin-Oxide layer sputtered on the surface of a common glass in order to make it conductive) (*Fig. 6.10*):
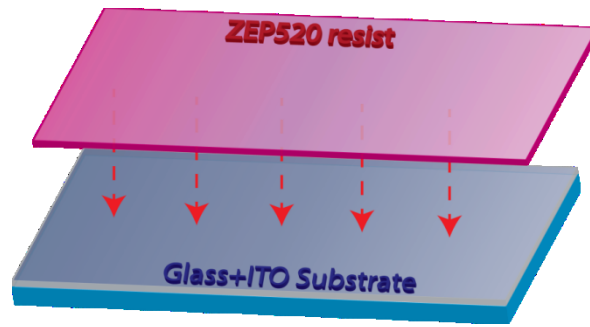
Fig 6.10 : ZEP520 Spin Coating.

3. *Pattern design by GDSII editor*

The next step was to design the pattern of the structure that we wanted to transfer on the samples after exposure by EBL tecnique. (*Fig. 6.11 a-b-c-d-e-f*)
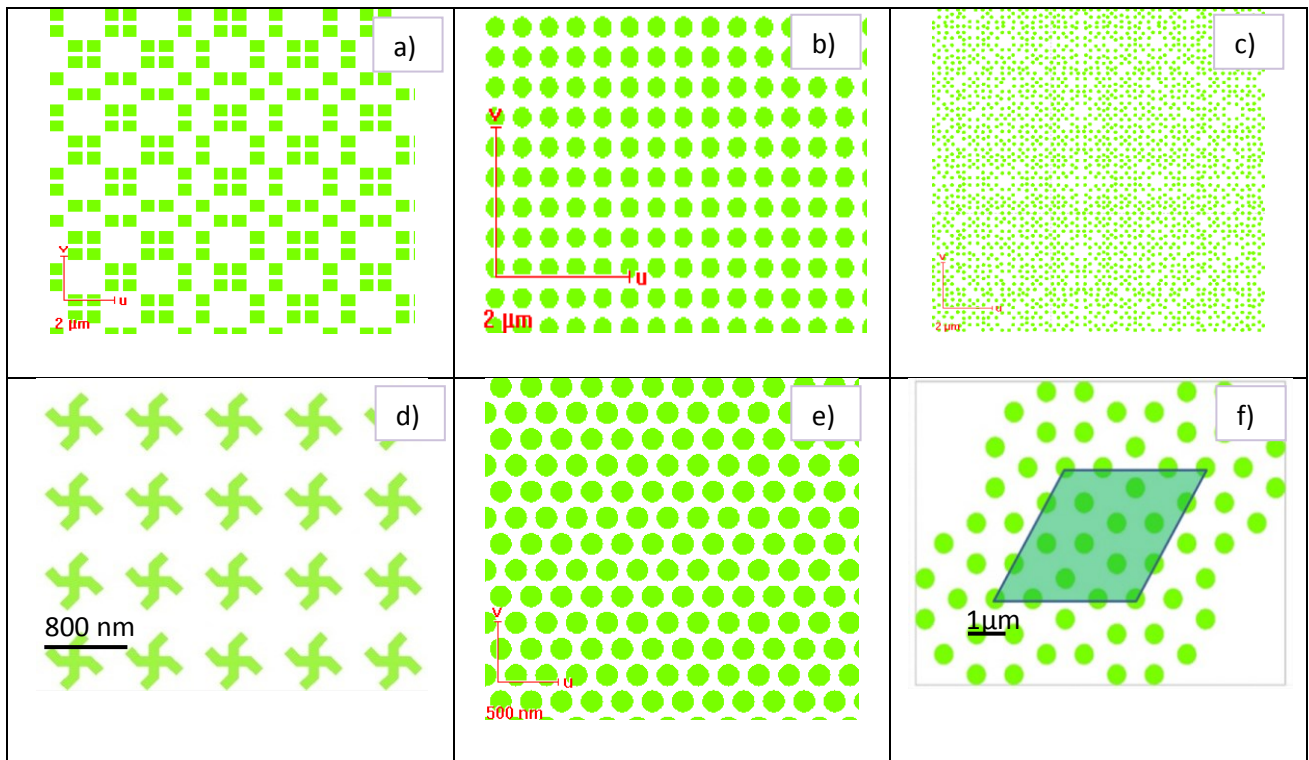
Fig.6.11: Some example of patterns realized by GDSII editor ad hoc for our reasearch activity: a) Thue Morse PQC of squares; b) periodic square based PC of circles; c) 8-fold arrangement of circles; d) periodic square based arrangement of gammadions; e) periodic triangular based PC of circles; f)12-fold arrangement of circles

These designs have been realized using the 2D CAD software of EBL Raith 150. Such software allows the generation, in a two-dimensional environment, of simple geometric shapes, such as regular polygons or not, and of complex geometric shapes also expressible in analytical form. *Fig. 6.12* shows an example in which some objects have been grouped into different levels, you will notice how it was even possible to design objects with non-trivial geometries.
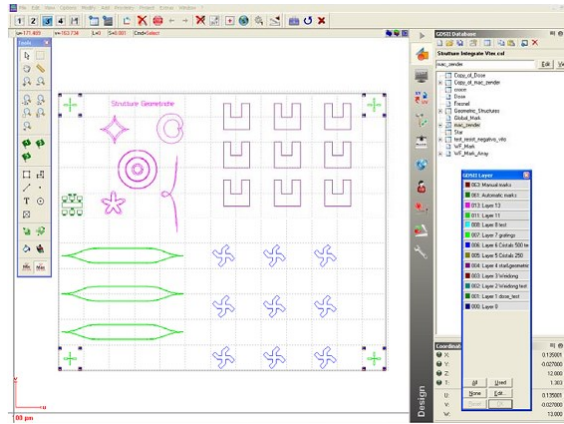
Fig.6.12: Example of a GDSII project in which different layers are specified in different colors.

4. Sample exposure by Electron Beam Litography Tecnique

The exposure process is the heart of the work done for this PhD thesis, since both the understanding of the behavior of electron beam lithography and the use of the facility that allows similar projects show many difficulties, which we will now describe.

a. Optimization of SEM column working parameters

As described in the previous Chapter 5, SEM column is the principal nucleus of an EBL system, and the first difficulty to be faced in order to observe, and then expose a sample, is the optimization of the working parameters of the SEM column: *stigmation* and *apertures*. It consists in correcting electronic lenses aperture and eliminating the effects of electron beam astigmatism introduced by the electronic lenses themselves. Only if these parameters are properly set the operator manage to get a good focus and then a good visualization of the sample. In the following Fig.s we show examples tests (*Fig. 6.13 a-b-c*) for proper focus and aperture optimization (*Fig. 6.14*).

Fig. 6.13: Example of a) lack of focus; b) test made in order to obtain the correct aperture parameter; c) tests made in order to obtain the correct aperture and stigmation parameters
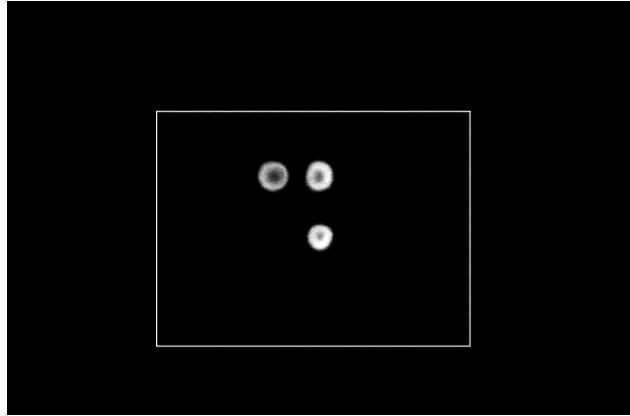
Fig.6.14: Example of tests in order to obtain the correct aperture and stigmation parameter. In this case we want to underline improvements respect to the previous images Fig.6.13 c

These values must be optimized for each exposure, since they depend on many variables which are:

- type of resist;
- type of substrate;
- total thickness of the sample given by the sum of the thickness of the resist and the substrate;
- accelerating voltage of the electron beam (EHT)
- set apertures.

It is clear that the variation of each of these elements will determine the search for a new working point. It should be noted, moreover, that even working at different points of the same sample could determine a variation of these parameters. These changes will be negligible for displacements between the points whose distance is of the order of hundreds of microns and will become increasingly important with increasing distance.

b. *Exposure Dose Optimization*

Once the working area is fixed and all the parameters are optimized, we proceed with the sample exposure. The next problem is to optimize the exposure energy.

Having understood the effects of a lower or higher dosage than the optimal dose (*Section 5.5 Chapter 5*) we show now operationally tests to search for the right dose. We created a dose test for the specific structures we wanted to transfer onto the substrate. The SEM analysis of the obtained structures identifies a range of doses with which the best results were obtained (*Fig. 6.16*). Iterating the process we are able to achieve the optimal dose. *Fig. 6.15* shows the method applied to explicate just a generic photonic structure:
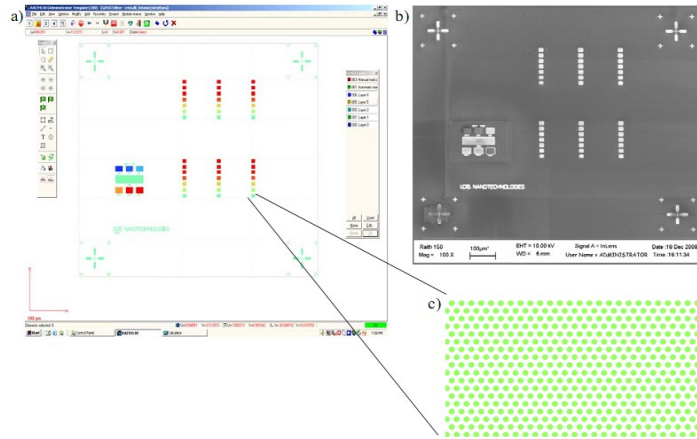
Fig.6.15 a) Generic test to achieve the optimal dose in order to completly remove the resist. Different colors are associeted to different doses. b) SEM image of the test c)Magnification of the generic PC projected and tested

In *Fig. 6.16* we report some examples of SEM images of nanostructures (***Periodic Square based PC of circles*** with *d=180nm* and *A=200nm*) exposed with wrong and right doses showing how critical can be the dose choice. We can distinguish different situation (EHT=10KeV) starting from an underdosed result exposed with *Ad=18 μC/cm²* (*Fig. 6.16 a*) passing through a right dosed PCs (*d=180nm, A=200nm*) at *Ad=22 μC/cm²* (*Fig. 6.16 b*), to a overdosed PC at *Ad=25 μC/cm²* (*Fig.6.16 c*), to finish with a very High Overdosed PC at *Ad=25 μC/cm²*(*Fig. 6.16 d*).
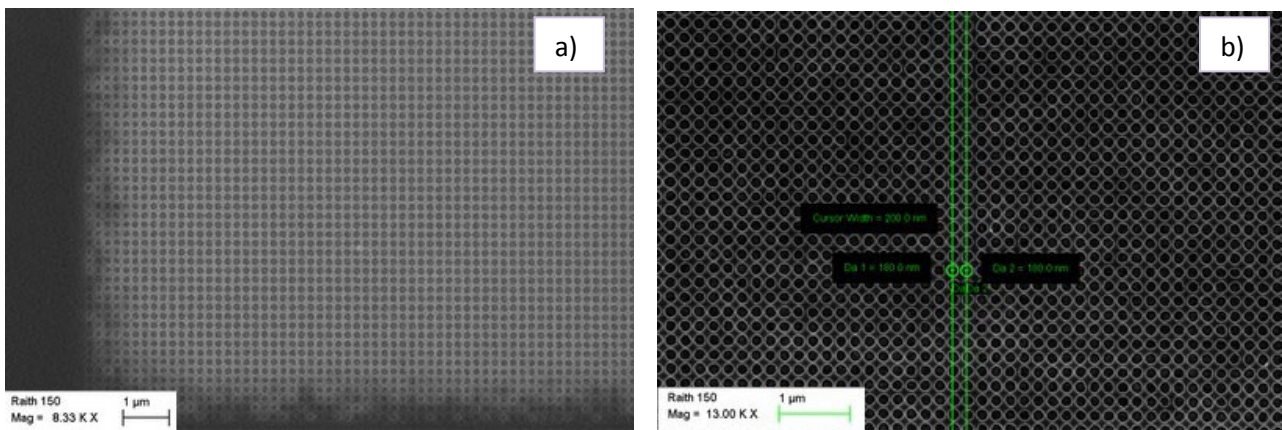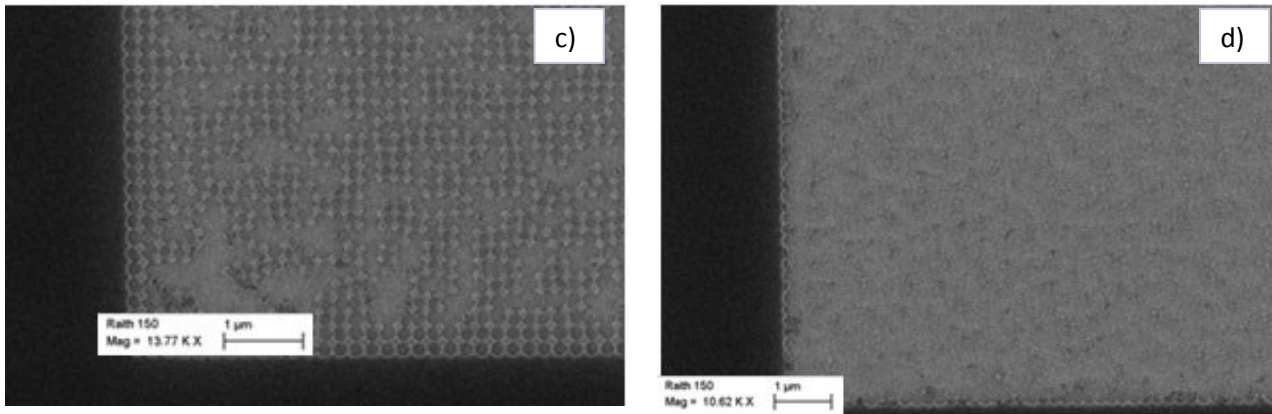
*Fig.6.16: Some SEM images of tests on **periodic square based PC of circles (d=180nm, A=200nm)** realized by EBL, with EHT=10KeV, in order to investigate the right dose: a) Underdose example at Ad=18 µC/cm²; b) Right-dose example at Ad=22 µC/cm²; c) Overdose Ad=25 µC/cm²; d) High Overdose example at Ad=30 µC/cm²*

5. *Sample development*

Next step is the development of the exposed specimen. The profile of the exposed structures will also depend on the developing time. It's important to underline as the ideal removal of the resist occurrs when the walls of every elements of the nanostructure are perfectly orthogonal to the substrate. Using too short development time you can not completely remove the resist layer; by increasing development time you are able to completely remove the resist approaching the ideal situation. To be more schematic clearing of resist means:

- ✓ Perfect Development
  - Smallest holes (vias) clear of resist at bottom,
  - Smallest lines with acceptable width
  - No "stringers" between closest lines
  - Usually overdevelop to 5-10% is necessary so to obtain all structures clear
- ✓ Incomplete development: thick resist in openings
- ✓ Underdeveloped: sloped edges at bottom may leave resist scum (especially small opens)
- ✓ Overdeveloped: sloped sidewalls of resist or lines too small (may disappear or lift off)

The most significant situations are reported in the following Fig. (*Fig. 6.17*):
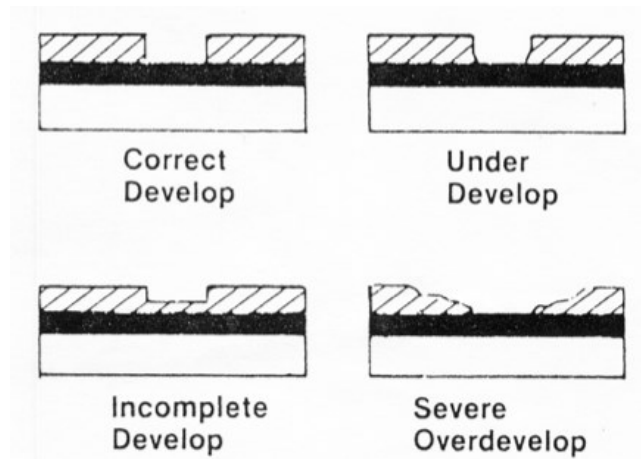
Fig. 6.17 The most significant situations in term of clearing of the resist

We optimized our development time to meet the strong demands for a simple and effective lift-off method i.e., to obtain the re-entrant resist profile (*Fig. 6.18*) necessary for proper metal lift-off. We developed 200nm-thick ZEP520A exposed samples for 90 seconds in ZED N50, a n-Amyl acetate solvent, then rinsed for 90 seconds in 1:3 MIBK:IPA solution (Methyl isobutyl ketone:Isopropyl alcohol), the develop process has been stopped immersing the sample for 30 seconds in IPA (Isopropyl alcohol) and then dried with nitrogene flux.
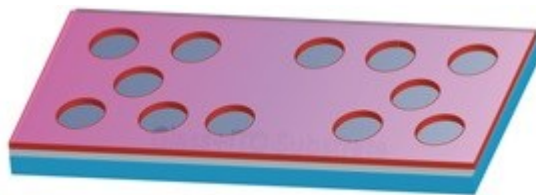
Fig 6.18: Positive Resist after the chemical development. In this case the nanostructure is composed by air holes.

6. Metal Thin Films Deposition Tecniques

After the development operation of the samples, and the metrological SEM analysis of them whose results will be presented in detail in *Section 6.3*, we proceed with the deposition of thin metallic films in order to obtain metal reticular structures (in this specific case in Gold, Chrome/Gold).

The **Physical Vapor Deposition** (PVD), is a common method for thin films deposition under vacuum.

A deposition is defined atomic or molecular when on a substrate occurs a growth atom by atom of the film (also called *overlayer*). The resulting layer can vary from single crystal to amorphous, more or less compact, pure or impure, thin or thick. Usually are defined **thin** films

whose thickness is of the order of a few microns or less, and in this case there is often the influence of the substrate with regard to the chemical and physical properties of the overlayer. The Physical Vapor Deposition (PVD) processe consists in atomic depositions in which the material is evaporated from a liquid or a solid source in the form of atoms or molecules and transported as vapor through a vacuum or plasma environment to the substrate where it condenses. Generally, the PVD is used to realize coatings of a few tens or hundreds of nanometers, for deposits in different layers (*multilayer*), for films composed of variable percentage alloys (*graded composition deposite*); the shapes of the substrate may vary from flat to very complex geometries as decorative objects or tools, and the *rate* (speed) of growth of the deposit varies depending on the specific case from 1 to 10 nm per second. The PVD can be used to realize both elementary films or alloys and also compounds coatings through the so-called *reactive deposition*: in such processes the compounds are formed through a chemical reaction that occurs between the material that we go to evaporate and the gaseous environment created in the room, for example with nitrogen inlet if you want to create nitrides, or oxygen in the case of oxides depositions.

The deposition tecniques used for this activity, and related to metallic films of Gold and Chromium/Gold, consisted in:

- Thermal evaporation
- E-beam evaporation

*** Thermal evaporation process***

In a thermal evaporation process, metal to be evaporated is placed in a molybdenum melting-pot, heated by Joule effect by a current generator. The upper part of the evaporation chamber is provided with a platform with a central housing in which is placed the sample, which in the preliminary stages of evaporation, ie as long as it does not have reached the optimum conditions for the deposition of the metal, is protected by a shutter.

As for the other depositions, also thermal evaporation takes place in vacuum conditions in order to guarantee a good purity of the metallic film. The pumping system consists of a turbomolecular group and the pressure is detected by a ionization head.

We used two Thermal evaporator systems: a Leybold one composed by Turbotronik NT 150/360 VH and Combivac IT230 at the Cybernetic Institute of CNR (*Fig. 6.19 a*), and a "Mini-SPECTROS" Thermal evaporator by Kurt J. Lesker Company @ UTTP –ENEA (Portici) (*Fig. 6.19 b*). Both processes are monitored through a thick controller made by quartz crystals which, in

real time, provides the deposition rate and the thickness of the film already deposited. For Thermal evaporations of gold thin films done in ICIB-CNR, using the Leybold system,after reaching the pressure of about 10^{-4} Pa, we proceed with a *degassing* in order to remove surface impurities. The degassing operation consists in increasing the current in discrete steps (typically using steps of about 30A) and keeping it constant for a time interval of 30-60 s. The completion of the dagassing is characterized by the return to the initial conditions of pressure. When the deposition rate stabilizes at around 0.2 Å/s we open the shutter and the deposition starts up to the desired thickness (60 nm). After a relaxation time, that varies between 15-20 minutes, we can retract the system, then remove the sample and proceed with the lift-off operations sequence.

Fig. 6.19: a) Leybold Thermal evaporator @ Cybernetic Institute-CNR (Pozzuoli); b)"Mini-SPECTROS" Thermal evaporator by Kurt J. Lesker Company @ UTTP –ENEA (Portici)

For Thermal evaporations of gold thin films done in UTTP-ENEA (Portici), they took place in a high vacuum chamber, using a MiniSpectros system produced by Kurt J Lesker Company. The base pressure is about 5E-8 mbar. To control the gold films thickness, the evaporation rate is continuously monitored by quartz crystal microbalance (thickness monitor). During the whole process, the rate was kept constant at 0.2 Å/s, and the final thickness of the gold films obtained was 60 nm.

E-beam evaporation process

Ideal for lift-off because of low incident angle, it is characterized by low pressure processing. E-beam evaporation is a process similar to thermal evaporation i.e. a source material is heated above its boiling/sublimation temperature and evaporated to form a film on the surface that is stroke by the evaporated atoms. A noticeable advantage of e-beam evaporation over thermal evaporation is the possibility to add a larger amount of energy into the source material. This yields a higher density film with an increased adhesion to the substrate. Because the electron beam only heats the source material and not the entire crucible, a lower degree of contamination from the crucible will be present than in the case of thermal evaporation. By using a multiple crucible E-beam gun, several different materials can be deposited without breaking the vacuum. In the case of this PhD activity we used this method to realize a bi-layer consisting in Chromium and Gold by a SISTEC CL-400C produced by "Angelantoni Group" e-beam evaporator, property of UTTP-ENEA (Portici) (*Fig. 6.20*).
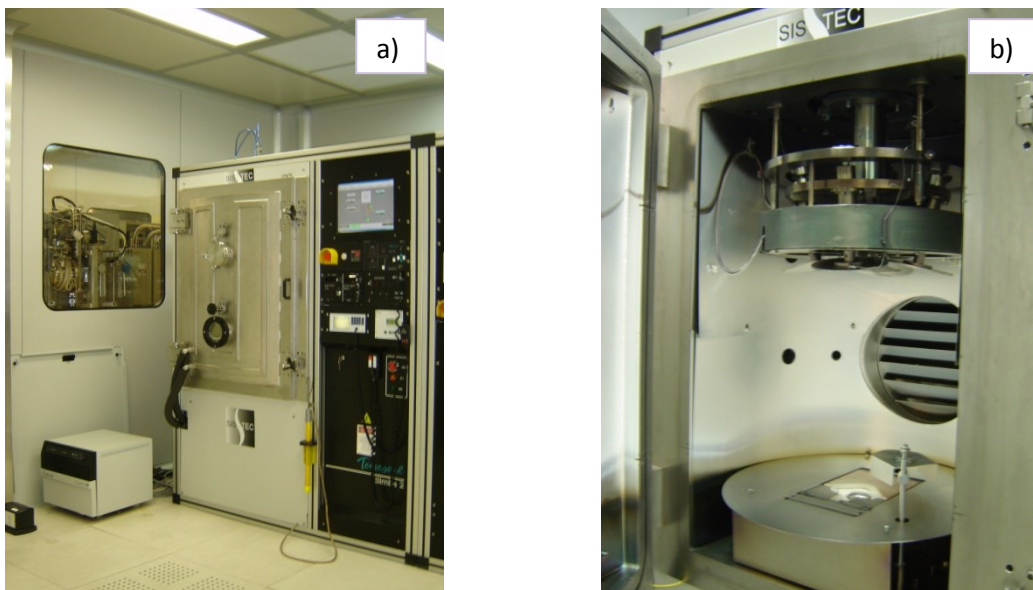
Fig. 6.20 a) SISTEC CL-400C "Angelantoni Group" e-beam evaporator, property of UTTP-ENEA (Portici); b)evaporation chamber

With the source material placed in the crucible a filament below the crucible is heated. By applying a large voltage, electrons are drawn from the filament and focused as a beam on the source material by several bending magnets. The beam is swept across the surface of the source material to heat all of the material.

Evaporation is remotely controlled by an INFICON controller which has several parameters to be set for each material / layer; Evaporation times are determined by the set rate, measured in real time, and the final thickness can also be set. Temperature is controlled with

the thermocouple inside the evaporation chamber, not in contact with the samples. During the process, evaporation rate is kept contant to 0.2 Å/s both for Cr and Au. Vacuum pressure before the evaporation of Cr is: 1.9×10^{-7} mbar, during the evaporation it ranges from 2.4×10^{-7} to 1.9×10^{-7} mbar, Temperature in chamber is set to be $T_{start} = 22°$ C, $T_{end} = 25°$ C; the real rate is 0.1Å/s . As far as the Gold layer evaporation is concerned the following are the normal working conditions used each time: vacuum pressure before the evaporation of Au is 1.4×10^{-7} mbar, during the evaporation it ranges from 7.2×10^{-7} to 3.8×10^{-7} mbar, Temperature in chamber is $T_{start} = 25°$ C, $T_{end} = 35°$ C, the real rate ranges from 0.1 to 0.2Å/s.
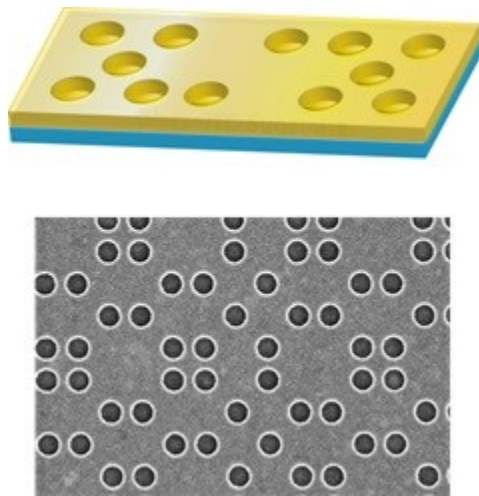
Fig 6.21 : a) Metallization of the nanostructure, b) SEM image of a Thue Morse of circles just after metallization

7. *Lift-off process*

Lift-off is an easy way to transfer metal patterns on any substrate, especially in the case of metal thin films such as platinum, tantalum, nickel or iron, which are particularly difficult to stick with the conventional etching method.

The general protocol for a lift-off process is the following (*Fig. 6.22*):

    a. The desired pattern is transferred onto the resist that covers the substrate, in our case through the electron beam lithography tecnique;

    b. A metal film is deposited by evaporation or sputtering, on the entire substrate so as to cover the resist and the areas in which the resist, after the development of the sample, are removed;

    c. With the use of proper solvents, the resist under the metal film is removed carrying with itself part of the metal on the substrate and leaving only the metal film directly deposited on the same (ie, where the operation of the development of the sample had removed the resist).

(a)   *(b)*   *(c)*
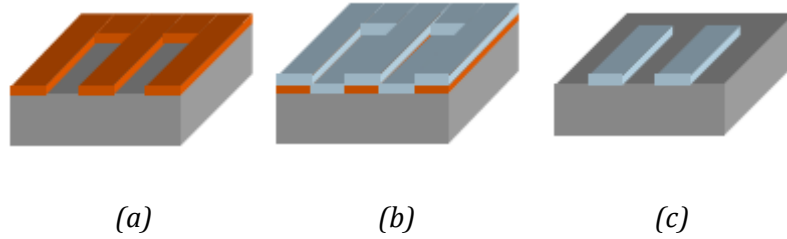
Fig. 6.22: Lift-off process: (a) Pattern realization on a resist covering a substrate; (b) Metal thin-film deposition on the whole sample; (c) Resist removing: metal film deposited on the resist is removed, those deposited directly on the substrate remains attached on its surface.

As regards to ZEP520A, it has been used a protocol that provides some variants compared to the general method due to the different nature of such polymer: after immersion in acetone for about 20 minutes, it is necessary to immerse the substrate in N- MethylPyrrolidinone (NMP) heated at 80°C for 5 minutes, and then spray with a squizzle of NMP to remove the metal film [2].
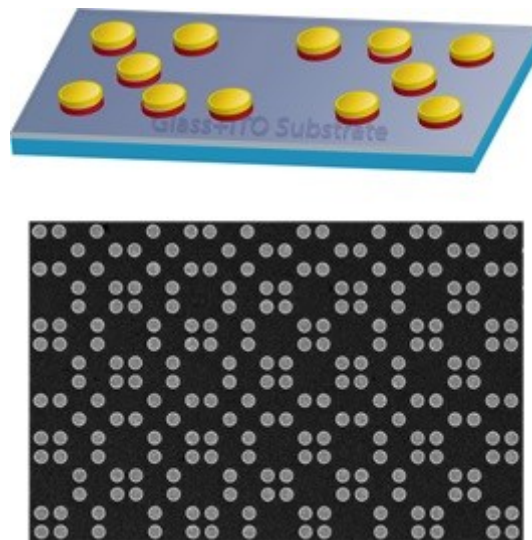
Fig 6.23 : a) Effect of lift-off of the nanostructure: a cylindrical columnar nanostructure has been realized; b) SEM image of a Thue Morse of rods just after lift-off process

As illustrated in *Fig. 6.23*, the lift off procedure enables the appearance of gold nanocolumns. This particular geometry exhibits a strong anisotropy and, therefore, some interesting plasmonic behavior.

To summarize the nanofabrication steps for a generic engineered SERS substrate, we show the flow of operation made (*Fig. 6.24*)

Resist spin-coating

Styrene Methyl Acrilate based Resist

Ebl nanopatterning

GDSII PATTERNS of a Thue Morse PQCs and a PCs

Raith 150 EBL SYSTEM @ ICIB -CNR

SEM inspection & Metrology

a) Before LIFT-OFF

b) After LIFT-OFF

Au deposition

E-beam evaporation

Thermal evaporation

Developing

Positive resist
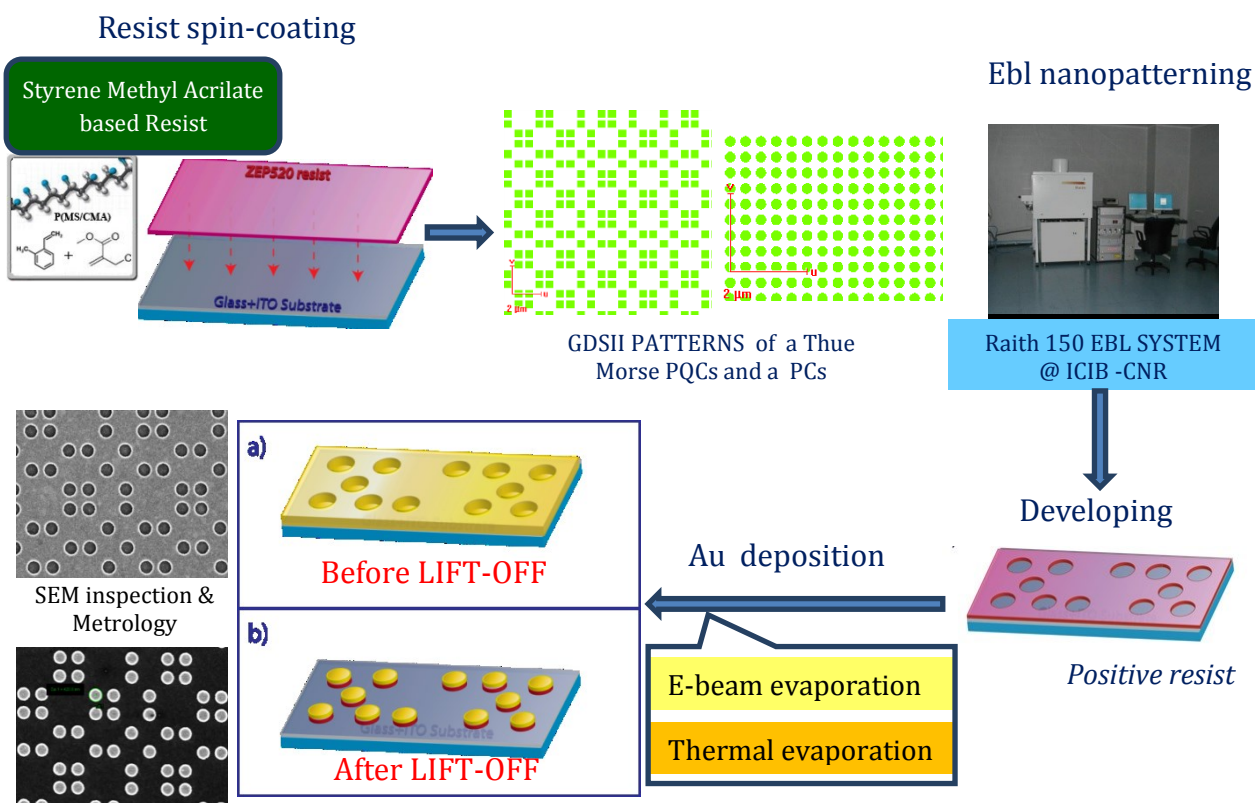
Fig. 6.24: Nanofabrication of an engineered SERS substrate step by step

6.3 SEM metrological analysis

A wide part of the PhD activity has been dedicated to the Scanning Electon microscopy (S.E.M) morphological and metrological analysis of the realized SERS substrates. SEM allowed us to acquire, through a sample scan, surface images of the sample itself. A first fundamental parameter to take into account in a SEM imaging is the acquired image *contrast* between exposed and not exposed zones. Infact, these zones have to be characterized by different depths respect to the surrounding surface. As an example *Fig. 6.25 a* shows a SEM image of a polymeric Thue Morse PQC of circles in which is clearly detectable a good contrast between exposed and not exposed zones; on the other hand, *Fig 6.25 b* shows a SEM image of a AgNWs based surface in which a good contrast is detectable between nanowires and glass substrate.
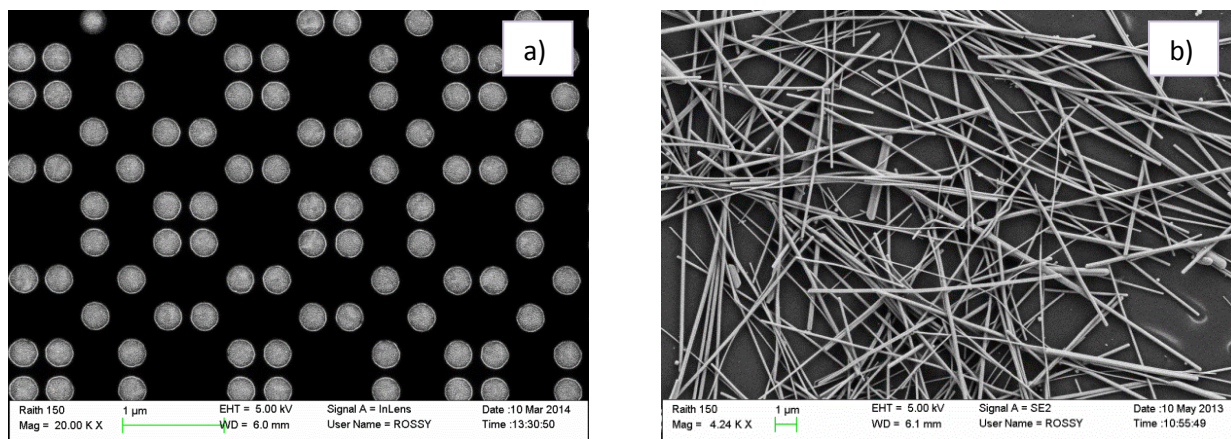
Fig. 6.25: a) S.E.M image of a Thue Morse arrangement of cylindric holes denoting a very good contrast between exposed (light) and not exposed (dark) areas; b) SEM image of a AgNWs based surface in which a good contrast is detectable between nanowires and glass substrate.

Once acquired each image, a metrological analysis of the image is performed to detect all the relevant elements. Such two-dimensional analysis allows any measure in two dimensions: distances between points but even corners or circumference areas can be detected (*Fig.6.26 a-b*).
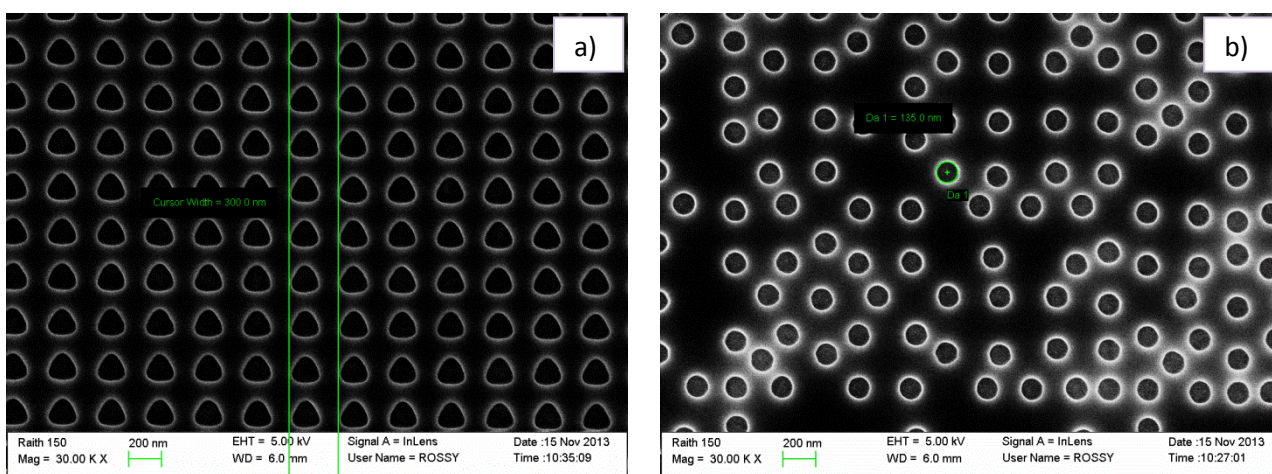
Fig.6.26 S.E.M images of a) a periodic PC of triangles with period 300nm in which distance between two points is taken and b) 8fold PQC of circles with diameter135nm in which the diameter of a single circle is provided. Both the structures shown are in polymer

Morphological and metrological characterization of AgNWs based SERS substrates

The following Fig.s (*Fig. 6.27*) show examples of SEM images and metrological analysis applied to the AgNWs surfaces obtained as described in *Section 6.1*, taking into account the characteristic sizes of Nanowires. In particular:

-Diameter: *d*

-Lenght: *L*
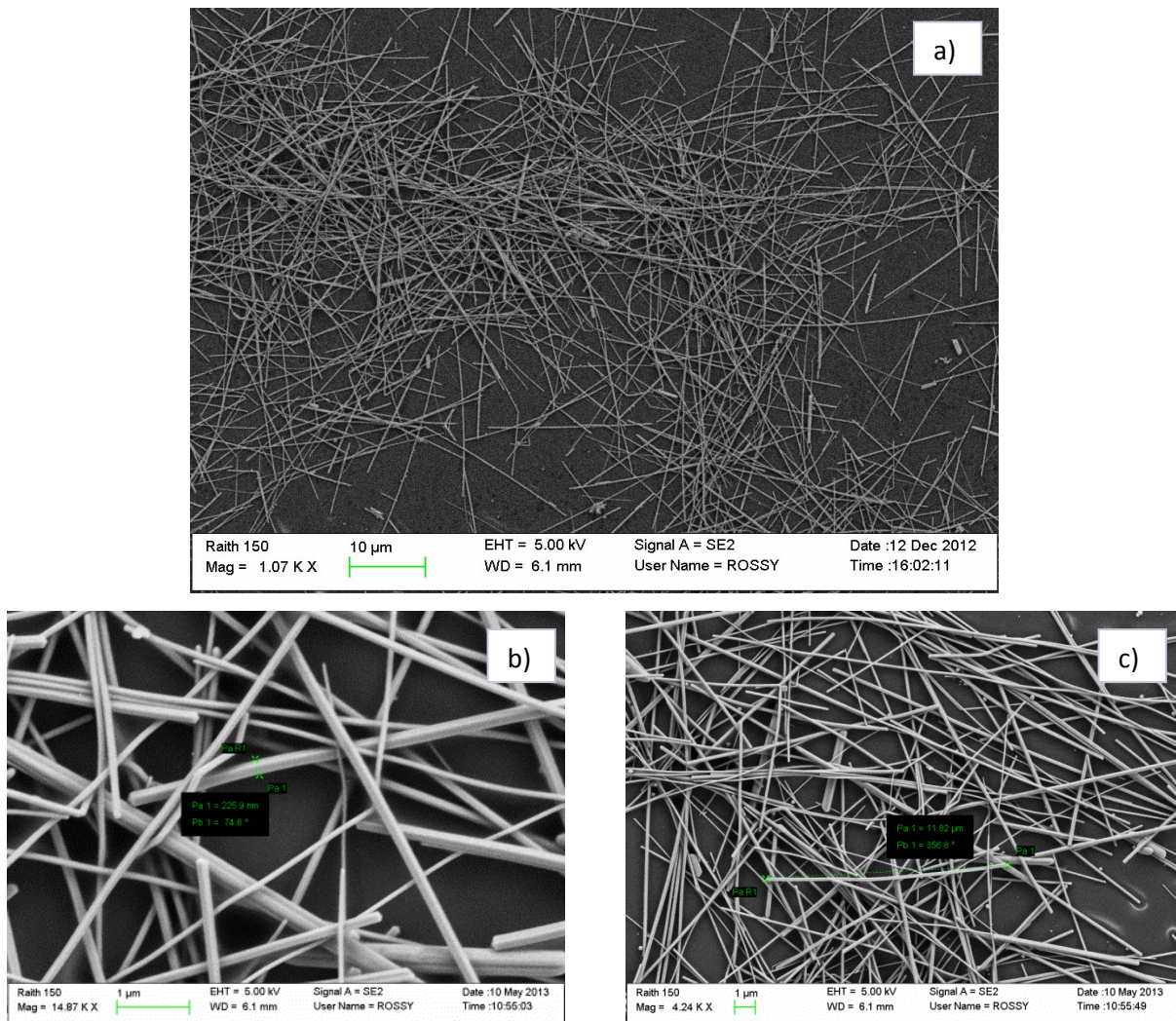
Fig 6.27: Scanning electron microscopy (SEM) AgNWs surface a) at MAG 1KX ; b) at 15KX to investigate the diameter d, ranging from 150 to 230 nm; c)at 5 KX to investigate NWs length L, ranging from 5 to 15 µm

We achieved a not uniform NanoWires distribution on the surface of the substrate (*Fig. 6.27 a*) as confirmation of the lack of reproducibility of those kind of substrates. From the SEM analysis we found Nanowires with diameter ranging from 150 to 230 nm and lengths ranging from 5 to 15 µm

Morphological and metrological characterization of Engineered SERS nanostructures

We realized both Periodic square based and triangular based Photonic Crystals of circlular and trianglular-shaped rods (*Fig. 6.30*), and Aperiodic Photonic Quasi-Crystals in a Thue Morse arrangement of circles and squares, and in a 8-fold arrangement of circles with different sizes (*d*), period (*A*), interparticle separations (*s*) and filling factors (FF),

summarized in the following Tables *Tab 6.1* and *Tab 6.2*. Filling factor reflects the ratio of the covered and the non-covered metal areas and was calculated for each fabricated nanostructure in the following ways (*Fig. 6.28-6.29*) taking into account that in PQCs case the number of gold nanoparticles (*N*) was counted in the specific case of the total areas involved (A_{TOT}) considered:
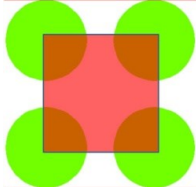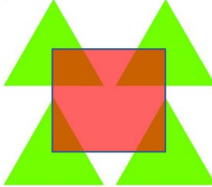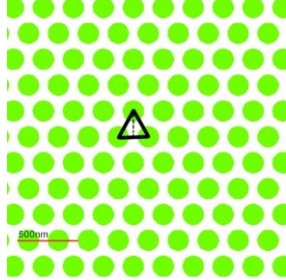
Periodic square based PCs of circles	
	d=diameter; *r=d/2*
	a=period
	Total area= πr^2
Filling Factor= $(\pi r^2)/a^2$	

Periodic square based PCs of triangles	
	d=side size
	a=period
	Total area= $(\sqrt{3}/4)d^2$
Filling Factor= $((\sqrt{3}/4)d^2)/a^2$	

Periodic triangular based PCs of cylinders	
	d=diameter; *r=d/2*
	a=period
	Total area=$(\sqrt{3}/2)a^2/2$
Filling Factor= $(1/2\pi r^2)/(\sqrt{3}/2)a^2/2$	

Fig. 6.28: Filling factor evaluations for the three families of Periodic PCs realized
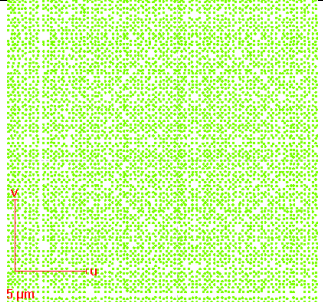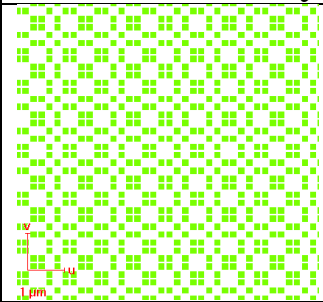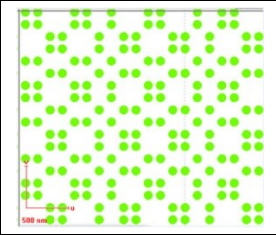
8-fold QPC of cylinders	
	d=diameter; *r=d/2*
	a=period
	A_{TOT}=Total Area involved
	N=n° gold nanoparticles
	Gold Total covered area=$N\pi(r)^2$
Filling Factor= $N\pi(r)^2/A_{TOT}$	

Thue Morse QPC of squares	
	d= side size
	G=period
	A_{TOT}=Total Area involved
	N=n° gold nanoparticles
	Gold Total covered area=$N(d)^2$
Filling Factor= $N(d)^2/A_{TOT}$	

Thue Morse QPC of cylinders	
	d=diameter; *r=d/2*
	G=period
	A_{TOT}=Total Area involved
	N=n° gold nanoparticles
	Gold Total covered area=$N\pi(r)^2$
Filling Factor= $N\pi(r)^2/A_{TOT}$	

Fig. 6.29: Filling factor evaluations for the three families of Quasi-crystals realized
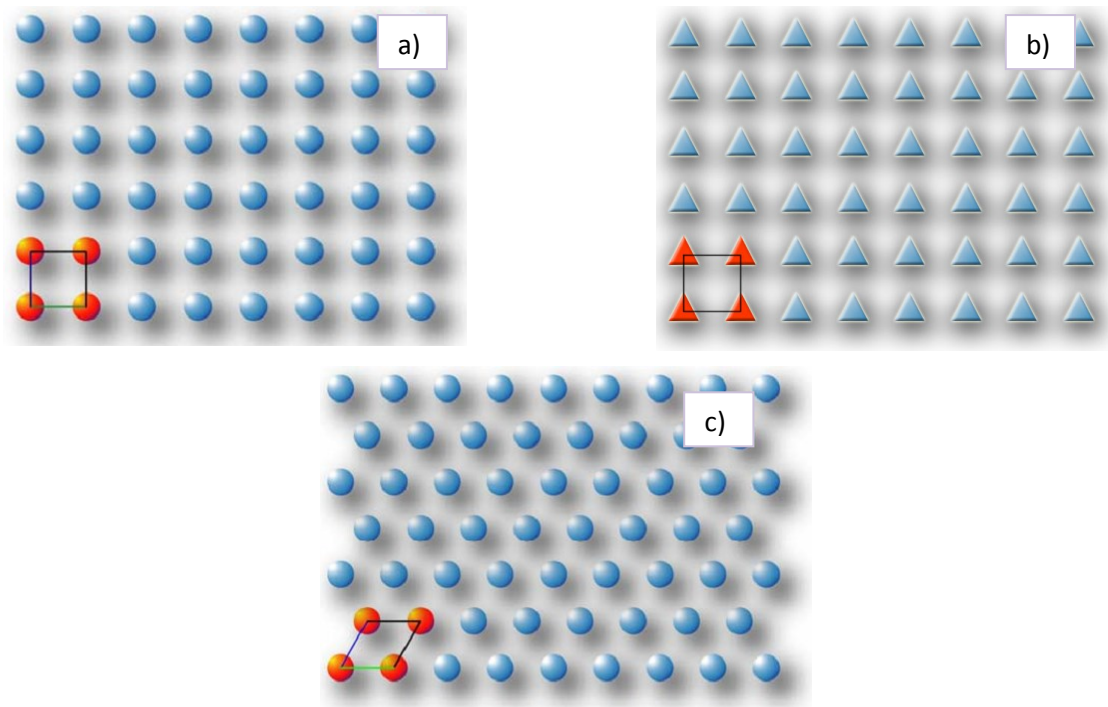
Fig 6.30: Graphic representation of periodic PCs realized: a) Square based arrangement of circles; b)Square based arrangement of triangles; c) Triangular based arrangement of circles

PERIODIC STRUCTURES					
SHAPE	ARRANGEMENT	SIZE (d)	PERIOD (A)	INTER-PARTICLE SEPARATION (s)	FILLING FACTOR (*FF*)
Cylinder	Square based	180nm	200nm	20nm	0,64
Cylinder	Square based	180nm	240nm	60nm	0,44
Cylinder	Square based	150nm	175nm	25nm	0,58
Cylinder	Square based	150nm	200nm	50nm	0,44
Cylinder	Square based	150nm	250nm	100nm	0,28
Cylinder	Triangular based	100nm	150nm	50nm	0,4
Cylinder	Triangular based	175nm	250nm	75nm	0,44
Triangle	Square based	200nm	225nm	25nm	0,34
Triangle	Square based	200nm	250nm	50nm	0,28
Triangle	Square based	200nm	300nm	100nm	0,19
Triangle	Square based	200nm	500nm	300nm	0,06

Tab. 6.1: Summary of the periodic Photonic Crystals realized

SEM and metrological analysis of the periodic nanostructures summarized in the previous table, realized firstly in polymer and then in metal deposited in the different ways previously described, are shown in *Fig. 6.31-6.41*. In each Fig. a comparison between different deposition methods is reported together with the starting structure made of air squared/circular/triangular-shaped holes nanopatterned in polymer.

*Fig 6.31: SEM images of the PC pattern consisting of a **Square based arrangement of circles with d=180nm, A=240nm, s=60nm** on an area of 200 μm x 200 μm : (a) Air rods arranged into the ZEP matrix before thermal evaporation; (b,c) gold-based periodic SERS substrate after thermal evaporation Au (60nm) at different magnifications, 7.5 and 20 KX, respectively; (d) air rods arranged into the ZEP matrix before e-beam evaporation; (e,f) gold-based periodic SERS substrate after e-beam evaporation of Cr/Au (2nm/60nm) at different magnifications, 10 and 20 KX, respectively.*
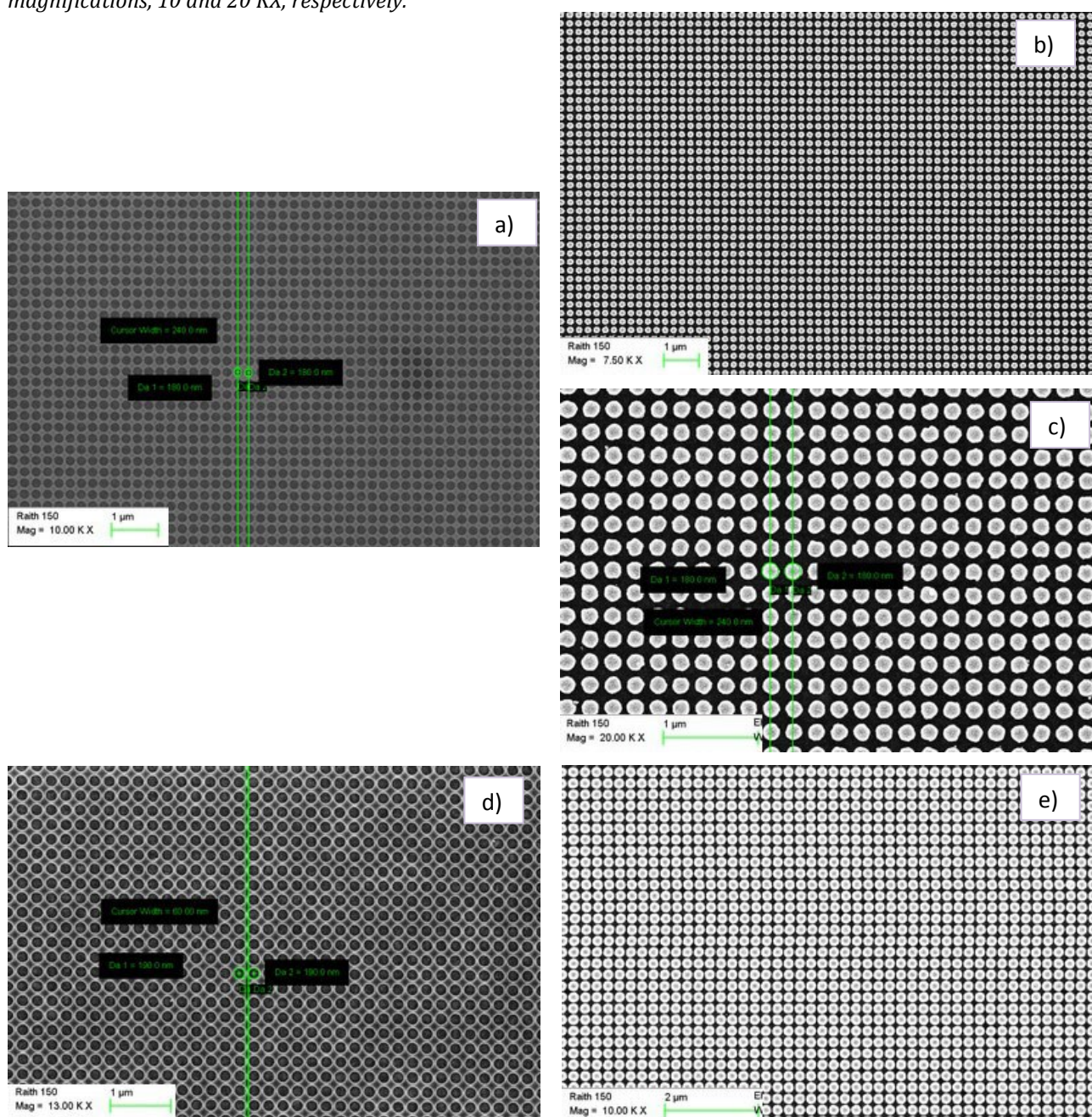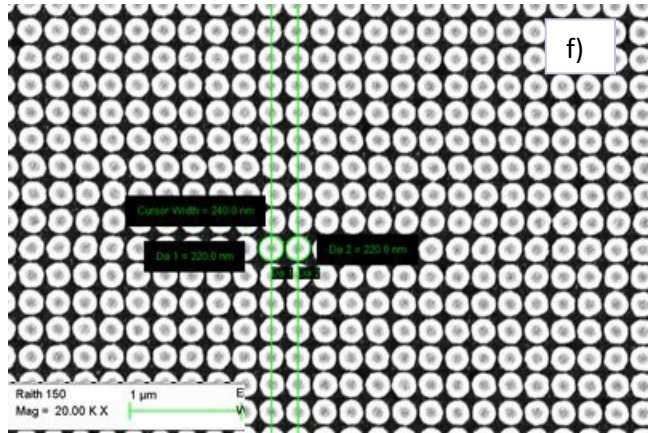
*Fig 6.32: SEM images of the PC pattern consisting of a **Square based arrangement of circles with d=180nm, A=200nm, s=20nm** on an area of 200 μm x 200 μm (a) Air rods arranged into the ZEP matrix before thermal evaporation at magnification 13 KX; (b) gold-based periodic SERS substrate after thermal evaporation Au (60nm) at magnification 11K X.*
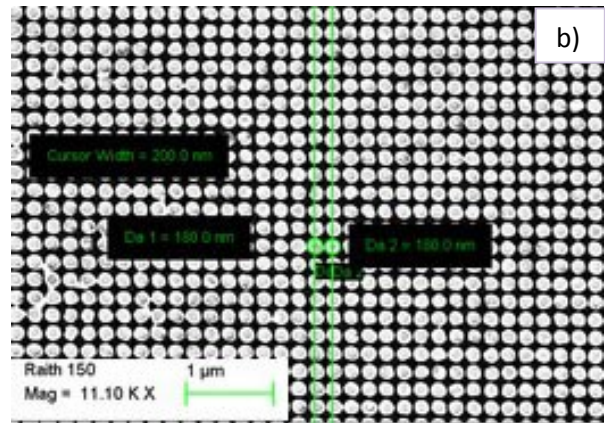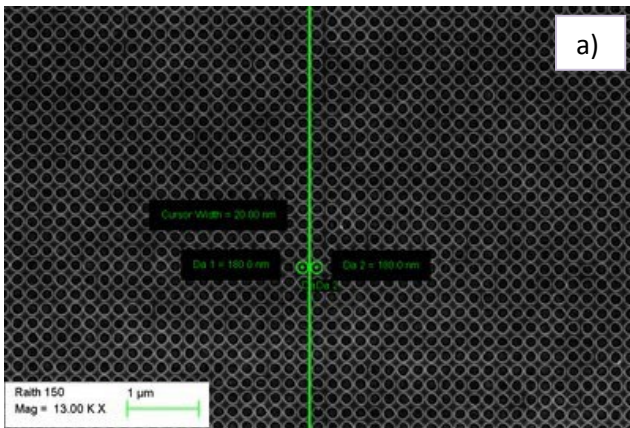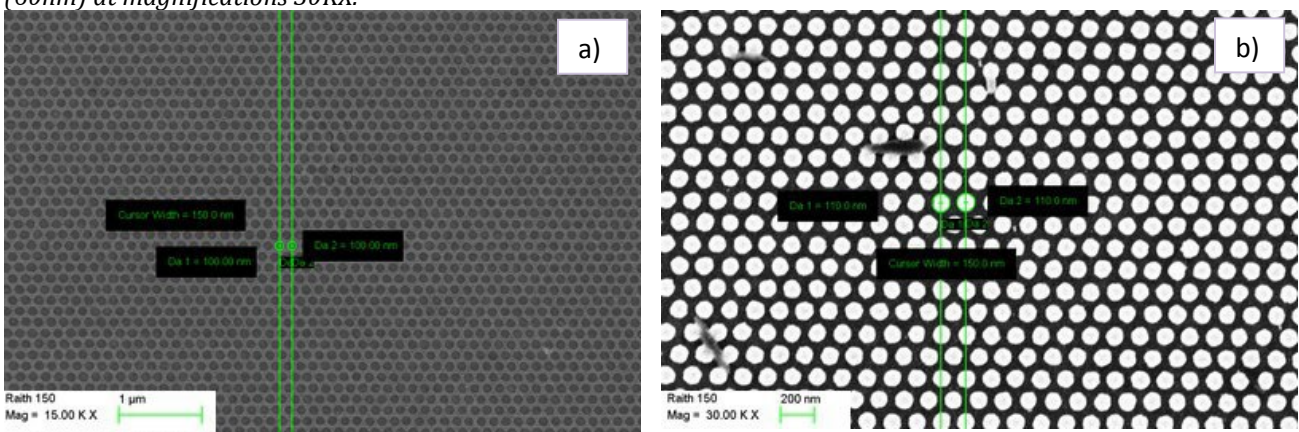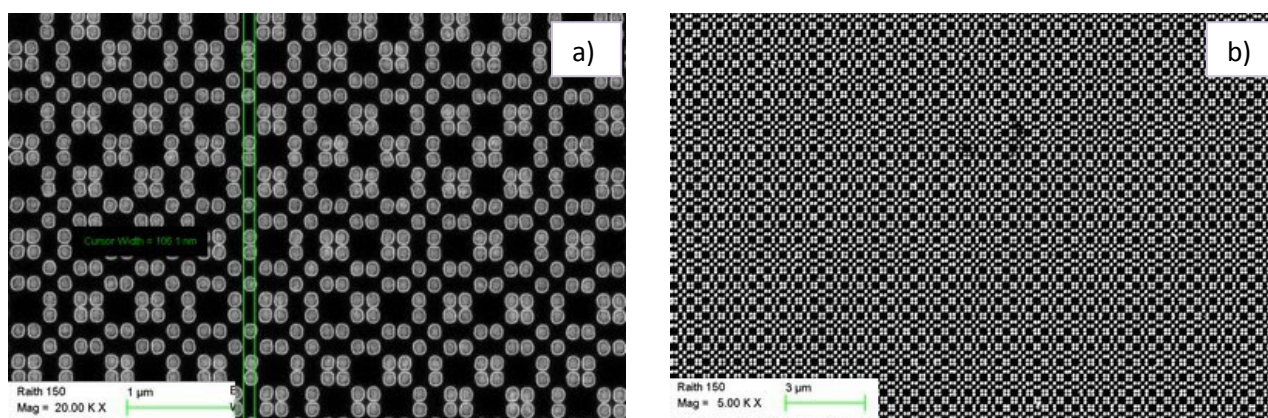

*Fig 6.33: : SEM images of the PC pattern consisting of a **Square based arrangement of circleswith d=150nm, A=175nm, s= 25nm** on an area of 200 μm x 200 μm: (a) Air rods arranged into the ZEP matrix before thermal evaporation at magnification 15 KX; (b) gold-based periodic SERS substrate after e-beam evaporation Cr/Au (2nm/50nm) at magnification 20K X.*
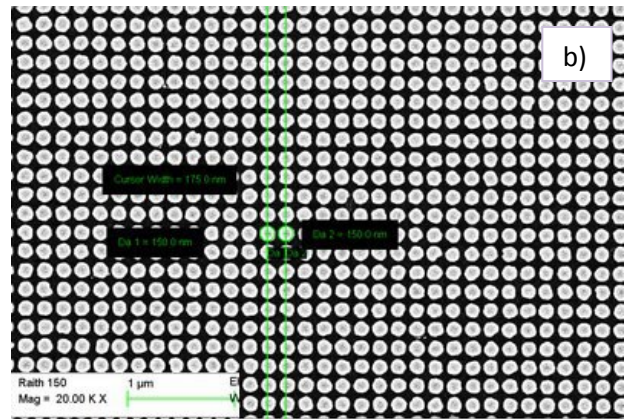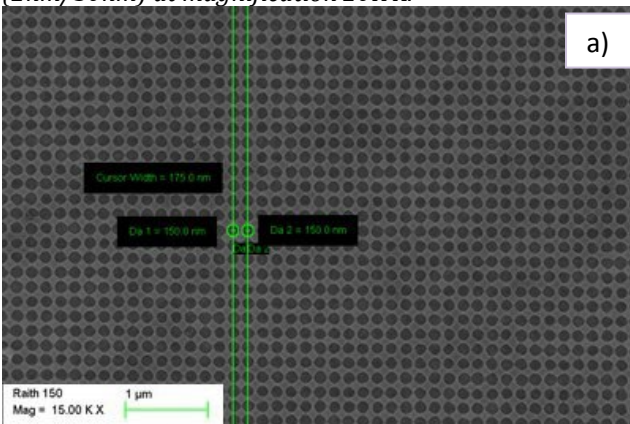
*Fig 6.34: SEM images of the PC pattern consisting of a **Square based arrangement of circles with d=150nm, A=200nm, s=50nm** on an area of 200 μm x 200 μm (a) Air rods arranged into the ZEP matrix before thermal evaporation at magnification 10 KX; (b,c) gold-based periodic SERS substrate after e-beam evaporation of Au (60nm) at different magnifications, 10 and 20K X, respectively;*
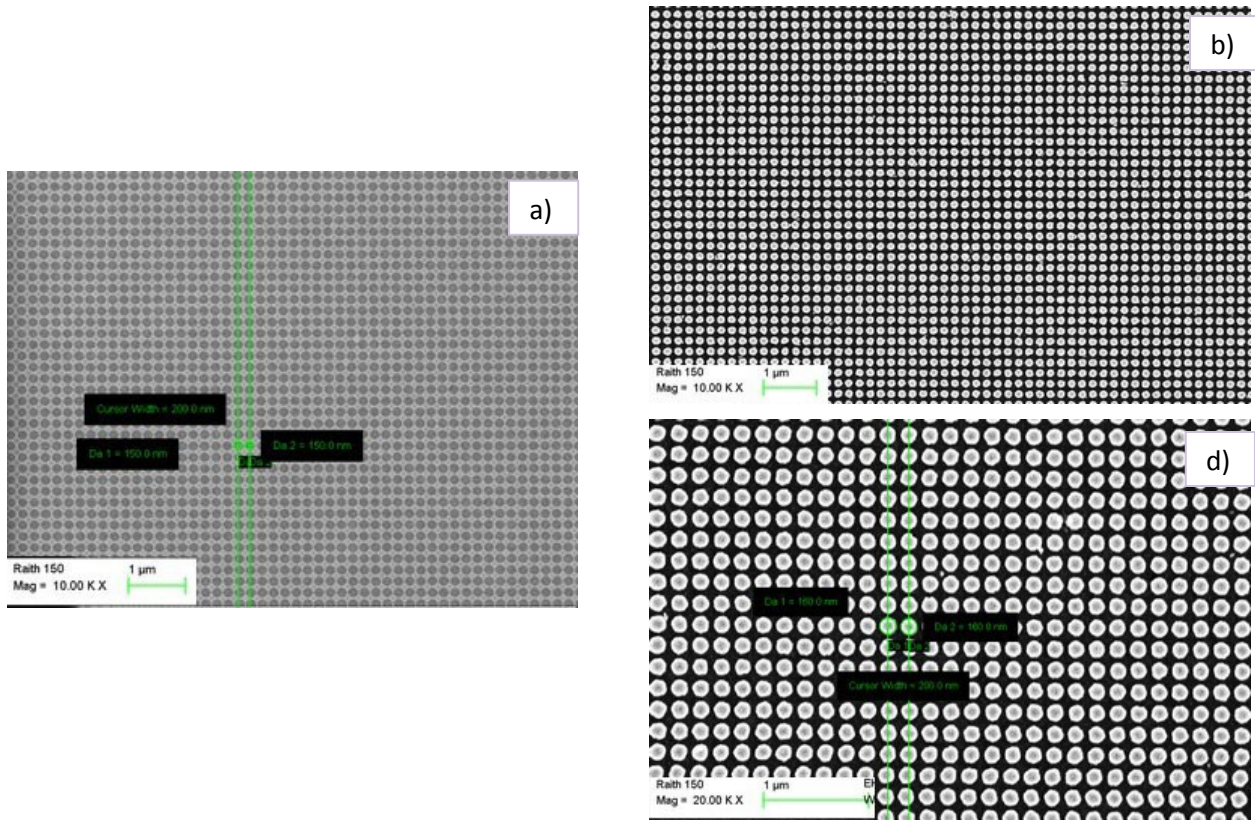
*Fig 6.35: SEM images of the PC pattern consisting of a **Square based arrangement of circles with d=150nm, A=250nm, s=100nm** on an area of 200 μm x 200 μm (a) Air rods arranged into the ZEP matrix before thermal evaporation at magnification 10 KX; (b,c) gold-based periodic SERS substrate after thermal evaporation of Au (60nm) at different magnifications, 10 and 20KX, respectively; (d) Air rods arranged into the ZEP matrix before e-beam evaporation at magnification 10 KX (e,f) gold-based periodic SERS substrate after e-beam evaporation of Cr/Au (2nm/60nm) at different magnifications, 10 and 20 KX, respectively.*
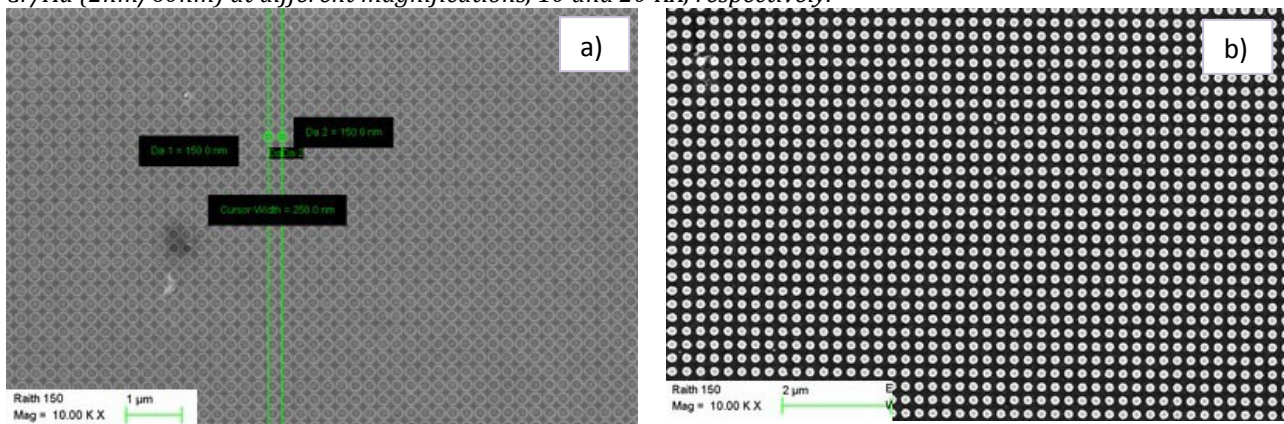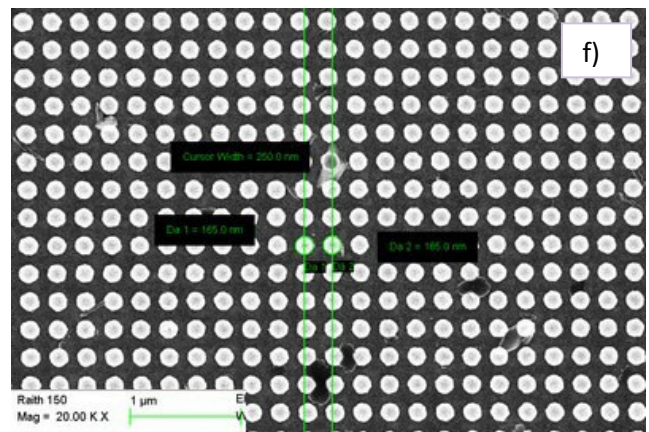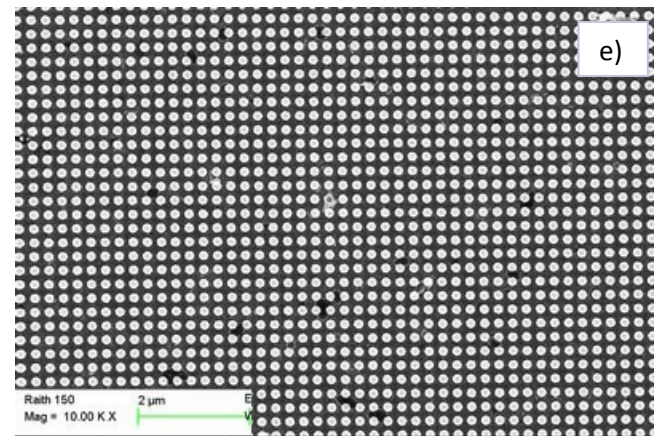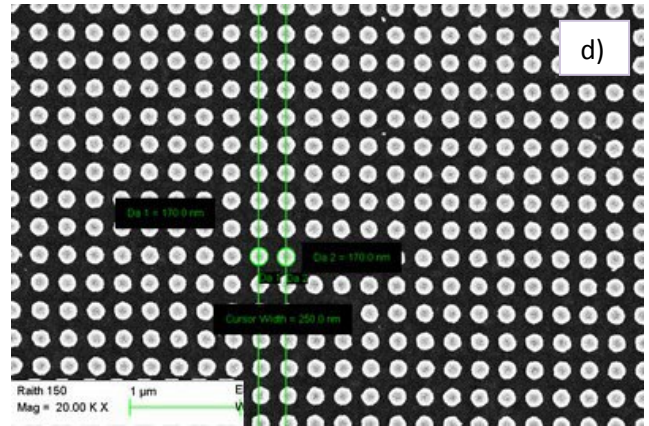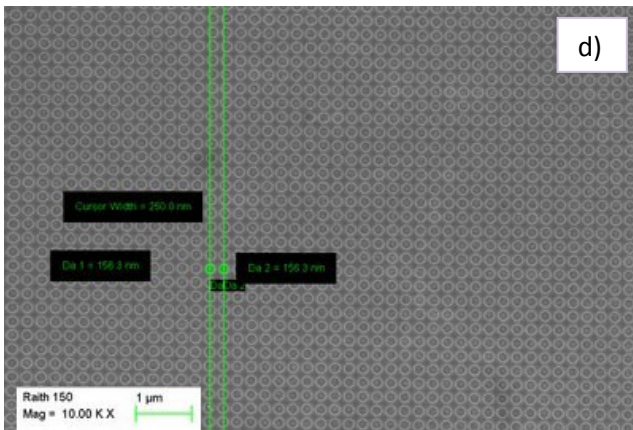
*Fig 6.36: SEM images of the PC pattern consisting of a **Square based arrangement of triangles with d=200nm, A=225nm, s= 25nm** on an area of 200 µm x 200 µm (a) Air triangles arranged into the ZEP matrix before thermal evaporation at magnification 10 KX; (b,c) gold-based periodic SERS substrate after thermal evaporation of Au (60nm) at different magnifications, 15 and 30KX, respectively; (d) Air triangles arranged into the ZEP matrix before e-beam evaporation at magnification 10 KX; (e)gold-based periodic SERS substrate after e-beam evaporation of Cr/Au (2nm/60nm) at magnification 20 KX.*
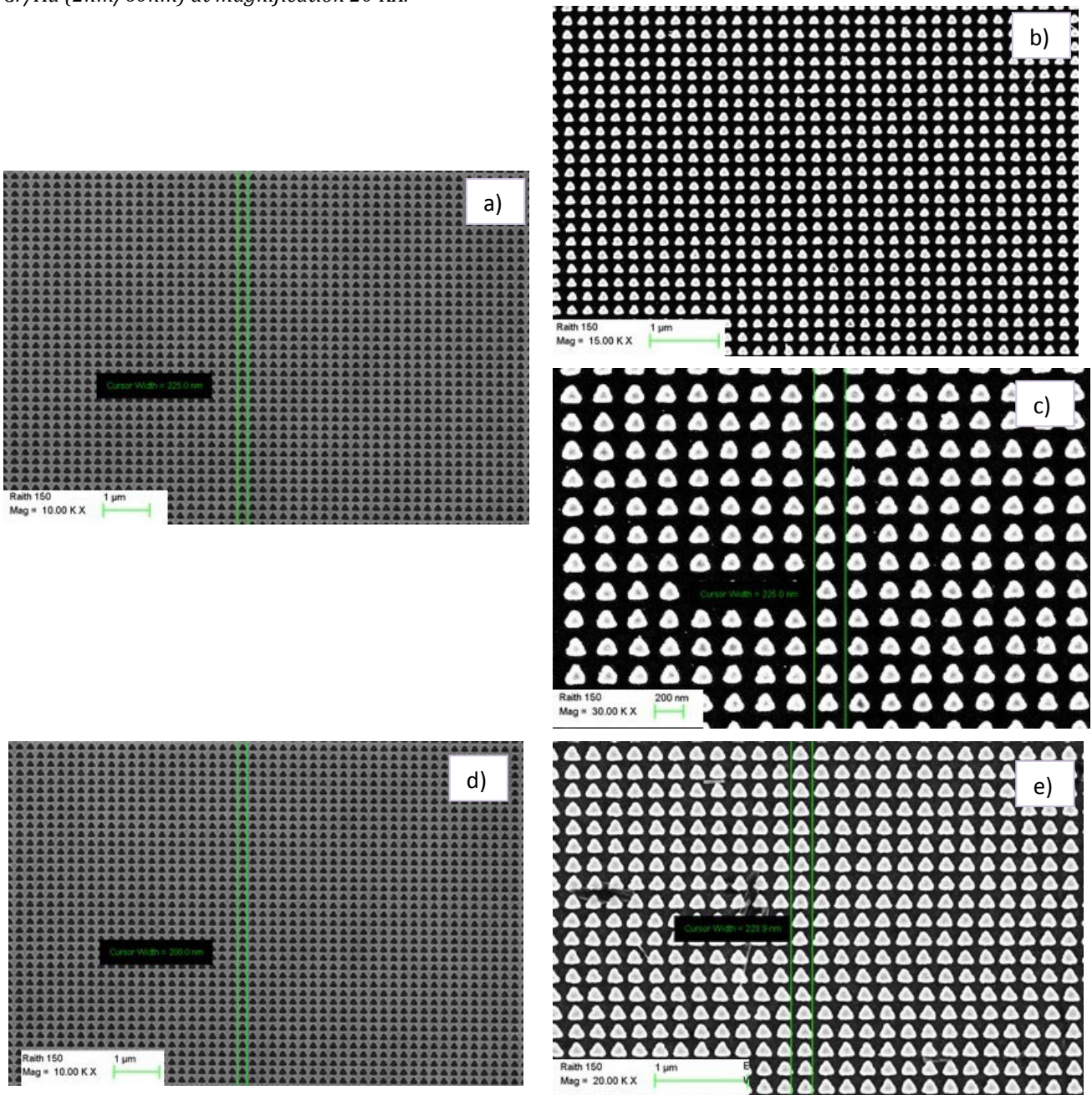
*Fig 6.37: SEM images of the PC pattern consisting of a **Square based arrangement of triangles with d=200nm, A=250nm, s=50nm** on an area of 200 µm x 200 µm (a) Air triangles arranged into the ZEP matrix before evaporation at magnification 20 KX; (b) gold-based periodic SERS substrate after thermal evaporation of Au (60nm) at magnification 30KX; (c) Air triangles arranged into the ZEP matrix before e-beam evaporation at magnification 10 KX; (d) gold-based periodic SERS substrate after e-beam evaporation of Cr/Au (2nm/60nm) at magnifications 20 KX.*
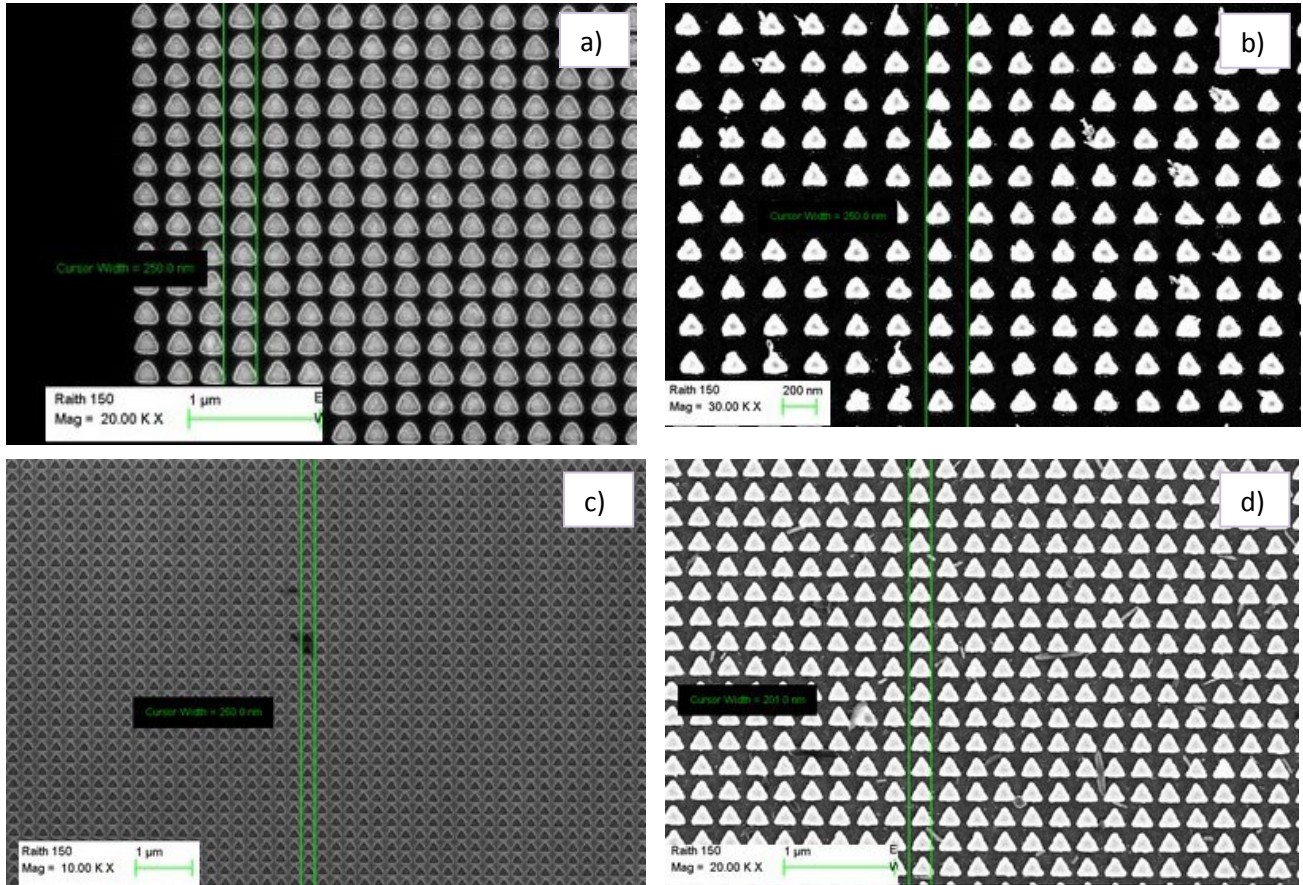
*Fig 6.38: SEM images of the PC pattern consisting of a **Square based arrangement of triangles with d=200nm, A=300nm, s=50nm** on an area of 200 µm x 200 µm (a) Air triangles arranged into the ZEP matrix before evaporation at magnification 20 KX; (b,c) gold-based periodic SERS substrate after thermal evaporation of Au (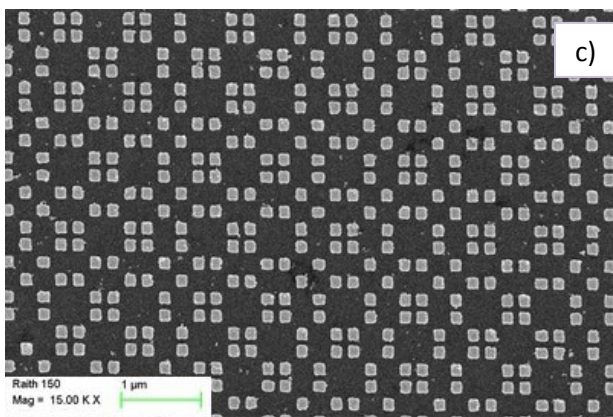60nm) at different magnifications, 10 and 30KX, respectively; (d) Air triangles arranged into the ZEP matrix before evaporation at magnification 20 KX; (e,f) gold-based periodic SERS substrate after e-beam evaporation of Cr/Au (2nm/60nm) at different magnifications, 5 and 20KX, respectively.*

c)

e)

d)

f)
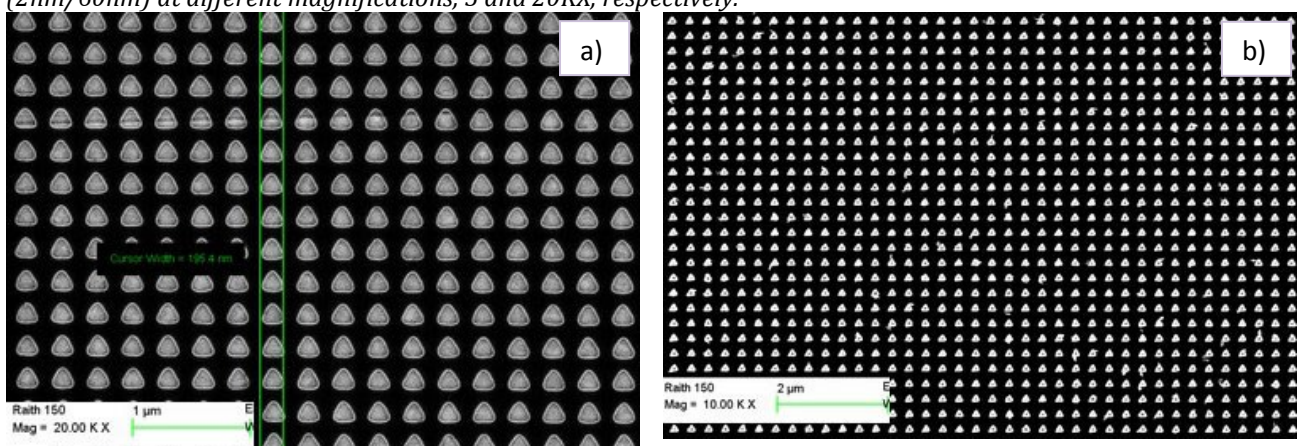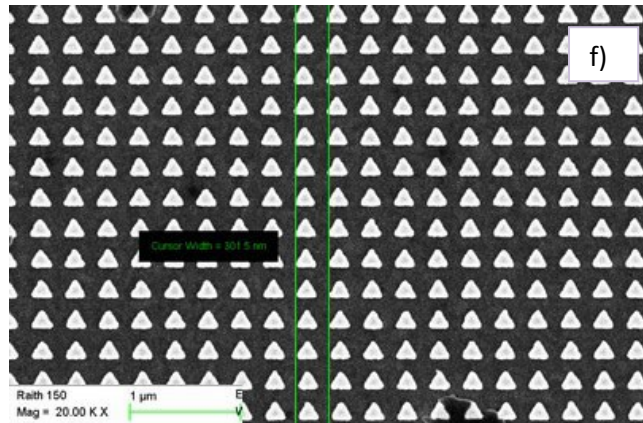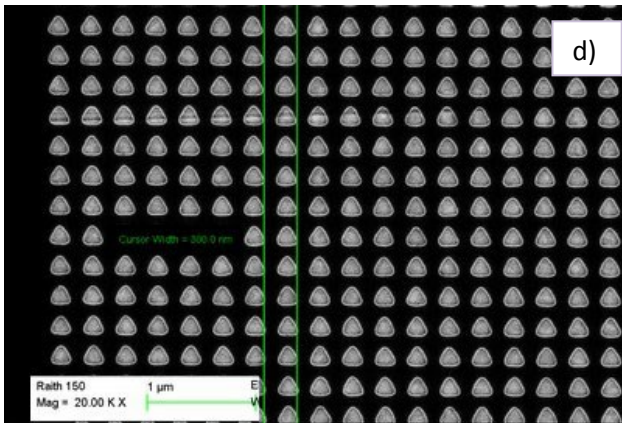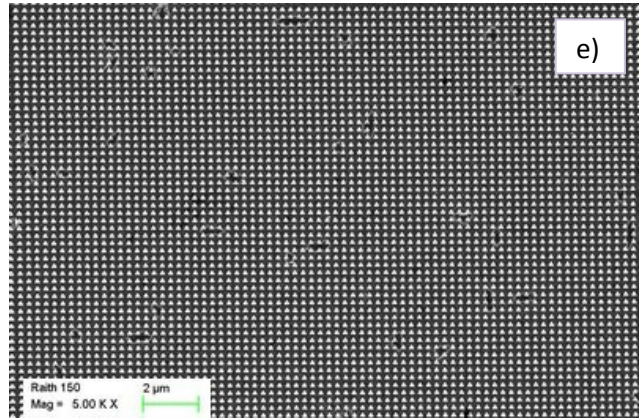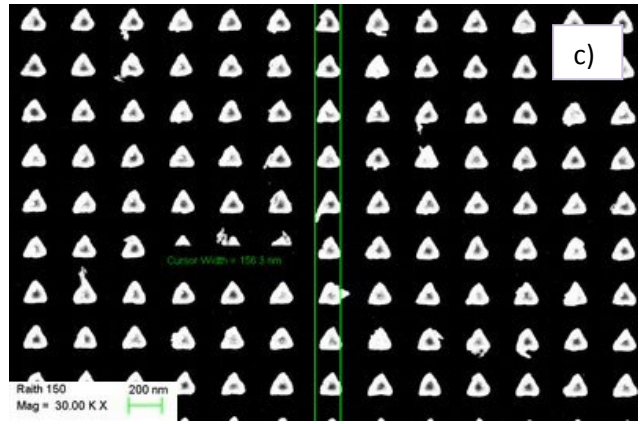
*Fig 6.39: SEM images of the PC pattern consisting of a **Square based arrangement of triangles with d=200nm, A=500nm, s= 300nm** on an area of 200 μm x 200 μm (a) Air triangles arranged into the ZEP matrix before thermal evaporation at magnification 20 KX; (b,c) gold-based periodic SERS substrate after thermal evaporation of Au (60nm) at different magnifications, 2.5 and 30KX, respectively.*
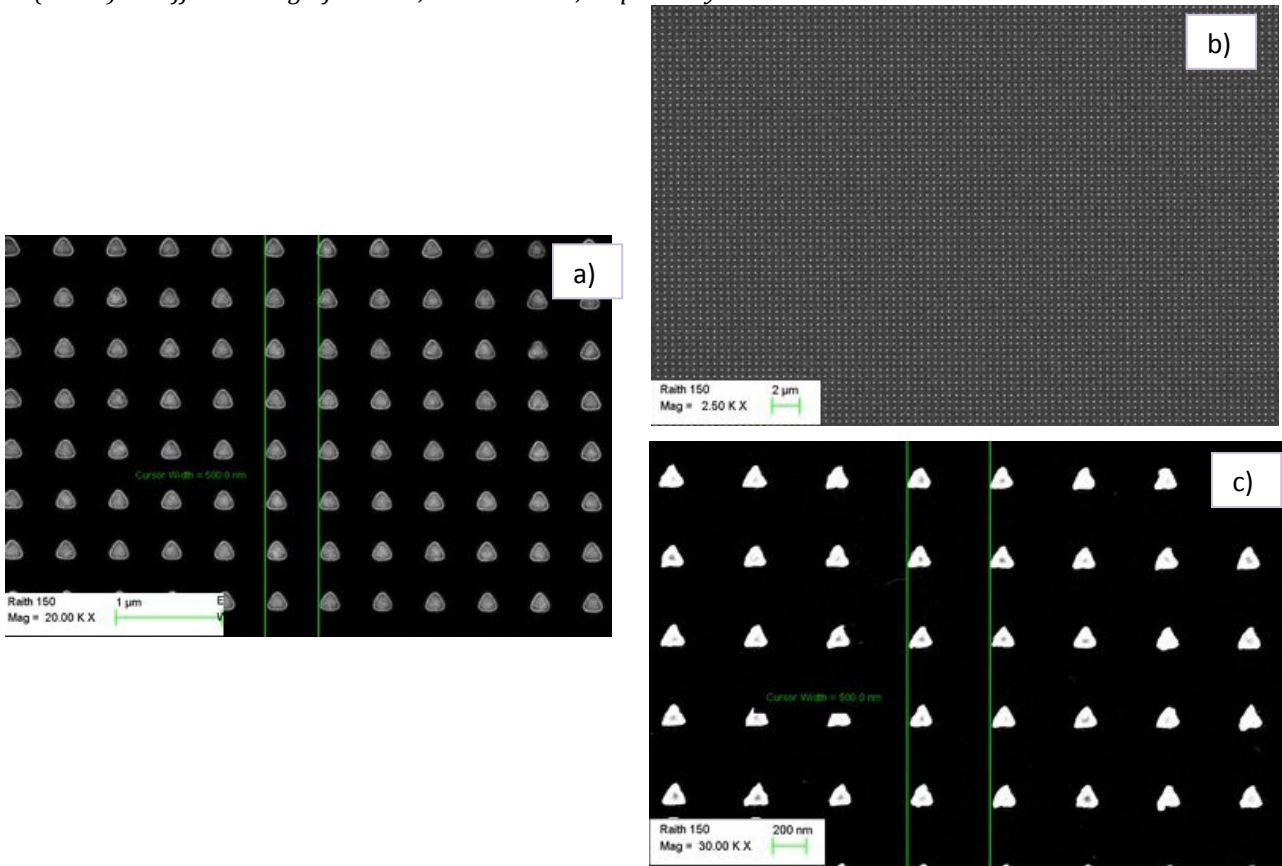
*Fig 6.40: SEM images of the PC pattern consisting of a **Triangular based arrangement of circles with d=100nm, A=150nm, s= 50nm** on an area of 200 μm x 200 μm (a) Air rods arranged into the ZEP matrix before thermal evaporation at magnification 15 KX; (b) gold-based periodic SERS substrate after thermal evaporation of Au (60nm) at magnifications 30KX.*

*Fig 6.41: SEM images of the PC pattern consisting of a **Triangular based arrangement of circles with d=175nm, A=250nm, s= 75nm** on an area of 200 μm x 200 μm (a) Air rods arranged into the ZEP matrix before e-beam evaporation at magnification 10 KX; (b,c) gold-based periodic SERS substrate after e-beam evaporation of Cr/Au (2nm/60nm) at different magnifications, 10 and 20KX, respectively.*
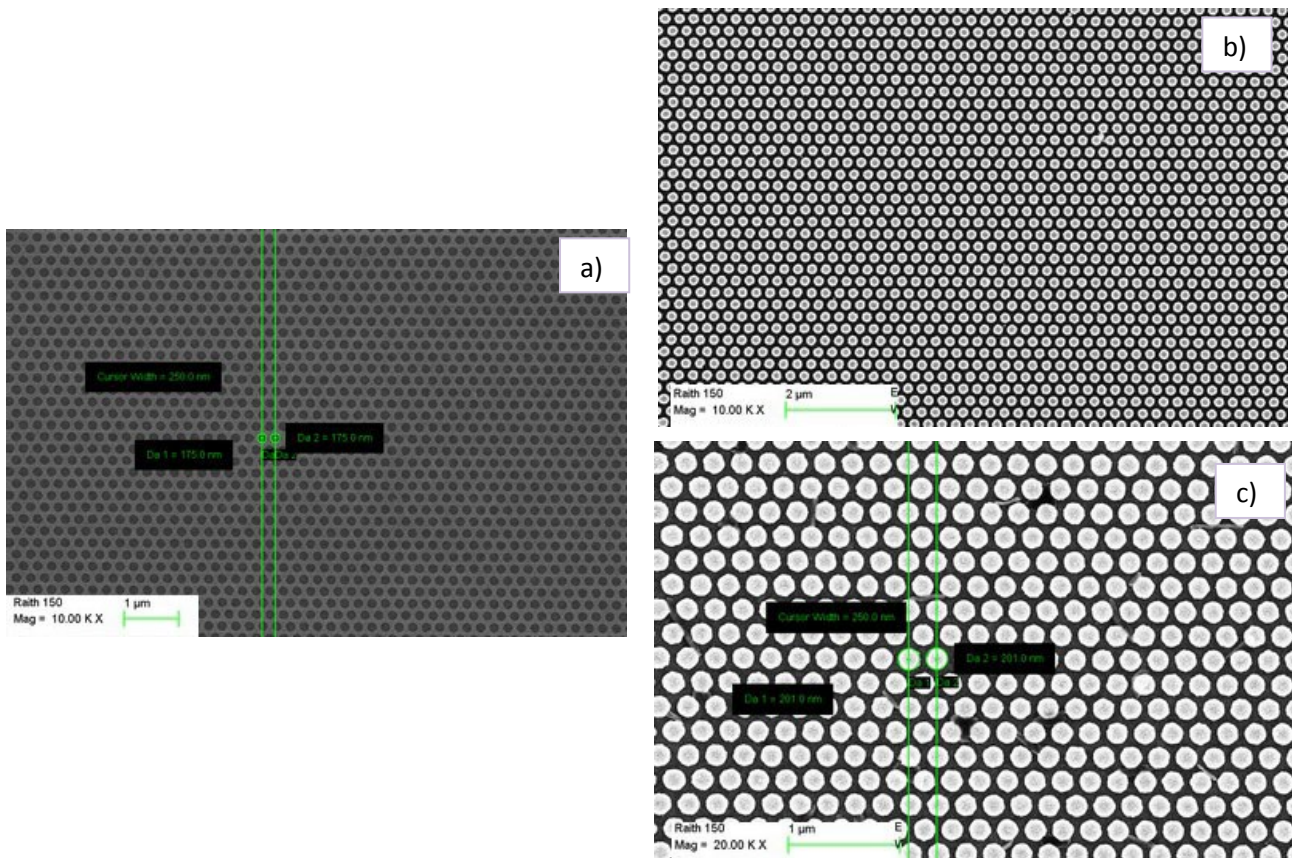
In Table *Tab. 6.2* aperiodic Photonic Quasi-Crystals in a Thue Morse arrangement of circles and squares, and in a 8-fold arrangement of circles, with different sizes (diameter or side size d), lattice constant (G) and interparticle separations (minimum distance between the two closest rods-s) are reported. As in the previous case of periodic photonic structures, SEM and metrological analysis of the aperiodic nanostructures summarized in *Table 6.2*, realized firstly in polymer and then in metal deposited either thermally or e-beam, are shown in *Fig. 6.41 - 6.53.* In each Fig. a comparison between different deposition methods is reported together with the starting structure made of air rods holes nanopatterned in polymer.

APERIODIC STRUCTURES					
SHAPE	ARRANGEMENT	SIZE (d)	Lattice Constant (G)	Minimum Interparticle Separation (s)	FILLING FACTOR (*FF*)
Square	Thue-Morse	100nm	144nm	44nm	0,26
Square	Thue-Morse	150nm	216nm	66nm	0.26
Square	Thue-Morse	185nm	264nm	79nm	0,27
Square	Thue-Morse	200nm	288nm	88nm	0,26
Square	Thue-Morse	250nm	360nm	110nm	0.26
Square	Thue-Morse	500nm	710nm	210nm	0.26
Cylinder	Thue-Morse	100nm	144nm	44nm	0.19
Cylinder	Thue-Morse	150nm	216nm	66nm	0.19
Cylinder	Thue-Morse	250nm	360nm	110nm	0.20
Cylinder	8-Fold	100nm	/	25nm	0.14
Cylinder	8-Fold	125nm	/	30nm	0,18
Cylinder	8-Fold	150nm	/	35nm	0.16
Cylinder	8-Fold	250nm	/	70nm	0.18

Tab. 6.2: Summary of PQCs realized

*Fig 6.42: SEM images of the PQC pattern consisting of a **Thue Morse arrangement of squares with d=100nm, G=144nm** on an area of 37 µm x 37 µm. (a) Air squares arranged into the ZEP matrix before thermal evaporation; (b,c,d) gold-based aperiodic SERS substrate after thermal evaporation Au (60nm) with measured d=100nm, s=44nm at different magnifications, 5, 10 and 30 X, respectively.*
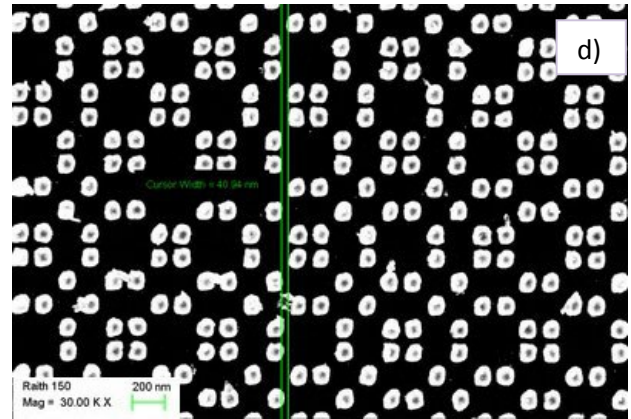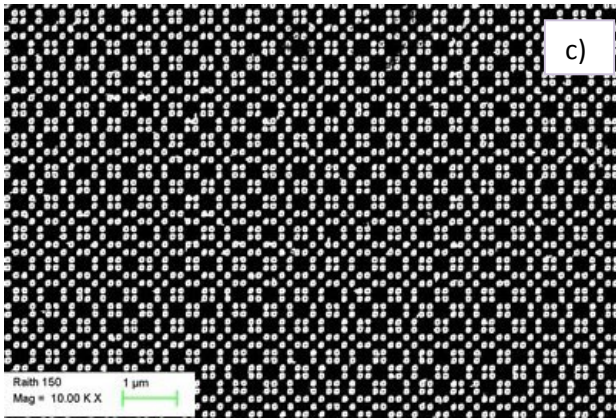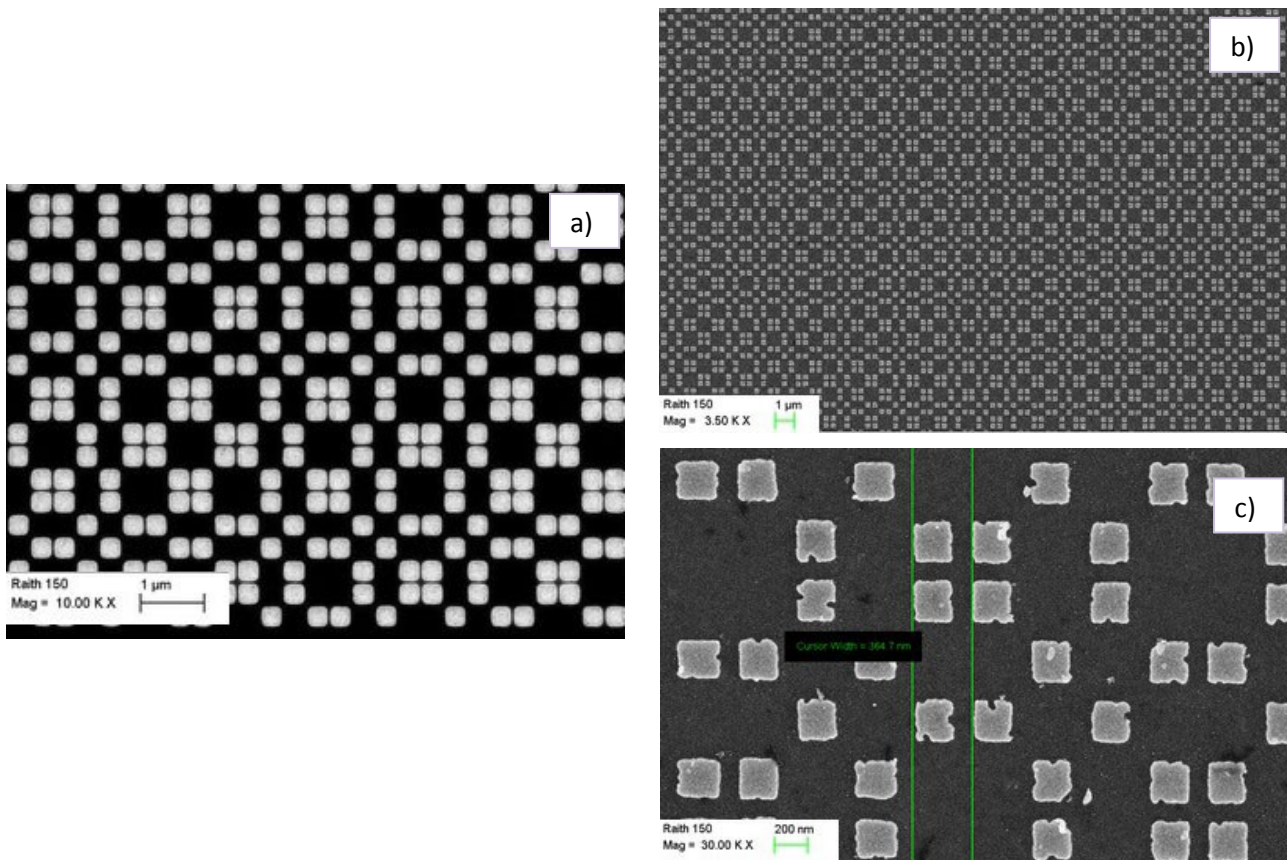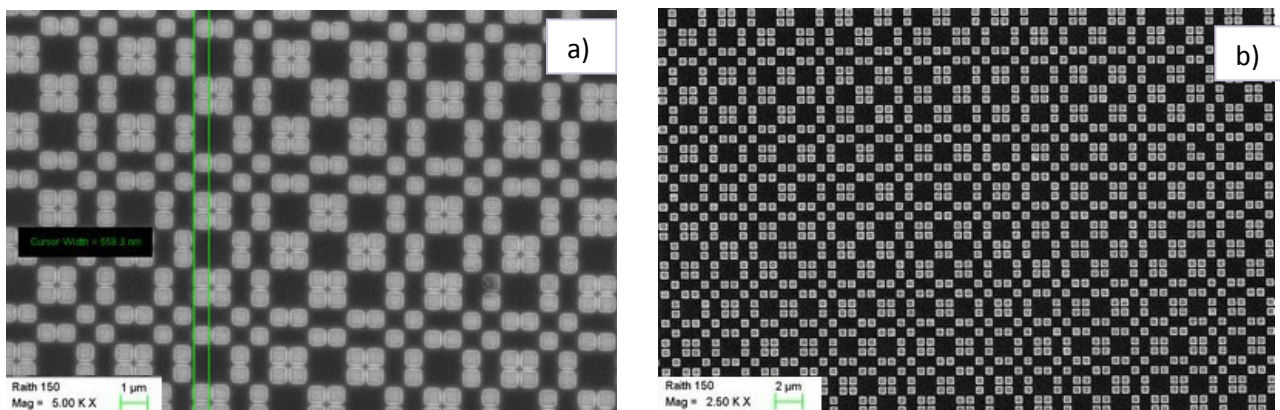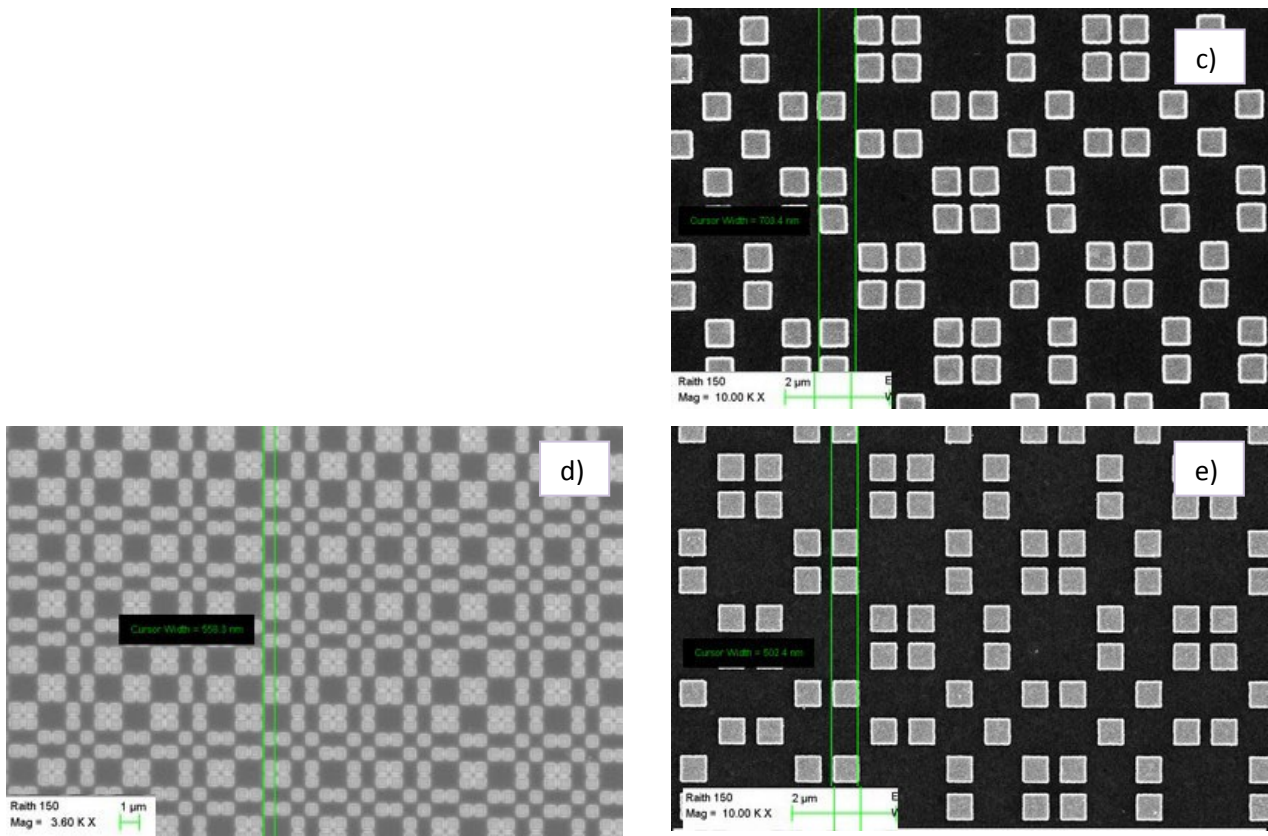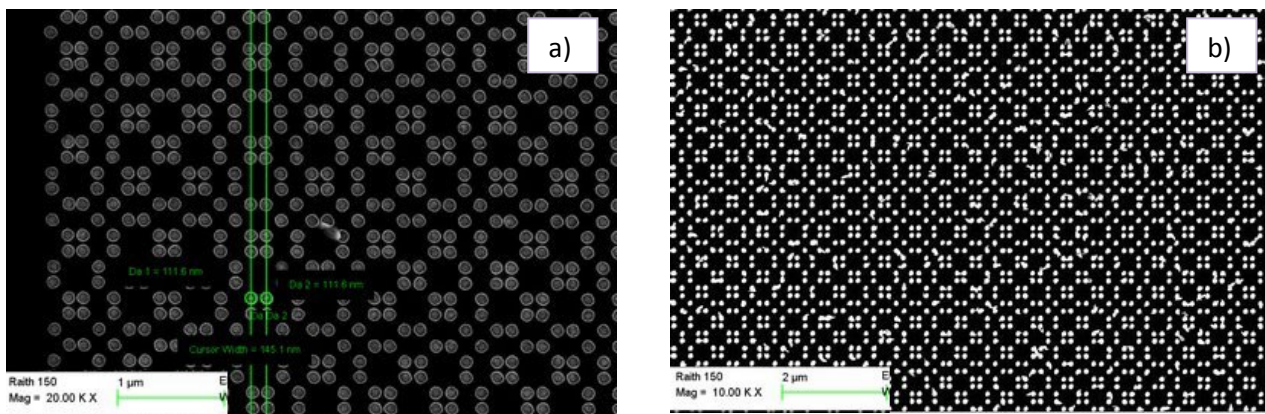
Fig 6.43: SEM images of the PQC pattern consisting of a **Thue Morse arrangement of squares with d=150nm, A=216nm** *on an area of 55 μm x 55 μm. (a) Air squares arranged into the ZEP matrix before thermal evaporation; (b,c,d) gold-based aperiodic SERS substrate after thermal evaporation Au (60nm) with measured d=152nm, s=64nm at different magnifications, 2.5, 15 and 30 X, respectively.*
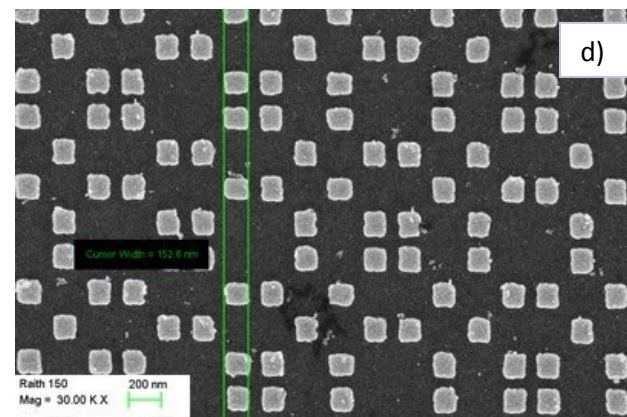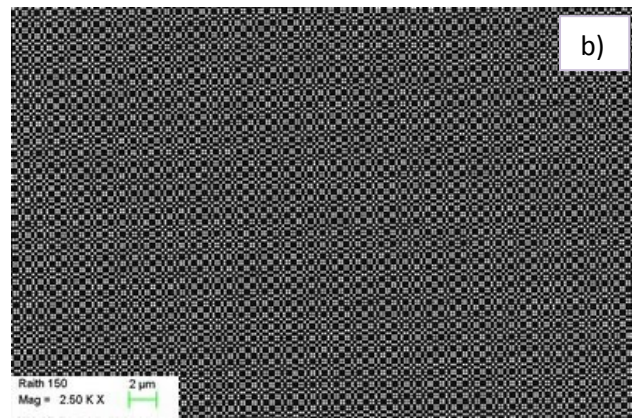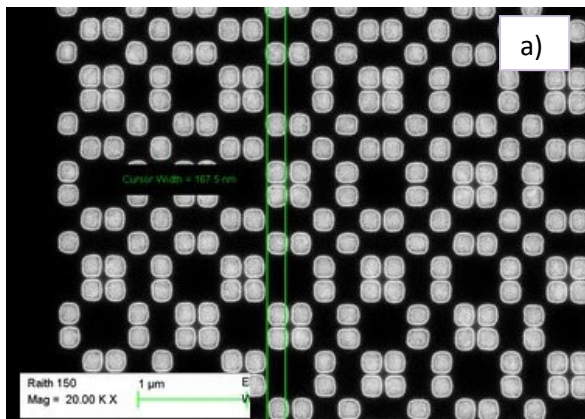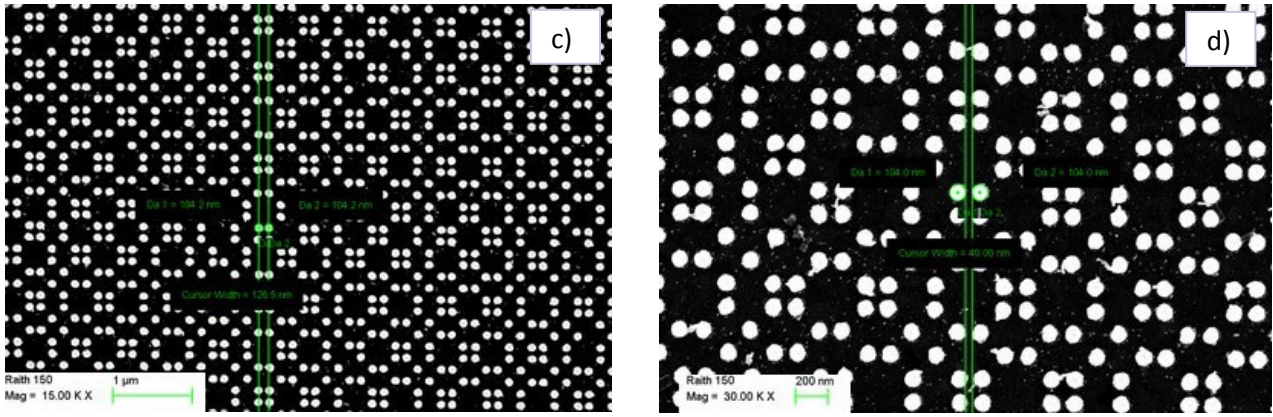
*Fig 6.44: SEM images of the PQC pattern consisting of a **Thue Morse arrangement of squares with d=185nm, A=264nm** on an area of 90 µm x 90 µm. (a) Air squares arranged into the ZEP matrix before thermal evaporation; (b,c) gold-based aperiodic SERS substrate after thermal evaporation Au (60nm) with measured d=178.8nm at different magnifications 15 and 30 X, respectively; (d) Air squares arranged into the ZEP matrix before e-beam evaporation; (e,f) gold-based aperiodic SERS substrate after e-beam evaporation of Cr/Au (2nm/60nm) with measured d=184.2 G=273.5 at magnifications 20 K X.*
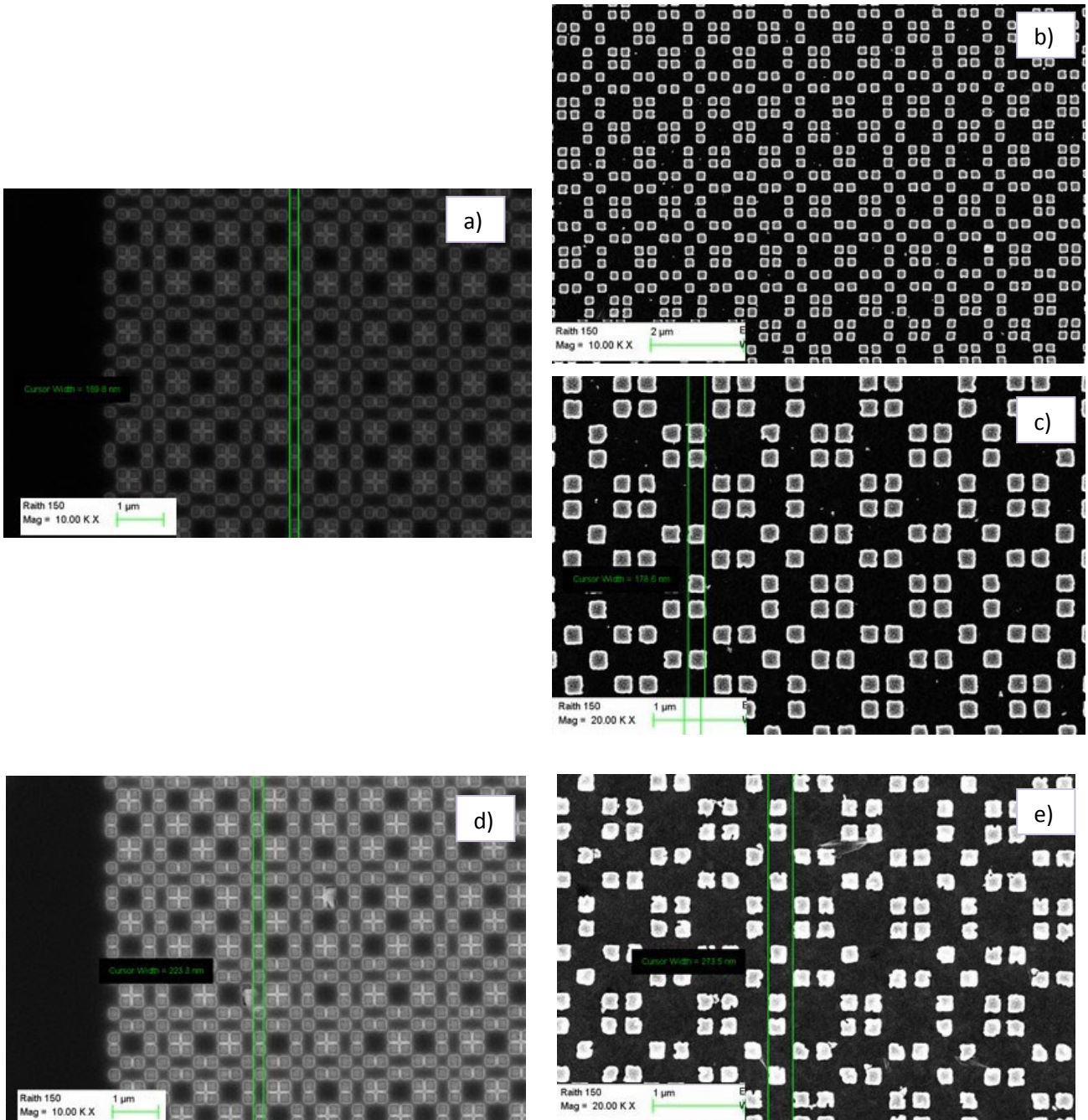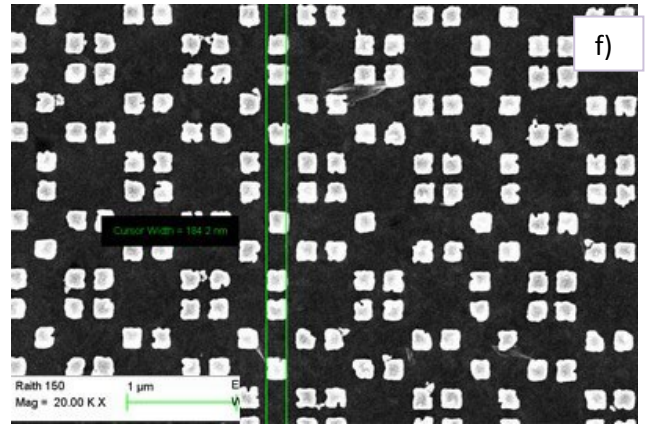
*Fig 6.45: SEM images of the PQC pattern consisting of a **Thue Morse arrangement of squares with d=200nm, A=288nm** on an area of 74 µm x 74 µm. (a) Air squares arranged into the ZEP matrix before thermal evaporation; (b,c,d) gold-based aperiodic SERS substrate after thermal evaporation Au (60nm) with measured d=200nm, s=75nm at different magnifications, 5 and 23 KX, respectively.*
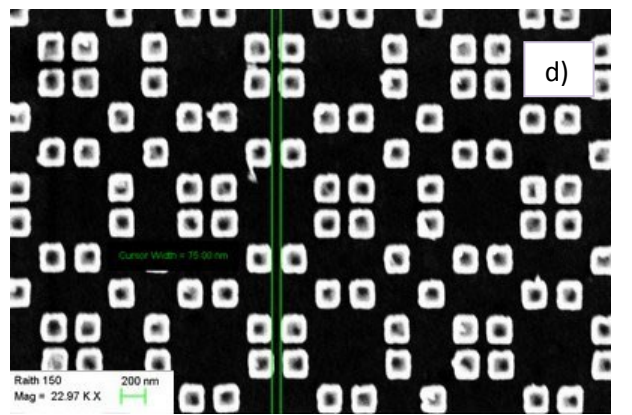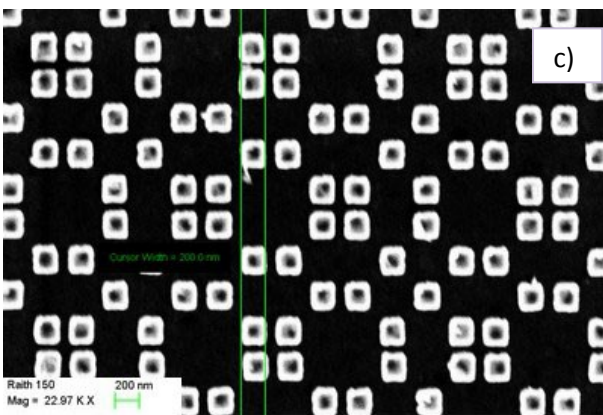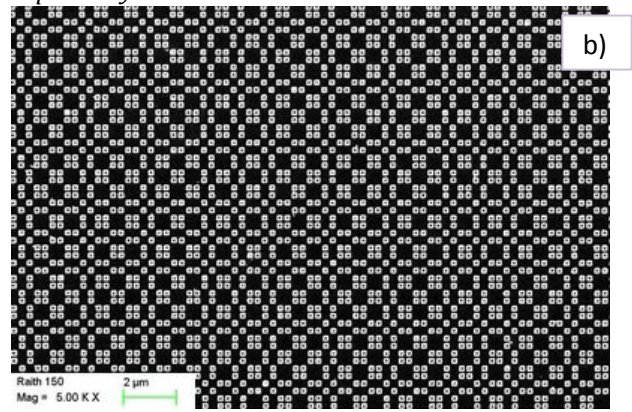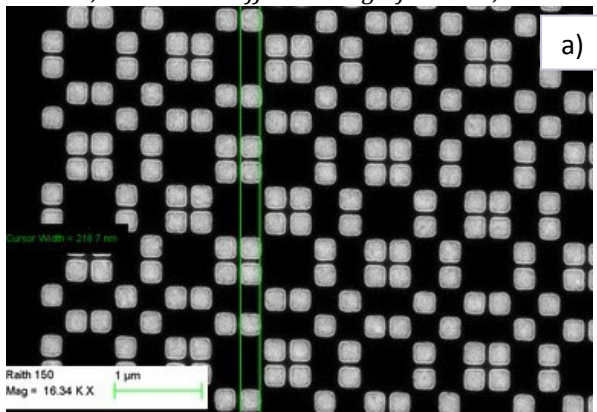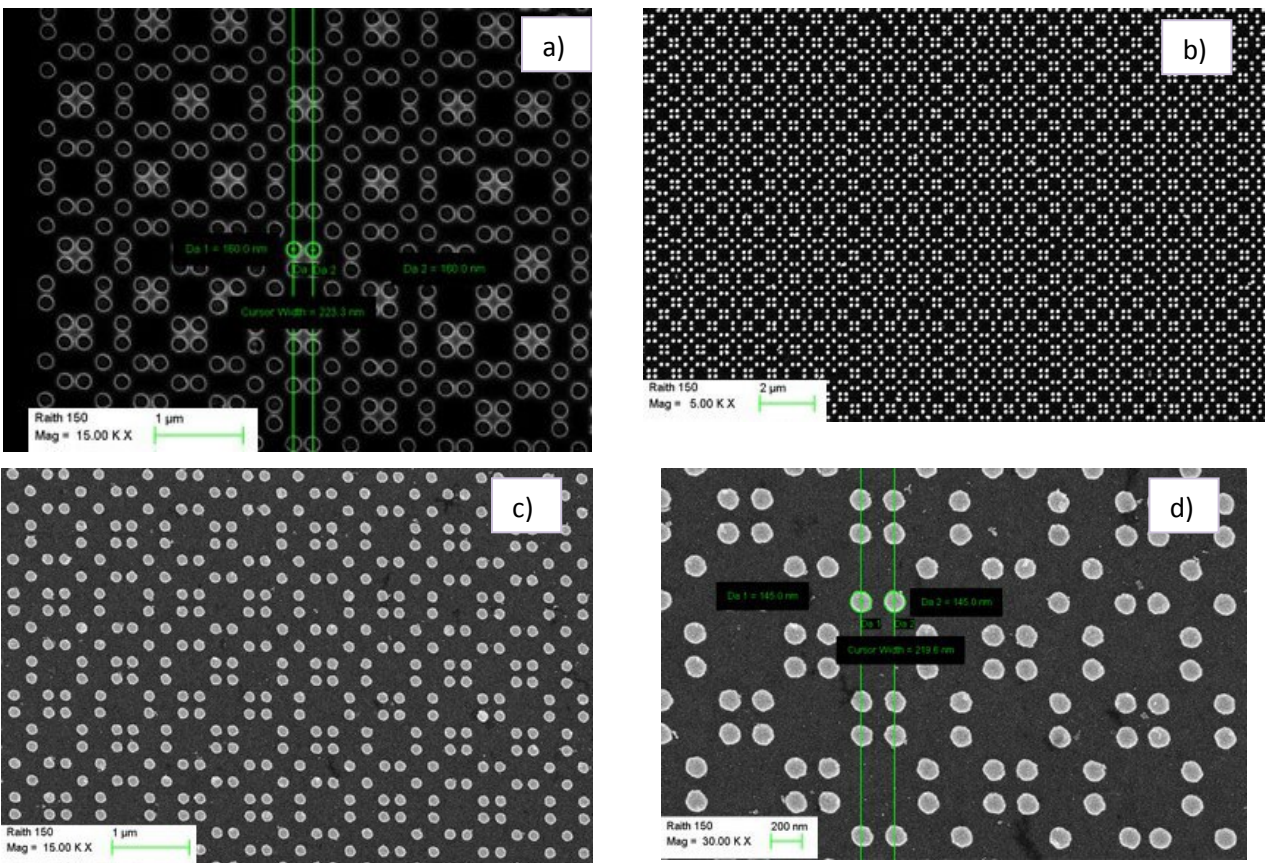
*Fig 6.46: SEM images of the PQC pattern consisting of a **Thue Morse arrangement of squares with d=250nm, A=360nm** on an area of 92 μm x 92 μm. (a) Air squares arranged into the ZEP matrix before thermal evaporation; (b,c) gold-based aperiodic SERS substrate after thermal evaporation Au (60nm) with measured G=364.7nm at different magnifications 3.5 and 30 X, respectively.*
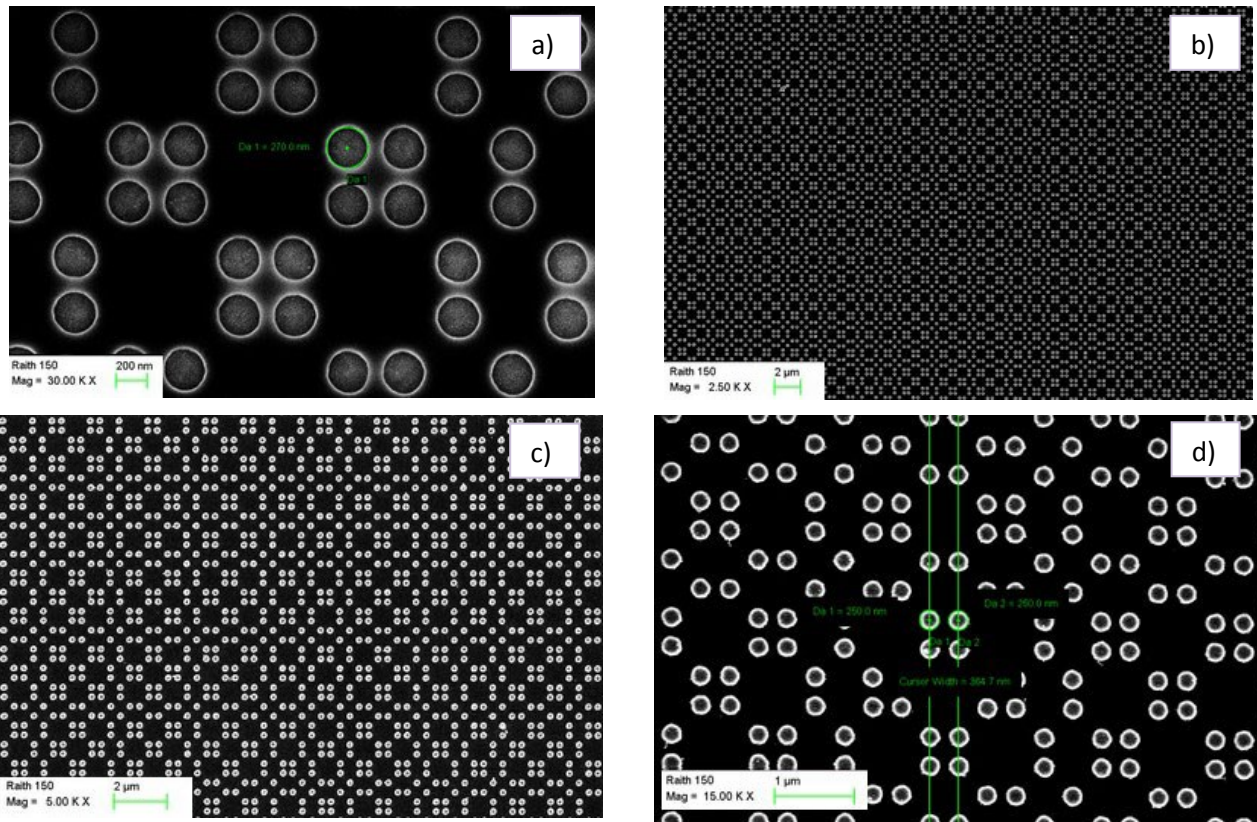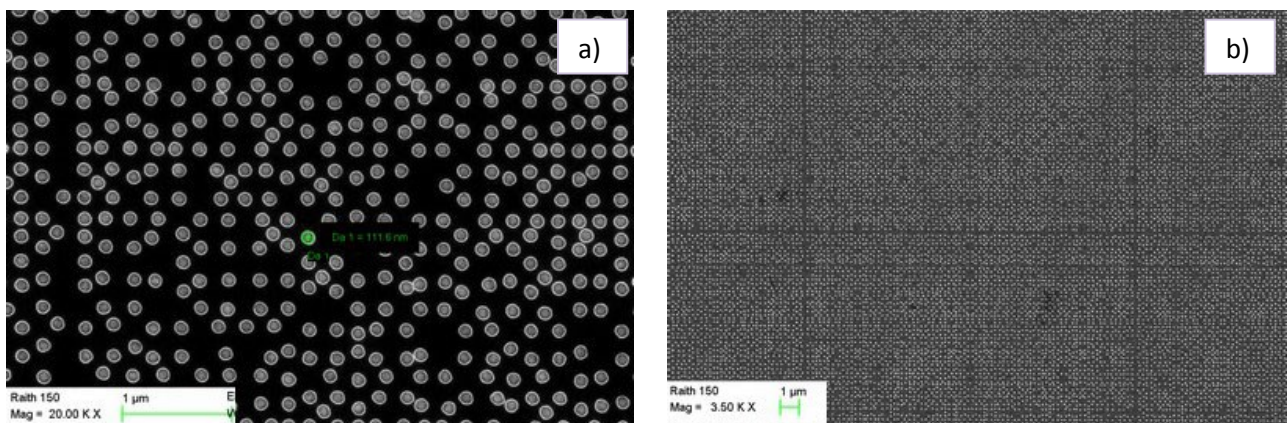

*Fig 6.46: SEM images of the PQC pattern consisting of a **Thue Morse arrangement of squares with d=500nm, A=710nm** on an area of 950 μm x 950 μm. (a) Air squares arranged into the ZEP matrix before thermal evaporation; (b,c) gold-based aperiodic SERS substrate after thermal evaporation Au (60nm) with measured G=708.4nm at different magnifications 2.5 and 10 X, respectively; (d) Air squ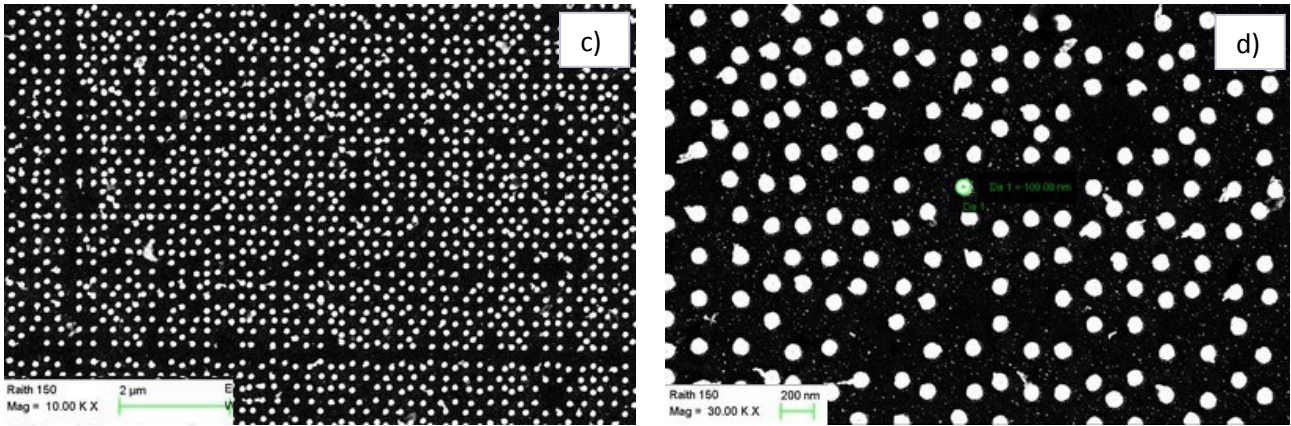ares arranged into the ZEP matrix before e-beam evaporation; (e) gold-based aperiodic SERS substrate after e-beam evaporation of Cr/Au (2nm/60nm) with measured d=502.4nm at magnifications 10 KX*

*Fig 6.48: SEM images of the PQC pattern consisting of a **Thue Morse arrangement of circles with d=100nm, A=144nm** on an area of 150 μm x 150 μm. (a) Air rods arranged into the ZEP matrix before thermal evaporation; (b,c,d) gold-based aperiodic SERS substrate after thermal evaporation Au (60nm) with measured d=104nm, G=136nm, s=40nm at different magnifications, 10,15 and 30 KX, respectively.*

Fig 6.49: SEM images of the PQC pattern consisting of a **Thue Morse arrangement of circles with d=150nm, A=216nm** on an area of 160 μm x 160 μm. (a) Air rods arranged into the ZEP matrix before thermal evaporation; (b,c,d) gold-based aperiodic SERS substrate after thermal evaporation Au (60nm) with measured d=145nm, G=219nm at different magnifications 5, 15 and 30 KX, respectively.
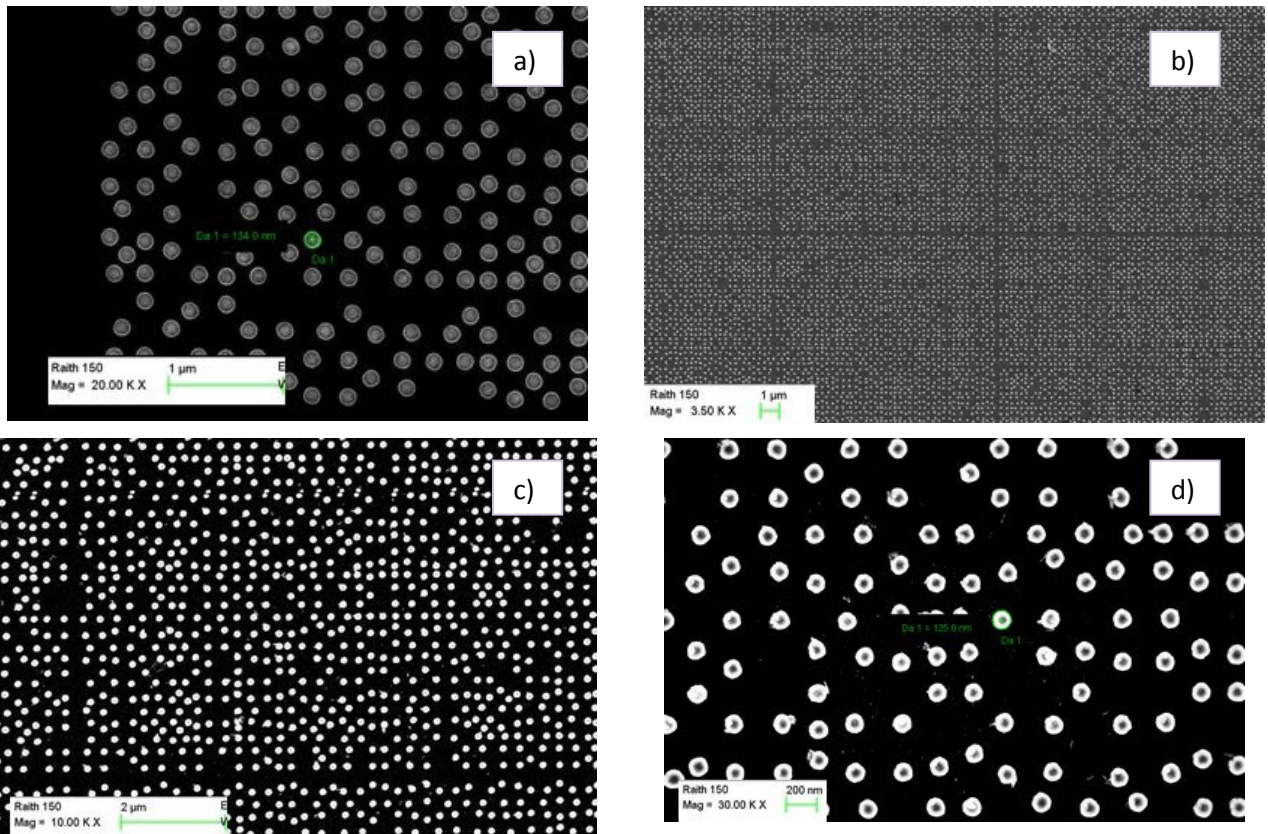
Fig 6.50: SEM images of the PQC pattern consisting of a **Thue Morse arrangement of circles with d=250nm, A=360nm** on an area of 130 μm x 130 μm. (a) Air rods arranged into the ZEP matrix before thermal evaporation; (b,c,d) gold-based aperiodic SERS substrate after thermal evaporation Au (60nm) with measured d=250nm, G=364.7nm at different magnifications 2.5, 5 and 15 KX, respectively.
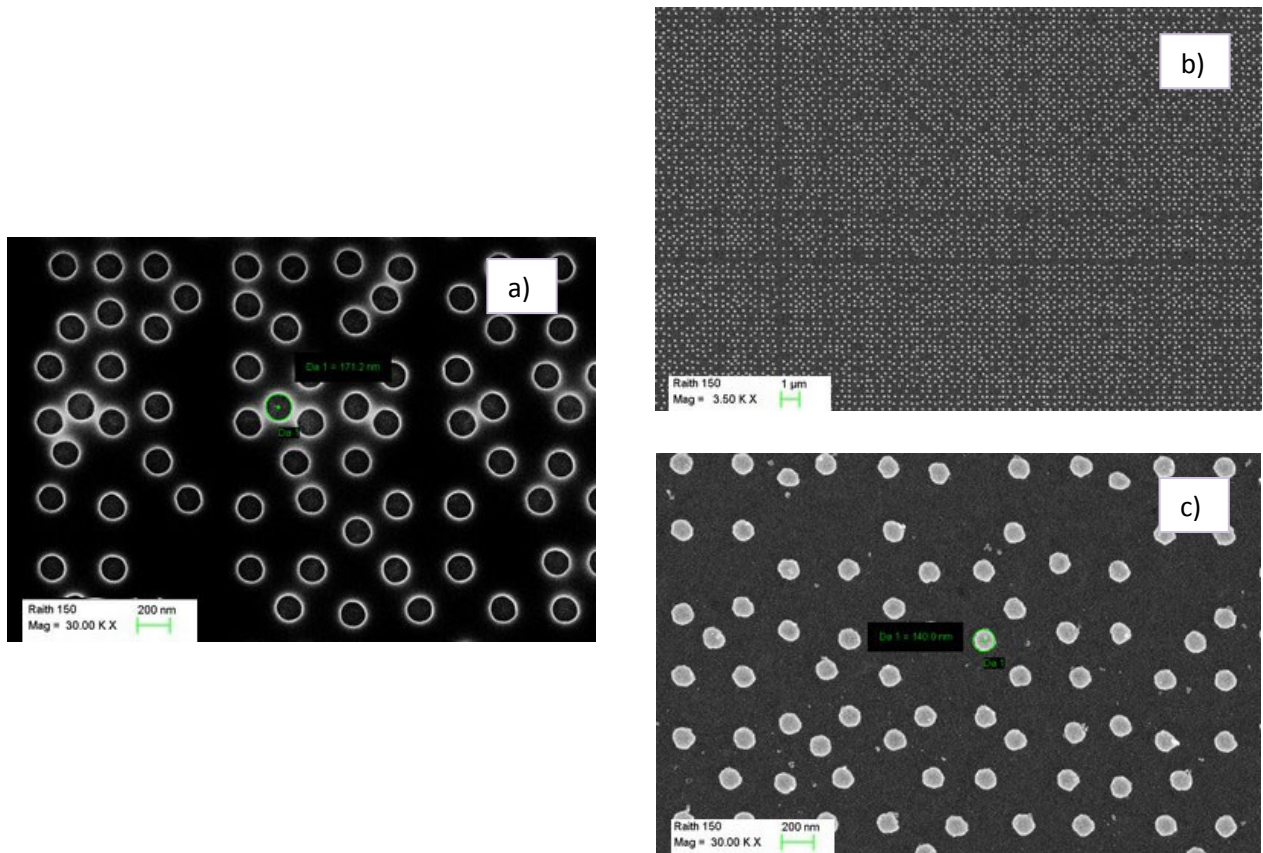

Fig 6.51: SEM images of the PQC pattern consisting of a **8-fold arrangement of circles with d=100nm** on an area of 125 μm x 125 μm. (a) Air rods arranged into the ZEP matrix before thermal evaporation; (b,c,d) gold-based aperiodic SERS substrate after thermal evaporation Au (60nm) with measured d=100nm at different magnifications 3.5, 10 and 30 KX, respectively.
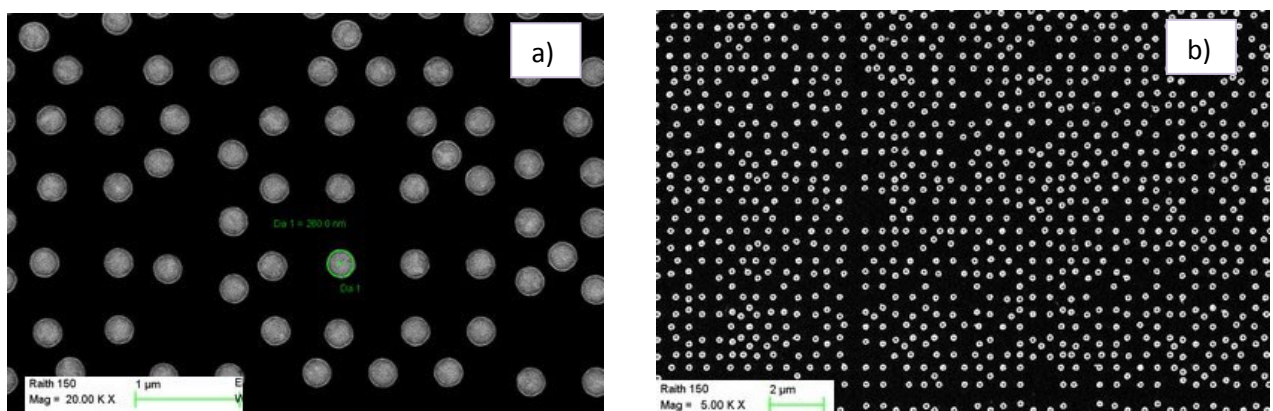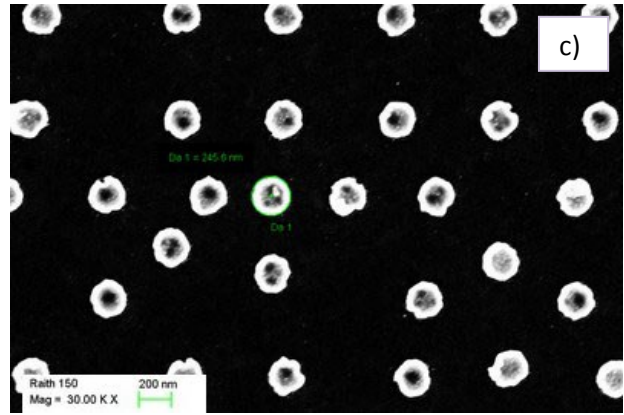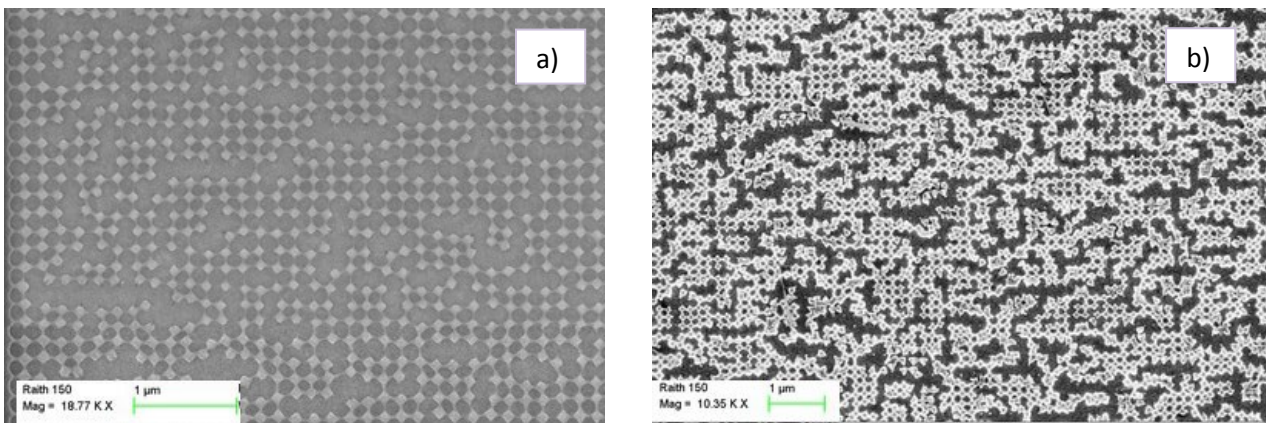
*Fig 6.52: SEM images of the PQC pattern consisting of a **8-fold arrangement of circles with d=125nm** on an area of 155 µm x 155 µm. (a) Air rods arranged into the ZEP matrix before thermal evaporation; (b,c,d) gold-based aperiodic SERS substrate after thermal evaporation Au (60nm) with measured d=125nm at different magnifications 3.5, 10 and 30 KX, respectively.*

*Fig 6.53: SEM images of the PQC pattern consisting of a **8-fold arrangement of circles with d=150nm** on an area of 185 μm x 185 μm. (a) Air rods arranged into the ZEP matrix before thermal evaporation; (b,c,d) gold-based aperiodic SERS substrate after thermal evaporation Au (60nm) with measured d=140nm at different magnifications 3.5 and 30 KX, respectively*

*Fig 6.53: SEM images of the PQC pattern consisting of a **8-fold arrangement of circles with d=250nm** on an area of 300 μm x 300 μm. (a) Air rods arranged into the ZEP matrix before thermal evaporation; (b,c,d) gold-based aperiodic SERS substrate after thermal evaporation Au (60nm) with measured d=245nm at different magnifications 3.5 and 30 KX, respectively.*

During the optimization of the fabrication protocol we have also found some problems in the procedures. As an example, *Fig. 6.54* shows how the overdose effect on polymeric structures could propagates onto the metal counterpart seriously compromising the final result.

*Fig. 6.54: SEM images of the PC pattern consisting of a **Square based arrangement of circles with d=180nm, A=200nm, s=20nm** on an area of 200 μm x 200 μm (a) Air rods arranged into the ZEP matrix before thermal evaporation at magnification 19 KX affected by a high overdose (Ad= 18 μC/cm²); (b) gold-based periodic SERS substrate after thermal evaporation Au (60nm) at magnification 11K X clearly showing the overdose effect.*

While, *Fig. 6.55* shows common errors that can occur during the lift-off process due to two different potential motivations: it can happen, as an example, that not all the resist is removed, so it remains a Gold layer attached on the surface (*Fig. 6.55 a*), or the Gold Layer isn't anchored to the glass/ITO surface, so during che lift-off process some nanoparticles could be missed (*Fig. 6.55 b*)
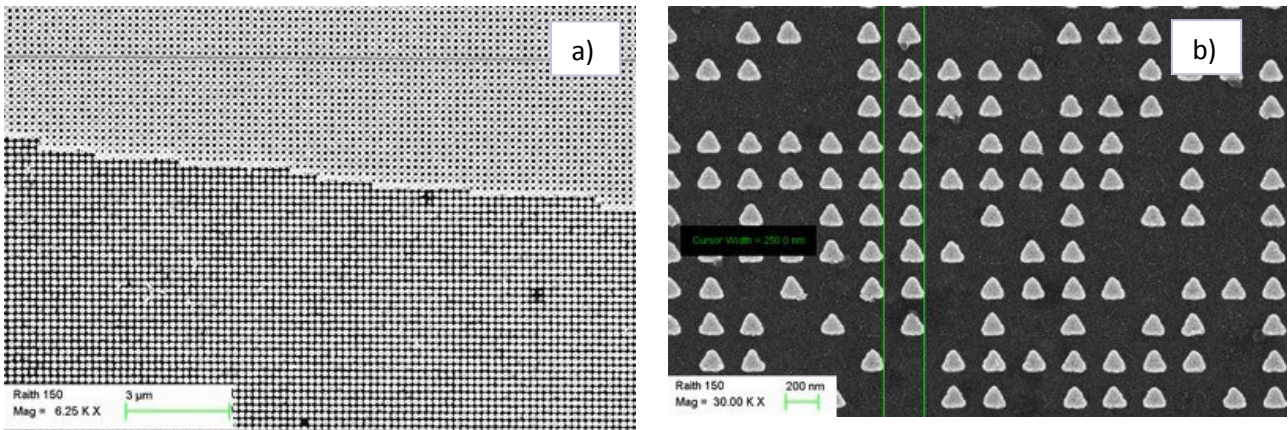
Fig. 6.55: SEM images of the PC pattern consisting of (a) gold-based periodic SERS substrate after thermal evaporation Au (60nm) showing a not completely removed Gold layer during the lift-off process; (b) gold-based periodic SERS substrate after thermal evaporation Au (60nm) showing some nanoparticles missing due to an error in the lift-off process

References

[1] ZEON CORPORATION Electronics Materials Division, **ZEP520A Technical Report**, ZEONREX® Electronic Chemicals

[2] Na Zhang, "*Literature Research Report for Lift-Off Method*"

Chapter 7: Optical & Raman characterizations

In this chapter we shall describe the optical characterization made on the realized engineered SERS substrates in term of Fast Fourier Diffraction (FFD) patterns, and the activation of the fabricated devices and the determination of the SERS enhancement factors through Raman measurements. We shall present SERS spectra of the analyzed samples and we shall discuss the way to evaluate the experimental G_{SERS}.

7.1   Optical characterizations

The studies of quasicrystalline structures have widened the existing concepts of wave diffraction and interference. The light propagating in a structured medium is scattered with the scattering intensity determined by the Fourier transform of a space-dependent function describing the optical response of the medium. Diffraction is the primary technique for examining the structures of solid materials, and the consequences of aperiodicity on diffraction patterns provide a challenge and an opportunity to gain a deeper understanding of both diffraction and of quasicrystal structures. It was performed a far field diffraction analysis (FFD) in order to better investigate the morphology of the fabricated nanostructures. By examining the laser diffraction patterns obtained from these structures, the effects of aperiodic order on the diffraction pattern was observed. This analysis allows a morphological characterization in reciprocal space where interesting properties related to nanopatterns can be obtained through the experimental determination of their Fourier spectrum. It should be emphasized that while the SEM allows a local analysis of the structure fabricated, the diffraction pattern obtained by FFD instead provides an information on the whole structure and on the regularity with which the elements are arranged in the metallic matrix. Furthermore, we should mention the difficulty (or the impossibility) to perform a similar SEM analysis especially in the case of quasi-periodic structures in which the relative distances between the various elements are not regular. Far field diffraction patterns of the experimental Thue-Morse structures have been measured and compared with the calculated theoretical Fourier spectra.

7.1.1 Far field diffraction analysis

Due to the connection between the diffraction pattern of a quasi-crystal and the order characterizing its geometry, and between pattern's rotational simmetry order and rotational order of a quasi-crystal itself, it appears clear, therefore, the importance of analysis of the pattern of diffraction for a direct morphological characterization of the quasicrystal, in addition to the one already carried out performing an analysis with the metrological S.E.M. Taking into account a diffraction grating in a vacuum, like the one shown in *Fig. 7.1.*
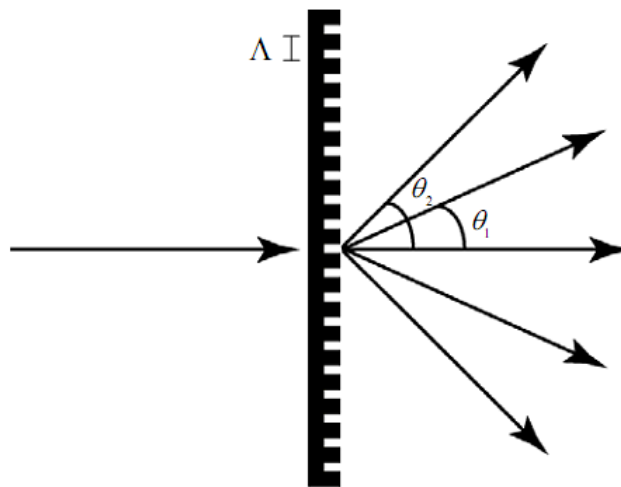
Fig. 7.1: Representation of maximum directions obtained by diffraction of light trough a lattice

The angles at which the diffraction maxima of order *n* are placed, are given by the relation:

$$\sin \theta_n = \sin \theta_i + n \frac{\lambda}{\Lambda} \tag{7.1}$$

where:

-   λ is the wavelength of the radiation used,
-   θ_i is the angle of inclination of the beam incidence with respect to the optical axis;
-   Λ is the grating pitch .

If we consider a lattice with a step equal to the radiation wavelength, from the relationship (7.1) we obtain that, the only observable order will be the order zero. In fact, for other orders the product $n\lambda/\Lambda$ will be greater than or equal to "1" and the equation does not admit solutions except for the first order to which correspond a 90° angle, and then in any case will not be observable.

For lattice steps less than the wavelength of the considered radiation, the same behaviour is repeated and different diffraction orders will not be observable. Concerning the realized quasicrystals, a good estimate of the pitch of the diffraction grating which they represent is given by the average distance between two successive columns along the x axis. It ranges in the case of the realized Thue - Morse quasicrystals from 144 to 710nm, while in the case of 8-fold quasicrystal, the minimum distance between adjacent elements ranges from 25nm to 115nm. Visible light has a wavelength in the range 400-700 nm. We understand, therefore, that visible radiation wavelength will always be less than the lattice constant of the realized 8-fold quasi-crystals and of most of the Thue Morse stuctures, and the related diffraction pattern could not be achievable.

To observe such patterns, in the specific case, we should need a light source in the far ultraviolet whose wavelength, $\lambda = 200$nm, remains minor than steps lattice. However, to observe the diffraction pattern similar of those of the realized nanostructures, other quasicrystals have been manufactured with the same geometry and in the same way of those object of this dissertation, but scaled to at least a factor of 4. In this way the average pitch of the Thue Morse quasicrystal will be equal to or greater than 500nm, while the average pitch of the 8-fold quasicrystal will be equal to or greater than 1132nm . In both cases, these structures can be analyzed with visible radiation. For the morphological analysis of the other quasicrystals manufactured, those with smaller lattice, it is still valid the analysis carried out by previously described SEM metrology (*Section 6.3*).

The far field diffraction patterns related to the nanostructures shown in Fig. 7.2 were acquired through the experimental set-up [1] reported in *Fig. 7.3*:
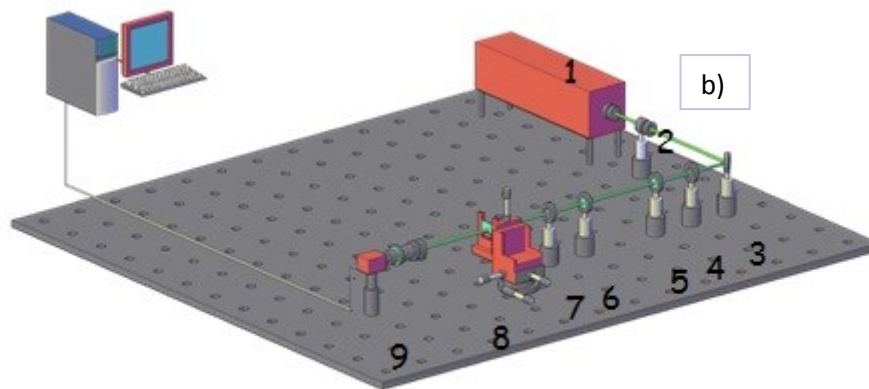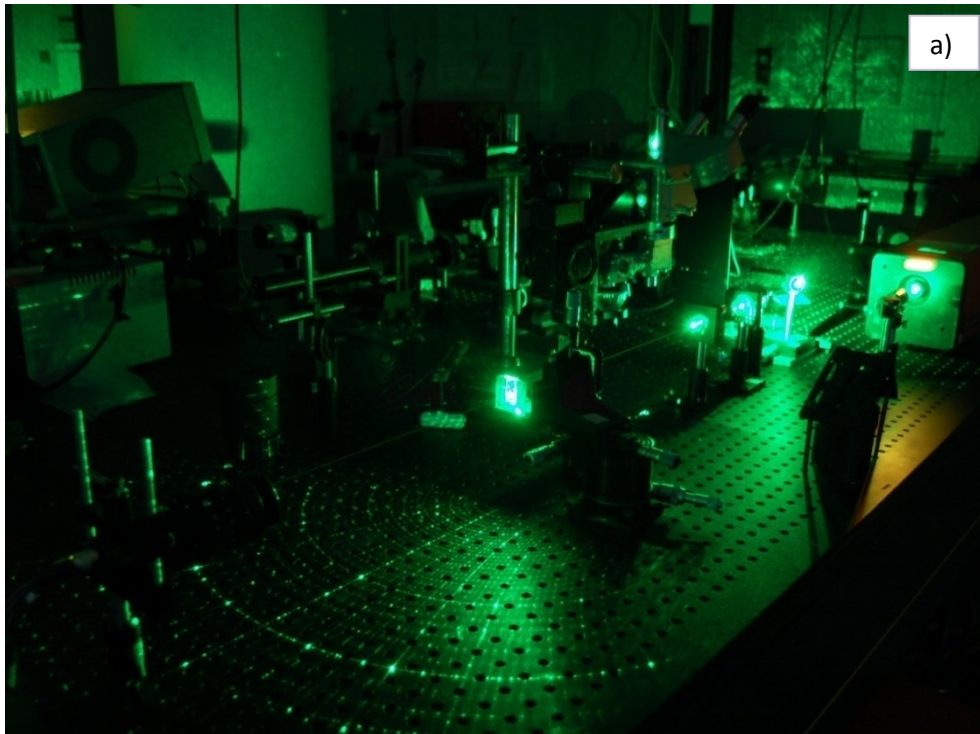
Fig. 7.2: a) Photograph of the experimental setup used at Cybernetic Institute of CNR (Pozzuoli); b) Schematization of the experimental set-up for spectra acquisition: 1) Laser Ar+; 2) attenuator; 3) mirror; 4) pinhole of 500mm; 5) biconvex lens with focal length f=88.3mm; 6) biconvex lens with f=25.4mm; 7) pin hole; 8) sample positioning system; 9) CCD camera and focusing lens system.

The laser source used is a *Coherent Innova 90* Ar+ laser with tunable wavelenght (λ={454, 457, 465, 476, 488, 496, 501, 514}nm), TEM_{00} emission mode and beam waist 4mm. In the shown experimental setup, the monochromatic light has been properly spatially filtered, through a system of pinhole – lenses – pinhole. Light is diffracted by a first pinhole making a zero-spatial order at the center, described by an Airy pattern. That pattern shows an eccellent spatial choerence and, therefore, represents a very good approximation of a planare wave. Then the diffraction patter is magnified with a suitable system of two confocal lenses placed between the two pinholes. The second pinhole allows to filter only the central spot related to the zero-

order spatial frequence and to cut the remaining orders. Such light spot impinges on the the entire structure and the generated Fourier spectra is collected in trasmission mode through a CCD camera. .

As already explained, Photonic Quasi-crystals shown in this section are the same of those already described in this dissertation (*Chapter 6*), but with bigger dimensions. In the next sub-sections will be shown SEM images and related FFD pattern of the represented structures.

Thue Morse Quasi-crystals

In next Figures (*Fig. 7.3, Fig. 7.4*) we show the Far Field Diffraction patterns of Thue-Morse quasi-crystals of circles with different diameter (*500nm, 750nm*). Analysis of the far field diffraction pattern of the fabricated structures reveals a lot of diffuse scattering, namely, the singular continuous part of the diffraction pattern. Singular continuous spectra usually appear in structures where the constructive interference that is responsible for the Bragg peaks is impaired by some randomness. Nonetheless, some long range order is still strong enough to prevent the peaks from becoming completely diffuse. Note that singular "peaks" can never be isolated – a property that further complicates their analysis.
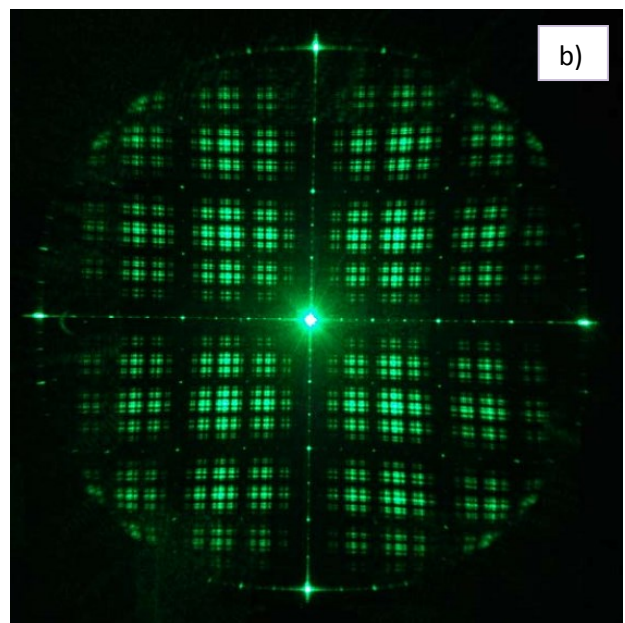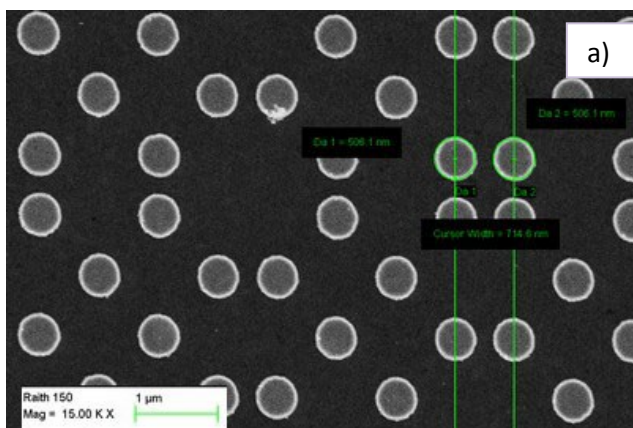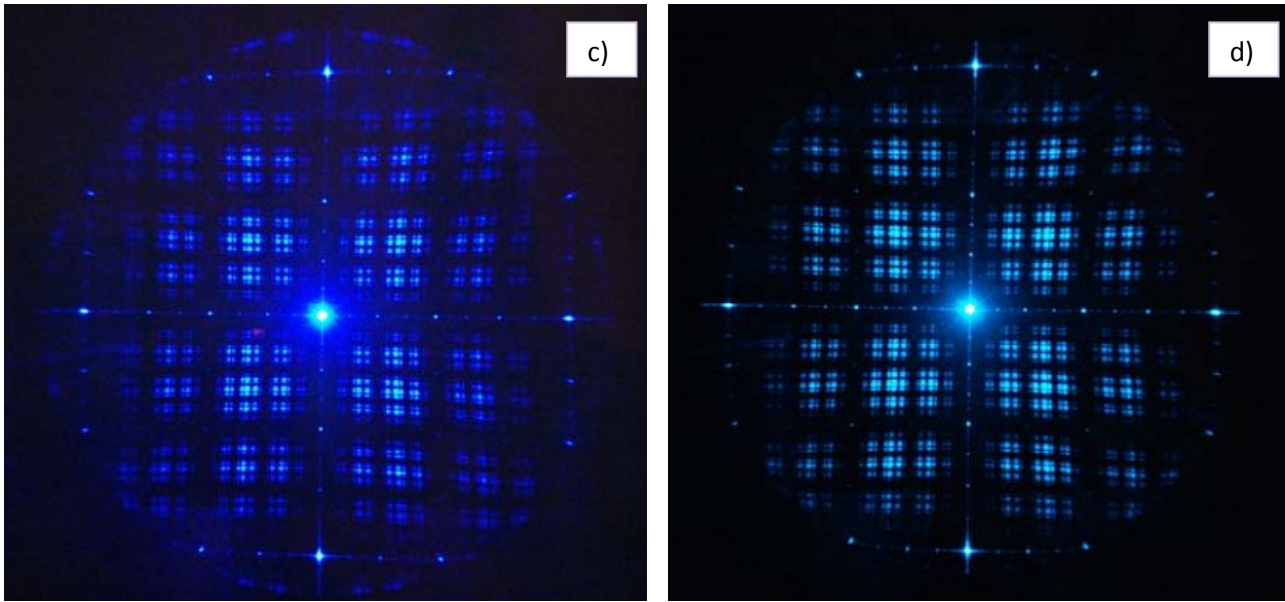
Fig. 7.3: a) Thue Morse arrangement of circles with D=508nm; b)FFD pattern acquired using a laser source with λ=514nm; c) FFD pattern acquired using a laser source with λ=457nm; d) FFD pattern acquired using a laser source with λ=488nm;

As shown in *Fig. 7.3 c-d*, we also characterized quasi-crystal in *Fig. 7.4 a* at laser wavelenghts λ=457nm and λ=488nm respectively. to underline the absolutely independance of FFD patterns to different laser wavelenghts.

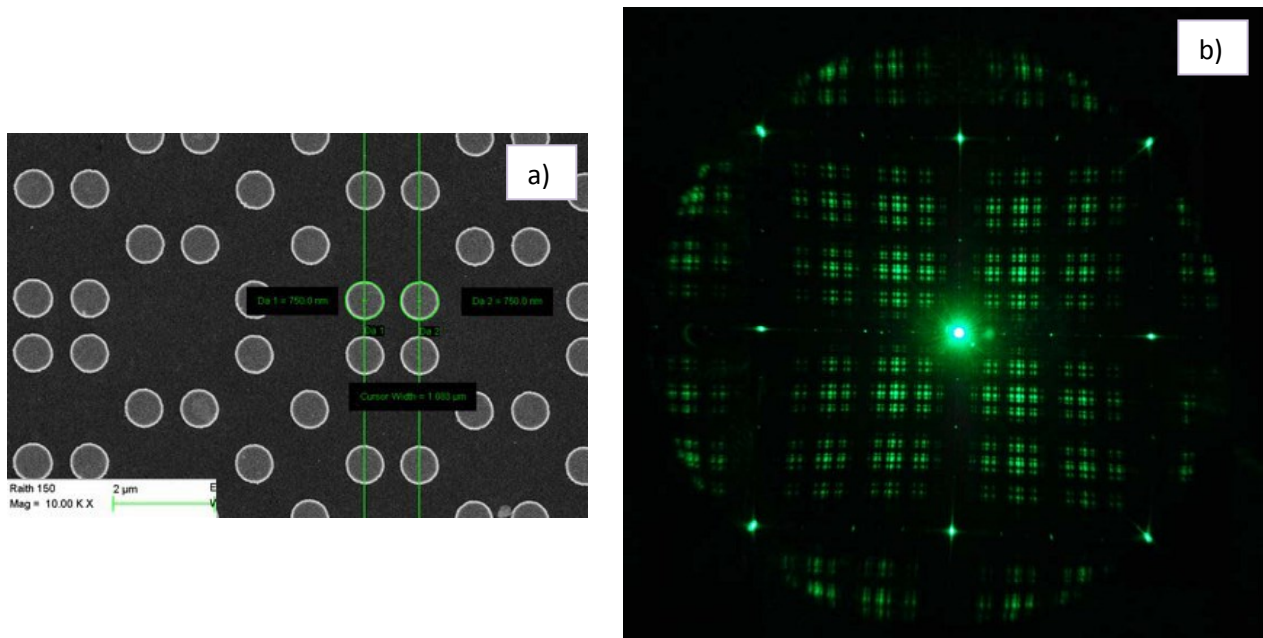*Fig. 7.4: a) Thue Morse arrangement of circles with D=750nm; b)FFD pattern acquired using a laser source with λ=514nm*

Comparing *Fig. 7.3b* and *Fig. 7.4b*, we want to underline that the two FFD patterns are perfectly the same, only except for a greater divergence related to the smaller quasi-crystal, in agreement with relation (7.1). In *Fig. 7.5* is shown the FFD pattern of a Thue-Morse quasi-crystal of squares with side size *d=750nm*.
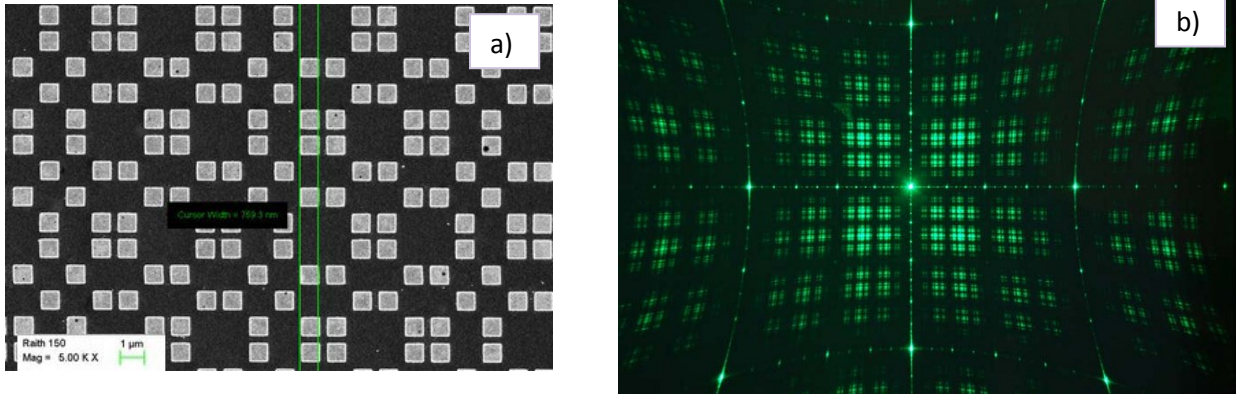

Fig. 7.5: a) Thue Morse arrangement of squares with D=750nm; b)FFD pattern acquired using a laser source with λ=514nm

The experimental diffraction pattern is in very good agreement with the calculated diffraction pattern produced by a two-dimensional Thue-Morse structure reported in *Chapter 4* (see *Fig. 4.10*).

8-Fold quasi-crystals

In the following *Fig. 7.6* is shown the FFD pattern obtained with a 8-fold quasi-crystal of circles with diameter *d=535nm*.
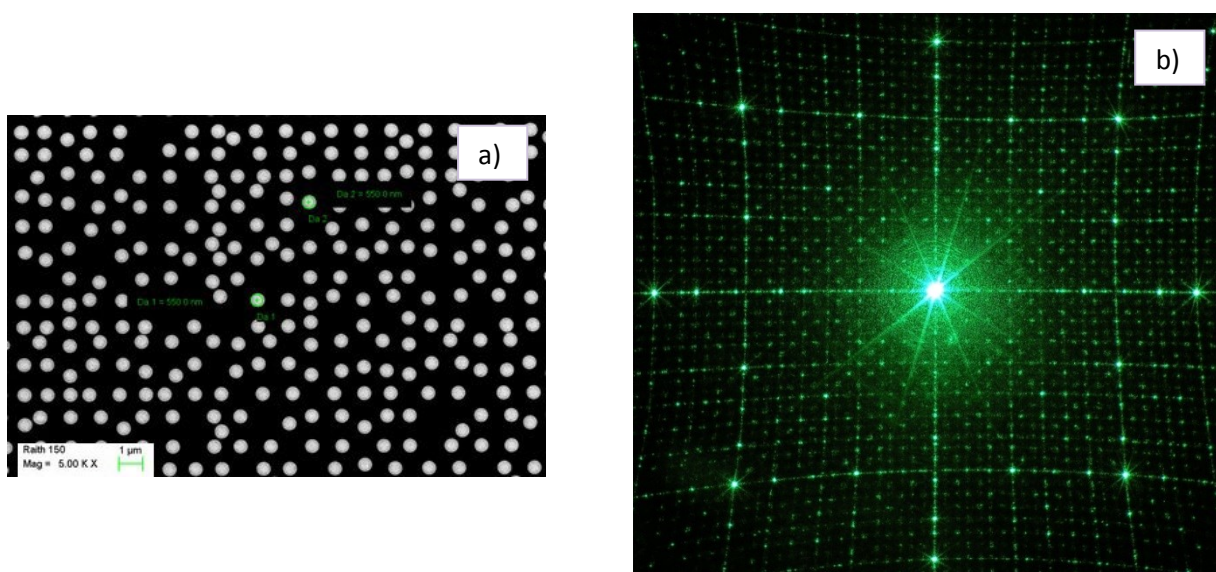

Fig. 7.6: a) 8-fold arrangement of circles with d=550nm; b)FFD pattern acquired using a laser source with λ=514nm

In particular in *Fig. 7.7* we want to underline the maximum of diffraction obtained: We depicted with the same color maximum of the same order by which appears evident the 8-fold simmetry of the pattern.
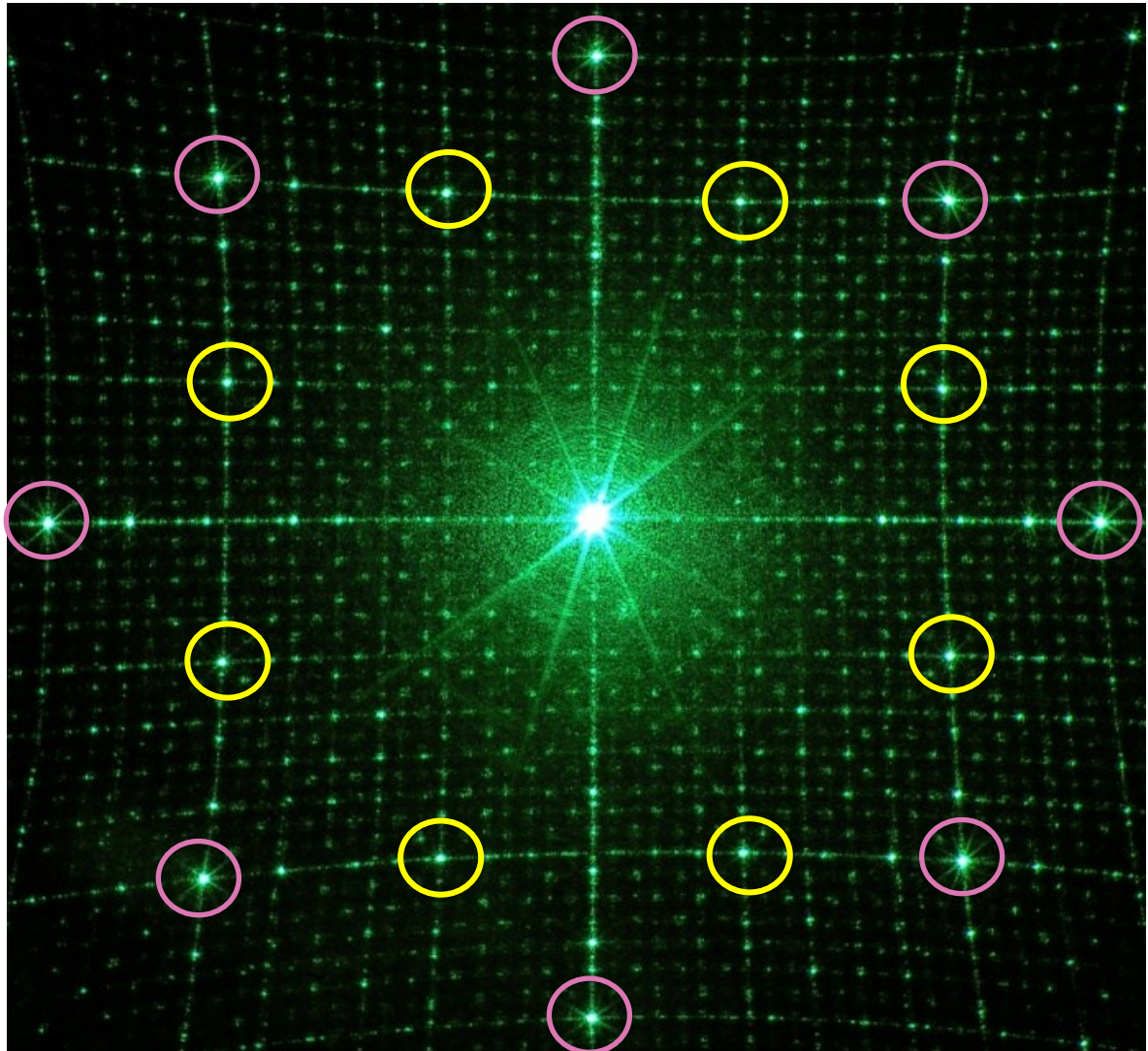

Fig. 7.7: FFD pattern acquired using a laser source with λ=514nm from a 8-fold arrangement of circles with d=550nm showing in detail the maxima of diffraction of different orders.

The diffraction pattern possesses eightfold rotational symmetry, and contains a series of spots of different intensity, surrounding the central undiffracted beam. These spots can be associated with vectors in reciprocal space. The observed peaks are sharp and symmetrically distributed. Each order has rings of spots at different cone angles around the zero-order central spot. The picture clearly reveals the presence of quasiperiodicity within the sample.

7.2 Raman Spectroscopy

Raman spectra were obtained using confocal Raman spectrometer (Horiba-Jobin Yvon Mod. Labspec Aramis) (*Fig. 7.8*) equipped with an integral microscope (Olympus BX 40). A diode laser emitting at 785nm was used as the excitation source. The 180° back-scattered radiation was collected by an Olympus metallurgical objective (MPlan 50x, NA = 0.75) with completely open confocal hole and slit apertures and an acquisition time of 10 seconds. The radiation was focused onto a Peltier cooled (- 70 °C) charged-coupled device (CCD) camera (Synapse Mod. 354308). The holographic grating with 600 grooves/mm was used throughout. The Raman band of a silicon wafer at 520 cm^{-1} was used to calibrate the spectrometer

Fig.7.8: Confocal Raman spectrometer LabRam Aramis HORIBA JOBIN YVON @ ICTP-CNR (Pozzuoli)

The spectra were collected in the range 1800 – 800 cm^{-1} for both single point measurements and mapping experiments. The latter, were carried out in mapping mode (x,y) with 2 μm step resulted in a total collection time of 1-2 hours for imaging the SERS substrates, depending on its size. The data gathered by the instrument were converted to ASCII format and transferred to the MATLAB computational platform for further processing. The Raman images were elaborated by programs written in the ICTP-CNR laboratory, making use of the image processing facilities and the surface interpolating algorithms of the MATLAB environment.

7.2.1 Materials

The p-mercaptoaniline (pMA or p-aminothiophenol) molecule is an organosulfur compound purchased from Sigma-Aldrich. pMA is a yellow solid whose chemical formula is C_6H_7NS. Its chemical structure is shown in *Fig. 7.9*: it has a thiol group (−SH) and a primary amine group (−NH$_2$) covalently bonded at the para position of an aromatic ring where the dashed line indicates the presence of delocalized bonds, typical of the benzene ring in Kekule model.
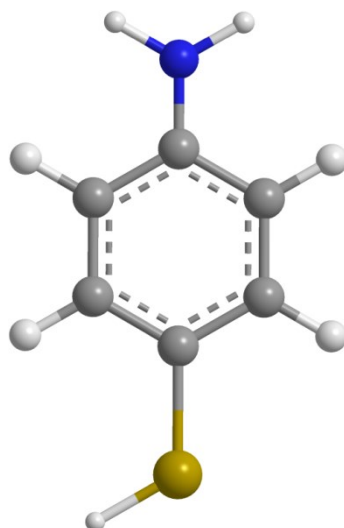
Fig. 7.9: Chemical structure of p-mercaptoaniline (IUPAC name 4-Aminothiophenol).
Atom color codes*: Grey: C, White: H, Yellow: S, Blue: N.*

pMA is a very good probe molecule for identifying the electronic properties of the SERS substrates: it can be strongly adsorbed onto most SERS substrates, producing very unique and strong surface-enhanced Raman signal, it has a large cross section and is photochemically stable [2-11]. Moreover, thiols are able to form compact self-assembled monolayer (SAM) [6, 12-13]. Bonding of pMA to Ag and Au surfaces is generaly believed to occur via a covalent interaction of the sulfur atom to the metallic substrate with loss of the hydrogen atom [14].

7.2.2 Activation of the SERS substrates

Before the Raman experiments, the gold nanostructures substrates have been cleaned in O_2 plasma for 10 min, rinsed in deionized water and Acetone and dried with nitrogen flows. The SERS substrates were immersed (overnight) in a 10 µM aqueous solution of pMA. Subsequent washing of the surface with water was conducted to remove any excess of azobenzene molecules or aggregates that were non covalently adsorbed onto gold. Before the SERS characterization, the sample was dried for 15 minutes at room temperature and further dried with a nitrogen flux. In the case of the SERS-active silver nanowires (Ag_NWs) a diluted ethanol solution of Ag_NWs was dropped on an optical glass. After the ethanol evaporation the 10 µM aqueous solution of pMA was dropped on Ag_NWs substrate and dried for about 30 minutes at room temperature.

7.3 Results and discussions

7.3.1 SERS measurements

p-mercaptoaniline, whose spontaneous Raman spectrum is shown in *Fig. 7.10*, can spontaneously form a close-packed monolayer on the metal surface based upon the strong covalent bonding between the thiol group and the metal substrate. Here, Raman spectroscopy with an excellent surface enhancement is used to investigate the presence of pMA monolayer on the nanostructured Au surface and Ag_NWs.
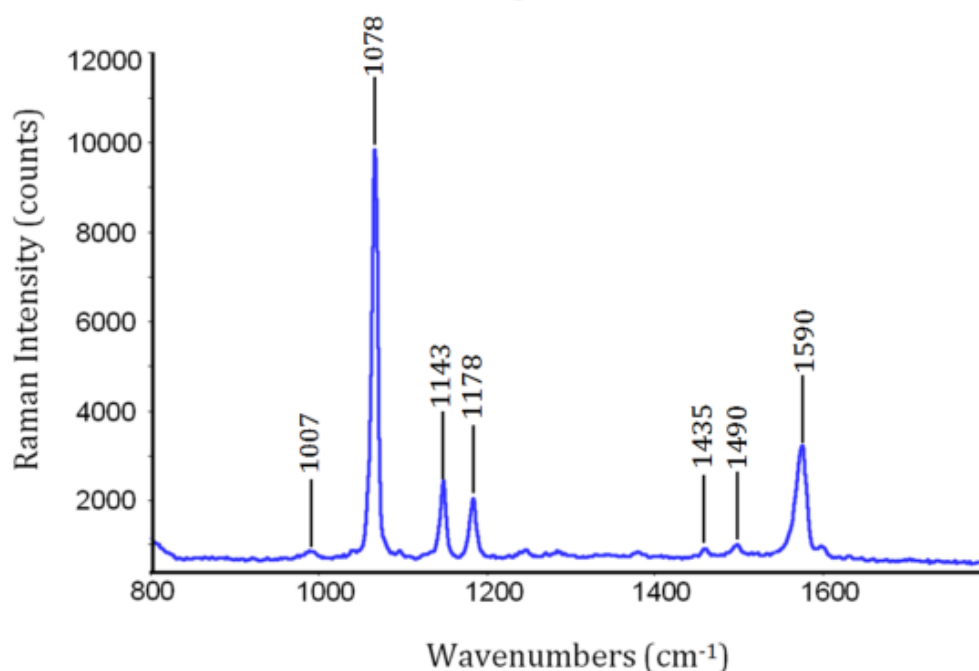

Fig. 7.10: Spontaneous Raman Spectrum of bulk (powder) pMA molecule

The SERS spectra of a self-assembled monolayer of pMA on the Au nanostructured substrates varies with the geometries, sizes and arrangement of the Au nanostructured substrates (see *Fig. 7.11 - 7.16*), whose principal characteristics are listed in *Tab. 7.1*. The SERS spectrum of pMA on Ag_NWs substrate is shown in (*Fig. 7.17*). For comparison the spontaneous Raman spectrum of the molecule (powder) is reported with blue trace in every SERS spectrum. The SERS spectra are significantly different if compared with the spontaneous Raman spectrum of pMA.

PERIODIC STRUCTURES					
SHAPE	ARRANGEMENT	SIZE (d)	PERIOD (A)	INTER-PARTICLE SEPARATION (s)	FILLING FACTOR (*FF*)
Cylinder	Square based	180nm	200nm	20nm	0,64
Cylinder	Square based	180nm	240nm	60nm	0,44
Cylinder	Square based	150nm	175nm	25nm	0,58
Cylinder	Square based	150nm	200nm	50nm	0,44
Cylinder	Square based	150nm	250nm	100nm	0,28
Cylinder	Triangular based	100nm	150nm	50nm	0,4
Cylinder	Triangular based	175nm	250nm	75nm	0,44
Triangle	Square based	200nm	225nm	25nm	0,34
Triangle	Square based	200nm	250nm	50nm	0,28
Triangle	Square based	200nm	300nm	100nm	0,19

DETERMINISTIC APERIODIC STRUCTURES					
SHAPE	ARRANGEMENT	SIZE (d)	Lattice Constant (G)	Minimum Interparticle Separation (s)	FILLING FACTOR (*FF*)
Square	Thue-Morse	185nm	264nm	79nm	0,27
Square	Thue-Morse	500nm	710nm	210nm	0,26
Cylinder	8-Fold	125nm	/	30nm	0,18
Ag_NWs-BASED SUBSTRATES					
SHAPE	ARRANGEMENT	SIZE (d)	Lenght (L)	Interparticle Separation (s)	FILLING FACTOR (*FF*)
Wires	Random	190nm	5-15µm	N/A	0,4*

Tab. 7.1: Summary of characterized substrates with their main features

*Filling Factor for Ag_NWs-based substrates was calculated from the SEM images, by means of statistical analysis employing a specific software.
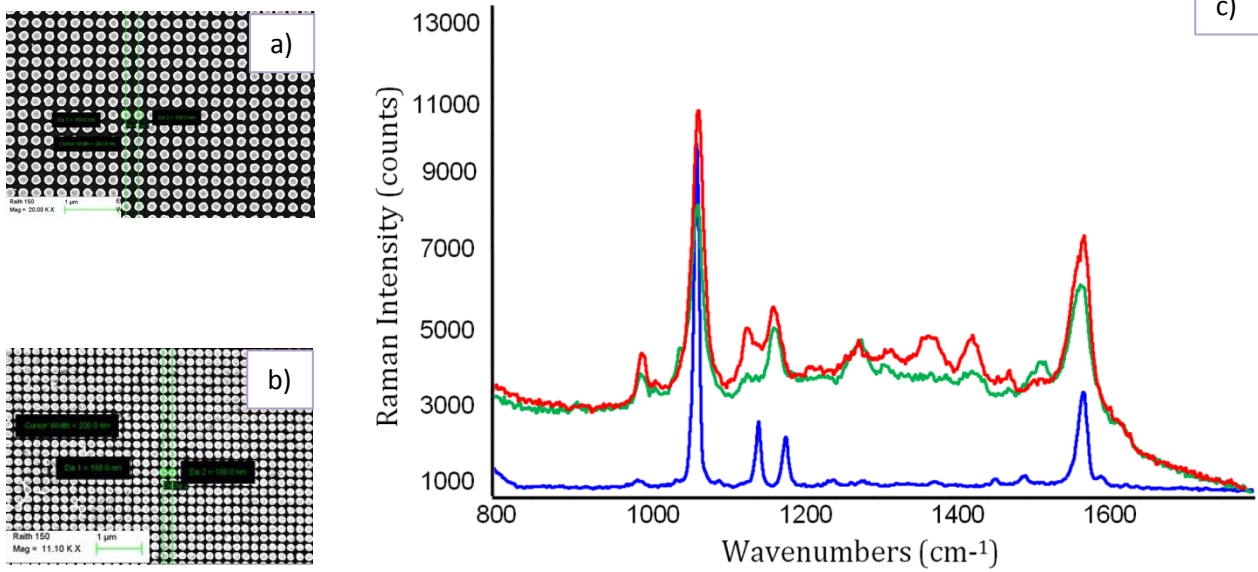
*Fig. 7.11: (a) SEM image of the PC of cylinder rods with d=180nm and A=240nm; (b) SEM image of the PC of cylinder rodss with d=180nm and A=200nm; (c) Spectra of pMA molecule on **Square-based periodic PCs of Au cylinder rods**: Raman spectra (blue curve), SERS spectra on the PC described in (a) (green curve); SERS spectra on the PC described in (b) (red curve)*
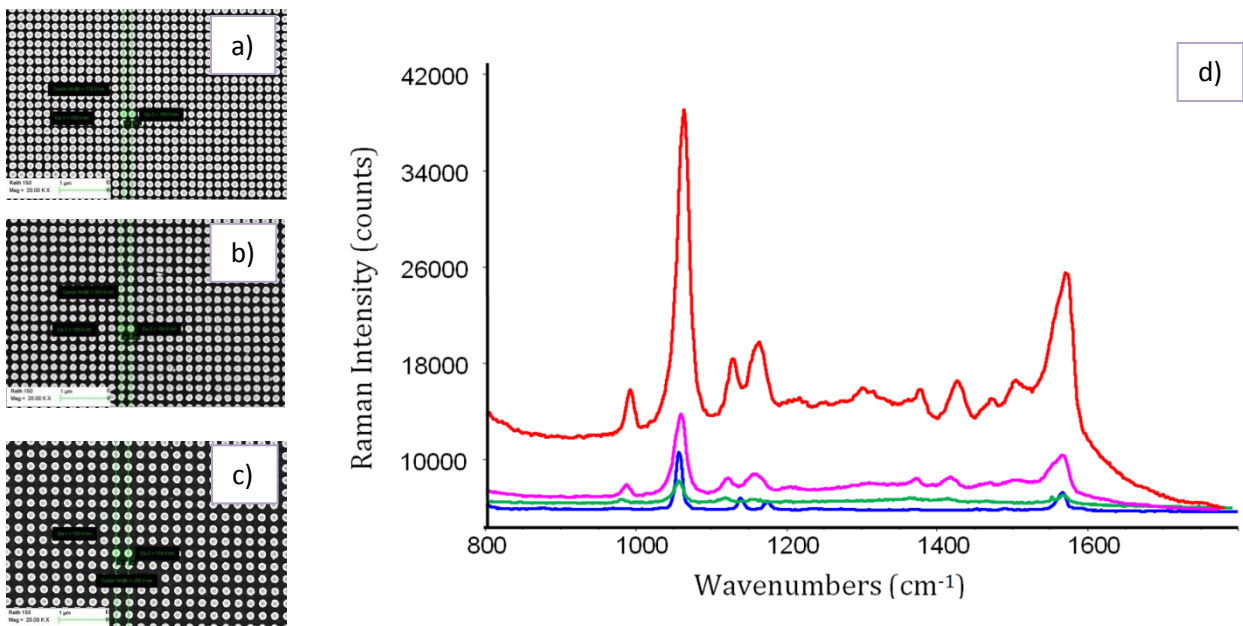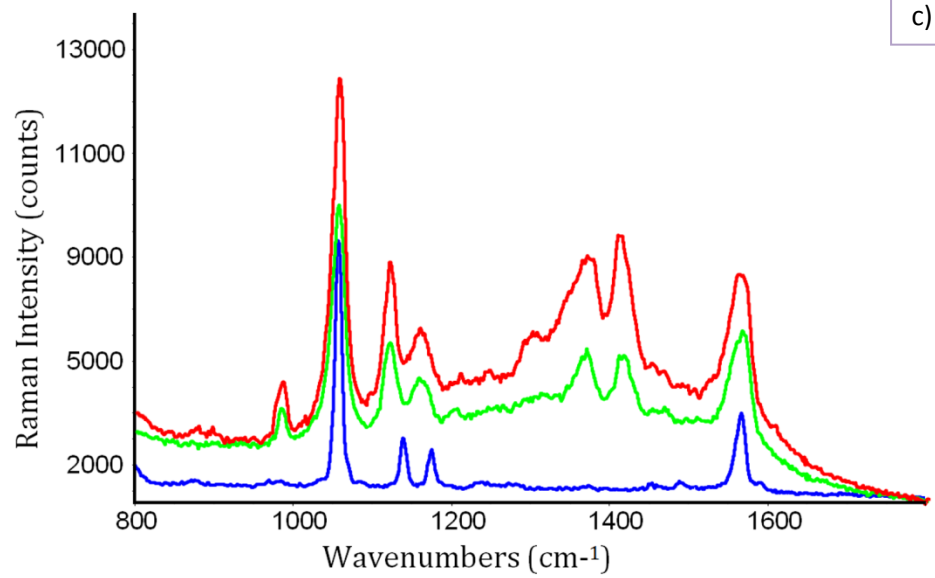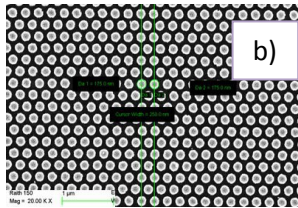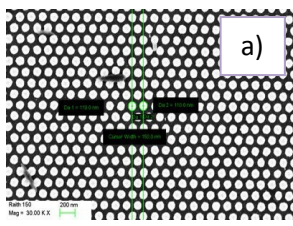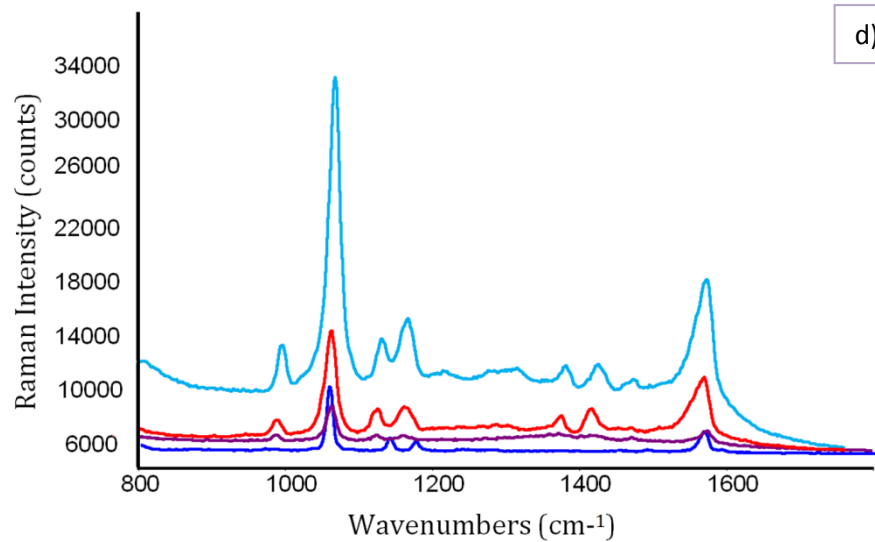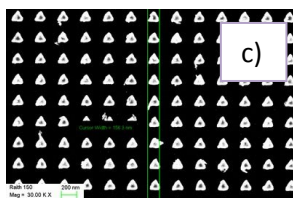

*Fig. 7.12: (a) SEM image of the PC of cylinder rods with d=150nm and A=175nm; (b) SEM image of the PC of cylinder rodss with d=150nm and A=200nm; (c) SEM image of the PC of cylinder rods with d=150nm and A=250nm ; (d) Spectra of pMA molecule on **Square-based periodic PCs of Au cylinder rods**: Raman spectra (blue curve), SERS spectra on the PC described in (a) (red curve); SERS spectra on the PC described in (b) (pink curve); SERS spectra on the PC described in (c) (green curve)*

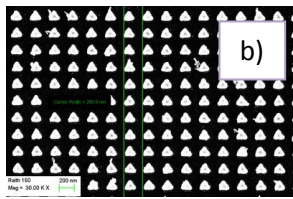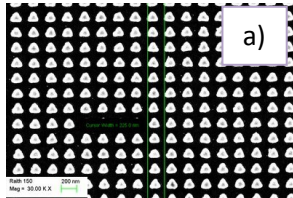*Fig. 7.13: (a) SEM image of the PC of cylinder rods with d=175nm and A=250nm ; (b) SEM image of the PC of cylinder rods with d=100nm and A=150nm ; (c) Spectra of pMA molecule on **triangular-based periodic PCs of cylinder**: Raman spectra (blue curve); SERS spectra on the PC described in (a) (green curve) and on thePC described in (b) (red curve)*

*Fig. 7.14: (a) SEM image of the PC of triangular rods with d=200nm and A=225nm ; (b) SEM image of the PC of triangular rods with d=200nm and A=250nm ; (c) SEM image of the PC of triangular rods with d=200nm and A=300nm ; (d) Spectra of pMA molecule on **Square-based periodic PCs of triangles**: Raman spectra (blue curve); SERS spectra on the PC described in (a) (purple curve); SERS spectra on the PC described in (b) (red curve); SERS spectra on the PC described in (c) (light blue curve)*
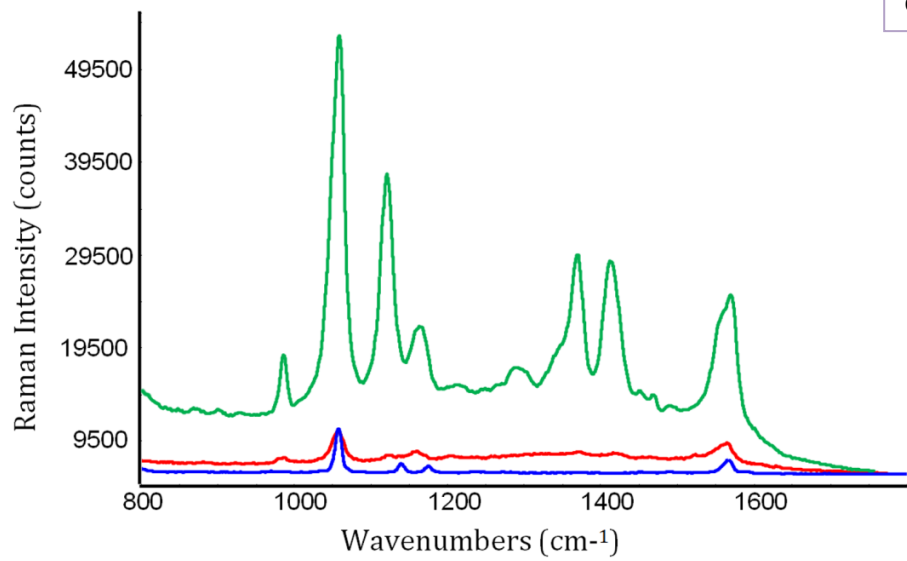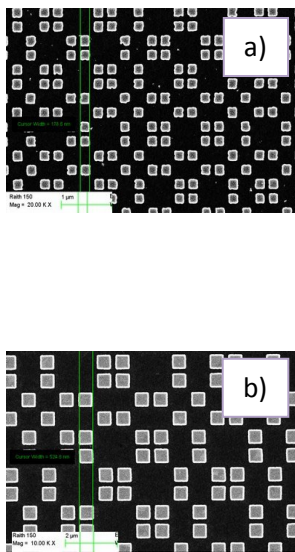
*Fig. 7.15: (a) SEM image of the Thue Morse arrangement of squares with d=185nm; (a) SEM image of the Thue Morse arrangement of squares with d=500nm; (c) Spectra of pMA molecule on **Thue Morse PQCs of squares**: Raman spectra (blue curve); SERS spectra on the QPC described in (b) (red curve); SERS spectra on the QPC described in (a) (green curve)*
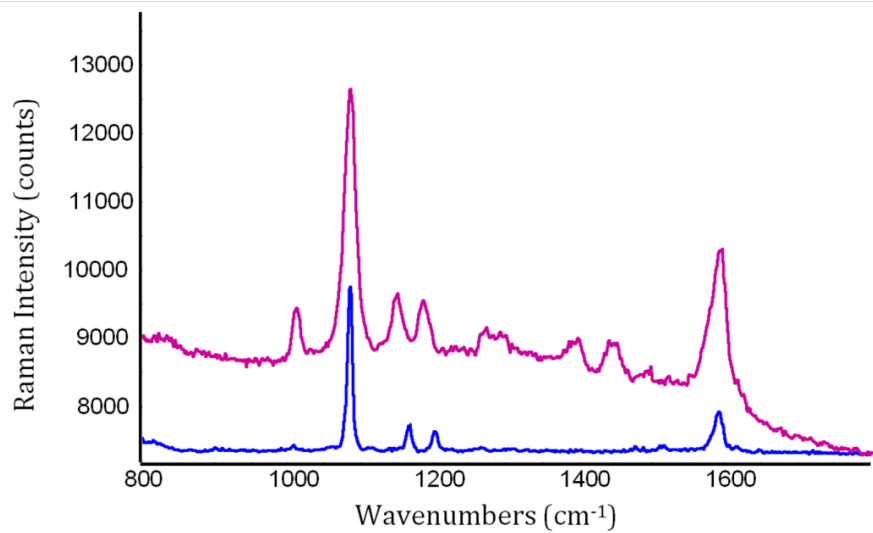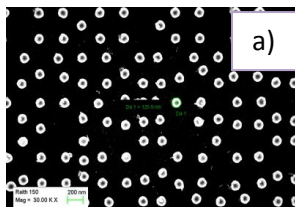
*Fig. 7.16: (a) SEM image of the 8-fold arrangement of cylinder rods with d=125nm;(b) Spectra of pMA molecule on **8-FOLD PQCs of cylinders**: Raman spectra (blue curve); SERS spectra on the QPC described in (a)*
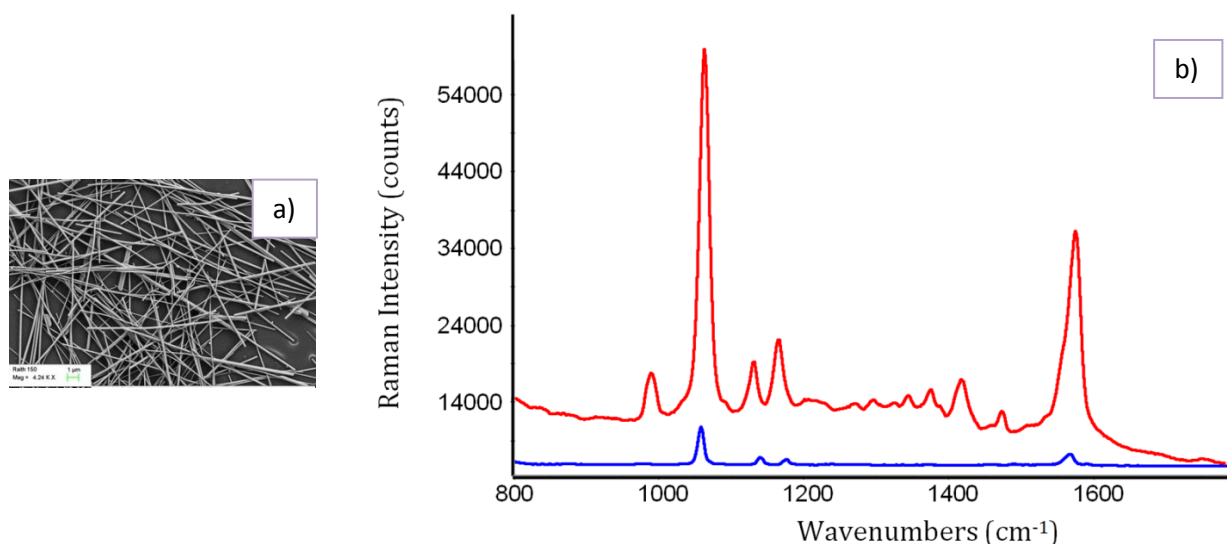
*Fig. 7.17: (a) SEM image of the Ag_NWs-based substrate; (b) Spectra of pMA molecule on **AgNWs covered substrate:** Raman spectra (blue curve); SERS spectra (red curve)*

Assignments of the pMA vibrational modes as detected in the spontaneous Raman spectrum are presented in *Tab. 7.2*. The strong Raman bands centered at 1590 and 1078 cm^{-1} have been assigned to the stretching vibrations (CC) of the benzene ring and to the ν(CS) mode, respectively. The medium bands centered at 1178 and 1143 cm^{-1} are associated to the in-plane deformation modes of the ring [(bending vibrations, δ(CCC)]. Two very weak bands at 1435 and 1490 cm^{-1} have been associated to highly coupled vibrations, with contributions from (CC) and δ(CCH) modes. Finaly, a further weak feature is observed at 1007 cm^{-1}, for which ambiguous and inconclusive assignements have been proposed [5, 14].

Raman frequencies [a] (cm^{-1})	Assignment [b]
1590 s	ν(CC)
1490 vw	ν(CC)/δ(CCH)
1435 vw	ν(CC)/δ(CCH)
1178 m	δ(CCH)
1143 m	δ(CCH)
1078 s	ν(CS)
1007 vw	?

Tab. 7.2 Assignments of vibrational modes for pMA spontaneous Raman spectrum

[a] Frequencies followed by relative intensities: s, strong; m, medium; vw, very weak.

[b] Approximate description of the modes: ν, stretching; δ, bending.

In the SERS spectra of pMA all the bands undergo a significant intensity enhancement. The intensity ratios change with the size, arrangement and geometry of the Au nanostructures, possibly reflecting changes in the preferential orientation of the molecules with respect to the metal surface.

Toward a quantitative assessment of the SERS effect in the various substrates, the absolute enhancement factor, G_{SERS} was calculated. It is defined as:

$$G_{SERS=} \frac{RS_{EN} \times N_{REF}}{RS_{REF} \times N_{EN}} \tag{7.2}$$

In equation (7.2), RS_{EN} and RS_{REF} are the intensities of a specific Raman band (at 1078 cm^{-1}, in our case) for the SERS and the spontaneous Raman spectrum, respectively. Analogously, N_{EN} and N_{REF} represent, the number of molecules contributing to the measured signal on the nanostructure and in the bulk, respectively.

More specifically, N_{REF} represents the average number of molecules in the scattering volume and is evaluated as:

$$N_{REF} = \frac{B_v \times D_{pMA} \times A}{M_{pMA}} \tag{7.3}$$

where B_v is the optical excitation volume, D_{pMA} is the density of pMA (1.06 g/cm^3) in the reference bulk crystal, A is the Avogadro number and M_{pMA} is the pMA molecular weight (125.19 g/mol). Due to the ability of pMA molecules to form a monolayer on metal surfaces [7, 15] the number of molecules contributing to the SERS effect (N_{EN}) can be estimated by the ratio of the total metal surface illuminated by the laser beam (radius of the spot) and the geometrical cross section of the individual pMA molecules (0.3 nm^2 per molecule) [16]. This number (N_{EN}) must be divided by the filling factor (FF) which reflect the ratio of the covered and the non-covered metal areas (see *Tab. 7.1*).

The volume of the focal point, B_v, was determined by measuring the change of the Raman signal of silicon (520 cm^{-1}) substrate as a function of the *Z* position of the objective. The *Z profile* measurements were obtained using a confocal Raman spectrometer (Horiba-Jobin Yvon Mod. Aramis) with the same operating conditions used for sample tests: diode laser excitation source emitting at 785 nm, metallurgical objective (MPlan 50×, NA = 0.75) with completely open confocal hole and slit apertures. By varying the focus of the laser on the silicon sample (*z profile*), the intensity variation of the silicon peak shows a Gaussian-type variation as shown in *Fig. 7.18.* The Full Width at Half Maximum (FWHM) gives the waist

length of the focal volume (z = 30.6 μm), the transverse dimension i.e. the radius of the beam (1.28 μm) is determined in view of the numerical aperture of the objective (N_A) used for the specific wavelength (λ_{LASER}) according to the relation: $1.22 \times \lambda_{LASER} / N_A$. The resulting B_v is about 50.1 μm³.
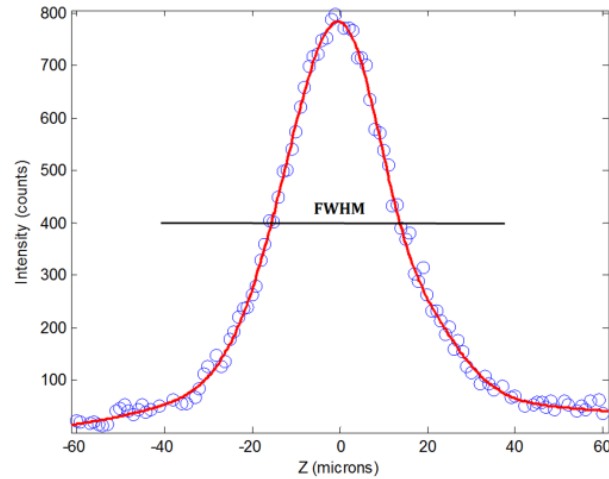

Fig. 7.18: Variation of the Raman signal of silicon (520 cm⁻¹) as a function of the Z position of the objective. The Full Width at Half Maximum (FWHM) is about 30.6 μm.

The enhancement factors calculated for the periodic and aperiodic Au nanostructured substrates and for the Ag_NWs are listed in *Tab. 7.3.*

SERS substrate	G_{SERS}
Square-based periodic PCs of cylinder d=180nm A=240nm	$1,4 \cdot 10^6$
Square-based periodic PCs of cylinder d=180nm A=200nm	$1,5 \cdot 10^6$
Square-based periodic PCs of cylinder d=150nm A=175nm	$3,3 \cdot 10^6$
Square-based periodic PCs of cylinder d=150nm A=200nm	$6,4 \cdot 10^5$
Square-based periodic PCs of cylinder d=150nm A=250nm	$3,1 \cdot 10^5$
Triangular-based periodic PCs of cylinder d=100nm A=150nm	$1,1 \cdot 10^6$
Triangular-based periodic PCs of cylinder d=175nm A=250nm	$1,1 \cdot 10^6$
Square-based periodic PCs of triangles d=200nm A=225nm	$6,7 \cdot 10^5$
Square-based periodic PCs of triangles d=200nm A=250nm	$1,1 \cdot 10^6$
Square-based periodic PCs of triangles d=200nm A=300nm	$1,3 \cdot 10^7$
Thue Morse arrangement of squares D=500nm	$1,5 \cdot 10^6$
Thue Morse arrangement of squares D=185nm	$1,4 \cdot 10^7$
8-Fold arrangement of cylinder D=125nm	$1,4 \cdot 10^8$
Ag_NWs	$4,7 \cdot 10^5$

Tab. 7.3: Enhancement Factors (G_{SERS}) achieved by the characterized SERS substrates

In literature, it has been shown that by engineering the shapes of nanoparticles high values of field enhancement can be achieved and Raman Enhancement factors>10^6 have been observed [15]. Our efforts of these three years of research activity in this field allowed us to get SERS enhancement factors G$\simeq$$10^6$ in lithographically defined PC arrays of Au nanoparticles, G$\simeq$$10^7$ – 10^8 for PQC arrays of Thue Morse and 8-fold arrays of Au nanoparticle, respectively, as summarized in the following histrograms (*Fig.7.19 – 7.20*):
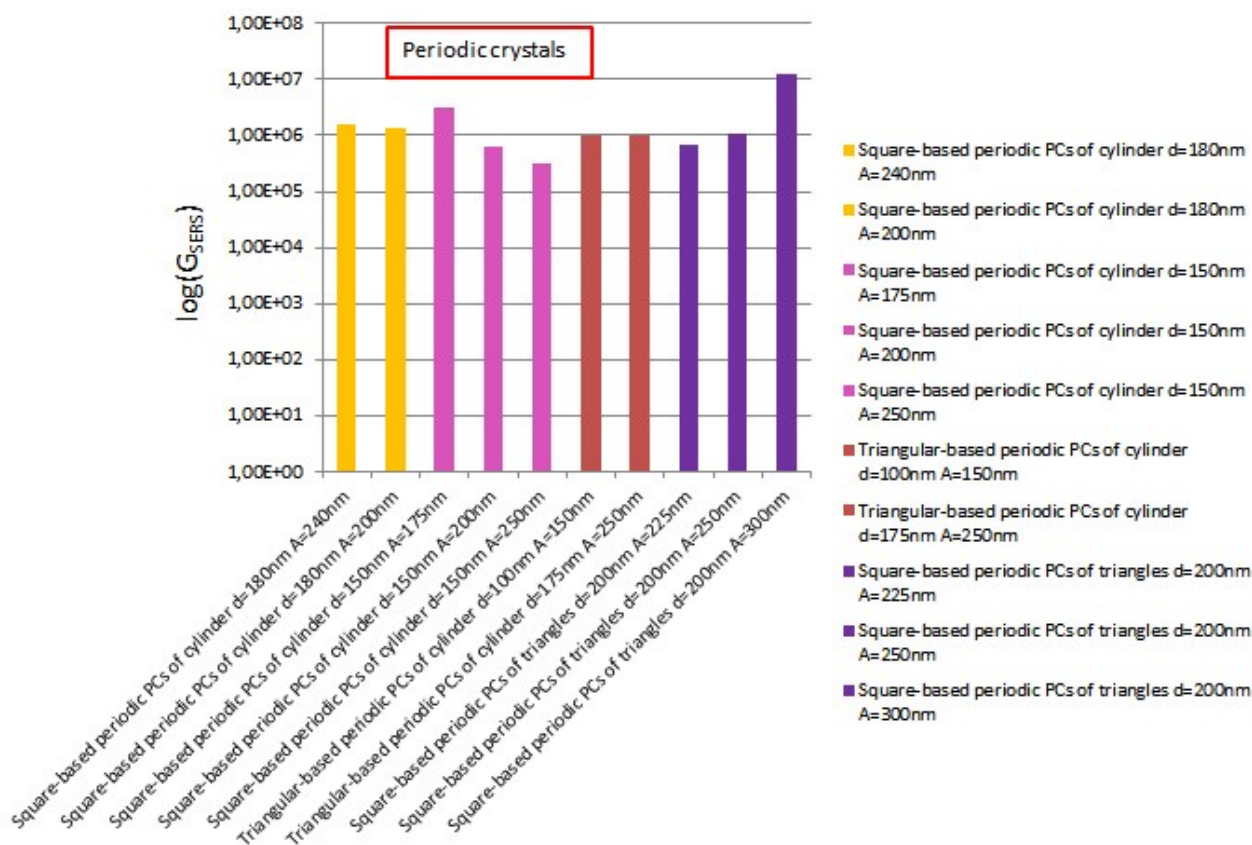

Fig. 7.19: Histogram summarizing and comparing G_{SERS} of the characterized Periodic nanostructures
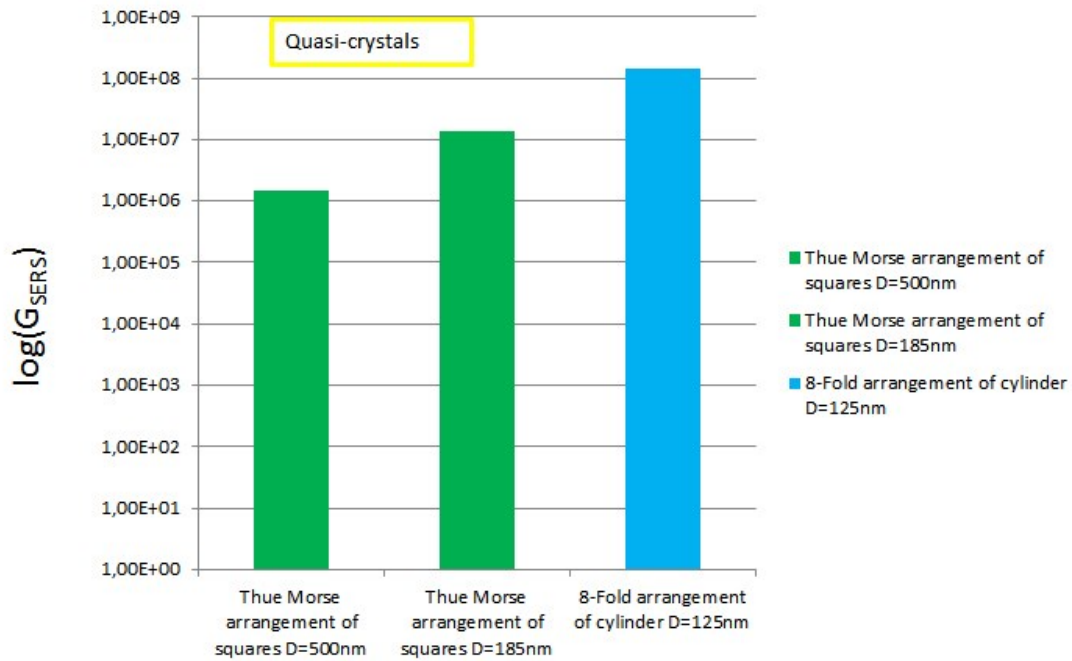
Fig. 7.20: Histogram summarizing and comparing G$_{SERS}$ of the characterized Quasi-crystalline nanostructures

7.3.2 Device homogeneity quality and reproducibility

Two important concepts in device fabrication are homogeneity quality and reproducibility. The latter, also called repeatability, is the degree to which repeated measurements under unchanged conditions show the same results. It is related to the dispersion of experimental data around an average and it is therefore measured by the statistical error σ.

One of the project's objectives was indeed the reproducibility and uniformity of the response, fundamental for a SERS-active substrate suitable for sensing applications. In order to test the homogeneity of the signal, a number of samples has been produced using the same fabrication parameters. On every sample many chips with the same geometrical characteristics (period, duty cycle and gold thickness of the grating) have been replicated. In order to further investigate the quality and homogeneity of the realized engineered nanostructures, a x,y mapping measurement has also been performed on the fabricated samples. As examples we reported in *Fig. 7.21-7.22-7.23* the results obtained for the three typologies of SERS substrate realized. On the Periodic Photonic Crystal of cylinders with d=180nm and A=200nm (*Fig. 7.21*) and the Thue Morse arrangement of gold nanoparticles with side size=185nm and lattice constant=264nm (*Fig. 7.22*): spectra were acquired point by point, in mapping mode (x,y) on a nanostructured area of 45x45 μm^2, with 2 μm step. The Raman image, reconstructed by

considering the intensity of the pMA peak at 1078 cm^{-1}, is reported in *Fig. 7.21 a - 7.22 a* in the form of a color map, where high signal intensity corresponds to the red colour, and low intensity is represented by the blue colour. Both maps evidence that a conspicuous SERS signal is present in the whole area. Regions of intense SERS activity (4.5 – 7 x 10^5 A.U.) are uniformly distributed within the sampled area and represent the majority of the analyzed surface. Around these areas, there are regions where the SERS signal is slightly reduced (3.5 – 4.0 x 10^5 A.U.), but remains strong enough to be readily detected.
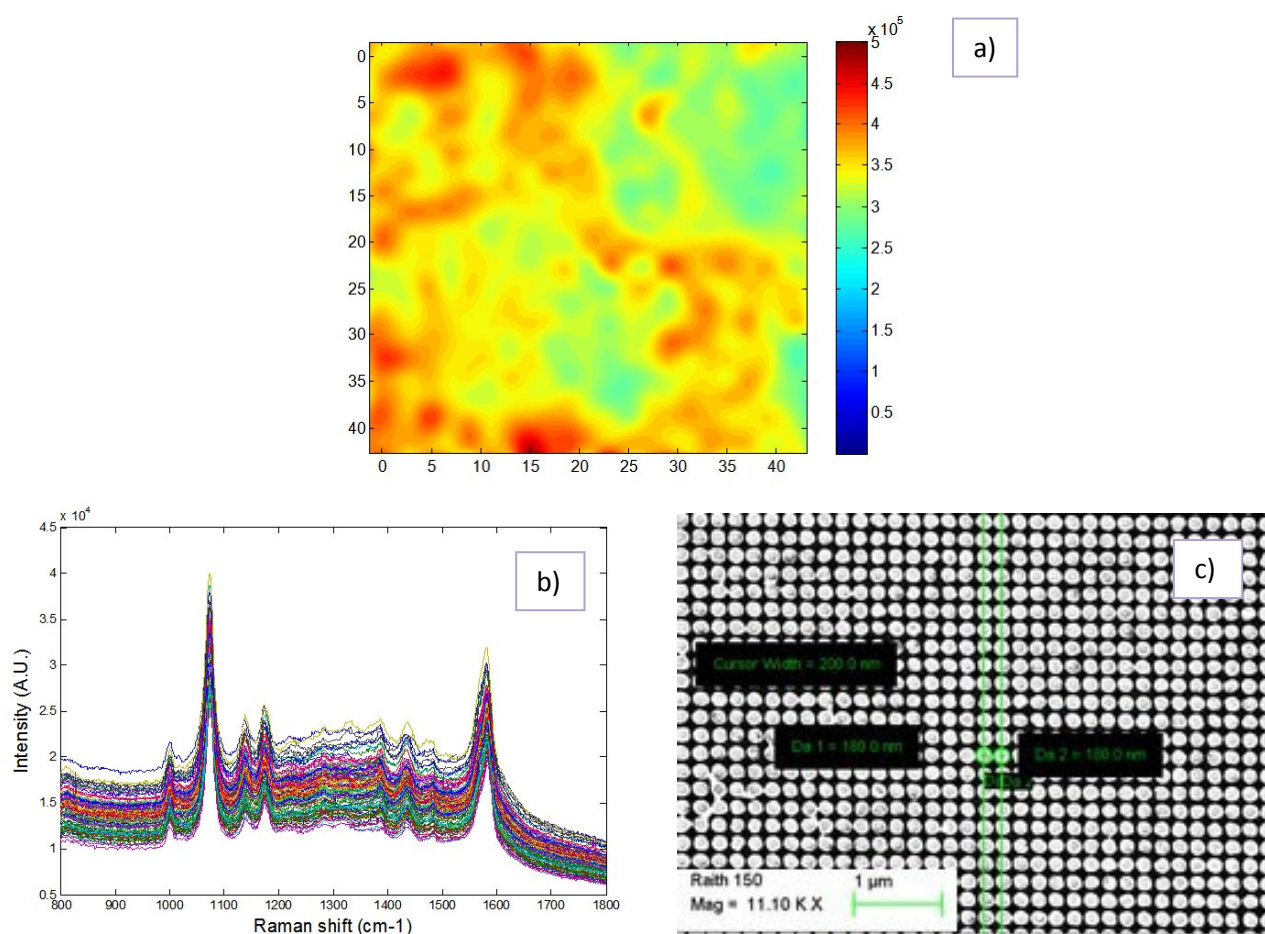
Fig. 7.21: (a) Raman imagine obtained considering the intensity of the peak at 1078 cm^{-1} scanning a 45x45 μm^2 PC array of cylinders (d=180nm and A=200nm) area which SEM image is showed in (c); (b) SERS spectra sequences collected in the mapped area
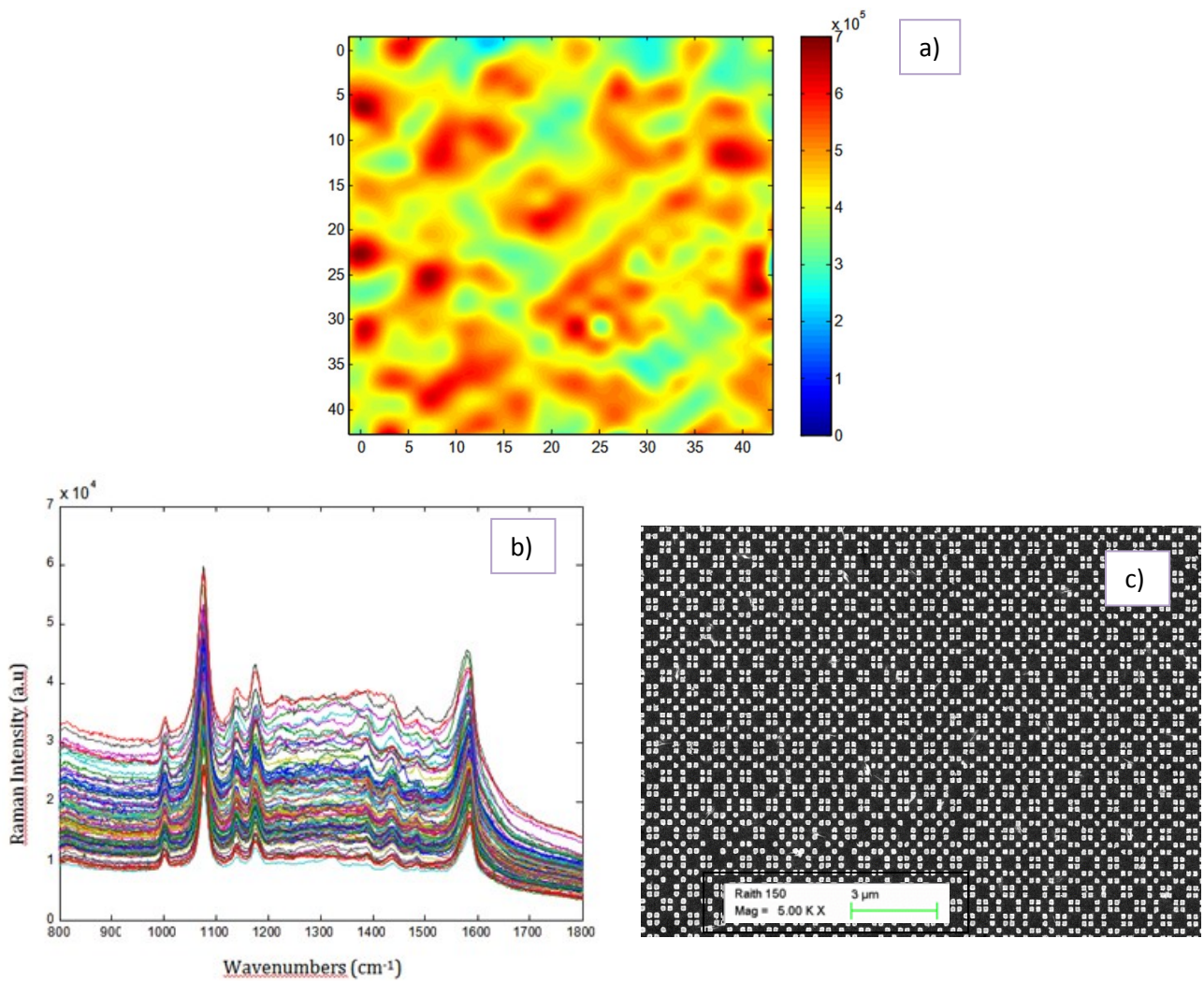
Fig. 7.22: (a) Raman imagine obtained considering the intensity of the peak at 1078 cm⁻¹ scanning a 45x45 µm²
Thue Morse (d=185nm) area which SEM image is showed in (c); (b) SERS spectra sequences collected in the
mapped area

The same analysis carried out on Ag_NWs and made scanning a substrate area of 40x20 μm², with 2 μm step, is reported in *Fig. 7.23*.
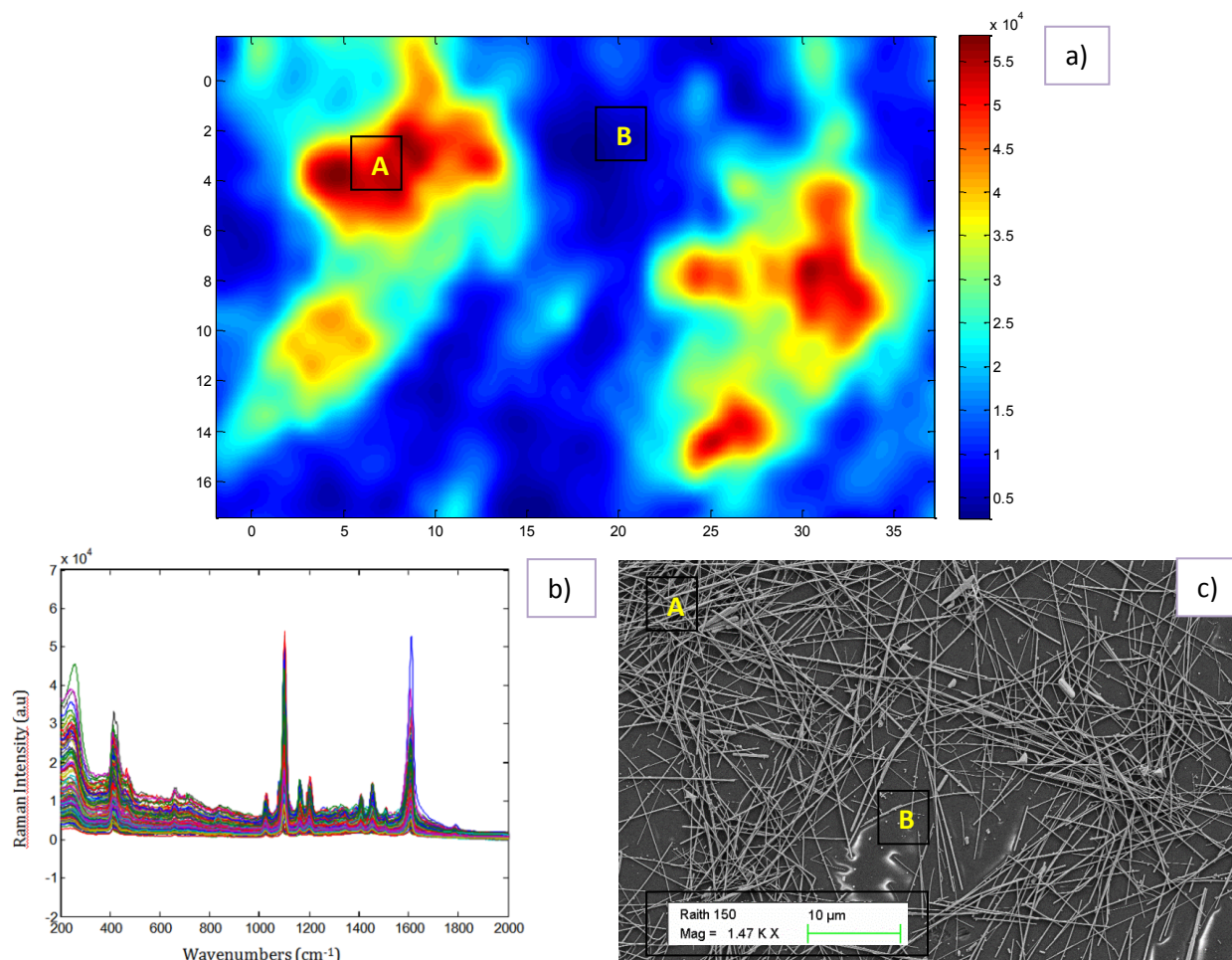
Fig. 7.23: (a) Raman imagine obtained considering the intensity of the peak at 1078 cm⁻¹ scanning a 40x20 μm² Ag_NWs substrate area which SEM image is showed in(c); (b) SERS spectra sequences collected in the mapped area

In this case the pattern is much more heterogeneous, with two well defined regions of very high SERS activity embedded into a background where the signal is essentially absent. This situation reflects the morphology of the substrate (see *Fig. 7.23 c*): the SERS signal is localized where the density of Ag nanowires is higher and tends to zero in the areas where few or no nanowires are present. The comparison between the Raman images of the two substrates highlights the much improved performance of the engineered nanostructures with respect to the Ag_NWs substrates in terms of response homogeneity, which is a very relevant factor for the analytical applications.

References

[1] V. Matarazzo, S. De Nicola, G. Zito, P. Mormile, M. Rippa, G. Abbate, J. Zhou, and L. Petti, *Spectral characterization of two-dimensional Thue-Morse quasicrystals realized with high resolution lithography*, **Journal of Optics**, 13, 015602 (2011). DOI: 10.1088/2040-8978/13/1/015602.

[2] Nielsen, J. U.; Esplandiu, M. J.; Kolb, D. M. *4-Nitrothiophenol SAM on Au(111) Investigated by in Situ STM, Electrochemistry, and XPS*, **Langmuir, 17, 3454 (2001)**

[3] Manolova, M.; Boyen, H. G.; Kucera, J.; Gross, A.; Romanyuk, A.; Oelhafen, P.; Ivanova, V.; Kolb, D. M. , *Chemical Interactions* at *Metal/Molecule Interfaces* in Molecular *Junctions*—A *Pathway Towards Molecular Recognition,* **Adv. Mater.** 2009, 21, 320.

[4] Hill, W.; Wehling, B., *Potential- and pH-dependent surface-enhanced Raman scattering of p-mercapto aniline on silver and gold substrates*, **J. Phys. Chem**. 1993, 97, 9451.

[5]Osawa, M.; Matsuda, N.; Yoshii, K.; Uchida, I., *Charge transfer resonance Raman process in surface-enhanced Raman scattering from p-aminothiophenol adsorbed on silver: Herzberg-Teller contribution*, **J. Phys. Chem.** 1994, 98, 12702

[6] Oldenburg, S. J.; Westcott, S. L.; Averitt, R. D.; Halas, N. J., *Surface enhanced Raman scattering in the near infrared using metal nanoshell substrates*, **J. Chem. Phys**. 1999, 111, 4729

[7] Jackson, J. B.; Halas, N. J., *Surface-enhanced Raman scattering on tunable plasmonic nanoparticle substrates*, **PNAS**. 2004, 101, 17930.

[8] Zhou, Q.; Li, X. W.; Fan, Q.; Zhang, X. X.; Zheng, J. W., *Charge Transfer between Metal Nanoparticles Interconnected with a Functionalized Molecule Probed by Surface-Enhanced Raman Spectroscopy*, **Angew. Chem., Int. Ed.** 2006, 45, 3970.

[9] Fromm, D. P.; Sundaramurthy, A.; Kinkhabwala, A.; Schuck, P. J.; Kino, G. S.; Moerner, W. E., *Exploring the chemical enhancement for surface-enhanced Raman scattering with Au bowtie nanoantennas*, **J. Chem. Phys.** 2006, 124, 061101

[10] Piorek, B. D.; Lee, S. J.; Santiago, J. G.; Moskovits, M.; Banerjee, S.; Meinhart, C. D., *Free-surface microfluidic control of surface-enhanced Raman spectroscopy for the optimized detection of airborne molecules*, **PNAS**. 2007, 104, 18898

[11] Wang, Y. L.; Chen, H. J.; Dong, S. J.; Wang, E. K., *Intensification of* surface enhanced *Raman scattering of thiol-containing molecules ... scattering of silver-gold bimetallic nanostructures with hollow interiors* **J. Chem. Phys.** 2006, 125, 044710

[12] Boettcher, C. J. F. *Theory of Electric Polarization*; Vol. 1; Elsevier Scientific Publishing: London, 1973; pp 74-82.

[13] van de Hulst, H. C. *Light Scattering by Small Particles*; Dover Publications: New York, 1981;p 71

[14] L. S. Jiao, Z. Wang, L. N. J. Shen, T. Y. You, S. J. Dong, A. Ivaska, *In-situ electrochemical SERS studies on electrodeposition of aniline on 4-ATP/Au surface,* **J. of Solid state Interaction**, 10, 886-893 (2006)

[15] Ashwin Gopinath, Svetlana V. Boriskina, Björn M. Reinhard, Luca Dal Negro,*Deterministic aperiodic arrays of metal nanoparticles for surface-enhanced Raman scattering (SERS)*, 2009 / Vol. 17, No. 5 / **OPTICS EXPRESS** 3742- 3753

[16] Mohri, N.; Matsushita, S.; Inoue, M.; Yoshikawa, K., *Desorption of 4-Aminobenzenethiol Bound to a Gold Surface*, **Langmuir** 1998, 14 (9), 2343-2347

Chapter 8: Nanobiosensor devices: realization and testing

8.1 Introduction

Recently, imaging techniques based on vibrational spectroscopy have emerged as powerful tools for the molecular characterization of cells and tissues, capable to complement or, in many cases, to provide information unavailable with the more conventional approaches. In particular Raman imaging with confocal sampling has a number of distinct advantages: it provides good contrast due to the specificity of the spectrum, molecular-level information and the possibility to implement quantitative or semi-quantitative analysis. With respect to FTIR, it offers the additional benefit of a limiting space-resolution one order of magnitude higher (0.8 – 1.0 μm), a benefit particularly relevant when sampling subcellular structures. Moreover, being Raman spectroscopy a scattering technique, it is capable of imaging the chemical composition of cellular structures based on their vibrational properties, without the need of staining procedures or the introduction of fluorescent probes which may perturb the biochemical properties of the molecules of interest. Raman spectroscopy is non-invasive so it can be used to analyze substances contained in transparent packaging. This makes it particularly well suited for the pharmaceutical industry during the manufacturing process. Some applications include identification of raw materials, quantitative analysis of active ingredients, identifying polymorphs and quality assurance during production [1]. It is also non-destructive when using low powered lasers making it useful for determining differences in the composition of in-vivo healthy tissue versus diseased tissue without causing further damage. Differences between cancerous and healthy tissue have been observed in the Raman bands related to lipids, proteins and nucleic acid [2]. By far its most common use has been in analytical chemistry for the determination of how molecules interact with each other and how they interact with surfaces. The interaction of ligands to proteins is widely studied with resonant Raman scattering. Perhaps analytical chemists are the most enthusiastic about SERS as it could offer a tool to detect a single molecule as well as its chemical structure.

Thus, the aim of this preliminary biological tests is to investigate the SERS behaviour of the realized engineered SERS substrates with human prostate cancer cells (PC-3) cells (*Fig. 8.1*) using imaging techniques based on confocal Raman spectroscopy. The peculiar features and the relevant information provided by this approach will be discussed in this chapter.
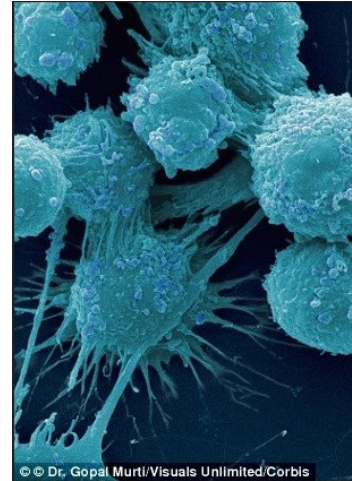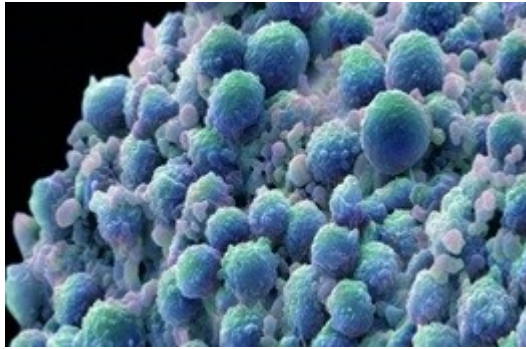
Fig. 8.1: Human prostate cancer cells

8.2 Motivation

Prostate cancer is a form of cancer that develops in the prostate, a gland in the male reproductive system. Most prostate cancers are slow growing [3]; however, there are cases of aggressive prostate cancers [4] . The cancer cells may metastasize (spread) from the prostate to other parts of the body, particularly the bones and lymph nodes. Rates of detection of prostate cancers vary widely across the world, with South and East Asia detecting less frequently than in Europe, and especially the United States [5]. Prostate cancer tends to develop in men over the age of fifty [6]. Globally it is the sixth leading cause of cancer-related death in men [7] (it is now the first in the UK and second in the United States) [6]. Prostate cancer is most common in the developed world with increasing rates in the developing world [7]. However, many men with prostate cancer never have symptoms, undergo no therapy, and eventually die of other unrelated causes. Many factors, including genetics and diet, have been implicated in the development of prostate cancer. Recently the prevalence of light pollution has been implicated in the development of prostate cancer [8]. Essentially all men with circulating androgens will develop microscopic prostate cancer if they live long enough, but the current understanding of biomarkers of disease and risk factors is limited. An understanding of the risk factors for prostate cancer has practical importance for public health research and policy, genetic and nutritional education and chemoprevention, and prevention strategies [9].

8.3 Experimental section

8.3.1 Cell culture and specimen preparation

Human prostate cancer cells (PC-3) were purchased from American Type Culture Collection (CRL-1435, Rockville, MD). Dulbecco's Modified Eagle's Medium (DMEM) high glucose, Ham's F-12 nutrient mixture, fetal bovine serum (FBS), phosphate buffered saline (PBS), l-glutamine, penicillin, streptomycin and trypsin were obtained from GIBCO (Milan, Italy). PC-3 were cultured in DMEM high glucose: Ham's F12 (1:1, v/v) supplemented with 50 U/ml penicillin, 50 mg/ml streptomycin, 10% Fetal bovine serum (FBS), 2 mM L-glutamine (growth media) at 37°C in a humidified atmosphere containing 5% CO_2. Cells were transported in low serum RPMI 1640 supplemented with 0.1% FCS, penicillin (50 U/ml), streptomycin (5 mg/ml) and L-glutamine (5 mg/ml) (serum-free media). The cells were washed three times in PBS and then fixed in paraformaldehyde 3.7%/PBS for 10 min. Before performing SERS experiment the fixed cells were dispersed in deionised water, and few drops of the aqueous dispersion were pipetted onto the SERS substrate. Water was allowed to evaporate for 1 h at room temperature.

8.3.2 Raman spectroscopy

The Raman spectrum of the cancer prostate cell was collected in the range 800-2000 cm^{-1}, by using a diode laser excitation source emitting at 532 nm, with 120 s exposure time. The 180° back-scattered radiation was collected by an Olympus metallurgical objective (MPlan 50x, NA = 0.75) with confocal and slit apertures both set to 200 μm. A grating with 600 grooves/mm was used throughout. The SERS spectra were collected in the same condition (objective, grating, hole and slit apertures) but with a diode laser excitation source emitting at 632 nm and an exposure time of 10 s.

8.4 Results and discussion

To demonstrate the feasibility of the fabricated nanostructures as efficient SERS substrates for biological applications, we devised a method to deposit single cells (human prostatic) on the photonic surfaces. An aqueous solution of a deseased prostatic human cell was dropped on a periodic photonic crystal consisting of Au triangles with d=170nm, A=225nm (*Fig. 8.2 a-b*).
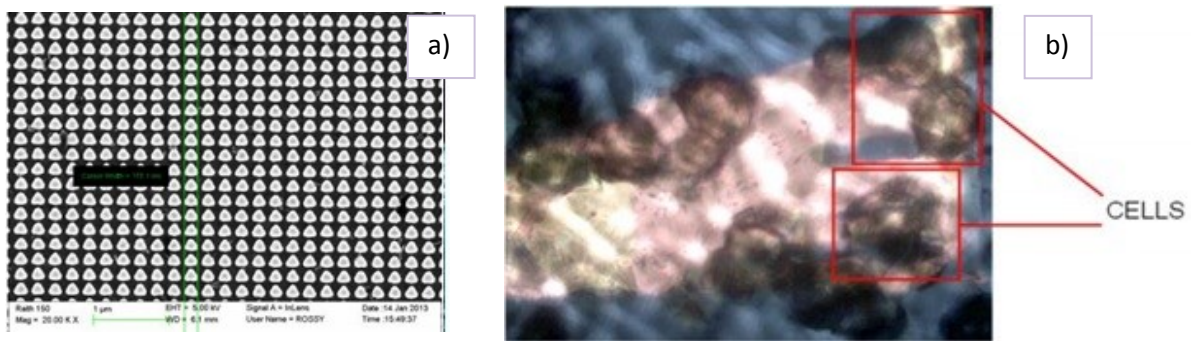
Fig. 8.2: a) SEM micrograph of periodic photonic crystal consisting of Au tringles (side size d=170nm, lattice period A=225nm); b) Optical microscope image (50 x) of cells deposited on the gold triangles periodic photonic crystal

The SEM micrograph of the employed substrate is shown in *Fig. 8.2 a*, while the visible image of the same substrate after cells deposition is presented in *Fig. 8.2 b*. The visible picture collected with the pointing device of the confocal Raman spectrometer, clearly evidences a number of cells lying on the gold nanostructure (the lighter area); these are suitable for Raman analysis. In *Fig. 8.3* is represented the Raman image obtained by confocal sampling of one of the cells highlighted in red in *Fig. 8.2 b*,

Fig. 8.3: Raman image of a single cell deposited on the gold nanostructure. Data collection was made on the middle cell among those highlighted in Fig. 8.2 b. Insets represent the SERS spectra collected at the indicated positions.

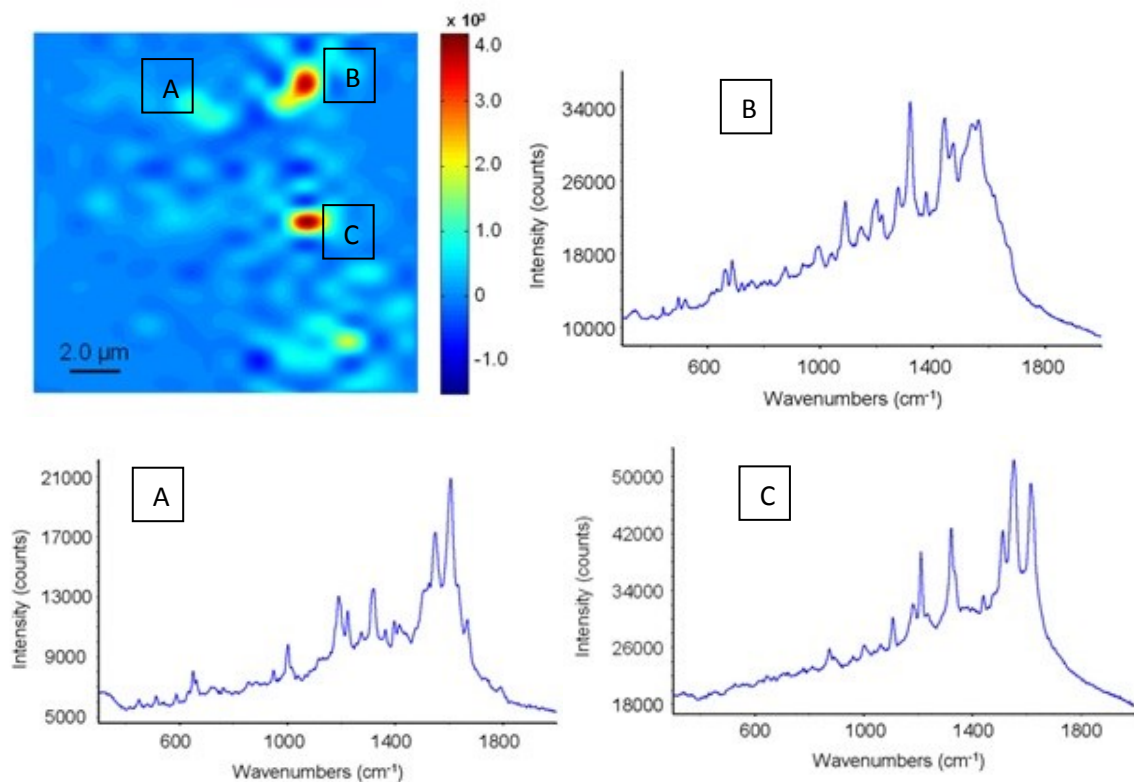Image reconstruction was performed by use of the peak intensity at 1325 cm^{-1}, a signal characteristic of the wagging vibration of CH_2 groups in the glycine unit. Insets A, B and C represent the spectra collected at the indicated positions. Spectra collected at different locations within the cell boundary display a widely variable scattering response. In point C the Raman signal is extremely intense, exceeding 50.000 counts of the CCD detector in the 1500 – 1700 cm^{-1} range [exciting radiation 632 nm (red source); exposure time 10 s]. SERS enhanced fluorescence is also observed in the 400 – 1800 cm^{-1} range.

In *Fig. 8.4* is reported a direct comparison between the spontaneous Raman and the SERS spectrum of a single prostate cell in the 800 – 2000 cm^{-1} range. This comparison highlights the strong enhancement of the Raman signal on the nanostructure and confirms the occurrence of the plasmonic effect for the biological sample under investigation. It provides evidence that a large amount of molecular information on the cellular environment can be accessed in this way.
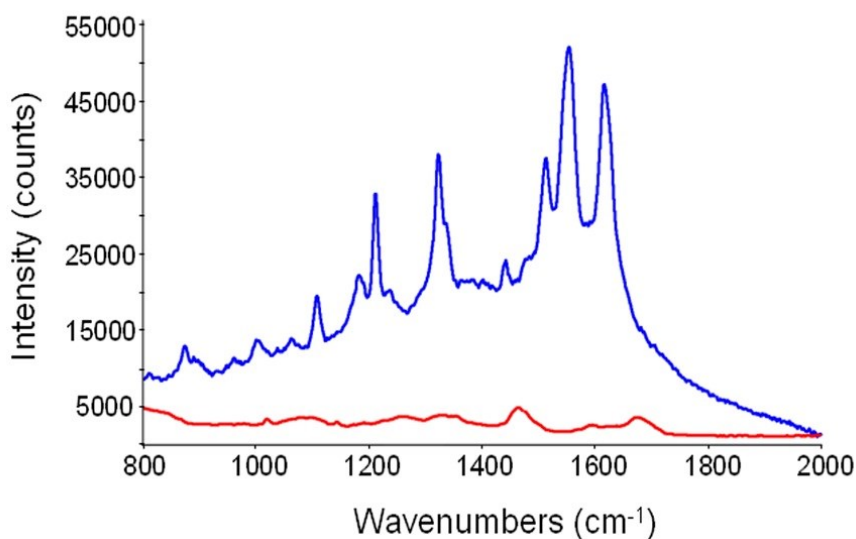
Fig. 8.4: Spectra of prostate cell: Spontaneous Raman (red trace); SERS (blue trace)

In *Fig. 8.5* the spontaneous and the SERS spectra are displayed at full scale (i.e. with the strongest peak corresponding to the maximum of the intensity scale). This comparison emphasizes the similarities and the differences between the two spectra in terms of frequency and intensity. The spontaneous Raman scattering of a single prostate cell (see *Fig. 8.5*, red trace) produces an intensity of about 3000 counts with a 532 nm laser source (green radiation) and an exposure time of 120 s. No signal is detectable with red radiation.

The spontaneous spectrum shows signals from the three major components of the cellular environment, i.e. the nucleic acids (DNA/RNA) at 1318, 1338, 1577 and 1677 cm^{-1}; the proteins at 1000, 1125, 1209, 1250, 1338, 1616, 1665 cm^{-1} and the lipids at 1450 cm^{-1} (see *Tab. 8.1* for a comprehensive assignment of the peaks in the frequency range 1000 – 2000 cm^{-1}). In the SERS spectrum several signals are observed at essentially the same position as in the spontaneous spectrum, namely those at 1000, 1125, 1209, 1337 cm^{-1}. The peak at 1445 cm^{-1} is present but its intensity is barely detectable; the strongest SERS signals are found in the 1550 – 1620 cm^{-1} range, a frequency region characteristic of the amide linkage. In particular, the 1615 cm^{-1} peak is specific of the tyrosine and tryptophan structures, while the component at 1555 cm^{-1} has been attributed solely to tryptophan. The SERS peak at 1512 cm^{-1} is the only one with no direct correspondence in the spontaneous Raman: its origin remains to be clarified [10-12].
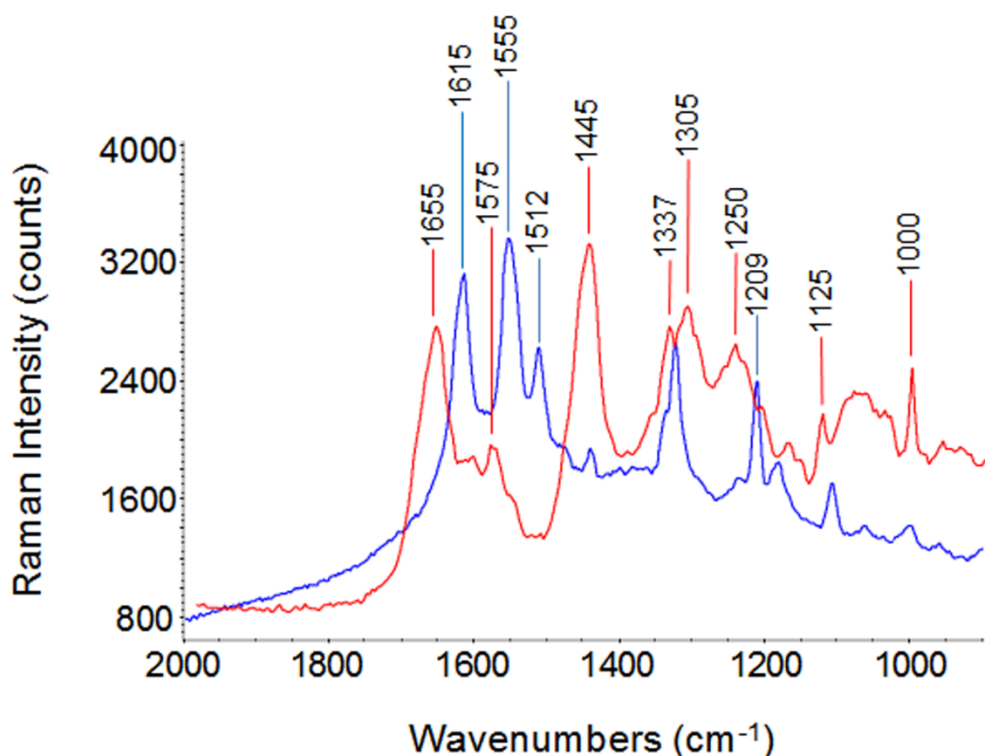
Fig. 8.5: Spontaneous Raman spectra (red trace) acquired with a diode laser source (532nm) and the SERS spectra (blue trace) acquired with a HeNe laser source (632nm) of prostate cell.

Frequency (cm^{-1})	DNA/RNA	Proteins	Lipids
1003		Phe	
1127		ν(C−N)	ν(C−C)
1209		Phe, Tyr	
1245		Amide III, β sheet	
1318	G		
1338	A	Trp	
1450			δ(CH$_2$)
1555		Trp	
1577	A,G		
1616		Tyr, Trp	
1667	T	amide I, β sheet	

Tab. 8.1:Assignement of peaks in the frequency range 1000 – 2000 cm^{-1}

Approximate description of the modes: ν, stretching; δ, bending.

G = guanine; A = alanine; T = thymine; Phe = phenylalanine; Tyr = tyrosine; Trp = tryptophan.

References

[1] T. Vankeirsbilck, A. Vercauteren, W. Baeyens, G. Van der Weken, F. Verpoort, G. Vergote, J. P. Remon, Trac-Trend Anal Chem 2002, 21, 869

[2] L. P. Choo-Smith, H. G. M. Edwards, H. P. Endtz, J. M. Kros, F. Heule, H. Barr, J. S. Robinson, H. A. Bruining, G. J. Puppels, Biopolymers 2002, 67, 1

[3] Sam Lister (February 11, 2009). "Urine test could speed treatment of prostate cancer". London: The Sunday Times. Retrieved 9 August 2010.

[4] "What Is Prostate Cancer?" American Cancer Society, Information and Resources for Cancer: Breast, Colon, Prostate, Lung and Other Forms. Web. 15 June 2010.

[5] "IARC Worldwide Cancer Incidence Statistics—Prostate". JNCI Cancer Spectrum. Oxford University Press. December 19, 2001.

[6] Siegel R, "Cancer statistics, 2011: the impact of eliminating socioeconomic and racial disparities on premature cancer deaths". CA Cancer J Clin 61 (4): 212–36. (2011).

[7] Baade, PD; Youlden, DR; Krnjacki, LJ (February 2009). "International epidemiology of prostate cancer: geographical distribution and secular trends". Molecular nutrition & food research 53 (2): 171–84. doi:10.1002/mnfr.200700511

[8] Haim, Abraham (2013). Light Pollution as new risk factor for human Breast and Prostate cancers. ISBN 978-94-007-6220-6

[9] Bostwick DG1, Burke HB, Djakiew D, Euling S, Ho SM, Landolph J, Morrison H, Sonawane B, Shifflett T, Waters DJ, Timms B., Cancer. 2004 Nov 15;101(10 Suppl):2371-490

[10] A. Taleb, J. Diamond, J. J. McGarvey, J. R. Beattie, C. Toland, P. W. Hamilton, "Raman Microscopy for the Chemometric analysis of Tumor cells, J. Phys. Chem. B 110, 19625-19631 (2006)

[11] H. Hayashi, Y. Nishimura, M. Katahira, M. Tsuboi, "The structure of nucleosome core particles as revealed by differnce Raman Spectroscopy", Nucleic Acids Res. 14, 2583 (1986)

[12] J. M. Benevides, S. A. Overman, G. J. Jr. Thomas, "Raman, polarized Raman and ultraviolet resonance Raman Spectroscopy of nucleic acids and their complexes", J. Raman Spectrosc. 36, 279 (2005)

Chapter 9: Conclusions

9.1 Summary

During the last decade, the tremendous advances in material science and technology have led to the synthesis and implementation of new classes of artificial materials, exhibiting anomalous effects, such as negative refraction, EM band-gaps, optical magnetism - all phenomena not readily available in natural materials at the frequencies of interest. Artificial materials are typically made of ordered or disordered arrangements of elementary electrically-small metallic or dielectric inclusions, spaced by distances which can be of the same order or very small compared to the operating wavelength. Among the possible classes, we have considered here the so-called "photonic crystals" and "photonic quasi-crystals" (PQCs) - also known as photonic band-gap materials - characterized by inclusion spacing of the same order of the wavelength, and the so-called "metamaterials" (MTMs), characterized by inclusion spacing smaller than the wavelength and, thus, describable through effective macroscopic constitutive parameters. The tremendous potentials that such materials have already demonstrated in different application scenarios are now eliciting great interest also in biological sensing. The degrees of freedom offered by artificial materials, in fact, allow an advanced and unprecedented control of the interaction between the EM field and biological matter, enabling the design of innovative EM sensors with superior performance with respect to their traditional counterparts.

One of the important driving forces in biosensor research is to develop large-scale biosensor arrays composed of highly miniaturized signal transducer elements enabling real-time and parallel monitoring of multiple species, especially for high-throughput screening applications such as drug discovery and proteomics research where many thousands of ligand-receptor or protein-protein interactions must be rapidly measured. To address these major challenges, plasmon resonant nanostructure biomolecule hybrids (nanobio hybrids), so-called *plasmonic nanobiosensors*, are being developed and viewed as one key breakthrough area for real-time and parallelized biomedical analysis with high sensitivity and selectivity. This synergetic combination of plasmonic nanostructures, plasmonics, and surface biofunctionalization offers plasmonic nanobiosensors the attractive advantages over other biosensors to better address the major challenges in biosensing. Recently, significant advancements in controlled synthesis and nanofabrication, theory and electrodynamic modeling of optical properties, and surface

functionalization of plasmonic nanomaterials greatly enhanced the ability to control and tune the unique optical and electronic properties of plasmonic nanostructures through their sizes, structures, composition, and shapes, enabling the utilization of huge libraries of probes for different analytes in formats such as microarray, microfluidics, MEMS, etc.

The proposed research activity was based on the development of SERS substrates based on MTMs and aperiodic arrays (PQCs) with different length scales providing a novel strategy to engineer plasmon-enhanced biosensors with chemical fingerprinting capability. The SERS substrates have been characterized by SERS spectroscopy.

Surface-Enhanced Raman Scattering (SERS) spectroscopy is a well-established and highly sensitive technique for investigating the specific vibrational response of a variety of different analytes with fingerprinting accuracy. In particular, the SERS technique has been successfully applied to label-free chemical and biological sensing, where it has proven to be an excellent method for sensing DNA hybridization, protein binding events, and even single molecules. In addition, it bears great promises for rapid identification of viruses and bacteria, potentially enabling whole-organism fingerprinting.

It is now generally believed that the dramatic enhancement of the Raman scattering efficiency observed in SERS experiments is mainly driven by the enhanced local electromagnetic fields in nanostructured metal surfaces. In fact, despite SERS enhancement can also be affected by the specific electromagnetic resonances (EM) of Raman-active molecules and by their direct contact with metal surfaces (chemical enhancement), the dominant factor originates from a resonance effect between the incident and the scattered radiation fields associated to the excitation of surface plasmon resonances. Therefore, in SERS spectroscopy it is of crucial importance to develop systems of interacting metal nanostructures capable of producing high field enhancement with highly reproducible characteristics on controllable metal-dielectric substrates.

9.1.1 Label-free Biosensors Design/Fabrication/Characterization

As SERS effect allows a selective and sensitive detection of low concentrations of chemical and biological analytes through a label-free detection, hence, non-invasive, safe and fast, the development of substrates with high amplification of the Raman signal, highly reproducible and useful also for point-of-care diagnostics is the main key in order to increase the use of this technique in the diagnostic and therapeutic applications.

In this frame, the proposed PhD research activity, articulated in three years, had as main aim to develop "*label-free*" nanosensors represented by **SERS substrates** with high enhancement factor (G_{SERS}), for a chemical fingerprinting of molecules of interest for biological and environmental applications.

These objectives have been achieved through the development of innovative plasmonic nanostructures working in the visible frequency range to realize efficient SERS substrates. Specifically, through the use of photonic crystals and photonic quasi-crystals nanostructures it has been possible to realize novel devices, characterized by a highly selective, sensitive, and tunable in frequency, electromagnetic response with a significant amplification of the SERS signal in presence of a specific analyte (pMA and human prostate cells).

In detail, the research activity has been developed through the following steps:

a. **Fabrication of AgNWs based substrates** by a bottom-up approach consisting in drop-casting a solution of Silver NanoWires dispersed in ethanol on a glass substrate (*Fig. 9.1*).
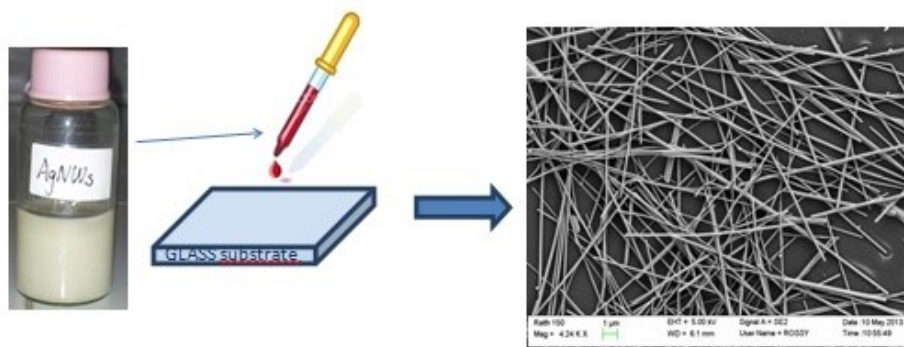

Fig. 9.1 Fabrication process of a AgNWs based SERS substrate

b. **Design and fabrication of the gold PCs and PQCs nanostructures** by a top-down approach exploiting high resolution electron beam lithography (EBL) process combined with a lift-off approach, that is essential to achieve reproducible plasmonic nanostructures. The EBL process is essential to achieve the well-control of size, shape, composition, and configuration of plasmonic nanostructures (*Chapter 6*). More in detail, the fabrication steps (*Fig. 9.2*) are:

1) pattern generation with GDSII editor and fabrication of nano-structures like PC and PQC samples with EBL process;

2) thermal or e-beam deposition of metal films and lift-off processes by physical or chemical attack for the construction of structures made of gold.
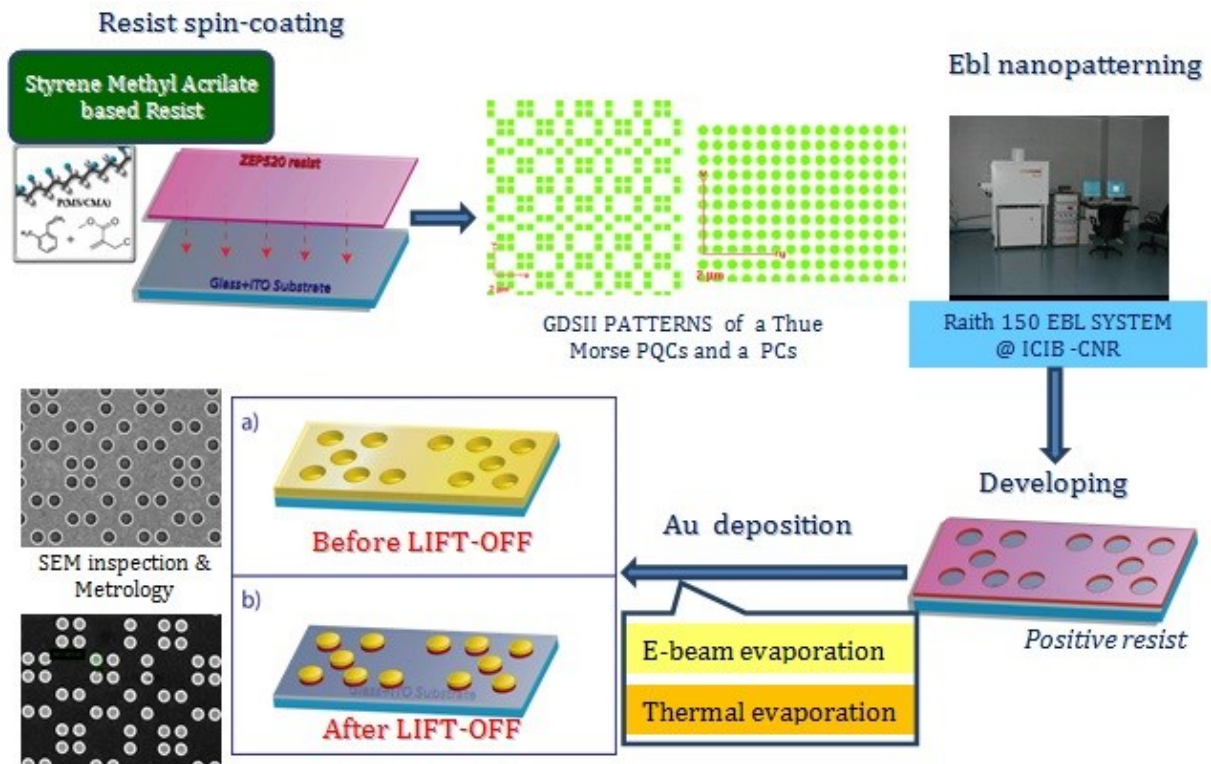
Fig 9.2: Ebl Fabriction process of a plasmonic nanostructure

c. ***Morphological characterization of substrates*** through the use of scanning electron microscope (SEM),metrology of all fabricated samples (*Chapter 6*) and Far Field Diffraction analysis (FFD) of engineered PQCs-based substrates (*Chapter 7*). It should be emphasized that while the SEM allows a local analysis of the structure fabricated, the diffraction pattern obtained by FFD instead provides an information on the whole structure and on the regularity with which the elements are arranged in the metallic matrix. In the Fig. below (*Fig. 9.3*) we reported the gold nanostructures which exhibited the best performances in SERS enhancement.
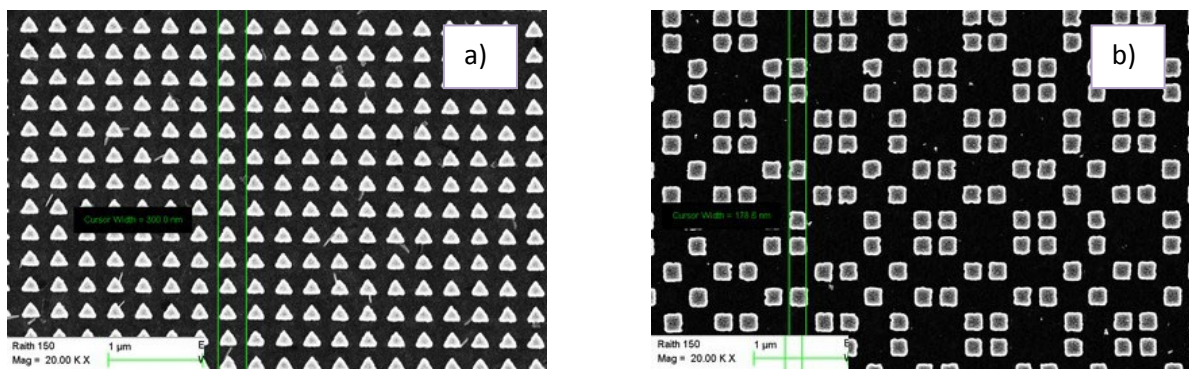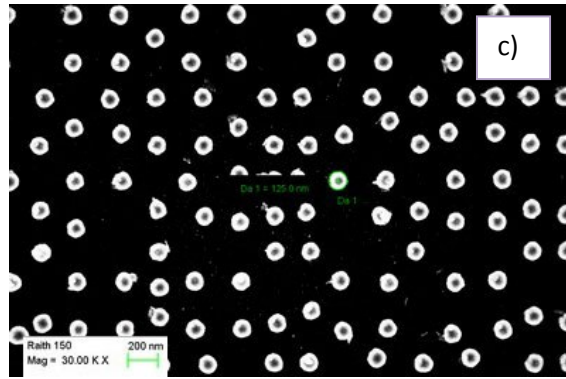
Fig. 9.3: SEM images and metrology analysis of a) Square-based PC array of triangles with side size d=200nm and period A=300nm; b) Thue Morse (ThMo) arrangement od squares with side size d=185nm and minimum interparticle separation s=80nm; c) 8-fold arrangement of cylinder with diameter d=125nm.

d. ***Characterization and validation of the realized substrates as SERS nanosensors*** using Raman spectroscopic system. The p-mercaptoaniline (pMA), has been used as a probe molecule for the determination of the enhancement factor G_{SERS} since such molecule can form a self assembled monolayer (SAM) on gold or silver surfaces. A characterization of the plasmonic surface by means of confocal Raman imaging has also been provided to achieve additional information on the homogeneity of the patterned substrate, which is strictly related to the reproducibility of the system's response. This analysis has been of great importance for the optimization of the functionalization procedures since it has permitted to identify possible defects of the surface. (*Chapter 7*).

The dropped Ag_NWs exhibit an efficient Raman scattering enhancement with a $G_{SERS}=4,7\cdot10^5$ estimated using pMA as a probe molecule which is attributed to the coupling electromagnetic SERS enhancement mechanism with additional localization field within Silver NWs on glass. It is worthwile to underline that nanowires size dispersion and position randomness limit the reproducibility of this approach. On the other hand, we have demonstrated experimentally measured SERS enhancement:

1) *$G_{SERS}=1,3\cdot10^7$* in lithographically defined Square-based periodic PCs of triangular shape rods with diameter d=200nm and pitch A=300nm (*Fig. 9.4 a-b*);

2) *$G_{SERS}=1,4\cdot10^7$* in Thue Morse (ThMo) PQC arrays of Au nanocylinders with 185nm side size and 80nm minimum interparticle separation (*Fig. 9.4 c-d*);

3) *$G_{SERS}=1,4\cdot10^8$* in 8-fold PQC arrays of cylinders with diameter d=125nm and FF= 0.18 (*Fig. 9.4 e-f*).

The resulting PQC nanostructured films, both ThMo and 8-fold arrangements, can serve as good SERS substrate, exhibit large electromagnetic field enhancement factors for pMA, and

can readily be used in ultrasensitive, molecule-specific sensing utilizing vibrational signatures.
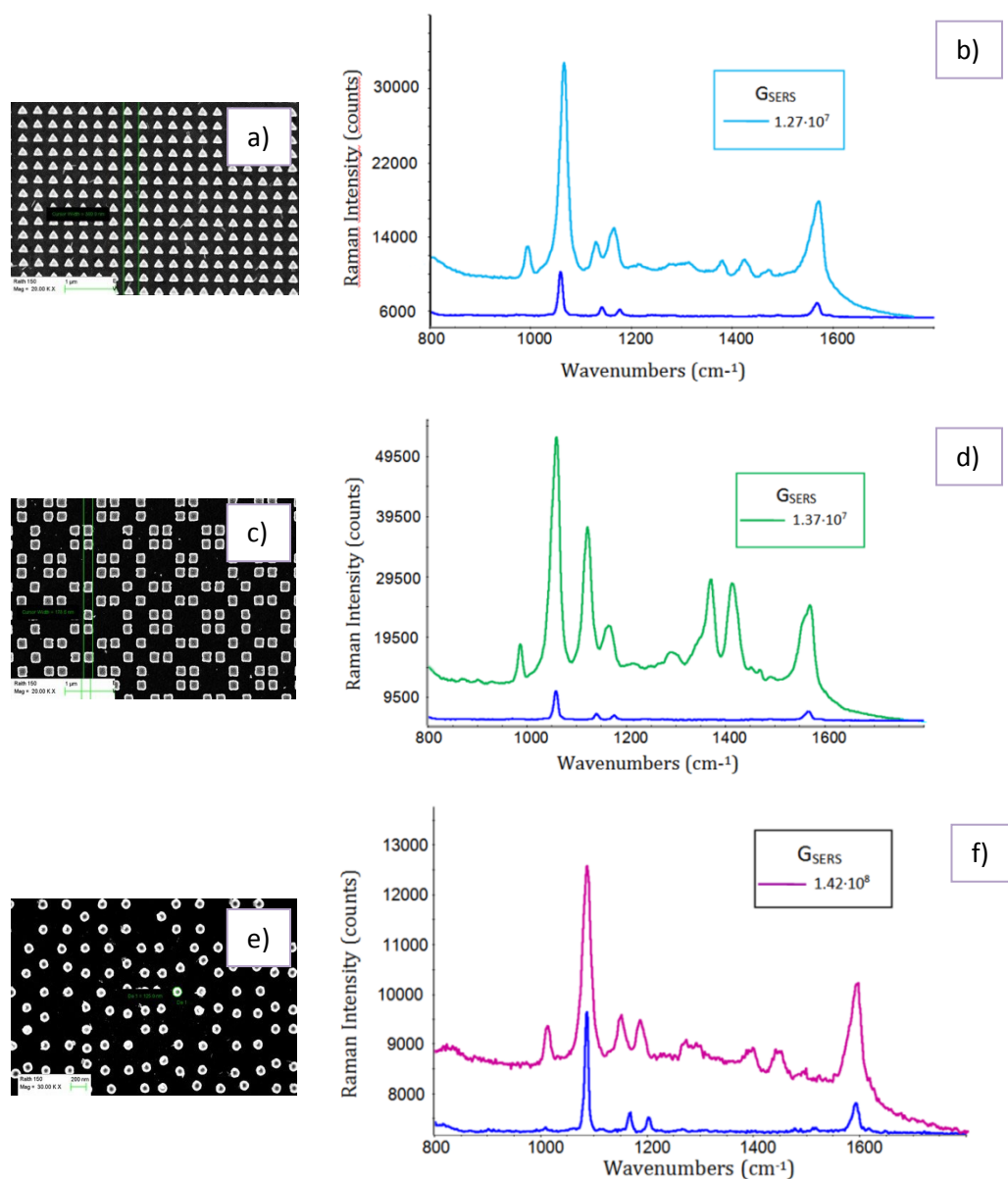

Fig. 9.4: Best results achieved in SERS enhancement: (a-b) Square-based PC array of triangles with side size d=200nm and period A=300nm; (c-d) Thue Morse (ThMo) arrangement od squares with side size d=185nm and interparticle separation s=80nm; (e-f) 8-FOLD PQCs of cylinders with d=125nm

In order to confirm the quality and homogeneity of the realized engineered nanostructures, a x,y mapping measurement has also been performed. x,y map of the engineered arrangement of gold nanoparticles (*Fig. 9.5 a*) is compared with that of Ag_NWs substrate (*Fig. 9.5 b*). The former shows regions of intense SERS activity uniformly distributed within the sampled area and representing the majority of the analyzed surface. The latter shows a pattern much more

heterogeneous, with two well defined regions of very high SERS activity (red colored) embedded into a background where the signal is essentially absent (blue colored). This result confirms the better performances of the engineered substrates in term of reproducibility and homogeneity.
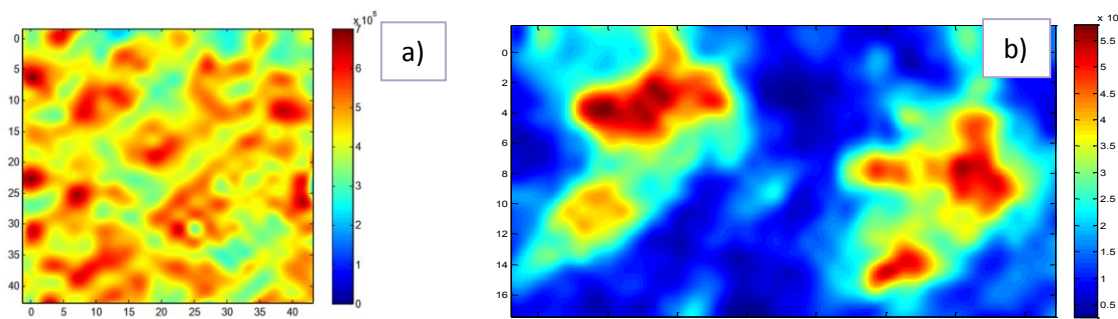

Fig. 9.5: x,y mapping for a) Thue Morse PQCs of squares (d=185nm) and b) Ag_NWs substrate

e. ***Surface activation of nanostructures for the detection of specific analytes*** of interest for biological applications, for instance human deaseased prostate cells (*Chapter 8*). To demonstrate the feasibility of the fabricated nanostructures as efficient SERS substrates for biological applications, we devised a method to deposit single cells (human prostatic) on the photonic surfaces. An aqueous solution of a deseased prostatic human cell was dropped on a periodic photonic crystal consisting of Au triangles with d=170nm, A=225nm In *Fig. 9.6* is reported a direct comparison between the spontaneous Raman and the SERS spectrum of the cell in the 800 – 2000 cm^{-1} range. This comparison highlights the strong enhancement of the Raman signal on the nanostructure and confirms the occurrence of the plasmonic effect for the biological sample under investigation. It provides evidence that a large amount of molecular information on the cellular environment can be accessed in this way.
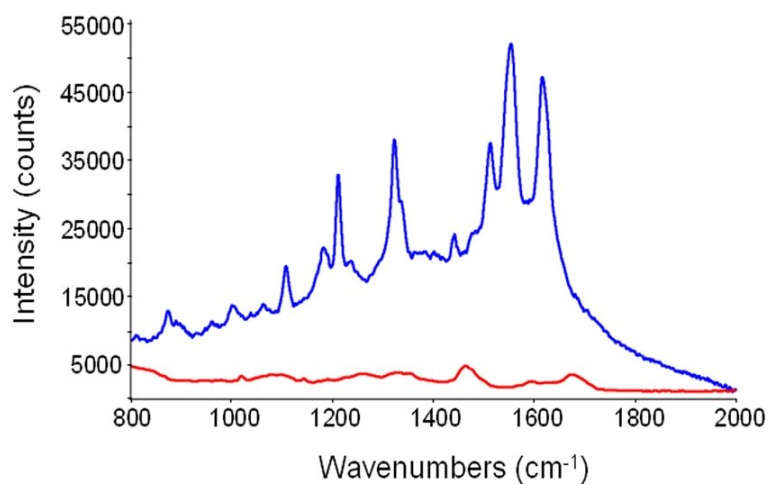

Fig. 9.6: Spectra of prostate cell: Spontaneous Raman (red trace); SERS (blue trace)

9.2 Future work

All the obtained results confirm the occurrence of the plasmonic enhancement effect for the biological samples under investigation, and provide evidence that a large amount of molecular information on the cellular environment can be disclosed in this way. We believe that the present approach is very promising and more convenient, in principle, than the conventional SERS sampling of biological systems, consisting in a homogeneous dispersion of colloidal gold particles in the samples. This ultrasensitive Raman probe can be used to monitor subtle molecular changes in the cell and opens up interesting new opportunities in the early diagnosis of diseases (e.g. tissue analysis). In the next few months other improved SERS substrates will be realized and characterized through Raman Spectroscopy with both biological materials (cells and tissues) and with some kind of pesticides to investigate water pollution. Based on these results and insights, there are several directions for future exploration and development. The first suggested projects described below describe possible improvements to the underlying technology, with an emphasis on device design, simulation approaches, and fabrication methods. We then describe extensions of this work that would address various biomedical applications, focusing on a few key areas where the cost-effectiveness and multi-modality capabilities of such a platform have the potential to disrupt existing markets and enable new functionality.

9.2.1 Increased simulation and Design capabilities

To improve the limit-of-detection, we would like to maximize the field intensity in areas of the sensor that are accessible to analytes. Modern simulation tools are just now becoming fast enough to enable the optimization of geometric and materials parameters of structures like photonic crystal slabs. This will allow for more efficient design of future structures; however, additional simulation tools are needed to ensure designs that are robust to testing conditions. Based on our experiments, we describe here some key simulation tool functions that would enable more effective optical biosensor design. Regarding theoretical, phenomenological, and simulation aspects related to PCs and to PQCs, we propose to focus on the optimization of nanoparticles (NP) shapes and geometrical arrangements for the control of plasmonic resonances and broadband field enhancement respectively. Modelling of the nanostructures consisting of metallic inclusions working at visible frequencies will be performed using the Fullwave FDTD simulation. As far as PQCs, we intend to explore the properties of resonances

by varying the geometrical and constitutive properties of the structures, as well as the surrounding environment. Additionally, different lattice geometries based on aperiodic tilings (dodecagonal, etc.) will be studied highlighting similarities and differences with respect to the periodic and aperiodic cases already examined. Also in this case, the ultimate goal will be the identification of configurations that maximize the local field EM enhancement and radiation EM in order to have the strongest SERS response. In the design task, numerical simulations of the frequency response of the nanostructured substrate will be performed in order to maximize the detected SERS signal. This optimization will be done using the Fullwave Finite Difference in Time Domain technique - FDTD and Finite Elements Methods - FEM simulations by studying the frequency response variation of the structures, when varying the geometrical and constitutive properties of the structures, i.e the lattice elements shape and the lattice geometry, as well as the surrounding environment, that will simulate the biological fluid where the molecules in analysis are dispersed. In fact a stable and reproducible surface Raman enhanced signal depends on the shape and distribution of the gold nanoparticles of the PQCs and PCs lattice on which the metallic inclusions are deposited. Specifically, the coupling between PCs or PQCs resonances and the plasmonic Raman signal inhibits the leakages due to the transmission through the structure and allows strong and narrowband field localization in lattice defects that makes the SERS substrate highly sensitive and selective for the sample under analysis. In conclusion, the ultimate goal will be the identification of the configurations that maximize the amplification of the local electromagnetic field in order to obtain a SERS signal as highest as possible.

9.2.2 Interface with Biology and Users

The development of sensors that allow the rapid detection of pathogens in agricultural, veterinary, environmental and especially medical has a very important social, economic and technological impact, since a suitable prevention and diagnostic determine not only an appropriate and effective intervention and, in a lot of the cases, the survival of people and animals or the preservation of common goods, but has a significant effect on the cost of health care in general and on national economic budget. Many diseases with a great impact on the population, such as cardiovascular disease, diabetes or cancer, to name but a few, or even the detection of toxic substances or drugs at low concentrations, depending on the case, require high sensitivity and selectivity, timely intervention, daily or frequent point-of-care analysis (for example in the case of glucose monitoring done by diabetic patients themselves) low cost

and finally non-invasive methodologies in order to limit both the discomfort caused to patients and the increase in the probability of contracting infections due to same mode of diagnosis.

In this scenery, the biosensors are found increasingly acclaim in the environments of research and marketing for the relative ease of implementation and for the low cost of production.

Among them, in last years, the nanosensors SERS based appear to be very attractive because they combine the compactness with a high sensitivity. Compared to other analytical techniques, SERS has high sensitivity and selectivity for different types of target, allows a fingerprint of the molecules investigated and, moreover, it has the considerable advantages of "label-free" detection hence non-invasive, safe and fast. Also the development of systems that allow the application of this technique outside laboratories, contributes, in many cases, to significantly decrease the costs associated with this type of analysis and to perform investigations not executable in the laboratory. Moreover, it should be added that the development of such technology in recent years has stimulated a dynamic interaction between physicists, chemists and biologists, contributing, therefore, to strengthen cooperation and dialogue within the scientific community. It is noted, that in general, the study and development of nanopatterns with electromagnetic properties of interest, envisaged in this project, has a relapse in science and technology for the development of sensors of different type. For these reasons, we believe that the objectives of this project to achieve high efficiency nanostructured SERS sensors and devices that make them implementable even on portable Raman systems fully meet the current needs of the market and research.

9.2.3 Start up of the Research Project "Study on the immunological detection technology of tumor marker based on SERS characteristics of gold nanoparticle array"

Last but not least there will be the participation to the Major International Joint Research Project titled: "*Study on the immunological detection technology of tumor marker based on SERS characteristics of gold nanoparticle array*", Project grant number: 601320106014, proposed by Prof. J. Zhou of the Photonics Institute of the University of Ningbo City (Zhejiang Province, PRC), with a duration of four years (2014-2018) and funded by the National Nature Science Found of China. The Italian partner of this project is ICIB-CNR (PI: L. Petti).

Abstract: Cancer is a serious threat to human health, has become a major cause of death worldwide. Early diagnosis and treatment of cancer is the key to improve the survival rate of patients with cancer for five years, measuring technique and instruments is an urgent need to develop applied in early screening for cancer. The noble metal nanoparticles with localized surface plasmon resonance (LSPR) and surface enhanced Raman scattering (SERS) properties, application in biosensor has become an important research focus. This project will research on the effects of characteristics parameters of gold nanoparticle array and gold nanoparticles, their structure, dielectric properties and dielectric environment on the LSPR and SERS properties, in-depth understanding of physical mechanism of biological sensor based on LSPR-SERS effect, optimization design of gold nanoparticles and gold nanoparticle array structure; according to the modern immunology principle, using physical and chemical methods to synthetise the gold nanoparticles and fluorene-based fluorescent dye, and fabricate the SERS immune substrate of gold nanoparticles array and marked/unmarked immune probe, development the Raman spectroscopy measurement and analysis technology of immunological characteristics of tumor marker, reaching the single molecule detection level with the magnitude of fg/ml ultra high sensitivity. In this project, the investigation of biological immune sensing based on the LSPR-SERS effect of noble metal nanoparticles will be helpful to the development of high sensitive optical sensor for tumor markers, which will lay a important theoretical and technical foundation for the early detection and diagnosis of cancer.